Spectral and Temporal Studies of Supermassive Black Holes

COLLINSON, JAMES,STUART

Spectral and Temporal Studies of Supermassive Black Holes

James Stuart Collinson

Abstract

In this thesis, I present analysis and interpretation of the multiwavelength spectra and variability of Active Galactic Nuclei (AGN). The most luminous sustained sources in the Universe, these powerful objects are consistent with being the result of gas accretion on to central galactic supermassive black holes. Due to their compact sizes, the inner regions of AGN cannot be spatially resolved by conventional means, so we must instead use spectroscopy and temporal monitoring to determine their composition and structure.

I undertake a number of studies of the spectral energy distributions (SEDs) of AGN, using data from infrared–X-ray bands and employing a range of numerical models. Results from SED modelling of 11 moderate redshift ($1.5 < z < 2.2$) AGN are presented, in which there is a selection bias towards nuclei with cooler accretion discs. I find that the peak of the SED is sampled by our data for 5/11 objects, thereby breaking several of the model degeneracies that affected previous studies. This results in stronger constraints on the physical processes at work in these AGN, and provides a powerful tool with which I examine and discuss the relationships between the various radiating components, including those of the emission line regions, dusty torus and host galaxy. I then explore the nature of four 'hypervariable' AGN, for which the origin of their extreme variability is currently unknown. Through an investigation of their SEDs, I find that either an accretion rate change, or gravitational microlensing by a star in a foreground galaxy, are energetically consistent with the data.

The new insights provided by this work lead me to suggest several worthwhile routes for the future development of research in these areas. With the next generation of telescopes, satellites and surveys on the horizon, it will be possible to build on my results, to further our understanding of AGN.

Spectral and Temporal Studies of Supermassive Black Holes

James Stuart Collinson

A thesis presented in accordance with the regulations for admittance to the degree of Doctor of Philosophy

Centre for Extragalactic Astronomy
Department of Physics
University of Durham
United Kingdom

July 2016

Dedicated to

My family and friends

Declaration

The work described in this thesis was undertaken between 2012 and 2016 while the author was a research student under the supervision of Prof. Martin Ward in the Department of Physics at Durham University. No part of this thesis has been submitted for any other degree at Durham University or any other university.

Portions of this work appear in the following papers:

- *Reaching the peak of the quasar spectral energy distribution – I. Observations and models*, **James S. Collinson**, Martin J. Ward, Chris Done, Hermine Landt, Martin Elvis and Jonathan C. McDowell, 2015, MNRAS, 449, 2174 (Chapter 3)

- *Reaching the peak of the quasar spectral energy distribution – II. Exploring the accretion disc, dusty torus and host galaxy*, **James S. Collinson**, Martin J. Ward, Chris Done, Hermine Landt, Martin Elvis and Jonathan C. McDowell, 2016, accepted for publication in MNRAS (Chapter 4)

- *The broad-band SEDs of four hypervariable quasars*, **James S. Collinson**, Martin J. Ward, Andy Lawrence, Alastair Bruce, Chelsea L. MacLeod, Martin Elvis, Suvi Gezari, Philip J. Marshall and Chris Done, 2016, submitted to MNRAS (Chapter 6)

Additionally, the work presented in the final section of Chapter 5 is to appear as part of Kelly Denney et al. (in preparation).

The work in this thesis is entirely that of the author unless mentioned otherwise in the text. It has been made possible by the support of STFC grant number ST/K501979/1.

Acknowledgements

Firstly, I owe a great deal of gratitude to my supervisor Martin Ward, for his excellent guidance over the past few years. I could not have put this research together without his insightful comments, boundless knowledge and relaxed approach to management. Thanks must also go to Hermine Landt for her patience and wealth of ideas, and Chris Done, for her non-stop enthusiasm as my 'unofficial' co-supervisor. Many meetings with these three would begin with my preconceived idea of the route ahead being turned on its head, but by their conclusion I would always leave knowing that 'science just happened.' It was a pleasure to have the opportunity to work with Andy Lawrence and his team in Edinburgh, and I'm grateful to Alastair Bruce for showing me the ropes during that first observing run on La Palma, even if the weather conditions left a little to be desired.

There are many others who helped me along this journey – I found everyone willing to offer any advice they could, and everyone is a credit to the department. Thanks in particular go to Charles, Chris H., Jin and Mark S., for all of your advice on computing. My course mates at Durham have been a constant source of inspiration, as we all weathered the highs and lows of Ph.D. life together. Ben, Flora, George, Jack, Rob, Steve, Tom and Will – thank you for being such a great support group. Similarly, my office mates, past and present, have been brilliant; thanks Junayd, Emma, Ady, Greg and Daniel (plus the Andys and Hannah – and Ben and Flora again – who might as well have been office mates) for all of the hilarious conversations and truly exceptional/awful quotes that cultivated such an enjoyable working environment. Outside of the department, being a part of Grey College these past years has given me friends from all corners of the world. The times we spent together, in Durham and elsewhere, were an absolute blast.

Finally, I am hugely grateful to my family for your unwavering support. Thanks Mum and Dad for always allaying my doubts and encouraging me to pursue my aspirations, but mainly for showing me how to be the best I can be.

Contents

List of Tables **ix**

List of Figures **x**

1 Introduction **1**

1.1 Overview 1
1.2 Active Galactic Nuclei 2
1.3 AGN Emission across the Electromagnetic Spectrum 10
1.4 Measuring the Black Hole Mass in AGN 19
1.5 The Role of AGN and their Physics 23
1.6 This Thesis 24

2 Facilities, Instruments, Observations and Models **27**

2.1 Overview 27
2.2 Multiwavelength Data 28
2.3 Temporal Data 38
2.4 Models 39

3 AGN SEDs Part 1: Reaching the Peak **47**

3.1 Introduction 47
3.2 Sample and Data Assembly 50
3.3 Black Hole Mass Estimates 56
3.4 Bolometric Luminosity 60
3.5 Discussion 70
3.6 Summary and Conclusions 78

4 AGN SEDs Part 2: Exploring the Accretion Disc, Torus and Host Galaxy 81
4.1 Introduction . . . 81
4.2 Testing the SED Model . . . 85
4.3 Torus and Host Galaxy . . . 98
4.4 Variability . . . 101
4.5 Spectral Decomposition . . . 103
4.6 Discussion . . . 107
4.7 Summary and Conclusions . . . 126

5 AGN SEDs Part 3: Pilot Studies and Future Work 128
5.1 Introduction . . . 128
5.2 Large High-redshift Sample . . . 129
5.3 Pilot Study: The FUV SED of Two AGN . . . 133
5.4 The Low Accretion State of Mrk 590 . . . 141

6 The Broad-band SEDs of Four Hypervariable AGN 144
6.1 Introduction . . . 144
6.2 Sample and Observations . . . 147
6.3 Light Curves . . . 147
6.4 Estimating Black Hole Mass in HVAs . . . 150
6.5 X-ray Spectrum and Variability . . . 155
6.6 Broad-band Spectral Energy Distribution . . . 157
6.7 Discussion . . . 162
6.8 Summary and Conclusions . . . 167

7 Summary and Future Work 168
7.1 Synopsis of Key Findings . . . 168
7.2 The Future and Concluding Remarks . . . 171

Bibliography 173

Appendix 186

A Spectral and Photometry Data from Chapter 3 186
A.1 Observation Dates . . . 186
A.2 Spectra and Photometry Plots . . . 187

List of Tables

2.1 SED model parameters 42
2.2 Attenuation model parameters 45
3.1 Names, positions, redshifts and data sources for the sample of 11 objects . 52
3.2 Optical/IR spectral observation dates for the 11 AGN 55
3.3 Hα line measurements and $M_{\rm BH}$ estimates for the sample 59
3.4 Best-fit parameters for the X-ray spectral analysis 60
3.5 Optimum fitted parameters for the SED models 65
3.6 SED model properties 66
4.1 Optical/IR continuum regions used in the SED fitting 86
4.2 Optimum fitted parameters for the refined SED model 90
4.3 Key properties of the refined SED model 91
4.4 AGN/host galaxy/torus luminosities and dust properties 99
5.1 The two AGN with *HST*/COS, *XMM* and SDSS data 135
5.2 *HST*/COS objects: optimum SED model parameters 139
5.3 Optimum AGN SED model parameters for Mrk 590 142
6.1 The sample of HVAs; names, positions, redshifts and X-ray observations . 147
6.2 The key *r*-band magnitudes for the four HVAs 149
6.3 Measured line properties and $M_{\rm BH}$ estimates of the four HVAs 154
6.4 Best-fit parameters for the HVA X-ray spectral analysis 156
6.5 Optimum fitted parameters for the HVA SED models 160
A.1 Data sources and observation dates for Chapter 3 sample 186

List of Figures

1.1 Artist's impression of AGN on Durham Cathedral 2
1.2 The unified model of AGN 9
1.3 Simplified sum-of-blackbodies accretion disc SED 12
1.4 Vanden Berk (2001) optical–UV AGN spectral template 14
1.5 Broad-band AGN SED 17
2.1 Gemini North Telescope 28
2.2 William Herschel Telescope 32
2.3 Photometric and spectroscopic instrument coverages 35
2.4 The OPTXAGNF SED model 41
2.5 Comparison of MW, LMC and SMC extinction curves 44
3.1 Balmer line decomposition for J2328+1500 59
3.2 Data and SED fits: Model 1 67
3.3 Data and SED fits: Model 2 68
3.4 Data and SED fits: Model 3 69
3.5 SED Model Residuals 71
3.6 Potential host galaxy contributions to SED 74
3.7 X-ray spectra from different dates 76
3.8 Comparison of SMC and MW extinction curves for J1044+2128 77
3.9 Comparison of SMC and MW extinction curves for J1350+2652 78
4.1 Continuum sampling of MW, SMC and LMC extinction curves 89
4.2 SED dependence on $M_{\rm BH}$ 92
4.3 SED dependence on spin 95
4.4 SED dependence on $r_{\rm out}$ 97

4.5 Measured $r_{\rm out}$ compared to self-gravity radius 97
4.6 SED models including torus and host galaxy components 100
4.7 Examples of variable objects in the sample 102
4.8 IR–optical spectral decompositions 105
4.9 Dependence of $\dot{m}$ on $M_{\rm BH}$ 108
4.10 Photon index against Eddington ratio for the sample 108
4.11 Dependence of various BC factors on $\dot{m}$ 110
4.12 SED dependence on large changes in $M_{\rm BH}$ 113
4.13 Comparison of OPTXAGNF with OPTXCONV for high spin BHs 116
4.14 Measured host galaxy luminosities compared to literature 119
4.15 [O III] equivalent width against SED properties 122
4.16 Measured FWHM relations compared to Shen & Liu (2012) 123
4.17 Measured luminosity relations compared to Shen & Liu (2012) 125
5.1 Redshift distribution of the new sample of 233 AGN 131
5.2 Distribution of $M_{\rm BH}$ and $\dot{m}$ for the new sample 132
5.3 *HST*/COS objects: line fits for $M_{\rm BH}$ estimates 136
5.4 *HST*/COS spectrum of QSO J1208+4540 137
5.5 *HST*/COS spectrum of QSO B1630+3744 137
5.6 SED model of QSO J1208+4540 140
5.7 SED model of QSO B1630+3744 140
5.8 Mrk 590 in the low state 143
6.1 Long-term light curves for the four HVAs 149
6.2 LT light curves for the four HVAs 150
6.3 Line fits for HVA $M_{\rm BH}$ estimates 153
6.4 SED models for both unlensed and lensed scenarios 161
6.5 $L(\nu)_{\rm 2keV}$ against $L(\nu)_{\rm 2500\AA}$, compared to Lusso et al. (2010) sample . . . 162
6.6 $\alpha_{\rm OX}$ against $L(\nu)_{\rm 2500\AA}$ 163
6.7 $\alpha_{\rm OX}$ against $L(\nu)_{\rm 2keV}$ 163
A.1 All spectral and photometry data for Chapter 3 sample 187

CHAPTER 1

Introduction

1.1 Overview

At the centre of almost every galaxy, there is a supermassive black hole (SMBH). In some galaxies, large amounts of gas and dust fall under gravity towards this BH from great distances. As it falls, this matter attains tremendous velocities, and collisions between the gas and dust particles heat them to extreme temperatures. This superheated material emits enough thermal radiation to be visible across cosmic distances, thus forming an active galactic nucleus (AGN).

The study of the SMBHs powering AGN is a key means of illuminating the unknowns in modern physics. With implications for understanding the processes of galaxy formation and evolution in the Universe, these extreme objects lie at the edge of knowledge, where experimental and observational aspects of the subject confront each other.

But uniting what we observe with our various models remains a continuous challenge. The distances to these objects are so great that telescopes cannot resolve in sufficient detail their arrangement, and we must instead rely on more subtle analyses of spectra, and time-dependent brightness variation, to learn more about these galactic power plants.

Figure 1.1: A computer-generated image of an accreting SMBH, projected on to Durham Cathedral as part of the 2015 Lumiere light festival.

1.2 Active Galactic Nuclei

1.2.1 Black Holes

A black hole (BH) is formed when an amount of matter occupies a small enough volume in space that no physical force can prevent it from collapsing under its own gravity. This matter therefore shrinks to form a singularity – a point in space occupying zero volume, but still containing all of the precursory matter. The singularity is bounded by a theoretical surface, called the event horizon, at which the escape velocity is the speed of light (c). For this reason, nothing at the event horizon, including light, can escape the BH.

The existence of classical objects with escape velocities of c or greater was first proposed towards the end of the 18th century, by two scientists, Pierre-Simon Laplace and John Michell. Separately, they suggested that such objects could emit no radiation, if it was assumed that light obeyed the law of gravitation. The idea did not gain much attention at the time, as it was not directly testable, but the publication of the theory of general relativity (GR) 100 years ago (Einstein 1916) provided the first mathematically coherent prediction of BHs.

In 1908, astronomer Edward Fath observed that the 'spiral nebula' NGC 1068 was spectroscopically distinct from other nebulae, and notably included several emission features, in addition to the more familiar absorption features (Fath 1908). Fath had inadver-

tently discovered the first evidence of astrophysical BHs in the Universe. Several years later, in 1922, Edwin Hubble made new observations of spiral nebulae in the night sky, discovering for the first time that these "Island Universes" were a plethora of galaxies much more distant than the Milky Way (MW; Hubble 1922). Not only this, but Hubble realised that the galaxies were receding from us, in all directions, at a rate that increased with distance. This lead to the groundbreaking conclusion that the Universe is expanding. Hubble's seminal discovery firmly established the field of extragalactic astronomy, and paved the way for research into the nature of the Universe.

In Seyfert (1943), Karl Seyfert published his observations of 12 galaxies with strong, broad, nuclear emission lines. Seyfert noted that the lines were broadened, "presumably by Doppler motion." Most of the emission in Seyfert's objects originated in the galaxies' nuclei, which could have luminosities comparable to, or greater than, the luminosity of the entire rest of the galaxy. With increasingly advanced technology available to astronomers following World War II, new phenomena were discovered, including quasars (or 'quasi-stellar objects,' QSOs) and radio-loud galaxies. In 1964, Edwin Salpeter posited that accretion of gas on to sufficiently "massive objects" could be the means by which quasars acquired their huge luminosities (Salpeter 1964, Lynden-Bell 1969).

It is now widely accepted that gas accreting on to BHs and other compact objects is indeed the mechanism underlying a multiplicity of luminous astrophysical sources, from the quasars and Seyfert galaxies that fall under the category of AGN, to X-ray binaries and cataclysmic variable stars. Monitoring stellar motions in the heart of the MW has provided perhaps the most unambiguous evidence for a 4×10^6 solar mass ($M_\odot$) BH at the Galactic centre (Schödel et al. 2002, Gillessen et al. 2009). We therefore only observe BHs indirectly, by the impact they have on their surroundings.

Intrinsically, a BH has just three properties – mass, angular momentum, and charge. This is the 'no-hair' theorem; all other information about the progenitor material, and indeed any matter that falls into a BH, from chemical composition to thermal and mechanical properties, is lost (e.g. Netzer 2013).

The mass and charge are scalar properties denoted $M_{\rm BH}$ and Q respectively. The matter that forms and falls into astrophysical BHs is net-neutral, and so it is usually assumed that $Q = 0$. Angular momentum can be represented by the three dimensional vector,

$\underline{J}$, however, in astrophysics it is more normally expressed as the dimensionless 'spin' parameter, a_*, given by:

$$a_* = \frac{|\underline{J}|}{M_{\rm BH}}. \tag{1.2.1}$$

In addition to these physical properties, it is useful to define the Schwarzschild radius, $R_{\rm s}$, as:

$$R_{\rm s} = \frac{2GM_{\rm BH}}{c^2} \tag{1.2.2}$$

where G is the gravitational constant. $R_{\rm s}$ is the radius of the event horizon of a BH, and therefore if any massive object is smaller than its $R_{\rm s}$, it is, by definition, a BH. It is named after the physicist Karl Schwarzschild, who first derived $R_{\rm s}$ by solving the equations of GR for a non-spinning BH (Schwarzschild 1916). A more common distance used in this thesis is the gravitational radius:

$$R_{\rm g} = \frac{1}{2}R_{\rm s} = \frac{GM_{\rm BH}}{c^2} \tag{1.2.3}$$

which provides a convenient unit of distance measurement relating to a BH.

According to GR, gravity is an expression of the way matter curves space and time. BHs interact through gravity in the same way as all matter; if the Sun were instantaneously replaced by an equivalent mass BH, the dynamics of the solar system would go largely unchanged, as the population of planets, asteroids and comets would experience the same gravitational centripetal force keeping them in their current, quasi-stable orbits. However, as we consider circular orbits around a BH at smaller and smaller distances from the event horizon, there comes a point in GR where such orbits become unstable. The final radius at which a point particle can be in a stable orbit is known as the 'radius of innermost stable circular orbit,' $r_{\rm isco}$.

Spinning BHs (i.e. $a_* \neq 0$) differ from non-spinning (Schwarzschild, $a_* = 0$) BHs in terms of $r_{\rm isco}$. Kerr (1963) generalised the result of Schwarzschild (1916) for spinning BHs, in which the spin information is imprinted on the distorted spacetime just outside the event horizon. For a particle orbiting a Schwarzschild BH, $r_{\rm isco} = 6R_{\rm g}$, but a circular orbit around a spinning BH can be stable at smaller radii, if the particle is orbiting in the same direction as the BH is spinning. For a maximally spinning BH, $a_* = 0.998$, and

stable, co-rotational orbits can exist down to $r_{\rm isco} \simeq 1.24 R_{\rm g}$. Conversely, counter-rotating orbits around spinning BHs become unstable at larger radii than $6R_{\rm g}$. In such cases, it is taken that $a_* < 0$, with the minimal value $a_* = -1$ corresponding to $r_{\rm isco} \simeq 9R_{\rm g}$. The spin cannot exceed these limits due to the counter-torque from radiation emitted by accreting matter (Thorne 1974).

Given these basics, I will now more closely examine the physics of accretion and energy release in astrophysical BHs.

1.2.2 Accretion on to Black Holes

BHs cannot be directly observed, but their immense gravitational impact on nearby matter provides key observables that are partially understood. I have already noted that stars in the vicinity of the SMBH at the centre of the MW trace elliptical orbits that we can monitor, and Keplerian motion of stars and gas in local galaxies can be resolved using spectroscopy (Harms et al. 1994, Walsh et al. 2012). The recent detection of gravitational waves from two merging BHs opens another observational window on the Universe, which, when the interferometers that search for these phenomena are operating at full sensitivity, ought to produce many more such discoveries (Abbott et al. 2016). Finally, gas and dust accretion on to BHs provides observables that I will explore in this section.

There are two known classes of BH in the Universe, stellar mass BHs and SMBHs. They are distinguished by $M_{\rm BH}$ alone; whilst stellar mass BHs have $M_{\rm BH}$ in the (order of magnitude) range $1 - 100\,M_\odot$, SMBHs are typically of $10^5 - 10^{10}\,M_\odot$. The presence of a class of BHs in between these two ($10^2 - 10^5\,M_\odot$, though definitions vary), so-called intermediate mass BHs, is unconfirmed. Although evidence for their existence has been proposed (e.g. Miller et al. 2004, Earnshaw et al. 2016), this is currently tenuous.

In the local Universe it is believed that around half of all stars are in binary, or multiple, stellar systems (Horch et al. 2014). When stars reach the end point of their nuclear fusion burning lives, they may collapse to a white dwarf remnant, shedding their outer gas layers in the process. Alternatively, if the star is massive enough, it can undergo a runaway thermonuclear explosion, producing a Type II supernova. During this type of supernova, the core of the star collapses to either a neutron star or a (stellar mass) BH. It follows

that there are many binary systems comprising a star and a compact object, be it a white dwarf, neutron star or BH.

If the separation between members in such systems is sufficiently large, the two will orbit around their centre of mass (or barycentre) and few observable effects will result. However, for smaller separations, the point of gravitational equipotential between the two – the L_1 Lagrangian point – may lie close to, or at, the star's surface. In this case, the gas on the stellar surface closest to the companion experiences a net force towards the compact object, and mass transfer will occur. As the gas pours from the star, it is believed to form a high temperature 'accretion disc' (AD) orbiting the compact object. If the accreting compact member is a white dwarf, a cataclysmic variable star is formed, and if the companion is a neutron star or BH, an X-ray binary (XRB, or BH binary, BHB, if the companion is such) is produced. A subclass of these systems, called ultraluminous X-ray binaries (ULXs), is believed to be powered by either intermediate mass BHs (Colbert & Mushotzky 1999), or very high accretion rate stellar mass BHs (Poutanen et al. 2007, Middleton et al. 2013) or neutron stars (Bachetti et al. 2014). A review is presented in Roberts (2007).

In an AGN, the central SMBH is accreting matter, but, due to this object's huge sphere of influence, it attracts material from interstellar space. The accretion flow in AGN is typically of a much greater luminosity than that in XRBs and ULXs, as the BH is significantly more massive, and the rate of matter accretion can be far larger (Salpeter 1964, Shakura & Sunyaev 1973, Rees 1984). It is estimated that around 1 in 50 galaxies hosts a highly accreting SMBH in the local Universe (Netzer 2013).

The process of emission is broadly similar in both BHBs and AGN. At large distances from the BH, matter possesses a large amount of gravitational potential energy. This is converted to kinetic energy as it falls inwards, and when particles collide with one another, closer to the BH, friction converts some of the kinetic energy into thermal energy. According to Planck's law, matter radiates thermal energy with a characteristic radiance profile, known as blackbody radiation. The characteristic (peak) wavelength of a blackbody's radiation is only dependent on its temperature, T (Wien's displacement law), though the power emitted per unit area of the blackbody increases with T^4 (Stefan-Boltzmann law). Since the infalling matter is non-homogeneous, time-dependent variability is frequently

observed in AGN, as the properties of the accretion flow evolve.

The emitted radiation exerts a force on the infalling matter that opposes the gravitational attraction of the BH. This radiation pressure increases with the mass accretion rate, $\dot{M}$, while the gravitational force remains constant. Therefore, at a certain value of $\dot{M}$, the radiation pressure applies an equal and opposite force to that of gravity, preventing further accretion. This limiting case is called the Eddington limit, with a mass accretion rate denoted as $\dot{M}_{\rm Edd}$, and luminosity as $L_{\rm Edd}$. $L_{\rm Edd}$ is directly proportional to the mass of the BH, and is given by the following equation:

$$L_{\rm Edd} = \frac{4\pi G M_{\rm BH} m_{\rm p} c}{\sigma_{\rm T}} \simeq 1.26 \times 10^{38} \left(\frac{M_{\rm BH}}{M_{\odot}} \right) \text{ erg s}^{-1} \tag{1.2.4}$$

where $m_{\rm p}$ is the mass of a proton, $\sigma_{\rm T}$ is the Thomson scattering cross-section and 1 erg $= 10^{-7}$ J is a unit of energy in the centimetre-gram-second unit system used throughout this work. Because of this dependence on $M_{\rm BH}$, it is useful to express the accretion rate of AGN in terms of the Eddington fraction, $\dot{m}$:

$$\dot{m} = \frac{\dot{M}}{M_{\rm Edd}} = \frac{L}{L_{\rm Edd}}. \tag{1.2.5}$$

The Eddington limit in equation 1.2.4 is derived by considering a simple, spherically accreting system, but some AGN and ULXs appear to exhibit 'super-Eddington' accretion rates, $\dot{m} > 1$ (e.g. Gladstone et al. 2009, Wang et al. 2014). A possible means by which this may occur is if the accretion flow is in the form of an AD.

Matter in XRBs only accretes in the plane of orbit, strongly implying the formation of an AD. AGN, on the other hand, can accrete matter from any direction. Spherical, or Bondi accretion (Bondi & Hoyle 1944) is the simplest possible means by which this could occur, however, it is not an efficient energy radiation mechanism (Netzer 2013). Shakura & Sunyaev (1973) and Novikov & Thorne (1973) proposed that the formation of ADs in AGN, from angular momentum conservation considerations, would be efficient enough to return the energy outputs typically observed in AGN (see artist's impression in Fig. 1.1), and offers an explanation for apparently super-Eddington AGN. What was less clear in those early days was the underlying cause of the variety of AGN seen in the sky.

1.2.3 AGN Unification

There are two main varieties of AGN, classified as Type 1 and Type 2. In Type 1 AGN, spectroscopy reveals both narrow and broad emission lines, with the broad lines typically having a velocity width of $\gtrsim 1000\,\mathrm{km\,s^{-1}}$. These objects are also different in colour, with a greater spectral energy contribution at blue wavelengths than red. Type 2 AGN show different characteristics – they only exhibit narrow emission lines ($\lesssim 1000\,\mathrm{km\,s^{-1}}$) and do not display the same excess of blue light as Type 1 AGN. The different classifications are based on observational effects that are loosely defined, and additional intermediary objects (e.g. Type 1.5 AGN) have been discovered that do not fall definitively into either category.

Moreover, many AGN are noted to have strong radio emission, and jet structures visible at a range of wavelengths (Rees et al. 1982). These have been classified into two further subgroups by Fanaroff & Riley (1974) depending on the brightness and structure of their radio emission. Blazars are yet another type of AGN that show strong radio emission, are highly variable and often possess relatively featureless optical spectra.

Much research has been devoted to refining explanations for the multitude of AGN types that we observe. Osterbrock (1978) suggested that obscuration in the central region could be responsible for the lack of broad emission lines in Type 2 AGN. Additional spectropolarimetry of Type 2 AGN (Antonucci & Miller 1985) revealed that the broad emission lines were in fact present, lending weight to this theory, and forming the basis for a 'unified model' of AGN. In Antonucci (1993), it was suggested that Type 1 and 2 AGN were fundamentally the same type of object, viewed from different angles. In Type 1 AGN, there is a direct line of sight to the central engine, including both the broad and narrow line-emitting clouds. In Type 2 AGN, optically thick material prevents such a view, although the narrow line clouds, expected to be more distant from the BH, are still visible (e.g. Ward et al. 1991). Blazars are extreme examples of Type 1 AGN, where a relativistic radio jet is aligned with Earth, explaining these objects' intense radio loudness, variability and apparent luminosity.

This leads to the current picture of AGN structure. Surrounding the AD is a coaxially orbiting torus of optically thick dust. This is geometrically thicker than the AD, and so at high inclinations to face on, AD light is absorbed by the torus. The broad line

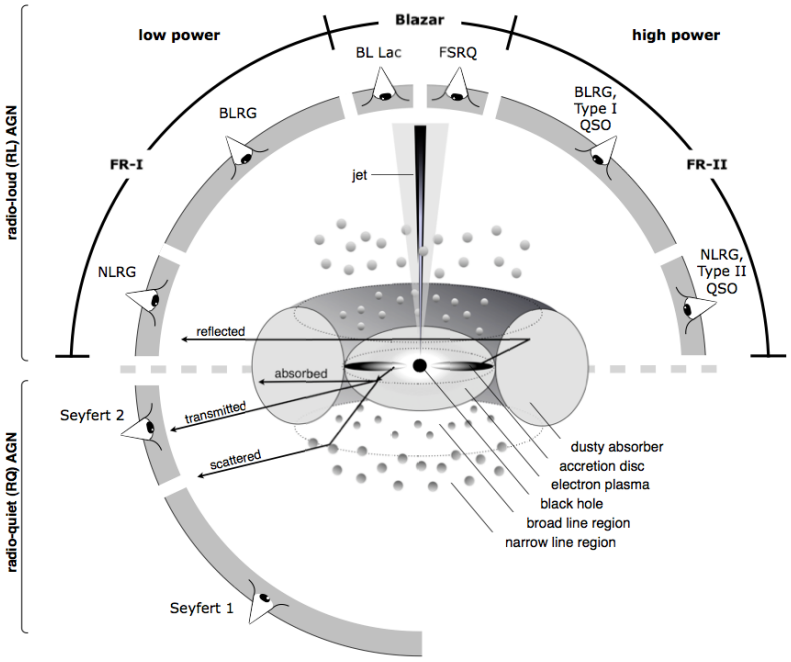

Figure 1.2: The unified model of AGN, showing the dependence of observed AGN class on orientation. Image from Beckmann & Shrader (2012).

region (BLR) comprises gas clouds close to the AD, in rapid orbital motion around the central potential, and the narrow line region (NLR) clouds are significantly further out, and therefore visible from a range of orientations. The jet is launched perpendicular to the AD, although the exact process underlying its formation is a subject of active research (e.g. Blandford & Znajek 1977, Sikora et al. 2007, Broderick & Fender 2011). A diagram of this arrangement is shown in Fig. 1.2.

Not all differences between AGN can be explained by the unified model. The previously mentioned radio-loud jets are only observed in some AGN, and the matter accretion rate is expected to have a large effect on the local environment, varying over time. Radiation pressure from the AD and jet, if present, has a large repulsive effect on matter within the line-of-sight, and is believed to drive strong winds of gas outwards from the AGN, making a large impact on the host galaxy (e.g. King 2010). Moreover, variability studies of AGN have identified some that appear to change from Type 1 to 2 and vice versa, in apparent defiance of the paradigm that orientation primarily governs AGN class (e.g. Denney et al. 2014, MacLeod et al. 2016).

Nevertheless, with this simple model of AGN structure, we are now able to more closely examine the observational characteristics of AGN from a physical point of view.

1.3 AGN Emission across the Electromagnetic Spectrum

With the advent of photography, astronomical observations, which had previously relied on sketches and notes to record the studies of the sky, underwent a revolution. Photographic plates enabled the first truly quantifiable observations, and filters were used to scientifically study the colours of objects visible in the night sky. This 'photometry' is still carried out today, as it enables wide field sky surveys to observe faint objects in relatively short periods of time. Developments in detector technology, and the advent of charge-coupled devices (CCDs) further advanced both the sensitivity and precision of observations, and allowed for data to be stored and shared with ease.

When a more precise study of the composition of light emitted by an object is required, astronomers utilise spectroscopy. This involves using a slit or fibre to pass the light from a particular target on to a prism or diffraction grating, whereupon it is separated by wavelength in the spatial direction on the detector. Spectroscopy allows for a more detailed analysis of astronomical objects, but is observationally expensive, as more light is required, and in general, fewer objects can be observed simultaneously.

In this section I detail several bands of the electromagnetic spectrum used to study AGN. As these systems are often seen to emit radiation from radio to gamma rays, this is not the complete picture, but covers the key ranges relevant to this thesis.

It is conventional in astronomy to refer to near-infrared (NIR) to ultraviolet (UV) energies by the wavelength of light in Angstroms (Å), where 1 Å $= 1 \times 10^{-10}$ m. In the mid-infrared (MIR), wavelengths are typically given in units of microns (μm), where 1 μm $= 1 \times 10^{-6}$ m. For X-rays, photon energies in keV are quoted instead, where 1 keV corresponds to a photon of wavelength 12.4 Å. The frequency of radiation, in Hz, is also commonly used, particularly when considering large ranges of the electromagnetic spectrum.

The spectral energy distribution (SED) of these different ranges is usually given in either frequency, energy or wavelength dependent forms: L_ν in erg s^{-1} Hz^{-1}, L_E in erg s^{-1} keV^{-1}, or L_λ in erg s^{-1} Å^{-1} respectively. The total energy emitted in a band, in erg s^{-1}, is thus found by multiplying by the band width, i.e. νL_ν, λL_λ, EL_E. In X-ray astronomy particularly, the energy unit, erg, is sometimes substituted for the number of photons at that given energy. These values represent the monochromatic luminosities at a

given frequency, energy or wavelength, which can be converted to observed flux as:

$$F = \frac{L}{4\pi D_L^2}, \tag{1.3.6}$$

where D_L is the luminosity distance to the source.

1.3.1 Optical–ultraviolet Emission Processes

In the optical–UV wavelength range, there is a disparity between Type 1 and 2 AGN. The emission lines are, as previously discussed, of different characteristic widths, and owing to the obscuration of the AD in Type 2 AGN, the spectral continuum is dominated by the starlight in the galaxy that hosts the AGN. The host galaxy also contributes to the optical spectrum in Type 1 AGN, but here there is an additional contribution by the AD, which can in some cases (e.g. quasars) dominate the total galaxy emission.

The AD contribution to the optical SED is well approximated by a power-law in energy space, but is more realistically represented by a Shakura & Sunyaev (1973) disc spectrum. To build this spectrum, we consider the disc to be divided into many annuli of small radial thickness. Each annulus in the disc is of constant temperature, and emits blackbody radiation. This temperature increases as radius decreases up to a peak value, dependent on $r_{\rm isco}$. A resulting SED is shown in Fig. 1.3, where it can be seen that over the optical to near-UV (NUV) range, the shape of the AD SED resembles a power-law of constant slope. Also plotted are two example galaxy templates, illustrating the frequency range this component can contribute to, but the relative contributions of these are highly dependent on the AGN power, and the type of galaxy hosting it.

On top of the AD (and host galaxy) continuum, there are discrete emission lines arising from the BLR and NLR. These originate in orbiting gas clouds, where AD emission excites atomic transitions. If a system absorbs an AD photon, it will attain an excited state, promoting an electron to a higher energy level. This excited system can return to a lower energy state by emitting photons, with each transition being associated with a characteristic energy change, and hence photon frequency. As this is a continuous process, some transitions occur preferentially, depending on the composition of the gas in the cloud. The emission lines seen in the optical spectra of AGN are attributed to transitions in a range of elements, and are Doppler broadened by the clouds' orbital motion around

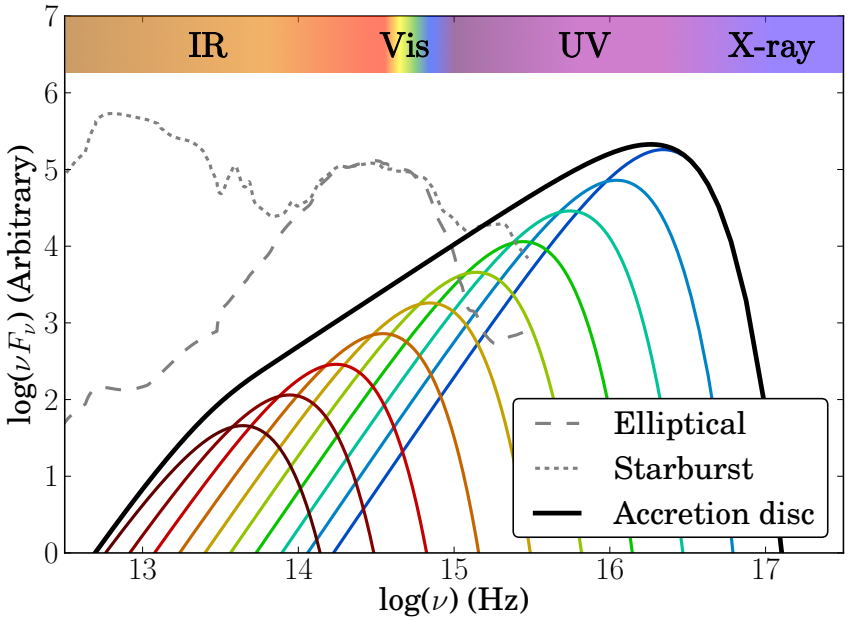

Figure 1.3: Typical SED contributions from AD and host galaxy in an AGN. The AD is represented by a sum of blackbodies (coloured lines), up to a maximum temperature of (in this case) $\sim 300,000$ K. Additional components in the X-ray and IR regimes are discussed in Sections 1.3.2 and 1.3.3. The two host galaxy templates are from Polletta et al. (2007) and demonstrate the different SEDs for an elliptical galaxy, which hosts mainly old, red stars, and a starburst galaxy, which hosts younger, bluer stars, and much more cold dust (the peak in the IR). The relative contributions of host galaxy and AGN are dependent on the AGN luminosity.

the BH. In addition to commonly observed 'permitted' transitions, lines corresponding to 'forbidden,' and 'semi-forbidden' mechanisms are often observed. Such lines can only be emitted under certain conditions, under which atomic transition selection rules do not apply.

If the AGN is moving with some bulk motion with respect to the observer, these lines are redshifted (or blueshifted) by an amount dependent on the recession (or approach) velocity. Based on the wavelengths at which emission lines are observed and emitted, we define the redshift, z. Hubble discovered that the Universe is expanding, and all distant galaxies are moving away from us, with a velocity proportional to their distance from us. Thus by measuring the redshifts of known emission lines in distant AGN, we can infer the distance to them. Additionally, due to the finite velocity of light, as we observe galaxies at greater distances/redshifts, we observe them at an earlier stage of the Universe.

The Type 1 AGN optical–UV emission template of Vanden Berk et al. (2001), built from more than 2200 AGN optical spectra is shown in Fig. 1.4. In higher redshift objects, the UV spectrum is shifted to optical wavelengths. Since the sample of AGN spans a

redshift range from $0.044 \leqslant z \leqslant 4.789$, this sample allows the Vanden Berk et al. (2001) template to cover $800 - 8555$ Å in the rest frame, in spite of the optical spectrograph covering $3800 - 9200$ Å (observed frame).

Several particularly important emission features observed in AGN spectra originate from electron transitions in ionised hydrogen. The Hα line is emitted by electrons falling from the second excited state to the first, emitting a photon of wavelength 6563 Å (in air). Hβ is emitted when electrons transition between the third and the first excited states, and Hγ when they drop from the forth to the first state. This is the Balmer series, which culminates in a continuum of fainter and fainter emission lines below 3646 Å (Grandi 1982). Further complicating the optical–UV spectrum is the multitude of Fe II and Fe III transitions at a range of wavelengths (Vestergaard & Wilkes 2001).

It can be seen in Fig. 1.4 that blueward of the Lyman-α λ1216 Å (Ly-α) emission feature the flux is attenuated. The Ly-α emission line originates close to the AGN, and is the result of electrons moving from the first excited state to the ground state in hydrogen, the most abundant element in the Universe. However, neutral hydrogen (H I) in intergalactic space preferentially absorbs this same wavelength of light, and as the light passes through the intergalactic medium (IGM) it typically interacts with many different H I-containing systems, each at slightly different redshifts. This produces the Ly-α forest of absorption features below 1216 Å (e.g. Gunn & Peterson 1965).

Finally, the optical–UV emission from AGN, and indeed all extragalactic objects, is affected by dust scattering along the line-of-sight. When optical light passes through dust in the interstellar medium (ISM), some of it is reprocessed in a process called Rayleigh scattering. This process is dependent on the composition of the scattering dust, but in general, blue light is preferentially scattered. Consequently, every object observed at Earth is 'reddened,' or 'extinguished' from its intrinsic level. This must be characterised and corrected if we are to recover the intrinsic spectrum of an extragalactic source. Astronomers have therefore been motivated to construct MW dust maps, and empirical reddening/extinction curves to perform such corrections (e.g. Cardelli et al. 1989, Pei 1992).

A similar process is expected to occur in AGN host galaxies, with the light being dust reddened at the start of its intergalactic journey to the MW. This is more difficult to characterise, and must usually be modelled by fitting redshifted extinction curves to spectral data from the AGN (e.g. Jin et al. 2012a, Castelló-Mor et al. 2016).

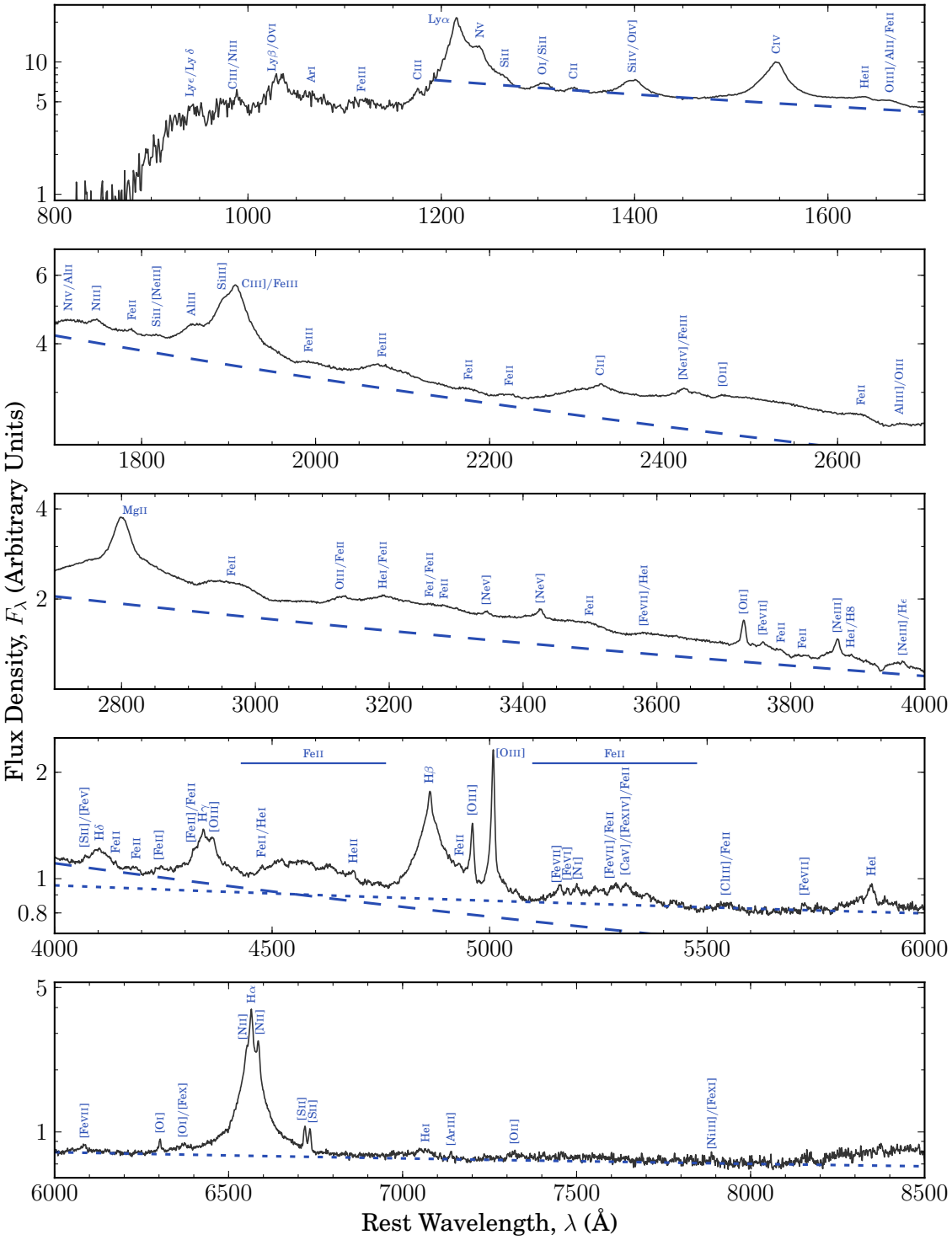

Figure 1.4: The Type I AGN optical–UV spectral template of Vanden Berk et al. (2001), with key emission features marked. A broken power-law continuum, calculated by Vanden Berk et al. (2001), is shown by the dotted and dashed curves. The break is likely to be due to a more significant contribution to the continuum by the host galaxy redward of ~ 5000 Å.

1.3.2 X-ray Emission Processes

Both AGN and BHBs are observed to strongly emit X-ray radiation. A number of processes are believed responsible for this. The AD temperature, T, is a function of radius, r, and, neglecting GR effects, depends on $M_{\rm BH}$ and $\dot{M}$ according to the equation (Netzer 2013):

$$T(r) \simeq 8.6\times10^{9}\left(\frac{\dot{M}}{M_{\odot}\ \mathrm{yr}^{-1}}\right)^{\frac{1}{4}}\left(\frac{M_{\rm BH}}{M_{\odot}}\right)^{-\frac{1}{2}}\left(1-\left[\frac{r_{\rm isco}}{r}\right]^{\frac{1}{2}}\right)\left(\frac{r}{R_{\rm g}}\right)^{-\frac{3}{4}}\mathrm{K}. \qquad (1.3.7)$$

Therefore the peak temperature increases with increasing accretion rate, but decreases with increasing mass, so BHBs ($M_{\rm BH}\sim10\,M_{\odot}$) have ADs of $T_{\rm max}\sim10^{7}$ K, much hotter than those of AGN (for $M_{\rm BH}\sim10^{8}\,M_{\odot}$, $T_{\rm max}\sim10^{5}$ K). BHBs typically host ADs that peak at X-ray wavelengths (e.g. Kolehmainen et al. 2011), whereas AGN generally have ADs that peak in the far-UV (FUV, e.g. Capellupo et al. 2015).

In both BHBs and AGN, an additional X-ray contribution is observed that extends to much higher X-ray energies than the AD. The spectral shape is power-law like, and it is attributed to inverse Compton scattering of AD photons by a hot, optically thin corona around the inner AD. In this scenario, the corona contains electrons of higher typical energy than the photons emitted by the AD. If these photons interact with the coronal electrons, some energy is transferred from electron to photon, raising the photons' energy. This results in a power-law tail (PLT) to high X-ray energies (Haardt & Maraschi 1991).

When these Compton up-scattered X-rays from the corona interact with optically thick material in the vicinity of the AGN, several physical processes modify the observed spectrum. Photoelectric absorption dominates at low X-ray energies, strongly attenuating the coronal emission, however, as the incident photon energy increases, so does the probability that the photon will be reflected. As the flux of seed photons is limited, this contributes to a 'reflection hump' at energies of between $20-50$ keV. The strength of the absorption column is usually characterised by the neutral hydrogen (H I) column density along the line of sight, in units of atoms cm^{-2}, although in practice, a range of elements from hydrogen to iron are responsible for this absorption column. These columns are present in both the MW and host galaxy (George & Fabian 1991, Done 2010).

In AGN, a significant additional SED contribution is observed at soft X-ray frequen-

cies (e.g. Arnaud et al. 1985, Gierliński & Done 2004). The origin of this component, referred to as the 'soft X-ray excess' (SX), is uncertain, with several possible scenarios suggested. Spectrally, the SX is consistent with being the result of reflection of PLT photons off the AD (Crummy et al. 2006). This could Compton down-scatter these high energy photons to more modest X-ray energies via a reverse process to that described above. This requires extreme source geometries however (Done & Nayakshin 2007), motivating alternative explanations. For instance, the SX may originate from the presence of a clumpy, partially ionised absorbing material, or possibly in warm Compton upscattering within the AD itself (e.g. Inoue & Matsumoto 2003, Done et al. 2012). Exploration of these possible scenarios requires precise timing measurements, in addition to spectroscopy, to search for frequency-dependent lag times between SX and PLT (e.g. Turner et al. 2007, Fabian et al. 2009, Gardner & Done 2015).

1.3.3 Infrared Emission Processes

In AGN, further SED contributions are seen in the IR that dominate the predicted AGN AD energy output at these wavelengths. This is observed in both Type 1 and 2 AGN, and is believed to be observational evidence for the dusty torus described in Section 1.2.3. It is thought that radiation from the central accretion flow heats the infalling dust to temperatures of up to ~ 2000 K. This hot dust emits blackbody radiation in much the same way as the AD (e.g. Barvainis 1987, Pier & Krolik 1993). It fits into the unified picture of AGN, as the torus is both geometrically and optically thick, and so is able to obscure lines of sight to the central engine in Type 2 AGN.

It is important to note that the torus emits reprocessed AGN emission. The dust effectively absorbs and re-radiates emission that is directed along different lines-of-sight to those directly from the central engine. Therefore the total intrinsic AGN energy output excludes the contribution of the torus, with the energy difference partly accounting for the observed luminosity difference between Type 1 and Type 2 orientations (Marconi et al. 2004).

Our understanding of the nature of the torus is incomplete, however. Studies of the extent, composition and dynamics of this structure make use of spectrophotometric observations, and time dependent variability. Previous work has found evidence that the torus

could be 'clumpy' in nature (e.g. Nenkova et al. 2002, Dullemond & van Bemmel 2005, Nenkova et al. 2008), but this is as yet uncertain (e.g. Lawrence & Elvis 2010).

The host galaxy also contributes to the observed IR emission in AGN (see Fig. 1.3). In galaxies with active star formation particularly, cooler gas strongly emits MIR to far-IR (FIR) radiation (Kirkpatrick et al. 2015). IR spectra of AGN also contain a number of smaller atomic/molecular absorption/emission features. Some of these are due to transitions in the BLR and NLR, while others are attributable to the host galaxy, such as polyaromatic hydrocarbons related to star formation (Schweitzer et al. 2006).

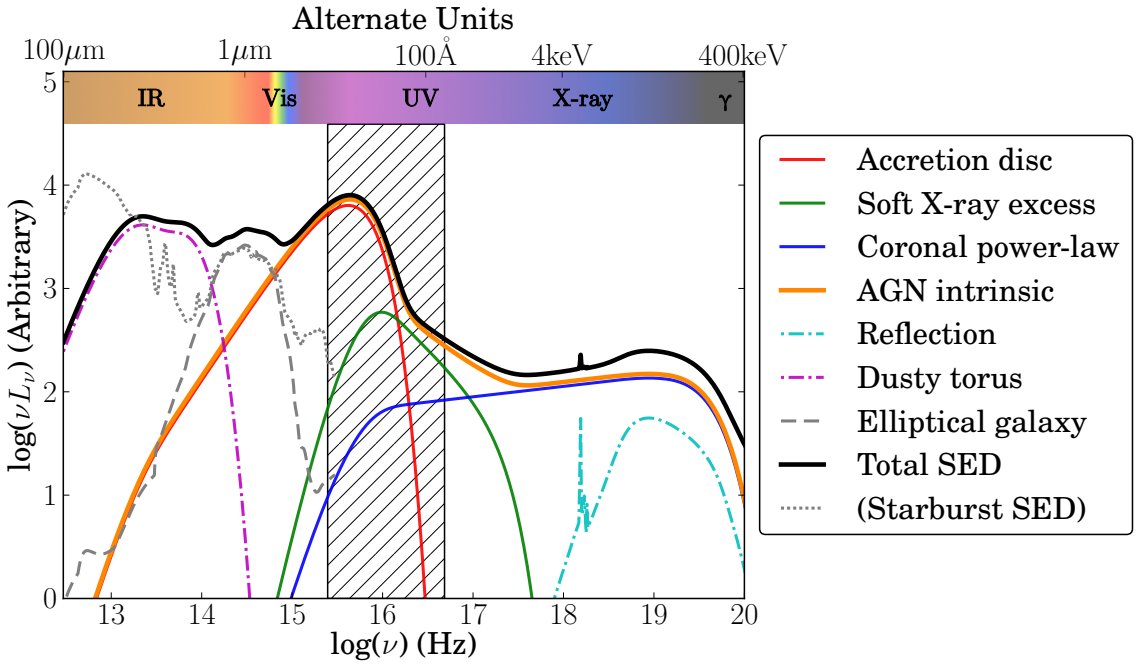

Figure 1.5: A diagram showing the broad-band SED of a typical AGN, including contributions from dusty torus and host galaxy. The 'intrinsic' AGN is defined to comprise three components: accretion disc (AD), soft X-ray excess (SX) and coronal power-law tail (PLT). These are all directly powered by accretion of gas on to the BH. The reflection and dusty torus components are reprocessed AGN emission, and the host galaxy (in this case an elliptical) is starlight dominated. The cross-hatched region highlights the frequency range that is heavily absorbed by neutral hydrogen and other elements in the ISM and IGM. For comparison, an SED of a starburst galaxy is shown, with contributions in the UV from young stars and the FIR from cold interstellar dust.

1.3.4 Spectral Energy Distributions

This completes the picture of the AGN IR–X-ray SED. Many of the components I have discussed so far are intrinsically linked, as they are derived from reprocessed emission. Thus all of the energy output comes from the conversion of gravitational potential energy, to kinetic energy, to thermal energy.

By studying the broad-band SED, we can build a picture of the interplay between these components, and derive the properties of the BH and its environment. A summary of the key SED components considered in this thesis is shown in Fig. 1.5. A more comprehensive discussion of the theoretical models used is given in Section 2.

The cross-hatched region in Fig. 1.5 shows the approximate range of frequencies at which emission is heavily absorbed by neutral hydrogen and other elements in the ISM and IGM. This means that for the majority of AGN, the peak of the SED, at which the most energy is radiated, is unobservable. In Chapters 3 and 4, I explore a sample of AGN in which the peak of the SED emerges at observable frequencies.

1.3.5 Variability

Since the energy-emitting regions in AGN are, in galactic terms, very small (comparable in size to the Solar System), changes in the local environment allows them to vary in brightness on measurable timescales. Interpreting the light curves as arising from specific physical mechanisms, however, is often difficult. The timescale of variability is an important diagnostic of the size of the emitting region, as extended structures cannot coherently vary faster than the time it takes light to cross them. Therefore, as the different wavelength ranges I discuss above all originate from regions at different radii from the BH, so the timescale of flux variation changes with wavelength.

Optical variability in AGN typically occurs over time periods of order weeks–months (e.g. McHardy et al. 2016), but is not always necessarily driven by intrinsic changes in the AD. Extrinsic effects, such as changing properties of an obscuring structure (e.g. a dust cloud, LaMassa et al. 2015) could also modify the observed optical flux, even if intrinsically the accretion flow is in a steady state. Several possible origins driving changes in the optical brightness of AGN are discussed in Chapter 6.

The X-ray emitting region is thought to be smaller than the AD, and concordantly, X-ray variability occurs on much shorter timescales than optical (of order minutes to days, depending on the mass of the BH). Thus, during the course of a single X-ray observation, X-ray light curves can be produced (e.g. Lawrence et al. 1985, Gierliński et al. 2008, Alston et al. 2016). As is the case with the optical, the variable flux can be due to changing properties intrinsic to the emission region, or absorption by intervening material (Turner & Miller 2009).

With an ever-expanding archive of data available for larger and larger variability studies, it is becoming increasingly feasible to study and test a range of processes that could give rise to changes in AGN.

1.4 Measuring the Black Hole Mass in AGN

Determining $M_{\rm BH}$ of the SMBHs in AGN is of great importance as, together with spin, it is one of only two properties intrinsic to astrophysical BHs. Consequently, much research has been devoted to refining methods of estimating $M_{\rm BH}$, several of which are discussed in this section.

1.4.1 Dynamics in the Sphere of Influence

In the MW, the resolved motions of individual stars in the sphere of influence of the central BH allows for very precise measurements of $M_{\rm BH}$, as the gravitational force experienced by each star can be directly calculated based on its orbit. This method provides the most accurately determined measurement of a SMBH mass (Gillessen et al. 2009).

In nearby galaxies, the BH's sphere of influence (typically of radius $1-100$ pc, depending on $M_{\rm BH}$ and stellar velocity dispersion, Peebles 1972) can be resolved with telescopes, although individual stars cannot. Nonetheless, if the velocity dispersion and orbital radii of stars/gas can be measured using spectroscopy, the BH mass can be estimated (e.g. Harms et al. 1994).

In more distant AGN, the sphere of influence cannot be resolved, and hence it is impossible to spatially resolve the kinematics of the orbiting matter. Other methods of inferring $M_{\rm BH}$, based on timing, have therefore necessarily been developed.

1.4.2 Reverberation Mapping

The AD-dominated optical continuum of AGN is noted to vary on short timescales. As it is believed that the BLR emission line transitions are excited by the central source, the line strengths are expected to correlate with continuum strength, with a characteristic time delay, corresponding to the light travel time from the AD to the BLR. This directly relates to the radius of the BLR ($R_{\rm BLR}$), and the velocity dispersion (v) can be estimated from the width of the broad lines. $M_{\rm BH}$ is then given by:

$$M_{\rm BH} = \frac{v^2 R_{\rm BLR}}{G}. \tag{1.4.8}$$

This technique is called reverberation mapping (RM) and was originally proposed by Blandford & McKee (1982). Since then, RM has proved remarkably effective at providing a sizeable sample of AGN, some of which are very distant, with $M_{\rm BH}$ estimates (e.g. Peterson 1993, Kaspi et al. 2000, Peterson et al. 2004, Bentz et al. 2009, Denney et al. 2010 and Bentz et al. 2013). The disadvantage of RM is that it requires long, spectroscopic monitoring campaigns, which are observationally expensive. Nonetheless, this technique has enabled the calibration of single epoch virial mass estimates.

1.4.3 Single Epoch Virial Mass Estimates

RM has allowed the characterisation of a radius–luminosity relationship in the BLR. In simple terms, the BLR size is well-correlated with the continuum or line luminosity, $R_{\rm BLR} \propto L^{\alpha}$, where α is a constant. The line width, usually parameterised by the full width at half maximum (FWHM), or sometimes the line dispersion (Peterson et al. 2004), offers a proxy for the velocity dispersion, and so, using a sample of AGN with RM $M_{\rm BH}$ estimates, it is possible to derive the relationship between $M_{\rm BH}$, linewidth, and luminosity (e.g. Wandel et al. 1999, Woo & Urry 2002, Greene & Ho 2005 and Kaspi et al. 2005).

As this method only requires a single spectroscopic observation of an AGN, it is possible to apply it to large samples. However, it is also less precise than RM, with errors arising from the uncertainties on the virial coefficient and BLR size–luminosity relationship. For instance, Park et al. (2012) estimated that single epoch virial masses are accurate to within a factor of ~ 3.

I use three relations for estimating $M_{\rm BH}$ in this work, each based on a different emission line and luminosity. Greene & Ho (2005) derived the following relation for Hα:

$$M_{\rm BH} = (2.0^{+0.4}_{-0.3}) \times 10^6 \times \left(\frac{L_{\rm H\alpha}}{10^{42}\ {\rm erg\ s^{-1}}}\right)^{0.55\pm0.02} \left(\frac{\rm FWHM_{H\alpha}}{10^3\ {\rm km\ s^{-1}}}\right)^{2.06\pm0.06} M_\odot \tag{1.4.9}$$

where $L_{\rm H\alpha}$ and $\rm FWHM_{H\alpha}$ are the luminosity and FWHM of the broad component of the Hα emission line.

Woo & Urry (2002) presented the following relation using Hβ:

$$M_{\rm BH} = 4.817 \times \left(\frac{\lambda L_\lambda}{10^{44}\ {\rm erg\ s^{-1}}}\right)^{0.7} \left(\frac{\rm FWHM_{H\beta}}{\rm km\ s^{-1}}\right)^2 M_\odot \tag{1.4.10}$$

where λL_λ is the monochromatic continuum luminosity at 5100 Å.

Finally, McLure & Dunlop (2004) calculated a means of estimating $M_{\rm BH}$ from Mg II:

$$M_{\rm BH} = 3.2 \times \left(\frac{\lambda L_\lambda}{10^{44}\ {\rm erg\ s^{-1}}}\right)^{0.62} \left(\frac{\rm FWHM_{MgII}}{\rm km\ s^{-1}}\right)^2 M_\odot \tag{1.4.11}$$

with λL_λ this time being the monochromatic continuum luminosity at 3000 Å.

More recent work has extensively tested these relations, finding general consistency at a range of redshifts and luminosities, see Shen & Liu (2012), Matsuoka et al. (2013), Ho & Kim (2015), Mejia-Restrepo et al. (2016), but also Wang et al. (2009), who note a systematic offset from the McLure & Dunlop (2004) Mg II relation of ~ 0.2 dex.

Single epoch virial mass relations are empirically defined, and as such the indices on the luminosity and velocity terms can vary from those expected from purely theoretical considerations. Specifically, if one assumes the broad emission lines originate in 'locally optimally emitting clouds,' the relation expected would be $M_{\rm BH} \propto L^{0.5}\ v^2$ (Baldwin et al. 1995, Korista & Goad 2000, Peterson 2006), which deviates slightly from the relations given above.

1.4.4 Alternative Methods of Estimating BH Mass

A brief summary of other means of estimating $M_{\rm BH}$ in AGN is as follows:

i. Host galaxy relationship: Magorrian et al. (1998) first found a strong correlation between $M_{\rm BH}$ and the bulge mass of the host galaxy. A stronger correlation was subsequently noted between $M_{\rm BH}$ and the stellar velocity dispersion by Ferrarese & Merritt (2000) and Gebhardt et al. (2000) – the $M_{\rm BH}$–σ relation. The origin of this relation is subject to ongoing research, as it is not immediately apparent how the two properties can be so closely related; the BH only constitutes 0.1 per cent of the mass of the galaxy. More recently, it has emerged that the $M_{\rm BH}$–σ relation does not hold well for galaxies with low $M_{\rm BH}$ (Greene et al. 2010). The difference is thought to be due to the nature of the stellar bulge (Ho & Kim 2014) and therefore contributes towards uncertainty in the virial relationship discussed in Section 1.4.3. Nonetheless, even in non-active galaxies, these relations make it possible to make a prediction as to $M_{\rm BH}$, from the host galaxy properties alone.

ii. SED fitting: $M_{\rm BH}$ affects the AD peak temperature (equation 1.3.7), as does the spin and accretion rate. Therefore, if sufficient quality data are available near to the SED peak, applying an SED model to the data can allow recovery of these properties. Unfortunately, there is degeneracy between the three properties, and solutions are often not unique. Accordingly, prior estimates of $M_{\rm BH}$ and the accretion rate are usually made first, and refined based on the model fit (Capellupo et al. 2015, Castelló-Mor et al. 2016).

iii. Megamasers: A maser is the microwave analogue of a laser, where a system in a state of population inversion allows for the amplification of incident radiation. Maser emission has been observed in AGN, arising from an amplified H_2O molecular transition. The source of these extragalactic 'megamasers' must be an (almost) edge on 'maser disc,' as the emission requires long path lengths to be sufficiently amplified. The redshift/blueshift of the observed maser radiation then allows the gravitational potential to be characterised, and an estimate of $M_{\rm BH}$ to be drawn (Kuo et al. 2011, Tarchi 2012, Castangia et al. 2016, Greene et al. 2016).

1.5 The Role of AGN and their Physics

I have so far discussed some of the known features of AGN, but there are many questions as yet unanswered. For instance, it is not currently known how the SMBHs grew to the masses we observe them at through cosmic history. At moderate redshifts of $z \sim 2$, there are many AGN of $M_{\rm BH} \gtrsim 10^9\,M_{\odot}$, in spite of the Universe being just ~ 5 Gyr old at this epoch. Clearly, over cosmic time, the SMBHs go through active and quiescent phases, depending on the availability of matter for accretion.

The properties of the BH itself hold information about its accretion history over the age of the Universe. $M_{\rm BH}$ is a record of the amount of matter that crosses the event horizon, and the spin ought to provide evidence of the manner in which the matter was accreted. For instance, random, omnidirectional accretion episodes will serve to impart no resultant angular momentum to the BH, whilst prolonged, unidirectional accretion, or BH mergers, may 'spin up' the BH (e.g. King et al. 2008, Fanidakis et al. 2011, Dotti et al. 2013, Volonteri et al. 2013).

The consequences of high accretion episodes on the host galaxy are not well understood, but the low apparent AGN duty cycle, combined with the strength of the $M_{\rm BH}$–σ relation, suggests strongly related evolution. High BH accretion episodes are believed to drive strong winds via radiation pressure, which feed energy back into the galaxy. Exploring these winds through observations of absorption features in the optical–X-rays can characterise their velocity, origin and energy (King 2010), and recent studies of the AGN PDS 456 have predicted winds energetic enough to explain AGN/host galaxy coevolution (Nardini et al. 2015). Moreover, McCarthy et al. (2010) compared two hydrodynamical galaxy simulations, one which included the effects of AGN feedback, and one which did not. Both simulations included the effect of supernova-driven galactic winds. They found that the simulation without AGN feedback could not reproduce the temperature profiles observed in galaxies, providing further evidence that AGN feedback has strong implications for the host galaxy.

Such large scale simulations can aid in our understanding of the way an AGN influences its host, but since those of e.g. the EAGLE and Illustris projects (Schaye et al. 2015, Vogelsberger et al. 2014) do not yet have the resolution required to model the gas and dust kinematics near the SMBH, effects such as AGN feedback must be approxi-

mated on a sub-grid level. The simulation is then dependent on these approximations, which may be based on physics that is partially understood.

There is thus a great need to better understand the BH and accretion flow properties, based on multiwavelength observations. These aid in the determination of how the gas accretes on to the BH, how winds and jets are driven, and how the BH grows. This is the motivation behind this thesis.

1.6 This Thesis

As previously discussed, the current understanding of AGN suggests that there are only a handful of properties influencing their observed SEDs. These include the mass and spin of the BH, the mass accretion rate, the structure and orientation of both infalling matter and outflowing jets/winds, and line-of-sight reprocessing by intervening systems (Ward et al. 1987, Richards et al. 2006, Done et al. 2012). Characterising observations as resulting from known phenomena has been the focus of a number of research groups in recent decades (e.g. Elvis et al. 1994, Vasudevan & Fabian 2007, Jin et al. 2012a, Capellupo et al. 2015) but many facets of the models remain poorly understood.

This task is made more complex by the great range of energies at which AGN radiate, and the various processes attenuating their emission. Taking multi-frequency flux measurements and numerically extrapolating across unobservable regions (e.g. Lusso et al. 2010) is a straightforward approach, but the results are uncertain. Jin et al. (2012a) used a physical AGN SED model to study 51 low redshift AGN, and were able to subdivide the sample into three main groups, with distinct optical and SED characteristics. A disadvantage of their study was that the majority of the sample had SEDs that peaked in the unobservable EUV range, and the results were therefore highly model-dependent. Additionally, they found it challenging to disentangle spectral contributions from the AGN and host galaxy. More recently, Capellupo et al. (2015, 2016) carried out a modelling campaign on 39 AGN at moderate redshifts, in which the AGN dominated the optical spectrum, and the SED peak was shifted closer to the observed range. However, their sample lacked high energy X-ray data, meaning the results were dependent only on a small part of the SED, increasing the potential model degeneracies.

My initial goal in this thesis is to reduce these model uncertainties and degeneracies by exploring a new AGN sample at a similar redshift range to that of Capellupo et al. (2015). I use an updated form of the numerical SED code used by Jin et al. (2012a), and data from IR–X-ray energies to more robustly constrain the model fits. The first study assesses the suitability of both model and data, and the extent to which the SED component can be reliably combined with representations of extinction/absorption.

I then characterise and quantify the main sources of uncertainty, and refine the models by including additional components attributable to the dusty torus and host galaxy. I test whether previously observed local relationships hold in this redshift range, and use the available information to search for new trends between various emissive components, interpreting these in the wider context of AGN physics when possible. Finally, based on the results of these studies, I offer some suggestions for future avenues to pursue in this field of research.

Following this, I carry out an investigation of four 'hypervariable' AGN. Whilst a number of these extreme transients have now been found (Lawrence et al. 2016), they are undoubtedly unusual. The mechanism driving their change in brightness is not yet known, but poses an intriguing avenue by which we may research AGN structure. An intrinsic origin for the variability would challenge the current understanding of accretion physics, whilst an external origin, such as foreground microlensing, may allow us to spatially resolve the structure of AGN by monitoring such events in the future. Once again, I use multiwavelength data and the SED accretion model to test these two hypotheses.

The structure of the thesis is therefore as follows:

- **Chapter 2:** In this chapter, I describe the data sources and theoretical models used throughout.

- **Chapter 3:** I present an NIR–X-ray SED study of 11 AGN at moderate redshifts ($1.5 < z < 2.2$), in which the peak of the AGN SED is shifted towards observable energies. Broad-band data are systematically modelled with a physical SED code which includes Galactic and extragalactic extinction/absorption. This allows for robust determination of the bolometric luminosities.

- **Chapter 4:** The study of Chapter 3 is extended. Several sources of uncertainty

are tested and quantified, and the SED parameter space is explored further. I refine the SED model to include contributions from the torus and host galaxy, and the properties of these components are compared to earlier work.

- **Chapter 5:** I discuss two future extensions to Chapters 3 and 4. First I describe the selection of a new, larger sample of AGN, which forms the basis of the next step in the SED modelling study. I then present pilot results from an SED study of two AGN with high-resolution UV spectra, allowing for unprecedented SED sampling. Finally I model the SED of Mrk 590, an AGN that has appeared to change from Type 1 to Type 2 in recent years.

- **Chapter 6:** The SEDs of four 'hypervariable' AGN are studied. I consider two mechanisms that may give rise to the variability, and test both for consistency with known physics.

Throughout this thesis I assume a flat cosmology, with $H_0 = 70$ km s^{-1} Mpc^{-1}, $\Omega_{\rm M} = 0.27$ and $\Omega_\Lambda = 0.73$.

CHAPTER 2

Facilities, Instruments, Observations and Models

2.1 Overview

This thesis is concerned with the application of theoretical spectral models to data from a number of observatories around the world, and beyond. In this chapter I summarise the technical aspects of the instruments and theoretical models used throughout.

Our multiwavelength observations include both photometric (imaging) and spectroscopic data from IR–X-ray wavelengths in Chapters 3 – 6. I introduce the telescopes that have contributed to this work, giving an overview of their capabilities, implementation and the relevant data reduction processes.

Next I describe the means by which the night sky is monitored, which allows the selection of the sample studied in Chapter 6. I outline two wide field optical surveys which are well-suited to the task of detecting and classifying transient AGN, and briefly discuss X-ray timing.

Finally, I encapsulate the theoretical models applied to data. I summarise the XSPEC software package and Levenberg-Marquardt χ^2 minimisation routines, before presenting the SED and spectral models used in Chapters 3 – 6.

2.2 Multiwavelength Data

2.2.1 Infrared

In this thesis, I use data in the NIR to MIR region. I classify the NIR range as being of wavelength $7500 - 25000$ Å ($0.75 - 2.5$ μm) and MIR as $2.5 - 25$ μm, although definitions can vary. Historically, these are separated into various different wavebands, corresponding to the filters that were used to observe each spectral region. As molecules of e.g. H_2O, CO_2 and O_3 in Earth's atmosphere absorb certain wavelengths of IR radiation strongly, these wavebands are generally calibrated to atmospheric transmission windows. Another difficulty of IR astronomy is mitigating against contaminating sources of IR radiation from the instrument/atmosphere, and detectors must be cooled down to minimise self-noise.

I use NIR spectra from two sources: TripleSpec (TSpec) on the Astrophysical Research Consortium (ARC) 3.5 m Telescope at Apache Point Observatory, New Mexico, USA (Wilson et al. 2004), and the Gemini Near-Infrared Spectrograph (GNIRS) on the 8 m Gemini North Telescope, situated at Mauna Kea Observatory, Hawaii, USA (Elias et al. 2006). A photograph of Gemini is shown in Fig. 2.1.

TSpec is primarily a cross-dispersed spectrograph, and GNIRS has a range of capa-

Figure 2.1: Photograph of the Gemini North telescope (foreground) at Mauna Kea Observatory, with the University of Hawaii 2.2 m (middle) and UKIRT (back right). Gemini hosts the GNIRS instrument, and UKIRT undertook the UKIDSS survey.

bilities, including imaging, but is chiefly used for spectroscopy. However, in this thesis I only use data from each instrument operating in cross-dispersed mode, and so this is what I focus on hereafter.

A cross-disperser is an optical diffraction system that maximises the wavelength coverage of a spectrograph by focussing higher order diffracted light on to a detector. It differs from long-slit spectroscopy (discussed in Section 2.2.2) in that the slit must be shorter, corresponding to a smaller spatial region of the sky. It is therefore better suited to small or point-like sources.

The disperser in TSpec separates the NIR light into a frequency spectrum using a combination of three prisms. This is passed to an order-sorting diffraction grating, which focusses the light on to the CCD. Diffraction orders 3 to 8 cover the wavelength range 2.46 μm to 0.77 μm with a resolving power of $R \sim 3500$ (Wilson et al. 2004).

In cross-dispersed mode alone, GNIRS has a range of setups available to observers. Our observations (PI: M. Elvis) used the SF57 glass SXD prism and 32 l/mm grating, which diffract, sort and focus the light on to the detector. Diffraction orders 3 to 8 in GNIRS cover the wavelength range 2.53 μm to 0.87 μm, and deliver a resolving power of $R \sim 1800$ (Elias et al. 2006).

The data reduction processes for both of these instruments are similar, and broadly involve the following steps. In addition to the science observation, several calibration observations are made on the same night. These include flat-fields, bias frames, an arc lamp spectrum, and a telluric standard star at a similar airmass to the science target. Detector bias is first subtracted from all science and calibration frames. The telluric and science frames are then divided by the flat-fields, to correct for variations in the detector response. Science and telluric observations are collected in sets of four observations, during which the target position in the slit is 'nodded' between two positions, called an 'ABBA' pattern. This allows the images to be combined in-place, simultaneously summing the target flux and subtracting the sky background from the spectrum.

Emission lines in the arc lamp spectrum are identified to provide a pixel-to-wavelength conversion matrix, and this wavelength solution is applied to the science and telluric frames. Finally the targets are traced along the wavelength axis and collapsed in the spatial direction over the extent of the (seeing-limited) point spread function to maximise

the signal-to-noise ratio (S/N).

The final step is to characterise the true, flux calibrated telluric stellar spectrum, either by using a high-resolution published spectrum of the same star, or simulating the spectrum with a blackbody, normalised to the same flux as the star. The ratio of the actual spectrum or blackbody to the observed telluric spectrum is the sensitivity function of the instrument at that airmass, and this can then be multiplied by the stacked science frame to obtain the flux calibrated science spectrum (e.g. Vacca et al. 2003, Farihi et al. 2008).

In addition to NIR spectroscopic data from GNIRS and TSpec, I use photometric data from three wide area NIR and MIR surveys: 2MASS, UKIDSS and *WISE*. Data from all three surveys is available in a reduced format.

The Two-micron All Sky Survey[1] (2MASS, Skrutskie et al. 2006) imaged the sky in three NIR bands, J, H and K_S, which have effective wavelengths of 1.24, 1.66 and 2.16 μm respectively. This was undertaken by two automated 1.3 m telescopes, at Mt. Hopkins, Arizona, USA and Cerro Tololo Inter-American Observatory, Chile. The survey commenced in 1997 and was completed in 2001. The final 2MASS all-sky data release took place in 2003 (Cutri et al. 2003).

The United Kingdom Infrared Telescope (UKIRT) at Mauna Kea Observatory carried out the UKIRT Infrared Deep Sky Survey[2] (UKIDSS, Lawrence et al. 2007), starting in May 2005. The survey was conducted using the UKIRT Wide Field Camera (Casali et al. 2007), and the Large Area Survey (LAS, Lawrence et al. 2012b) considered in this thesis covers a total sky area of 4000 sq. deg ($\sim$ 10 per cent sky coverage). UKIDSS covers similar bands to 2MASS – Y, J, H and K, at effective wavelengths 1.03, 1.24, 1.62 and 2.19 μm.

The final IR instrument I utilise is the National Aeronautics and Space Administration (NASA) *Wide-field Infrared Survey Explorer*[3] (*WISE*, Wright et al. 2010). This is a 0.4 m space telescope in low Earth orbit, that surveyed the sky in four photometric bands ($W1$, $W2$, $W3$ and $W4$ – respective effective wavelengths 3.4, 4.6, 12, and 22 μm) over the course of 10 months in 2010. Photometry data was released publicly in 2012 as the *WISE* All-sky Data Release (Cutri et al. 2012).

[1] http://www.ipac.caltech.edu/2mass/
[2] http://www.ukidss.org/
[3] http://www.jpl.nasa.gov/wise/

2.2.2 Optical

Compared to IR astronomy, observing the Universe at optical wavelengths is more straightforward, as the atmosphere is transmissive and there are fewer sources of noise. In this work, I consider wavelengths falling between 3800 and 7500 Å as being in the optical range. I predominantly use optical spectroscopy, with some photometry relevant to the variability studies of AGN (see Section 2.3).

The Sloan Digital Sky Survey[4] (SDSS, York et al. 2000) is a wide-field optical photometric and spectroscopic survey. At the time of writing, it is an ongoing survey entering the forth stage (SDSS-IV) of its science mission. The first stage, SDSS-I, was undertaken from 2000−2005, using a dedicated 2.5 m telescope at the Apache Point Observatory, New Mexico, USA. This imaged 8000 sq. deg of the sky in five photometric bands, u, g, r, i and z (with effective wavelengths 3595, 4640, 6122, 7440, 8897 Å) and took optical spectra of $\sim 700,000$ objects. SDSS-II further developed these goals between 2005 and 2008, adding surveys of both supernovae and stars in the MW to the expanding data archive. Following SDSS-II, the seventh data release (DR7) had categorised 105,783 AGN with optical spectra.

The SDSS spectrographs were overhauled for SDSS-III, and between 2008 and 2014, four more surveys were taken, three of which were focussed on the MW and extrasolar planets, and one which extended and improved the spectroscopic catalogue of distant objects – the Baryon Oscillation Spectroscopic Survey (BOSS). In DR12, the final data release of SDSS-III, 297,301 AGN had been spectroscopically classified.

SDSS-IV, running from 2014 to 2020, is adding southern sky observations from the Irénée du Pont Telescope at Las Campanas Observatory, Chile to the SDSS data archive.

The SDSS-I/II spectrographs covered the wavelength range $3800-9200$ Å with a spectral resolution of $R \sim 2000$. They used 640 optical fibres, each of diameter 3 arcsec ($3''$). SDSS-III/IV used the improved BOSS spectrographs, which delivered greater wavelength coverage ($3600-10400$ Å) from 1000 $2''$ fibres at higher S/N than SDSS-I/II.

All SDSS missions use a highly automated data reduction pipeline to present the data to the astronomy community in a ready-to-use format. The spectroscopic pipeline is described in detail in Stoughton et al. (2002), but a brief summary follows.

Science observations with the spectrograph are broken up into 15 minute exposures,

[4]http://www.sdss.org/

with a dichroic at $\sim$ 6000 Å splitting red and blue light on to separate arms. As is the case for the NIR spectrographs discussed in Section 2.2.1, additional calibration frames, including flat-fields, arcs, biases, sky backgrounds and standard stars are collected quasi-simultaneously. Each science and standard star frame is first bias subtracted and flat-field corrected. The flat-field frames are also used to characterise the position of each target on the detector, for source extraction. A wavelength solution is generated from the arc lamp spectra, and applied to the science and standard star frames. The sky background is subtracted, and the standard star spectra are used to characterise and correct telluric absorption features. The spectra are flux calibrated using the standard star observation and a composite stellar template, before the individual science frames are stacked, and red and blue arms combined.

In Chapter 6, I use data from the William Herschel Telescope Intermediate dispersion Spectrograph and Imaging System (WHT/ISIS). The WHT is a 4.2 m telescope situated at the Roque de los Muchachos Observatory on the Spanish island of La Palma, and operated by the Isaac Newton Group of telescopes (see Fig. 2.2). ISIS is a medium-resolution spectrograph which is used here for long-slit spectroscopy. Data must be reduced manually, or using custom-made reduction pipelines. The basic steps involved in reduction are similar to those described above for SDSS, and were performed using the Image Reduction and Analysis Facility (IRAF) V2.16. An advantage of long slit spectroscopy over the fibres of SDSS is the ability to set custom apertures, however, as my targets are point sources,

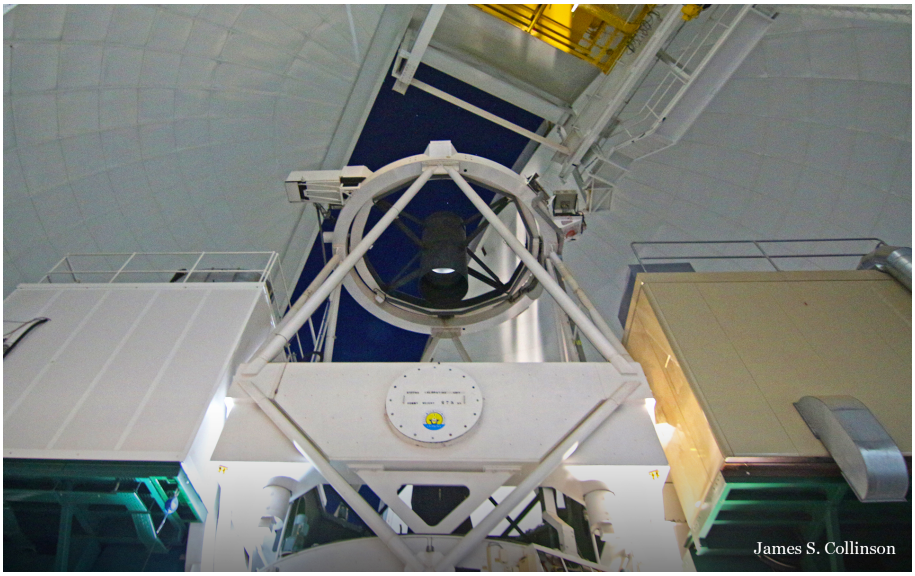

Figure 2.2: Photograph from within the William Herschel Telescope dome, showing the secondary mirror support structure.

the practical differences between the two approaches are small. Standard stars were observed throughout each night of observing, and science targets were flux calibrated to the standard star observed closest in time.

Lastly, some additional optical data comes from the Liverpool Telescope (LT, Steele et al. 2004) at the Roque de los Muchachos Observatory, and the Large Binocular Telescope (LBT, Hill & Salinari 2000) at Mount Graham International Observatory, Arizona, USA. The LT is a 2 m robotic telescope that was used for follow-up photometry of some of the transients in Chapter 6. In this imaging mode, the LT uses the same filters as SDSS, and offers comparable capabilities to the SDSS photometric surveys. The LBT is a considerably more complex instrument than most I have discussed so far, comprising two 8.4 m mirrors that share a common mount and therefore observe the same part of the sky simultaneously. In addition to the added light gathering, the binocular setup allows for interferometric observations, with a greater resolving power in the horizontal plane. The Multi-object Double Spectrographs (MODS, Pogge et al. 2010) on LBT offer wavelength coverage from 3200 – 11000 Å at medium resolutions. Like GNIRS and TSpec, they offer a range of observing modes, but our observations (PI: K. Denney) used long slit spectroscopy, and a procedure similar to that described above for WHT/ISIS.

2.2.3 Ultraviolet

The UV wavelength range is particularly challenging to observe, as the Earth's atmosphere absorbs radiation at these wavelengths, necessitating the use of space telescopes to collect data. As with the IR and optical ranges, I utilise both photometric and spectroscopic UV data at various points throughout this work.

The *Galaxy Evolution Explorer*[5] (*GALEX*, Martin et al. 2005, Morrissey et al. 2007) is a 0.5 m telescope in low Earth orbit that was launched in 2003. It has produced several imaging and spectroscopic surveys of the UV sky in two bands – NUV and FUV, at effective wavelengths 2274 and 1542 Å. The largest of these surveys, the All-sky Imaging Survey (AIS, Martin et al. 2005), took photometric observations covering 26,000 sq. deg (65 per cent of the sky), but limits on the safe detector flux exposure meant that bright sources (e.g. near to the Galactic plane) could not be observed.

[5] http://www.galex.caltech.edu/

The Optical Monitor (OM) aboard the *XMM-Newton* observatory (Mason et al. 2001) takes UV/optical observations contemporaneously with the primary X-ray instrument (described in Section 2.2.4). The telescope is 0.3 m in diameter, and has seven lenticular filters for photometry in different bands, and two grisms for taking low-resolution spectra in the UV and optical. The OM filters are: V, B, U, UVW1, UVM2, UVW2 and white, with effective wavelengths 5430, 4500, 3440, 2910, 2310, 2120 and 4060 Å respectively. Data from OM was processed by a pipeline using tools from the *XMM* Science Analysis System (SAS), and released as the *XMM-Newton* Serendipitous UV Source Survey catalogue, described in detail in Page et al. (2012).

The AGN considered throughout this thesis are generally too faint to use the spectroscopic capabilities of these instruments. Although they can still add useful data coverage in the UV, emission and absorption features within the filter bandpass bias the photometric measurements, which can be problematic for SED modelling. As such, in Chapter 5, I present a pilot study employing the medium resolution UV Cosmic Origins Spectrograph on the *Hubble Space Telescope*[6] (*HST*/COS).

Launched into low Earth orbit in 1990, *HST* has cemented its place as one of the most famous astronomical telescopes in operation, thanks to revolutionary observations of the deep sky. With a suite of multiwavelength spectroscopic and photometric instruments, *HST* remains an extremely capable space mission, and still delivers $\sim$ 1000 publications per year[7].

HST is a 2.4 m telescope, with a range of instruments operating from UV through to IR wavelengths. COS (Green et al. 2012) was installed as part of *HST* Servicing Mission 4 in May 2009 and offers a choice of gratings to deliver UV spectroscopy in the range 1150–3200 Å. Although tools are provided to aid COS data reduction, these are typically modified according to the needs of the observer. The data used in this thesis was archival, drawn from the Stevans et al. (2014) sample, and had already been reduced by our collaboration (C. Finn, private communication). Stevans et al. (2014) required that targets had been observed using both the G130M and G160M gratings, delivering both good wavelength coverage (1135 – 1795 Å) and excellent resolution (17 km s^{-1}). The reduction process is described in detail in Danforth et al. (2010) and Shull et al. (2012).

Wavelength coverage of all IR–UV instruments so far discussed is shown in Fig. 2.3.

[6] http://www.stsci.edu/hst/

[7] http://archive.stsci.edu/hst/bibliography/pubstat.html

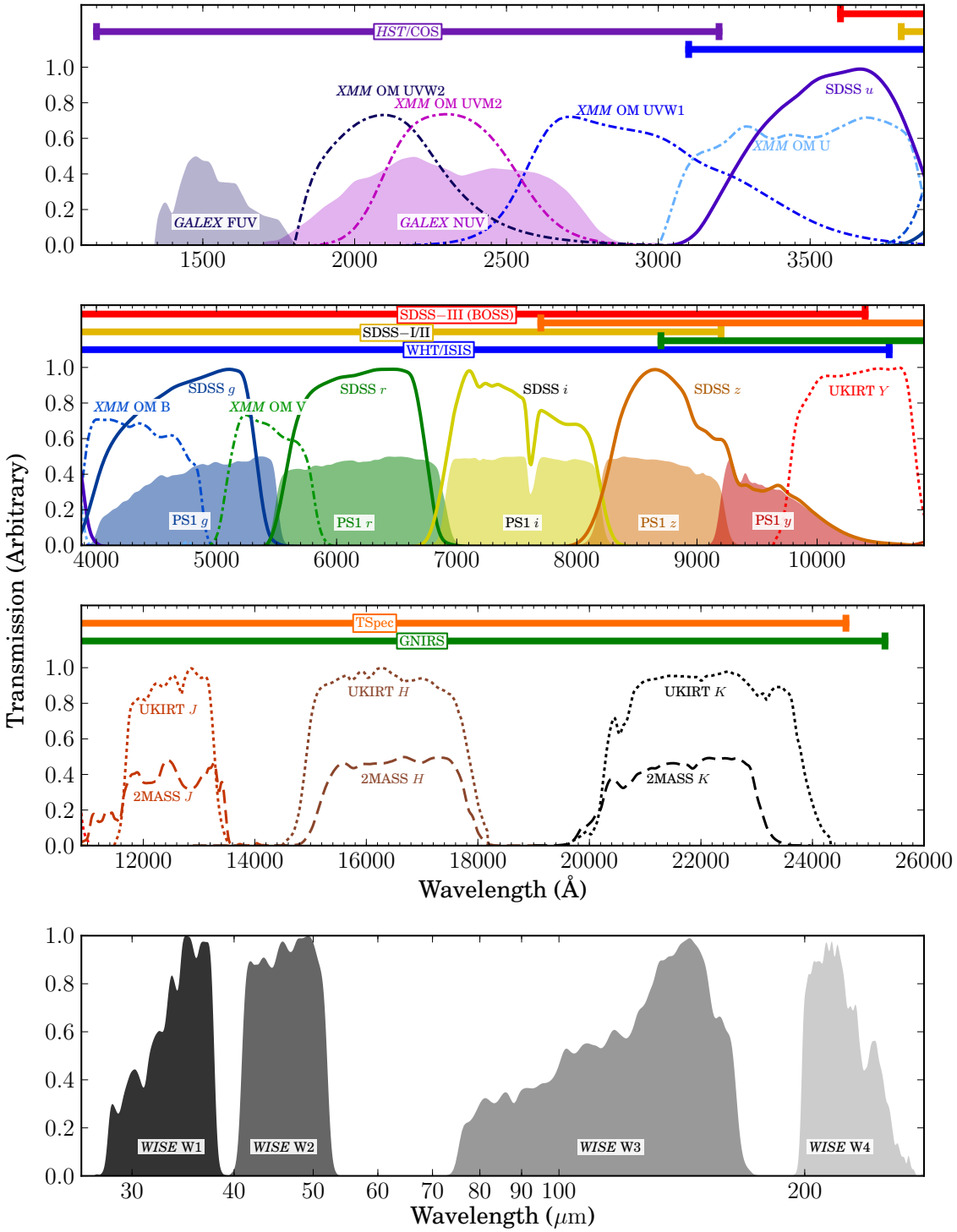

Figure 2.3: A plot of the wavelength coverages of the key MIR–UV instruments considered in this thesis. The curves and shaded regions show various photometric instrument responses, arbitrarily normalised. The bold ranges at the top of each panel show the coverage of the spectrographs used throughout.

2.2.4 X-rays

As is the case with UV light, the Earth's atmosphere is opaque to X-rays, so X-ray telescopes must be placed in space. I predominantly use data from *XMM-Newton*[8] (Jansen et al. 2001) throughout this work, an X-ray satellite launched by the European Space Agency (ESA) in 1999. *XMM* collects X-ray photons in the energy range 0.2–12 keV using the European Photon Imaging Cameras (EPIC). These three detectors are denoted MOS1, MOS2 (Turner et al. 2001) and PN (Strüder et al. 2001).

Data are collected by the *XMM-Newton* EPIC in a different manner to other wavelength ranges so far discussed, mainly due to the scarcity and energy of X-ray photons. Whilst an optical photon, for instance, can only induce a charge corresponding to a single electron's promotion across the silicon band gap in a CCD, a single X-ray photon is much more energetic, and can excite many electrons. The detector is read out at regular intervals during the course of an X-ray observation. Each pixel in each 'frame' is then assumed to have either detected one X-ray photon, or none, with the charge of activated pixels being used to determine the responsible photon's energy. If EPIC is recording too slowly for this assumption to be true, two or more photons may arrive at the same pixel in a single frame ('pile-up'). In this case, it is impossible to determine whether the pixel charge has arisen from one or multiple photons. Therefore, different readout modes are available for different brightness targets, with faster modes using a smaller detector area to decrease readout times. For the very brightest sources, EPIC PN has a 'burst' mode available, taking frames of duration 7 μs. However, due to the detector readout times, this mode has an inefficient duty cycle of 3 per cent. Observations are saved as events files, with each detected photon's energy, position and arrival time being recorded. This allows images, spectroscopy and light curves to be generated from a single observation, making X-ray observations extremely versatile.

XMM-Newton is not a survey instrument by design, but its $\sim$ 30 arcmin field-of-view and 16 year (and ongoing) mission length means it has accrued a fairly significant total sky

[8] http://sci.esa.int/xmm-newton/

coverage of ~ 2 per cent to date. An advantage of this is that during pointed observations of key science targets, *XMM* serendipitously observes any targets that happen to be close to the main objective. As such, a number of iterative serendipitous source catalogues (Watson et al. 2003, Watson et al. 2009, Rosen et al. 2016) have been assembled, that include nearly all of the objects observed both directly and indirectly by *XMM-Newton*.

Observations have been reduced by a pipeline according to the following steps, which are described in more detail in Watson et al. (2009). The pipeline employs routines in the *XMM* SAS. First, the detector events file is generated from the raw science frames. Only exposures deemed to be useful, requiring an exposure time, $T_{\rm exp} > 1000$s, a scientific instrument mode and sufficient observation quality, were included, and only photons detected during 'good time intervals' (GTIs), where the background radiation level (from e.g. the Sun) was low, were counted. X-ray images were generated from the events files that met these criteria, and sources were selected using a box detection algorithm and maximum-likelihood fitting routine. These sources were then cross-correlated with archival resources to reject spurious detections, and binned data products were extracted using the source list and GTI events file.

In Chapter 5, I include X-ray data from the *Chandra Observatory* (Weisskopf et al. 2000). Launched by NASA in the same year as *XMM-Newton*, *Chandra* is a space telescope that uses its onboard Science Instrument Module to collect X-rays in a similar manner to EPIC on *XMM*. *Chandra* offers higher-resolution X-ray spectroscopic capabilities than *XMM*, but an inferior effective collecting area. The different capabilities of the two instruments are complementary, although in this work, both *XMM* and *Chandra* are used for broadly similar purposes – generating low-resolution X-ray spectra of relatively faint AGN.

X-ray data are highly versatile due to the various spectral/timing analyses that can be made with a single observation. However, due to the scarcity of counts compared to other wavelength ranges discussed so far, more efficient flux calibration methods must be used, which incorporate the energy-dependent instrument response. An overview of this process is given in Section 2.4.

2.3 Temporal Data

The night sky is constantly evolving. The bodies of the solar system move with respect to Earth, and precise astrometry can track the relative motion of nearby stars over several years. In addition to these changes, a multiplicity of phenomena produce variations in the observed radiative flux of stars and galaxies; stars are seen to change their brightness over time, supernovae and gamma ray bursts can briefly outshine entire galaxies upon initiation, and AGN exhibit variability at a range of different frequencies.

This motivates astronomers to monitor the night sky over time. Initially, this involved pointed observations of objects of note, with chance playing a significant role in the detection of unpredictable phenomena, but as instrumentation and computation have become ever more powerful, this is increasingly undertaken by high-cadence, large area sky surveys.

Many such surveys, including the Catalina Sky Survey[9] (CSS, Larson et al. 2003) and the Panoramic Survey Telescope and Rapid Response System[10] (Pan-STARRS, Kaiser 2004, Kaiser et al. 2010) were designed around the goal of detecting and classifying near-Earth objects that pose a threat of collision. This involves taking photographs of large areas of the night sky every few days/weeks and using difference imaging to look for objects that have moved. The resulting data streams can also be used to generate light curves of any object in the survey area, with implications for monitoring any source bright enough to be detected.

CSS uses a 0.7 m telescope located near Tucson, Arizona, USA, and has surveyed 26,000 sq. deg (63 per cent) of the sky. For each area of sky under surveillance, observations are repeated over the course of the night (four observations spaced $\sim$ 30 minutes apart), suiting the survey to detecting transients on (non-contiguous) timescales of minutes to years. The Catalina Real-time Transient Survey (CRTS, Drake et al. 2009) is a program that performs this task – using data from CSS and its sister surveys to search for supernovae, variable AGN, cataclysmic variables, and other highly variable objects. CRTS observations are in white light, with no colour filters applied. This maximises the

[9] http://www.lpl.arizona.edu/css/
[10] http://pan-starrs.ifa.hawaii.edu/

S/N of detections, but makes photometric classification of transients impossible.

Pan-STARRS 1 (PS1) is a 1.8 m wide-field telescope, situated on Maui, Hawaii, USA. It saw first light in 2007, and the science mission commenced in 2010. Since March 2010, it has surveyed the sky in five photometric bands ($g_{\rm P1}$, $r_{\rm P1}$, $i_{\rm P1}$, $z_{\rm P1}$ and $y_{\rm P1}$); 56 per cent of the observing time is devoted to the 3π survey (75 per cent sky coverage), with additional, deeper observations of smaller sky regions making up the 'Medium Deep Survey' (Kaiser et al. 2010, Magnier et al. 2013). A program comparing data from the 3π survey with earlier SDSS observations, called the 'Faint Galaxy Supernova Survey' (FGSS, Inserra et al. 2013) searched for distant galaxies that showed evidence for supernovae through a large increase in luminosity.

These surveys are well suited to detecting AGN that are variable at optical wavelengths, and were used to select the sample studied in Chapter 6. As discussed in Section 1.3.5, the X-ray emission from AGN originates in the inner parts of the AD, and can vary over the duration of a single X-ray observation. Such variability is automatically monitored during normal operation of both *XMM-Newton* and *Chandra* (see Section 2.2.4), but longer timescale variability trends require repeated observations.

2.4 Models

2.4.1 Computation

All broad-band SED fitting in this work is performed in the XSPEC[11] spectral fitting program (Arnaud 1996). XSPEC is a command-line-based software package that is predominantly written in Fortran, and for 30 years has been widely used by the X-ray astronomy community. Its success as a tool for astronomers is partly due to the efficient implementation of X-ray data, in which often the scarcity of photons imposes limitations on the versatility of observations. The X-ray detector records some fraction of the incident X-ray photons, depending on both the energy of those photons, and their position on the detector. Therefore the observation is a convolution of the true distribution of X-ray photons that arrived at the telescope with the instrument response. XSPEC uses a model of this true

[11] http://heasarc.gsfc.nasa.gov/xanadu/xspec/

distribution (which is unknown) and the detector response (which is known) to produce a 'simulated' observation. The properties of the unknown model can then be changed, to minimise the difference between the observed and simulated counts distributions.

This is done using the Levenberg-Marquardt minimisation algorithm (e.g. Gill & Murray 1978). In brief, this routine is commonly used to solve non-linear least squares problems. It does this iteratively, and requires an initial guess of the optimum parameters. The algorithm uses the parameter gradient vector to refine the parameters, until a gradient of zero is achieved. As such, the algorithm is susceptible to local minima convergence, which may not be the global minimum. A greater chance of a successful minimisation therefore requires initial guesses close to the optimal solution.

All other model fitting, including of light curves and spectra, was performed with custom scripts written in the PYTHON programming language[12]. I used the Levenberg-Marquardt minimisation routine implemented in the LMFIT package[13] and also several useful tasks available in the ASTROPY library[14]. All original plots in this work were created in the MATPLOTLIB environment[15].

2.4.2 Spectral Energy Distribution

In Section 1.3 I discussed the fundamental principles of the thin AD SED model. This forms the basis of most disc models applied to AGN, with general relativistic, colour temperature and radiative transfer corrections applied (Hubeny et al. 2000, Davis et al. 2006). Various further modifications can be added, such as winds and outflows (Slone & Netzer 2012), and energetically consistent reprocessing to X-rays (Done et al. 2012). It has been suggested that at higher accretion rates, the thin AD assumption may no longer hold, and that the disc instead becomes 'slim,' due to photon trapping within the disc (e.g. Abramowicz et al. 1988, Wang et al. 2014), however these models are not well understood (Castelló-Mor et al. 2016), and are beyond the scope of this thesis.

I use a multi-component model called OPTXAGNF, which is based on studies of BHBs

[12]http://www.python.org/
[13]http://www.lmfit.github.io/lmfit-py/
[14]http://www.astropy.org/
[15]http://www.matplotlib.org/

and nearby Narrow-line Seyfert 1s (NLS1s) and described in Done et al. (2012). It is characterized by three principal components: AD, PLT and SX (see Section 1.3 for more on the physical origin of these components). A schematic SED diagram of OPTXAGNF is shown in Fig. 2.4. The AD is modelled as a relativistic, geometrically thin, optically thick Shakura & Sunyaev (1973) disc from the outer disc radius ($r_{\rm out}$) to a coronal radius ($r_{\rm cor}$), with a colour correction ($f_{\rm col}$) to account for the fact that the disc is not completely thermalized at all radii. Below $r_{\rm cor}$, the AD energy is reprocessed by inverse Compton scattering in the SX (by a thermal component in the disc) and PLT (by the hot corona).

As noted in Section 1.3.2, the origin of the SX component is the subject of open debate. Whilst OPTXAGNF assumes a warm Compton up-scattering origin, practical limi-

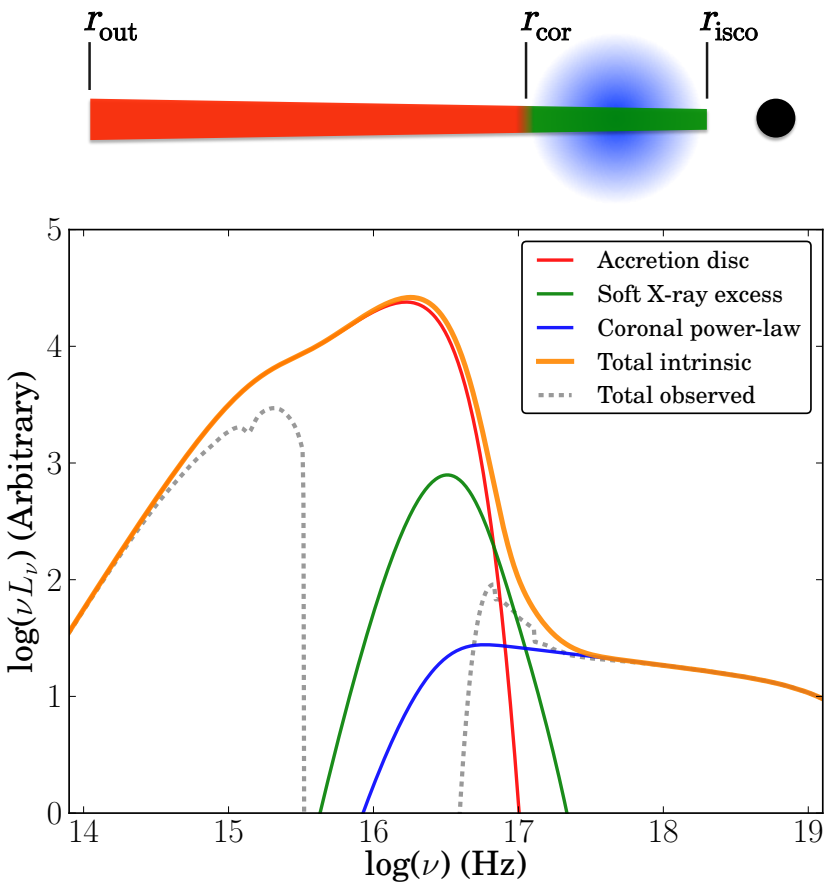

Figure 2.4: The OPTXAGNF SED model of a typical disc-dominated AGN. Colours correspond to the regions shown in the AGN schematic (top), with red representing the AD, green the SX and blue the PLT from the corona. The grey dotted line shows the resultant observed SED when it has been attenuated by typical Galactic and extragalactic extinction and absorption. The radii labelled are the outer disc radius ($r_{\rm out}$), coronal radius ($r_{\rm cor}$) and the radius of innermost stable circular orbit ($r_{\rm isco}$). Figure adapted from Done et al. (2012).

Table 2.1: Model parameters for the SED models OPTXAGNF and OPTXCONV.

Model	#	Parameter	Description	Units
OPTXAGNF	1	$M_{\rm BH}$	BH mass	$M_\odot$
	2	$r_{\rm c}$	Comoving distance	Mpc
	3	$\dot{m}$	Eddington ratio $= L/L_{\rm Edd}$	–
	4	a_*	BH spin	–
	5	$r_{\rm cor}$	Coronal radius	$R_{\rm g}$
	6	$\log(r_{\rm out})$	Logarithm of outer AD radius	$\log(R_{\rm g})$
	7	$kT_{\rm e}$	SX electron temperature	keV
	8	τ	SX optical depth	–
	9	Γ	PLT photon index	–
	10	$f_{\rm PL}$	Fraction of Comptonised energy in PLT	–
	11	z	Redshift	–
	12	Norm	Arbitrary normalisation $= 1$	–
OPTXCONV	1–10		Same as OPTXAGNF	
	11	Inc	Inclination angle to observer	deg.
	12	z	Redshift	–
	13	Norm	Arbitrary normalisation $= 1$	–

tations in the quality and energy coverage of the X-ray data mean that uncertainties in the origin of the SX cannot be unambiguously resolved in this work.

Importantly, this AGN SED model applies the constraint of energy conservation, as energy output is dependent on the amount of matter accreting on to the BH. So $M_{\rm BH}$, $\dot{M}$ and a_* set the total amount of energy that is in the three components. This model was designed for implementation into XSPEC, and has previously been tested on a moderate number of AGN (e.g. Jin et al. 2012a, Done et al. 2013, Matt et al. 2014). The model parameters in OPTXAGNF are presented in Table 2.1.

In Chapter 4, I compare my results with those from the updated OPTXCONV. Described in Done et al. (2013), this model refines OPTXAGNF by including relativistic effects. This is inclination dependent, so this model includes an additional inclination parameter – see Table 2.1. The dependence on inclination is small for low spin BHs, and correspondingly, there is little difference between OPTXAGNF and OPTXCONV. However, for highly spinning BHs, the relativistic effects and inclination angle become highly significant – see Section 4.6.2.

2.4.3 Torus and Host Galaxy

In Chapter 4, I model the dusty torus component using photometry from *WISE*. In practice, the torus has a complex SED, comprising blackbody emission from the (possibly clumpy – see Section 1.3.3) hot dust, and emission/absorption features. This means that accurately modelling the component is difficult, and requires radiative transfer and chemical evolution simulations (e.g. Silva et al. 1998). Alternatively, templates derived from such simulations or multiwavelength observations can be used. However, due to limited data coverage, I adopt a simpler approach in Chapter 4, modelling the torus with blackbody components.

To model the stellar contribution in AGN host galaxies, I use the templates of Polletta et al. (2007). Built from an X-ray selected sample of mainly active galaxies, this library includes IR-UV templates of Type 2 AGN in which radiation from the central engine is obscured. These are used to represent the flux from stars in galaxies hosting AGN.

2.4.4 Attenuation

I correct all IR–UV data for MW dust extinction. The extent of this reddening is parameterised by the photometric band dependent attenuation in magnitudes, $E(B-V)$, which is measured using the dust maps of Schlegel et al. (1998). Extinction correction must be applied before spectral analysis, to recover the true flux density at each pixel. With regard to the SED analysis, one has a choice of either fitting dereddened data, or fitting the observed data with a reddening component included. For reasons of convenience, I use both approaches at various points in the chapters that follow. For the former approach I use the extinction correction tool provided in the ASTROPYSICS PYTHON module[16], and for the latter, I use the multiplicative XSPEC model REDDEN. Both of these use the empirical extinction law of Cardelli et al. (1989).

Host galaxy extinction must be modelled as a free parameter in the SED fitting. I use the ZREDDEN and ZDUST models in XSPEC; ZREDDEN uses a redshifted version of

[16]http://www.pythonhosted.org/Astropysics/

the Cardelli et al. (1989) curve, and ZDUST offers a choice of three empirical curves – MW, Small Magellanic Cloud (SMC) and Large Magellanic Cloud (LMC), as derived by Pei (1992). The main difference between these models is the 2200 Å feature, caused by graphitic/silicate dust grains. A comparison of the three models is shown in Fig. 2.5.

To model the photoelectric absorption of soft X-rays, I use the WABS absorption model (Morrison & McCammon 1983) in XSPEC. $N_{\rm H}$ column densities are fixed to values from the Leiden/Argentine/Bonn survey of Galactic H I (Kalberla et al. 2005). I use the redshifted version of this model, ZWABS, for the host galaxy.

The parameters of all of these models are given in Table 2.2.

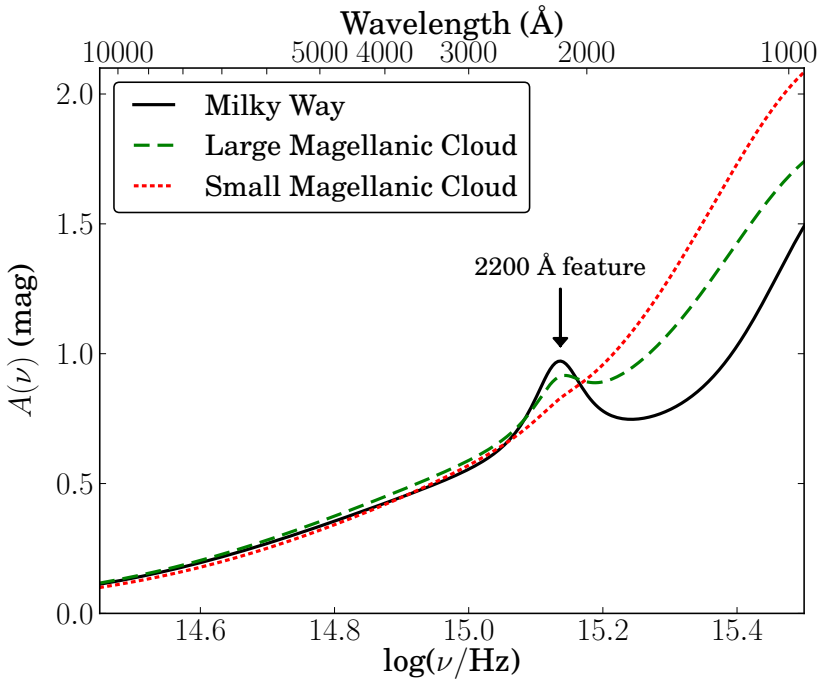

Figure 2.5: A comparison of the Pei (1992) extinction curves derived from three different galaxies – MW, LMC and SMC. Often, one must assume one of these profiles (with normalisation a free parameter) to model the extinction due to an AGN's host galaxy, and the variation (particularly in the 2200 Å feature) makes this choice an important one.

Table 2.2: Attenuation model parameters for the SED modelling.

Model	#	Parameter	Description	Units
REDDEN	1	$E(B-V)$	$B-V$ band extinction	mag
ZREDDEN	1	$E(B-V)$	$B-V$ band extinction	mag
	2	z	Redshift	–
ZDUST	1	Method	Set reddening curve – MW, SMC or LMC	–
	2	$E(B-V)$	$B-V$ band extinction	mag
	3	$R(V)$	Ratio of absolute to selective extinction, $R(V) = A(V)/E(B-V)$	–
	4	z	Redshift	–
WABS	1	$N_{\rm H}$	H I column density	10^{22} cm^{-2}
ZWABS	1	$N_{\rm H}$	H I column density	10^{22} cm^{-2}
	2	z	Redshift	–

2.4.5 Spectral Emission Features

The ubiquitous AGN emission lines are broadened by Doppler motion as the BLR/NLR clouds orbit the SMBH, and it is common practice to model these features using a combination of Gaussian profiles. The number of components that is statistically justifiable depends on the quality of the spectra, but for all but the lowest S/N observations at least two components are used, which are physically attributed to the 'broad' (emitted in the BLR) and 'narrow' (emitted in the NLR) components. Whilst the use of Gaussians only offer an approximation to the true emission line shape, they provide a versatile and widely adopted means of characterising the emission lines (see e.g. Greene & Ho 2007, Dong et al. 2008, Wang et al. 2009, Matsuoka et al. 2013). Alternative means include Gauss-Hermite polynomials (e.g. Assef et al. 2011, Park et al. 2012 and references therein), but are not considered in this work.

The multiplicity of possible energy transitions in iron, combined with its relative cosmic abundance, mean that in many AGN, a great number of blended features, mainly from the singly ionised species (Fe II) are seen at a range of wavelengths, shown in Fig. 1.4.

This presents a problem for AGN spectral modelling, as these features must be char-

acterised. One of the simplest, yet most effective means of fitting the Fe II contribution is to use empirical templates derived from local AGN with relatively narrow Fe II lines. I Zwicky 1 is an ideal candidate, from which iron emission templates have been constructed. I use the templates of Vestergaard & Wilkes (2001) in the UV and Véron-Cetty et al. (2004) in the optical for this purpose, and use the Verner et al. (2009) theoretical template for the gap between these two, at rest wavelengths of 3100 – 3500 Å. The templates are broadened by convolution with a Gaussian to fit Fe II emission in any AGN showing broader features than I Zwicky 1.

The continuum of Balmer emission lines below 3646 Å approximately takes the form (Grandi 1982):

$$F_{\nu,\mathrm{BC}} = F_{\nu,\mathrm{BE}}\, e^{-h(\nu-\nu_{\mathrm{BE}})/(kT_{\mathrm{e}})} \quad (\nu \geqslant \nu_{\mathrm{BE}}) \tag{2.4.1}$$

where ν_{BE} and $F_{\nu,\mathrm{BE}}$ are the frequency and flux density at the Balmer edge, respectively. I adopt this formula throughout.

CHAPTER 3

AGN SEDs Part 1: Reaching the Peak

3.1 Introduction

3.1.1 Motivation

Multiwavelength studies of AGN are an important means to further our understanding of these objects. Interpreting the AGN SED remains a challenge in astrophysics, although the last few decades have seen significant advances in the field (e.g. Ward et al. 1987, Elvis et al. 1994, Vasudevan & Fabian 2007). It is now widely accepted that accretion of gas on to a central SMBH is the ultimate source powering these extremely luminous objects. The SED contains clues to the structure and properties of the matter in the regions close to the BH. Better understanding of the SEDs has consequences for cosmology, as there is strong evidence that galaxy formation is influenced by the AGN, through the process of feedback (e.g. McCarthy et al. 2010, see Section 1.5).

The simplest interpretation of the unified model of AGN proposes that most of the diversity observed in SED properties can be attributed to differences in the orientation of the accretion flow and line-of-sight absorption (Antonucci 1993). In practice, however, this simple picture is incomplete, and other physical differences in the BH itself (e.g. spin) and the properties of the infalling matter also strongly influence the observed SED (Boroson & Green 1992, Done et al. 2012).

This situation has motivated us to develop new broad-band SED models, based on theoretical considerations and empirical studies of accreting stellar-mass BHs found in X-ray

binaries. Combining AGN SED models with representations of Galactic and extragalactic extinction, both via dust and photoelectric absorption, enables fitting of the multiwavelength data from an AGN, and recovery of the intrinsic SED, which relates directly to the properties of the BH and the material it accretes. Previous studies by Jin et al. (2012a, b, c) have successfully employed this technique. The peak of the energy output occurs at FUV/soft X-ray energies in the majority of these low redshift AGN. These energy ranges are mostly unobservable due to photoelectric absorption by neutral hydrogen in the IGM along the line-of-sight to the source (Gunn & Peterson 1965, see Section 1.3.4), and that intrinsic to the MW.

In order to overcome this restriction, I consider a sample of higher redshift AGN in this chapter, in which it is expected that the peak of the SED is shifted towards the observable optical/NUV energy range. This occurs for two reasons, the first being simply the redshift effect, and the second being that these more distant, luminous AGN contain more massive BHs which have cooler accretion discs peaking at lower energies (equation 1.3.7, McLure & Dunlop 2004, Done et al. 2012).

In this chapter, I describe the sample and discuss the selection process and the data that has been assembled. I next present model fits from rest-frame optical to hard X-rays, using the three component accretion model OPTXAGNF (see Section 2.4). Finally I explore the modifying effects of extinction and absorption, and the possible influence of a stellar component in the host galaxy. In Chapter 4, I investigate the parameter space further, including the toroidal dust component. In Chapter 5, I discuss the future application of these findings to the analysis of a larger, statistically significant sample.

3.1.2 Previous Work

Initial studies of AGN focused primarily on UV, optical and IR spectra (e.g. Wills et al. 1985, Zheng et al. 1997), but with improvements in ground-based instrumentation and new satellites, it is now routinely possible to study AGN samples across multiple wavelength bands.

Puchnarewicz et al. (1992) presented a study of optical and X-ray data of 53 AGN with ultra-soft X-ray excesses, and found a bias in their emission line profiles towards

narrow linewidths, which had implications for the position and size of the BLR. Grupe et al. (1998, 1999) confirmed this result and also reinforced the findings of Walter & Fink (1993) that there is a 'big blue bump,' now thought to be the result of the AD discussed in Section 1.3.1, from optical to X-ray spectra.

More recently, Jin et al. (2012a, b, c) presented a comprehensive SED modelling study of 51 AGN. In this study, they assembled optical and X-ray spectra from the SDSS and *XMM-Newton*. This was supplemented, when available, by photometric UV data from the *XMM* OM. These data ranges are not contiguous and leave the SED peak, unobservable due to the aforementioned absorption, devoid of data. Whilst SDSS and *XMM* OM data constrain only the optical edge of the AD, *XMM* EPIC data only lie in the energy range of the SX and PLT. Thus the AD peak (and hence SED peak in the disc-dominated objects) was unsampled and information as to its position and shape had to be inferred from the fitted models. Since the AD peak originates from the innermost part of the accretion flow, it contains key information about the BH spin and mass accretion rate, and hence the total luminosity of the AGN.

According to the 'no-hair' theorem (Section 1.2.1), BHs are characterised by just three properties – mass, spin and charge. Much study has been devoted to measuring the mass of a BH (Section 1.4), and charge is negligible in an astrophysical context. There is currently a great deal of interest in constraining spin, which can be estimated if some measurement of $r_{\rm isco}$ can be made. Attempts to do this have been made from profile-fitting the broad Fe Kα emission line (e.g. Fabian et al. 2009, Risaliti et al. 2013), whilst others use SED fitting to achieve this aim (e.g. Done et al. 2013, Capellupo et al. 2015), a technique highly relevant to this work. A more extensive study of BH spin is presented in Chapter 4.

Whilst previous works have successfully found evidence for the AD turnover by recovering the continuum from high-resolution UV spectra of high-redshift AGN, (e.g. Zheng et al. 1997, Finn et al. 2014, Lusso et al. 2015) no sizeable sample exists with X-ray spectra, although a pilot study is presented in Chapter 5. Furthermore, SED modelling studies ideally require reliable prior estimates of the BH mass, to restrict the number of unknown quantities in the models.

3.1.3 Estimating Black Hole Mass

RM represents the 'gold standard' in $M_{\rm BH}$ estimates (see Section 1.4.2) but requires extensive long-term monitoring programs, and is thus very expensive observationally. For this work, I therefore instead use the single-epoch virial mass estimation technique described in Section 1.4.3.

The problem with this technique arises in higher redshift AGN, where the well-studied Balmer lines are redshifted to IR wavelengths, and rest-frame UV lines are shifted to the optical regime. Much effort has been devoted to assessing the utility of the rest-UV lines for BH mass estimation, but the subject remains contentious. Vestergaard & Peterson (2006) studied the scaling relationships between mass estimates from Hβ, Hα and the rest-UV lines C IV and Mg II, finding that both offer viable alternatives to the Balmer lines for this purpose in a sample of low-redshift AGN. However, two studies of higher-redshift AGN, Netzer et al. (2007) and Shen & Liu (2012), contend instead that the line profile of C IV is unsuitable for mass estimation, but agree that Mg II shows reasonable correlation. Possible explanations put forward for this discrepancy in C IV are the presence of outflows that influence line profiles in high-redshift, high-Eddington-ratio AGN. It has also been claimed (Denney et al. 2013) that high S/N spectra are required to derive reliable mass estimates from C IV.

In any case, Hβ remains the mass estimator of choice (Woo & Urry 2002), simply by its virtue as the line best calibrated by RM. Greene & Ho (2005) proposed an alternative in Hα which shows excellent correlation with Hβ, but which, due to greater line strength, generally offers better S/N for the line analysis.

3.2 Sample and Data Assembly

3.2.1 Sample Selection

In order to define an AGN sample in which the SED peak would be observable, objects with redshifts of $z \sim 2$ were required. For SED modelling, data lying on both sides of the UV/soft X-ray absorption trough is needed, as was the case in the Jin et al. (2012a) sample. I thus required optical spectra, available from the SDSS ($\sim$ 35 per cent sky coverage) and X-ray data, available from *XMM-Newton*'s 3XMM DR4 data catalogue ($\sim$ 2 per cent sky coverage). In order to constrain physical parameters for the SED model, I also required

IR spectral data, so that BH mass estimates from the Balmer lines could be made.

I started by searching the Schneider et al. (2010) SDSS DR7 QSO catalogue for all AGN meeting the following criteria:

- $1.49 < z < 1.61$: This was so that Hα and Hβ would lie in the NIR *H* and *J* bands respectively, and Mg II and C IV lines would be visible in the SDSS spectra, for comparison purposes.

- $K_{\rm 2MASS} < 16.5$: Since medium resolution IR spectra were required, the objects needed to be suitably bright in the IR bands. Where *K* was unavailable in 2MASS, similar constraints were applied to the *J* and *H* bands. There were 1797 matching AGN after this step.

- *XMM-Newton* data: X-ray spectra were required from ESA's *XMM-Newton* instrument. 63 objects had matching observations with 18 of these being bright enough to have had a spectrum extracted by the *XMM* pipeline (typically requiring $\gtrsim 200$ counts).

We were awarded observing time in Cycle 2013B (PI: M. Elvis) to use the Gemini GNIRS instrument to obtain high quality IR spectra in the *J*, *H* and *K* bands. In practice 9 of our objects were visible to GNIRS in 2013B, and we proposed to observe the 6 with the highest SDSS S/N.

Simultaneously, I identified 4 objects in the Shen & Liu (2012) sample with *XMM* X-ray data of varying quality, and IR spectral data from the ARC 3.5 m telescope's TSpec instrument. One additional object with an *XMM* observation was selected from a publicly available, archival GNIRS 2004B dataset (PI: T. Boroson) that had not previously been reduced. This resulted in my final sample of 11 objects, listed in Table 3.1.

It is plausible that the selection criteria introduces some bias into the sample, for instance, by choosing objects with a higher than average IR/optical or X-ray/optical ratio. However, the mean value of $\alpha_{\rm OX}$ for Model 3 (see Section 3.4.3) is 1.61 ± 0.09, which is typical of large X-ray selected samples (e.g. Vignali et al. 2003, Lusso et al. 2010). There may be an inherent bias in the sample owing to the flux threshold of the parent SDSS spectroscopic database. It is of course true that the sample must have X-ray data, which will naturally bias against some sub-classes of X-ray weak AGN.

Table 3.1: The names, positions, SDSS pipeline redshifts and UV/IR data sources for the sample of 11 objects. The UV photometry is of limited use for my purposes (see Section 3.4.2).

ID	Name	R.A. (J2000)	Decl. (J2000)	$z_{\rm SDSS}$	IR Source	UV Phot[a]
1	J0041−0947	00 41 49.64	−09 47 05.0	1.629	TSpec[b]	N
2	J0043+0114	00 43 15.08	+01 14 45.6	1.563	GNIRS 13B	N
3	J0118−0052	01 18 27.98	−00 52 39.8	2.188	GNIRS 04B	–
4	J0157−0048	01 57 33.87	−00 48 24.4	1.551	TSpec[b]	N M2 W1
5	J0839+5754	08 39 06.53	+57 54 17.0	1.534	GNIRS 13B	N W1
6	J1021+1315	10 21 17.74	+13 15 45.9	1.565	GNIRS 13B	W1 B
7	J1044+2128	10 44 01.13	+21 28 03.9	1.494	GNIRS 13B	N
8	J1240+4740	12 40 06.70	+47 40 03.3	1.561	TSpec[b]	N F U
9	J1350+2652	13 50 23.68	+26 52 43.1	1.624	TSpec[b]	N F
10	J2328+1500	23 28 10.56	+15 00 12.8	1.536	GNIRS 13B	N
11	J2332+0000	23 32 28.21	+00 00 32.8	1.604	GNIRS 13B	N

[a] N $= NUV_{GALEX}$, F $= FUV_{GALEX}$, M2 $= UVM2_{\rm OM}$, W1 $= UVW1_{\rm OM}$, B $= B_{\rm OM}$.
[b] IR spectral data from TSpec courtesy of Yue Shen (Shen & Liu 2012).

3.2.2 Optical/IR Data Preparation

The IR spectra for the four objects selected from the Shen & Liu (2012) sample were kindly provided by Yue Shen (private communication).

The data resulting from Gemini cycle 2013B were reduced according to the guidelines provided on the Gemini website, using IRAF V2.14, and the Gemini IRAF package V1.12. The archival GNIRS 2004B object (J0118−0052) was reduced before the release of V1.12 and I thus used V1.11.1 of the Gemini IRAF package to reduce this object. A summary of the reduction procedure is provided in Section 2.2.1.

All Gemini spectra were created by GNIRS in cross-dispersed mode, and I was able to recover orders $3-8$ for the 2013B objects. I recovered orders $3-6$ in the 2004B object, due to a more limited range of flat-fields provided. All stages of the reduction were visually inspected, to ensure no errors had occurred.

Telluric stellar spectra were provided by Gemini. The purpose of these spectra is to provide a well-defined reference spectrum that may be used to correct object spectra for non-constant sky transmission across the IR wavelength range. I could not use the XTELLCOR routine discussed in Vacca et al. (2003) to correct for telluric features, as not

all of the standard stars observed were of spectral class A0V. Hence I corrected for telluric features in the following way.

Hydrogen absorption features in the telluric spectrum were first removed in IRAF, as these features are intrinsic to the star itself. Lorentzian absorption line profiles were assumed, as these fit the features better than Gaussian or Voigt profiles. The assumed template for the telluric star was a blackbody of a characteristic temperature dependent on the telluric stellar class, and flux normalised to the 2MASS J magnitude. The extracted object spectrum was then multiplied by the ratio of the assumed telluric template to the extracted telluric spectrum, producing a very satisfactory correction to the variable atmospheric transmission.

Two factors may affect the relative normalisations of the IR and optical spectra, observed as they were at different epochs. Variability of the AGN is one possible origin for such a change, and is discussed more in Section 3.5.3. The other factor is the accuracy of the flux calibration; if the optical or IR spectra were flux calibrated poorly (e.g. due to seeing problems or aperture effects), the resulting normalisation of the spectra will be incorrect. For the SDSS/BOSS spectra, I assumed that the flux calibrations were accurate.

The objects I reduced from Gemini were flux calibrated in the telluric correction step described above, which makes the assumption that the telluric star is not itself variable, and that weather conditions did not change between the object and telluric observations. The TSpec objects from Shen & Liu (2012), on the other hand, were all flux-normalised to the 2MASS H band magnitudes.

All of the objects in my sample have either UKIDSS or 2MASS (or both) photometry in each of J, H, and K bands. I first compared the flux of each photometry point with the average flux in the IR spectrum across the effective photometric bandpass, to estimate the percentage difference in flux density between these two values. As an additional check, I also compared how well the blue wing of each IR spectrum fitted a power-law extrapolated redward of the SDSS spectrum, or, if available, the region of spectral overlap between optical/IR spectra. This highlighted offsets of the IR spectrum relative to the optical spectrum. In doing this, I found that all but three of the objects showed evidence for less than 10 per cent difference between the IR spectrum and optical spectrum/IR photometry.

The three objects that showed greater than 10 per cent variation between optical and IR spectra are J0041−0947, J1044+2128 and J2328+1500.

In J1044+2128 and J2328+1500, I normalised to the *K*-band photometry, as there was evidence for some cloud cover at the time of observation that could have affected the flux calibration. In J0041−0947, the IR spectrum was normalised to 2MASS *H* by Shen & Liu (2012). However, it lies below the level predicted from the SDSS spectrum, possibly due to variability. I thus make the mass estimate from the spectrum as flux-normalised by Shen & Liu (2012), but normalise the spectrum to the optical level for the SED fit, as whether the difference was due to flux calibration error in either spectrum, or variability, I required agreement to fit the SED shape.

Finally, in all objects I corrected both the IR and optical spectra for extinction by the MW, using the dust maps of Schlegel et al. (1998) and the extinction law of Cardelli et al. (1989).

All of the optical data come from SDSS. Five of the objects had been observed multiple times in the SDSS-I/II spectroscopic surveys, or reobserved by BOSS as part of SDSS-III. As the BOSS spectrographs offer greater wavelength coverage and improved S/N, they are the preferred source of optical data. In the absence of BOSS spectra, I used the SDSS-I/II spectrum that best aligned with the IR spectrum.

The optical and IR spectral observation dates are tabulated in Table 3.2. I provide estimates of the spectral S/N by estimating and averaging the S/N per pixel in 10,000 random, 50-pixel subsamples from each spectrum. The optical spectra adopted for the SED fitting are highlighted in bold. A greater discussion of variability in general is given in Section 3.5.3.

3.2.3 UV and X-ray Data

I extracted all X-ray data from the *XMM-Newton* Science Archive, through NASA's High-Energy Astrophysics Science Archive Research Center (HEASARC). For each object, I obtained spectra for all available observations from the EPIC MOS1, MOS2 and PN cameras, to maximise the number of counts. Each spectrum comes in three parts: a source spectrum, a background spectrum, and an ancillary response function. These are supplemented by an instrument-specific canned response matrix, downloaded from the

Table 3.2: Optical/IR spectral observation dates for the sample of 11 objects. S/N values are approximate.

ID	Name	Survey	MJD-Plate-Fibre	Optical Obs. UT	Avg. S/N	IR Source	IR Obs. UT	Avg. S/N
1	J0041−0947	SDSS	52162-655-172	2001-09-10	36	TSpec	2010-01-02 & 11-28	7
2	J0043+0114	SDSS	51794-393-419	2000-09-07	18	GNIRS 13B	2013-08-16	12
		BOSS	**55186-3589-707**	2009-12-21	30			
		BOSS	55444-4222-902	2010-09-05	33			
3	J0118−0052	SDSS	51789-398-211	2000-09-02	16	GNIRS 04B	2004-11-29	9
4	J0157−0048	SDSS	51871-403-213	2000-11-23	17	TSpec	2009-11-07 & 11-28	3
		SDSS	52179-701-294	2001-09-27	14			
		BOSS	**55449-4233-152**	2010-09-10	24			
5	J0839+5754	SDSS	54425-1784-495	2007-11-21	32	GNIRS 13B	2013-10-27	19
6	J1021+1315	SDSS	53062-1746-491	2004-02-27	14	GNIRS 13B	2014-03-21	15
7	J1044+2128	SDSS	54097-2478-411	2006-12-28	18	GNIRS 13B	2014-03-20	14
		BOSS	**56039-5874-970**	2012-04-22	28			
8	J1240+4740	SDSS	53089-1455-424	2004-03-25	16	TSpec	2011-02-22	8
9	J1350+2652	SDSS	53848-2114-105	2006-04-23	27	TSpec	2011-02-22	8
		BOSS	**56105-6006-260**	2012-06-27	47			
10	J2328+1500	SDSS	52238-746-463	2001-11-25	10	GNIRS 13B	2013-08-18	11
11	J2332+0000	SDSS	**51821-384-438**	2000-10-04	13	GNIRS 13B	2013-08-19	13
		SDSS	52199-681-543	2001-10-17	13			
		SDSS	52525-682-355	2002-09-08	11			

XMM-Newton EPIC Response Files Page. These are all provided in a file format readable by XSPEC.

For two of the objects in my sample for which IR spectra were pre-existing, the X-ray spectrum had not been extracted from the EPIC source image, due to lack of counts. However, the 3XMM DR4 catalogue lists, for all detections, the X-ray flux in five bands: 0.2–0.5, 0.5–1.0, 1.0–2.0, 2.0–4.5, 4.5–12.0 keV, and I thus used these values in the SED fitting.

Where available, I also extracted the *XMM* OM photometry data. Targets that are too far off-axis are not covered, so many of the sources that were observed serendipitously by EPIC do not have OM data.

Finally, I also searched the *GALEX* database for UV photometry. All sources have some data in the *GALEX* AIS.

3.3 Black Hole Mass Estimates

The first step in analysing data was to make BH mass estimates from the IR spectra. Discussion of a full spectral decomposition is made in Chapter 4, but relies on the results of my broad-band SED fits, so at this stage I employ a localised decomposition of the Balmer line region, which is redshifted into the IR spectra.

3.3.1 Optical/IR Spectral Fitting

I first perform a continuum subtraction of the Balmer line region. Whilst the underlying, featureless continuum is in theory best described by an AD, on localised scales it may approximate a power-law continuum. As discussed in e.g. Vanden Berk et al. (2001) the continuum under the Balmer lines is more accurately represented by a broken power law, and so this is the approximation I use. For the power-law, I use the standard form:

$$F(\lambda) = C_1(\lambda/5100\,\text{Å})^{-C_2} \tag{3.3.1}$$

where C_1 is the normalisation and C_2 is the power-law slope, and in my case, implement the change in index at 5500 Å rest-frame.

The objects are all relatively bright, and so contamination from the host galaxy is expected to be small (see Section 3.5.2), however AGN spectra are also contaminated across the spectral range by broad, blended Fe II multiplets. Modelling of these features is usually accomplished by making use of an empirical template derived from spectral analysis of the Type 1 AGN I Zwicky 1. I use that of Véron-Cetty et al. (2004). There are two free parameters; the width of the convolving Gaussian, and the normalisation. I fit the broken power-law and Fe II pseudo-continuum to the spectral regions in between the strong emission lines, using the bands: 4000−4300, 4400−4750, 5050−5800, 5950−6300 and 6800−7500 Å. The fitted continuum is subtracted to leave the Balmer emission line spectrum.

I then fit the broad permitted emission lines Hα, Hβ and Hγ and the narrow, forbidden lines [O III]. There are two categories of object in the sample; those showing strong, narrow [O III] lines, and those that do not. This is discussed more in Chapter 4. Following common practice, I use multiple Gaussian components to model the emission lines, which offers a reasonable approximation to the line shape, and given the quality of the data, is perfectly adequate for this purpose. Lines are modelled as follows:

i. Hα is fitted with two Gaussian components – one broad and one intermediate. These are free in velocity shift and normalisation. For the objects that show strong narrow [O III], a third, narrow Gaussian component, of wavelength and velocity width tied to the strong member of the [O III] doublet is also included.

ii. Hβ is fitted with two Gaussians, with wavelengths and velocity widths tied to the corresponding components in Hα and with the same amplitude ratio. A narrow component is included if strong [O III] is observed.

iii. Hγ is fitted for completeness with 2 components, tied in amplitude ratio, velocity width and wavelength to the corresponding components in Hα.

iv. [O III] is a doublet; each member is fitted with a single Gaussian, tied together in velocity width, and with an amplitude ratio of 2.98 (Storey & Zeippen 2000).

I obtain the BH mass estimate for the objects from the Hα line, using the method derived by Greene & Ho (2005). It is common to use Hβ, as much study has been devoted

to calibrating mass estimates from Hβ with RM samples, due to the greater availability of Hβ in optical spectra (Hα being redshifted to IR wavelengths in AGN above $z \sim 0.3$), and also because Hα profiles may be blended with narrow forbidden lines [S II] and [N II]. However, given the limited S/N of the data, I prefer to use the $\sim 3\times$ stronger Hα profile. I note that the [S II] doublet is not detected in any of the objects (even those showing strong [O III]), which is supporting evidence that contamination of the Hα profile by [N II] is likely to be small. Whilst Hβ mass estimates are made using $\mathrm{FWHM}_{\mathrm{H}\beta}$ as a proxy for the velocity dispersion, and the continuum luminosity at 5100 Å ($L_{5100\text{Å}}$) as a proxy for the BLR size, Greene & Ho (2005) found strong correlations between $\mathrm{FWHM}_{\mathrm{H}\beta}$ and $\mathrm{FWHM}_{\mathrm{H}\alpha}$ and between $L_{5100\text{Å}}$ and $L_{\mathrm{H}\alpha}$, and used this as the basis for derivation of their relation between Hα profile and BH mass, given in equation 1.4.9.

Following the method of Greene & Ho (2005) and others, I use the full, broad Hα component to obtain BH mass estimates. Jin et al. (2012a) discussed the merits of drawing a distinction between the Gaussian components that form the broad profile, defining these as 'broad' and 'intermediate' components, but eventually they determined that the two combined yielded the most reliable BH mass estimates.

3.3.2 Results

I use custom PYTHON fitting scripts and a Levenberg-Marquardt minimisation method throughout. An example of the Balmer region spectral decomposition is shown in Fig. 3.1. Measurement errors are estimated using a Monte Carlo technique, where different iterations of the data are generated using the 'mean' (measured) flux value and the error on that value. For each different iteration, optimal values are recalculated, and this is repeated 100 times to estimate the error of each fitted value. This procedure is not perfect, as noise is added to the already noise-degraded spectral data, but serves as a suitable approximation. The fitting errors are added to the dispersion arising from the method, as given in equation 1.4.9. I tabulate the results of the emission line analysis in Table 3.3.

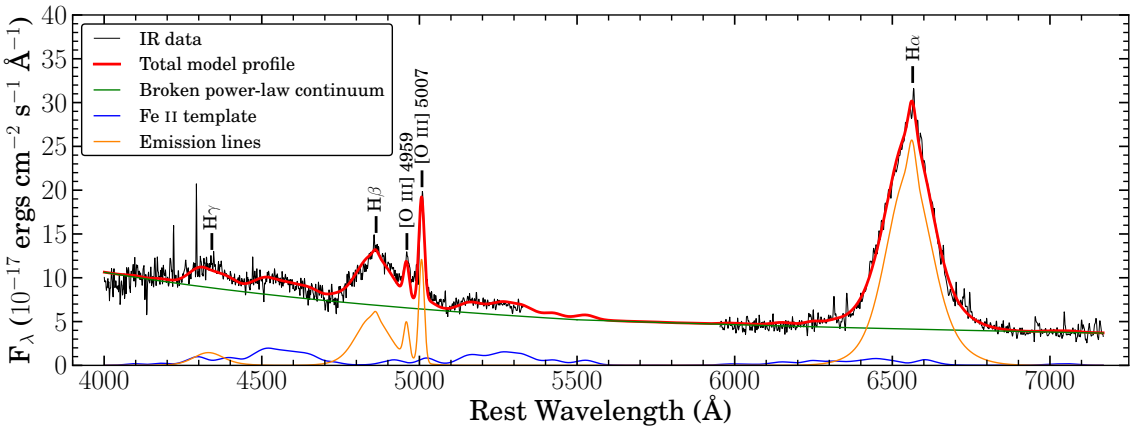

Figure 3.1: Spectral decomposition of the Balmer lines for J2328+1500. This object shows reasonable S/N (∼11) across the spectral range, whilst some of the other objects in the sample show significantly noisier spectra. Although I only use the FWHM and line luminosity of Hα in making the BH mass estimate, the other Balmer lines and the [O III] doublet were also modelled to more strongly constrain the fit, particularly of the Fe II emission.

Table 3.3: Hα line measurements for the sample. For objects common to the Shen and Liu (2012) sample, my measurements agree to within 2σ.

ID	FWHM$_{H\alpha}$ (km s^{-1})	$\log\left(\frac{L_{H\alpha}}{\text{erg s}^{-1}}\right)$	$z_{[OIII]}$	$\log\left(\frac{M_{BH}}{M_\odot}\right)$
1	5600±200	44.85±0.02	1.629	9.42±0.11
2	2940±90	44.57±0.01	1.567	8.68±0.10
3	4680±60	44.86±0.01	2.192	9.25±0.10
4	3100±100	44.40±0.04	1.545	8.63±0.10
5	5100±200	45.21±0.01	1.535	9.53±0.11
6	3200±100	44.53±0.01	1.577	8.73±0.10
7	2550±80	44.56±0.01	1.500	8.55±0.10
8	2460±20	44.87±0.01	1.562	8.68±0.09
9	3390±80	44.94±0.02	1.623	9.01±0.10
10	7810±80	44.81±0.01	1.539	9.68±0.10
11	5000±70	44.32±0.01	1.609	9.02±0.09

3.4 Bolometric Luminosity

With the $M_{\rm BH}$ estimates in hand, I can make measurements of the bolometric (total) luminosity ($L_{\rm bol}$) of each AGN by fitting the broad-band SED model OPTXAGNF to the optical/IR and X-ray data. I take $L_{\rm bol}$ to mean the total intrinsic luminosity of the nuclear source, excluding stars in the host galaxy and any associated reradiation.

3.4.1 X-ray Spectrum

I first fit the X-ray data with an absorbed power-law. I include attenuation attributable to both the MW (fixed) and the host galaxy (free). This will allow me to verify that the following section, in which I apply the Done et al. (2012) OPTXAGNF model, gives reasonable values. I calculate MW $N_{\rm H}$ values using the Leiden/Argentine/Bonn Survey of Galactic H I (Kalberla et al. 2005).

In Table 3.4 the X-ray exposure times and count values are presented, and the fitted parameters are shown, together with 90 per cent confidence limits.

Table 3.4: The model properties for the X-ray spectrum. I fit absorption components for both the MW (fixed) and the host galaxy (free). In many objects the host absorption is poorly constrained, due to the high redshift (only the tail of the absorption profile is sampled) and limited number of counts. The EPIC count errors are 1 σ, and the errors on the model parameters are 90 per cent confidence limits, in line with convention in X-ray astronomy. For similar reasons, I also quote Γ and its uncertainty to two decimal places.

ID	Exp. Time (s)	*XMM* EPIC Cts	$N_{\rm H,\,MW}$ ($\times 10^{20}\,{\rm cm}^{-3}$)	$N_{\rm H,\,int}$ ($\times 10^{20}\,{\rm cm}^{-3}$)	Γ	$\chi^2_{\rm red}$
1	12 519	410±20	2.64	0^{+16}_{-0}	$2.34^{+0.24}_{-0.22}$	1.29
2	21 304	850±30	1.83	0^{+11}_{-0}	$2.56^{+0.19}_{-0.16}$	0.89
3	10 523	142±17	3.89	50^{+110}_{-50}	$2.92^{+0.79}_{-0.52}$	1.71
4	7179	203±18	2.58	11^{+18}_{-11}	$2.07^{+0.12}_{-0.13}$	0.60
5	15 781	7200±100	4.48	45^{+13}_{-12}	$1.99^{+0.09}_{-0.08}$	1.32
6	19 591	550±30	4.04	20^{+40}_{-20}	$2.33^{+0.41}_{-0.31}$	0.77
7	154 071	4950±80	1.73	0^{+5}_{-0}	$2.30^{+0.07}_{-0.06}$	1.54
8	8117	760±30	1.31	0^{+19}_{-0}	$1.80^{+0.17}_{-0.11}$	1.45
9	23 543	1130±40	1.24	0^{+17}_{-0}	$2.20^{+0.19}_{-0.12}$	0.84
10	124 956	1350±50	3.85	0^{+13}_{-0}	$1.44^{+0.12}_{-0.11}$	1.14
11	34 705	710±30	4.00	0^{+19}_{-0}	$2.19^{+0.12}_{-0.13}$	0.62

3.4.2 Broad-band SED Fitting

There are a number of properties that affect the intrinsic AGN SED; these are discussed in Section 2.4.2 and Done et al. (2012). The observed SED is also affected by optical/UV extinction and soft X-ray absorption due to interstellar dust and photoelectric absorption (respectively) in the MW (see Section 2.4.4). I correct for the extinction (reddening) in the MW as discussed in Section 3.2.2, and as in Section 3.4.1 include the photoelectric absorption model WABS to fit the Galactic soft X-ray absorption.

The AGN host galaxy is assumed to have similar intrinsic processes reddening/absorbing the AGN emission. These components can be modelled with the ZWABS and ZREDDEN models, albeit with no means of constraining these other than the shape of the SED. I therefore also produce a second model in which these components are added.

In this redshift range the data may not be sufficient to constrain the properties of the SX. Equally, it is possible that either the X-ray data or optical data may sample this part of the SED, depending on the coronal radius. Since we know empirically (e.g. Done et al. 2013) that the SX ought to be taking up a significant fraction (~ 70 per cent) of the Comptonised energy, its properties are fixed to reasonable default values, detailed below.

In both scenarios, the constrained parameters are as follows. A discussion of specific exceptions follows.

i. BH mass, $M_{\rm BH}$: as previously described in Section 3.3, I constrain BH mass using the method of Greene & Ho (2005) based on Hα.

ii. Redshift, z: as measured in the Balmer region spectral decomposition.

iii. Distance, $r_{\rm c}$: I calculate the comoving distance to each source from the measured redshift assuming a flat cosmology (as defined in Section 1.6).

iv. BH spin, $a_\star$: initially I fix spin at zero, in line with the work of Jin et al. (2012a), but specific instances where a spinning BH is possible or implied are explored in Chapter 4.

v. Electron temperature of SX, $kT_{\rm e}$: fixed at a typical value of 0.2 keV.

vi. Optical depth of SX, τ: fixed at a typical value of 10.

vii. Fraction of Comptonised component in SX, $f_{\rm SX}$: fixed at a typical value of 0.7.

viii. Hydrogen column density (MW), $N_{\rm H,\,Gal}$: calculated using the Leiden/Argentine/Bonn Survey of Galactic HI (Kalberla et al. 2005).

The fitted parameters are as follows.

i. Mass accretion rate, $\dot{m} = L_{\rm bol}/L_{\rm Edd}$.

ii. Coronal radius, $r_{\rm cor}$: the radius at which the AD energy is reprocessed by SX and PLT.

iii. Radial extent of AD, $r_{\rm out}$: the outer radius, in $R_{\rm g}$ of the AD. In some objects this cannot be constrained – in these $r_{\rm out}$ is given as a limit.

iv. Power-law slope, Γ: The power-law index of the coronal PLT.

v. Intrinsic hydrogen column density, $N_{\rm H,\,int}$ (ZWABS): soft X-ray attenuation intrinsic to the host galaxy.

vi. Intrinsic reddening, $E(B-V)$ (ZREDDEN): redshifted extinction curve to account for reddening intrinsic to the host galaxy.

I also produce for each object a final model in which the SX normalisation is permitted to vary. This allows me to test the hypothesis that this component is constrained in some objects.

To summarise, the models fitted are:

i. Model 1: SX fixed, no intrinsic attenuation

ii. Model 2: SX fixed, including intrinsic attenuation

iii. Model 3: SX free, including intrinsic attenuation

Defining the data to be fit in XSPEC is not straightforward. The optical/IR spectral data are, as previously mentioned, contaminated by emission features, including complex, blended Fe II emission, and the Balmer continuum. I therefore select, using the

Vanden Berk et al. (2001) quasar template, spectral regions free from such emission, and bin these narrow wavelength ranges up into well-defined photometry points. The error on each point is defined as the flux density standard deviation across the bin. The rest-frame wavelength ranges used are (where available): 1300–1350, 1425–1475, 1700–1750, 2175–2225, 3900–4000, 4150–4250, 5600–5700, 6100–6200, 6900–7000 Å, unless any of these were unsuitable, e.g. for reasons of poor S/N. I then fit the full energy range of available X-ray data from *XMM* EPIC.

The bluest bins chosen also do not cover the absorption features observed by Kaastra et al. (2014), which may be expected in AGN with high $N_{\rm H}$ columns (see Table 3.4). I do not tie the $N_{\rm H,int}$ and intrinsic $E(B-V)$ values together.

The UV photometry from *XMM* OM and *GALEX* is not included in the modelling process. At the redshifts considered, the UV filters on these observatories cover a broad wavelength range over the strong Ly-α emission line, and the Ly-α forest beyond, and are therefore not a good indication of the continuum level. With high-resolution UV spectral data, it is possible to interpolate over the narrow absorption features in the forest, and recover the underlying continuum (e.g. Lusso et al. 2015) but this requires observations with e.g. *HST*/COS – see Chapter 5.

3.4.3 Results

The results of the SED fitting procedure are as follows. In Table 3.5 the best-fitting parameters for each model are tabulated, including the mass accretion rate in $M_{\odot}$ yr^{-1}. In Table 3.6 the key properties of these SED models are listed. In the manner of Jin et al. (2012a, c), I have calculated $\kappa_{2-10\,\rm keV} = L_{\rm bol}/L_{2-10\,\rm keV}$ and $\kappa_{5100\text{Å}} = L_{\rm bol}/L_{5100\text{Å}}$, the $2-10$ keV and 5100 Å bolometric correction coefficients, as these are commonly used proxies for $L_{\rm bol}$. I also compute $\alpha_{\rm OX}$, as defined in e.g. Lusso et al. (2010) as:

$$\alpha_{\rm OX} = -\frac{\log(L_{\rm 2keV}/L_{2500\text{Å}})}{2.605} \tag{3.4.2}$$

where $L_{\rm 2keV}$ and $L_{2500\text{Å}}$ are the monochromatic AGN luminosities at 2 keV and 2500 Å respectively. The uncertainties quoted are the 90 per cent confidence limits, as is conven-

tional in X-ray astronomy. I have estimated these using the Fisher matrix, which gives an indication of the measurement error. It should be remembered that this does not take account of the systematic errors, to which the main contributors are the uncertainties on the mass estimate (explored in Chapter 4) and the flux calibration.

I note that some of the models show the SX component to be unconstrained by the data, and in five objects this is manifested by large fitting errors on $r_{\rm cor}$ and $f_{\rm SX}$ in Model 3. For Model 3, in the interest of limiting the number of free parameters, and allowing the model to converge to a meaningful minimum, I lock $N_{\rm H,int}$, and $r_{\rm out}$ to the Model 2 values. I make an exception to this rule for J0839+5754, as the X-ray data are sufficient to well-constrain $N_{\rm H,int}$.

All of the SED models are plotted, together with the observational data, in Figs. 3.2, 3.3 and 3.4. Whilst all models include some modelled attenuation components (MW only in Model 1, and MW+intrinsic in Models 2 and 3), the intrinsic SED, after correcting for these sources, is shown in all cases. Therefore all data shown have also been corrected (dereddened and deabsorbed) to show the implied intrinsic flux levels.

A rather limited range of SED shapes is seen, with all but one object being disc-dominated, similar to the SEDs of NLS1s in the Jin et al. (2012a) sample. The lowest mass objects, J0043+0114, J0157−0048, J1021+1315, J1044+2128, J1240+4740 and J1350+2652 have unsampled SED peaks. The red wing of the AD is better constrained than for the Jin et al. (2012a) objects though, owing to the lower fraction of host galaxy contribution in these high luminosity AGN.

The objects with $M_{\rm BH} \gtrsim 10^9\ M_\odot$ – J0041−0947, J0118−0052, J0839+5754, J2328+1500 and J2332+0000 – all have observational data extending close to or at their SED peaks, enabling reliable estimates of $L_{\rm bol}$ in these objects.

In many of the objects in the sample, it can be seen that some combination of host galaxy contribution and dust reradiation become significant redward of Hα. The hot toroidal dust component is studied in greater detail in Chapter 4. Further discussion of the host contribution is presented in Section 3.5.2.

Table 3.5: The optimum fitted parameters for the SED models. Uncertainties quoted are the 90 per cent confidence limits, as is conventional in X-ray astronomy, and are estimated using the Fisher matrix. As such, they are only indicative of the true measurement error.

ID	$N_{\rm H,int}$ (10^{22} cm^{-2})	$E(B-V)$ (mag)	$\dot{m}=L_{\rm bol}/L_{\rm Edd}$	$\dot{M}$ ($M_\odot$ yr^{-1})	$r_{\rm cor}$ ($R_{\rm g}$)	$r_{\rm out}$ ($R_{\rm g}$)	Γ	$f_{\rm SX}$	$\chi^2_{\rm red}$	DOF
Model 1: No intrinsic attenuation, SX fixed (SX parameters: $kT_{\rm e}=0.2$ keV, $\tau=10$, $f_{\rm SX}=0.7$)										
1	(0.0)	(0.0)	0.389±0.018	44±2	23±3	>1000	2.21±0.03	(0.7)	10.4	18
2	(0.0)	(0.0)	2.79±0.05	56.8±1.0	11.6±0.6	790±80	2.53±0.09	(0.7)	0.97	40
3	(0.0)	(0.0)	0.39±0.06	30±5	24±9	300±60	2.45±0.03	(0.7)	2.39	9
4	(0.0)	(0.0)	2.22 ±0.07	40.3±1.4	9.87±0.16	330±30	1.94±0.05	(0.7)	3.61	7
5	(0.0)	(0.0)	0.231±0.018	33±3	88.3±1.4	> 1000	1.86±0.04	(0.7)	3.50	212
6	(0.0)	(0.0)	1.24±0.03	28.3±0.6	13.2±0.6	1800±600	2.14±0.11	(0.7)	2.60	19
7	(0.0)	(0.0)	2.9±0.2	44±3	10.2±0.4	>10000	2.27±0.03	(0.7)	2.63	172
8	(0.0)	(0.0)	2.10±0.04	42.7±0.8	15.9±1.1	>10000	1.79±0.07	(0.7)	6.38	37
9	(0.0)	(0.0)	1.410±0.016	60.1±0.7	10.8±0.3	700±60	2.18±0.07	(0.7)	1.78	42
10	(0.0)	(0.0)	0.0371±0.0011	7.6±0.2	21±3	56.0±1.9	1.63±0.06	(0.7)	1.77	91
11	(0.0)	(0.0)	0.317±0.010	14.2±0.5	20±3	237±14	2.18±0.08	(0.7)	0.89	33
Model 2: Incl. intrinsic attenuation, SX fixed (SX parameters: $kT_{\rm e}=0.2$ keV, $\tau=10$, $f_{\rm SX}=0.7$)										
1	0.0±0.3	0.051±0.006	0.61±0.12	68±14	25±9	240±40	2.38±0.03	(0.7)	5.01	16
2	0.0±0.3	0.015±0.010	3.3±0.4	67±8	10.9±1.3	790±60	2.52±0.19	(0.7)	0.95	38
3	0.15±0.12	0.025±0.015	0.50±0.14	38±11	25±11	260±60	2.50±0.06	(0.7)	2.48	7
4	0.20±0.10	0.060±0.015	4.1±0.7	75±12	9.0±0.3	400±40	2.07±0.07	(0.7)	0.51	5
5	0.18±0.06	0.065±0.003	0.338±0.007	48.8±1.0	80.1±1.2	>1000	1.86±0.05	(0.7)	1.45	210
6	0.2±0.2	0.024±0.010	1.58±0.16	36±4	13±3	970±130	2.32±0.22	(0.7)	2.52	17
7	0.00±0.11	0.033±0.006	4.1±0.3	62±5	9.4±0.2	>10000	2.26±0.06	(0.7)	2.54	172
8	0.01±0.17	0.052±0.014	3.06±0.12	62±2	13±2	>10000	1.80±0.13	(0.7)	1.77	35
9	0.0±0.3	0.030±0.008	1.98±0.18	84±7	9.8±0.5	500±30	2.18±0.13	(0.7)	1.62	40
10	0.0±0.3	0.094±0.015	0.067±0.007	13.6±1.4	19±4	53±2	1.50±0.09	(0.7)	1.30	89
11	0.0±0.3	0.023±0.015	0.42±0.08	19±3	16±4	211±17	2.18±0.14	(0.7)	0.88	31
Model 3: Incl. intrinsic attenuation, SX free (SX parameters: $kT_{\rm e}=0.2$ keV, $\tau=10$, $f_{\rm SX}=$free)										
1	(0.0)	0.051±0.005	0.60±0.04	67±4	25±2	(240)	2.17±0.21	0.83±0.09	4.69	17
2	(0.0)	0.011±0.008	3.2±0.3	64±6	15±40*	(790)	2.48±0.14	0.9±0.3*	0.93	39
3	(0.15)	0.028±0.013	0.51±0.05	38±4	26±5	(260)	2.47±0.09	0.74±0.10	2.14	8
4	(0.20)	0.060±0.014	4.1±0.7	75±12	9.0±1.1	(400)	2.07±0.06	0.7±0.2	0.42	6
5	0.51±0.07	0.051±0.006	0.336±0.009	48.6±1.3	82.7±1.7	(>1000)	2.06±0.05	0.56±0.05	1.29	211
6	(0.2)	0.024±0.008	1.58±0.07	36.1±1.5	10±80*	(970)	2.32±0.14	0.7±3*	2.38	18
7	(0.0)	0.033±0.006	4.1±0.3	62±4	9.9±1.8	(>10000)	2.25±0.05	0.8±0.2	2.53	171
8	(0.01)	0.056±0.004	3.16±0.10	64±2	10±10*	(>10000)	1.80±0.08	0.7±0.7*	1.70	36
9	(0.0)	0.030±0.005	1.97±0.11	84±5	10±14*	(500)	2.19±0.09	0.7±2*	1.58	41
10	(0.0)	0.091±0.015	0.066±0.006	13.5±1.3	17±4	(53)	1.49±0.06	0.64±0.16	1.28	90
11	(0.0)	0.023±0.009	0.42±0.05	19±2	15±40*	(211)	2.18±0.08	0.7±1.2*	0.85	32

*Large error indicative of unconstrained SX parameter

Table 3.6: The key properties of the various SED models, including bolometric correction coefficients.

ID	$\log(L_{\rm bol})$	$\log(L_{2-10\,\rm keV})$	$\kappa_{2-10\,\rm keV}$	$\log(\lambda L_{2500\text{Å}})$	$\log(\nu L_{2\,\rm keV})$	$\alpha_{\rm OX}$	$\log(\lambda L_{5100\text{Å}})$	$\kappa_{5100\text{Å}}$
	[log(erg s^{-1})]			[log(erg s^{-1})]			[log(erg s^{-1})]	
Model 1: No intrinsic attenuation, SX fixed (SX parameters: $kT_{\rm e} = 0.2$ keV, $\tau = 10$, $f_{\rm SX} = 0.7$)								
1	47.17±0.02	45.28	76.7	46.70	45.15	1.60	46.43	5.42
2	47.271±0.007	44.86	257	46.36	44.83	1.59	45.99	18.9
3	46.98±0.07	44.78	159	46.49	44.72	1.68	46.16	6.56
4	47.103±0.015	44.78	212	46.15	44.55	1.62	45.62	30.3
5	47.07±0.03	45.69	24.0	46.68	45.43	1.48	46.56	3.20
6	46.977±0.009	44.94	109	46.18	44.78	1.54	45.89	12.1
7	47.17±0.03	44.78	242	46.20	44.67	1.59	45.91	18.0
8	47.163±0.008	45.31	71.8	46.27	45.02	1.48	45.99	15.0
9	47.293±0.005	44.99	202	46.57	44.85	1.66	46.26	10.9
10	46.255±0.013	44.60	45.3	45.97	44.25	1.66	45.73	3.38
11	46.646±0.014	44.79	72.4	46.11	44.65	1.56	45.73	8.16
Model 2: Incl. intrinsic attenuation, SX fixed (SX parameters: $kT_{\rm e} = 0.2$ keV, $\tau = 10$, $f_{\rm SX} = 0.7$)								
1	47.33±0.09	45.27	116	46.85	45.19	1.63	46.48	7.15
2	47.36±0.05	44.86	312	46.41	44.83	1.61	46.02	21.7
3	47.08±0.12	44.82	181	46.56	44.78	1.69	46.20	7.56
4	47.38±0.07	44.86	332	46.34	44.68	1.64	45.80	37.7
5	47.233±0.009	45.84	24.6	46.86	45.58	1.49	46.65	3.80
6	47.08±0.05	44.95	135	46.25	44.85	1.54	45.94	13.7
7	47.32±0.03	44.78	348	46.31	44.66	1.63	46.02	20.1
8	47.323±0.017	45.30	106	46.39	45.01	1.53	46.10	16.7
9	47.43±0.04	44.99	278	46.67	44.85	1.70	46.29	13.8
10	46.50±0.05	44.63	73.0	46.22	44.23	1.76	45.86	4.32
11	46.76±0.08	44.79	93.5	46.19	44.65	1.59	45.77	9.77
Model 3: Incl. intrinsic attenuation, SX free (SX parameters: $kT_{\rm e} = 0.2$ keV, $\tau = 10$, $f_{\rm SX} =$ free)								
1	47.33±0.03	45.30	106	46.84	45.16	1.65	46.48	7.12
2	47.33±0.04	44.87	290	46.39	44.82	1.60	46.02	20.2
3	47.08±0.04	44.82	185	46.57	44.77	1.69	46.20	7.62
4	47.38±0.07	44.86	332	46.34	44.68	1.64	45.80	37.7
5	47.232±0.011	45.89	22.2	46.81	45.70	1.43	46.63	4.01
6	47.078±0.018	44.95	136	46.25	44.85	1.54	45.94	13.7
7	47.32±0.03	44.78	348	46.31	44.66	1.63	46.02	20.1
8	47.337±0.014	45.29	110	46.40	45.01	1.53	46.11	16.9
9	47.43±0.03	44.99	278	46.67	44.85	1.70	46.29	13.8
10	46.49±0.04	44.64	71.4	46.21	44.23	1.76	45.86	4.28
11	46.76±0.05	44.79	93.4	46.19	44.65	1.59	45.77	9.76

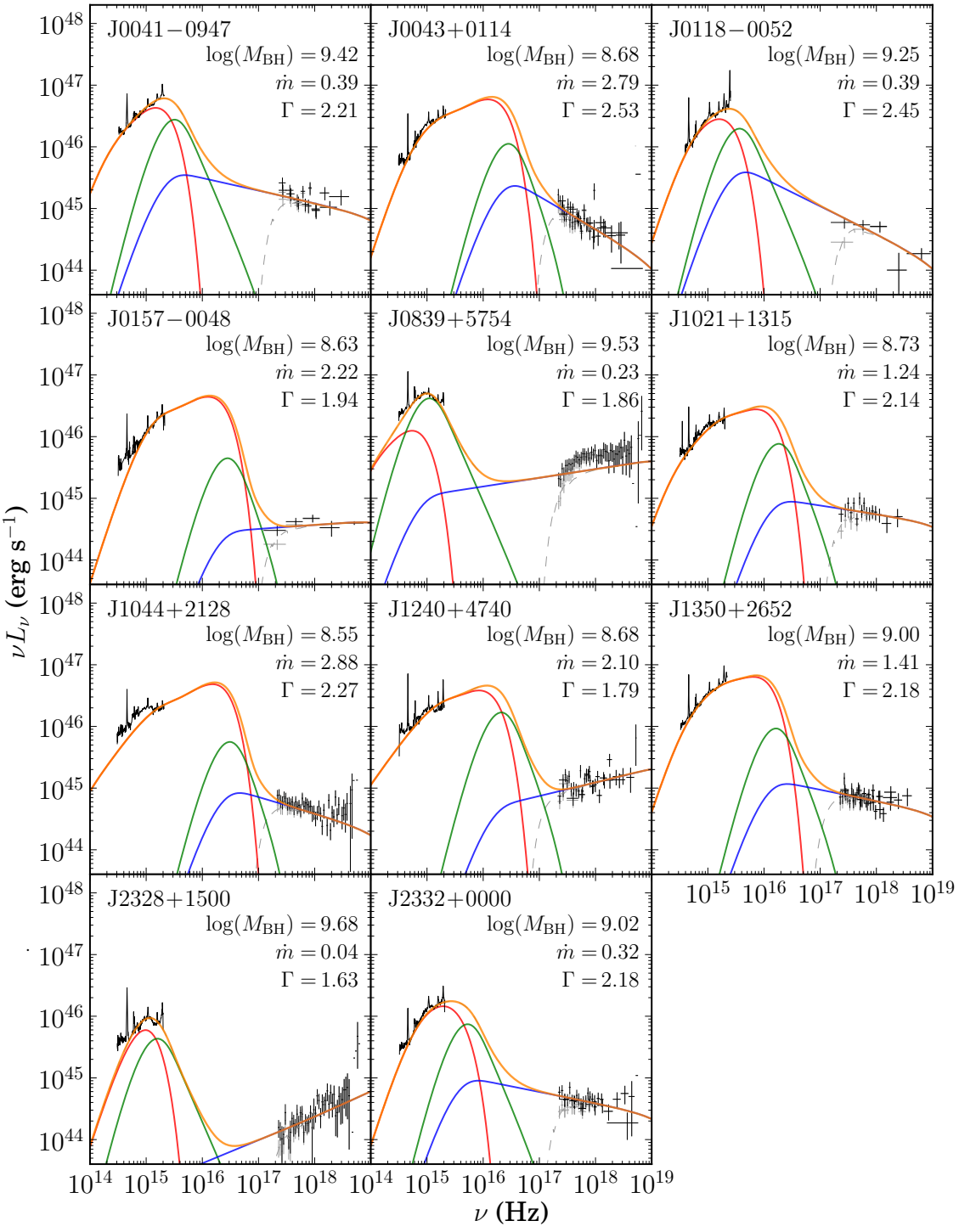

Figure 3.2: Data and SED models for the sample. Here, I show Model 1 (SX fixed, without intrinsic attenuation). I also plot the full IR–optical spectrum for each object. This spectral data are smoothed for clarity by convolving with a 20-pixel Gaussian. The different SED components are shown using the same colour scheme as in Fig. 2.4. The absorbed profile is shown by the dotted grey line. In each panel, I show $M_{\rm BH}$, the Eddington fraction, $\dot{m} = \dot{M}/M_{\rm Edd}$, and the photon index, Γ.

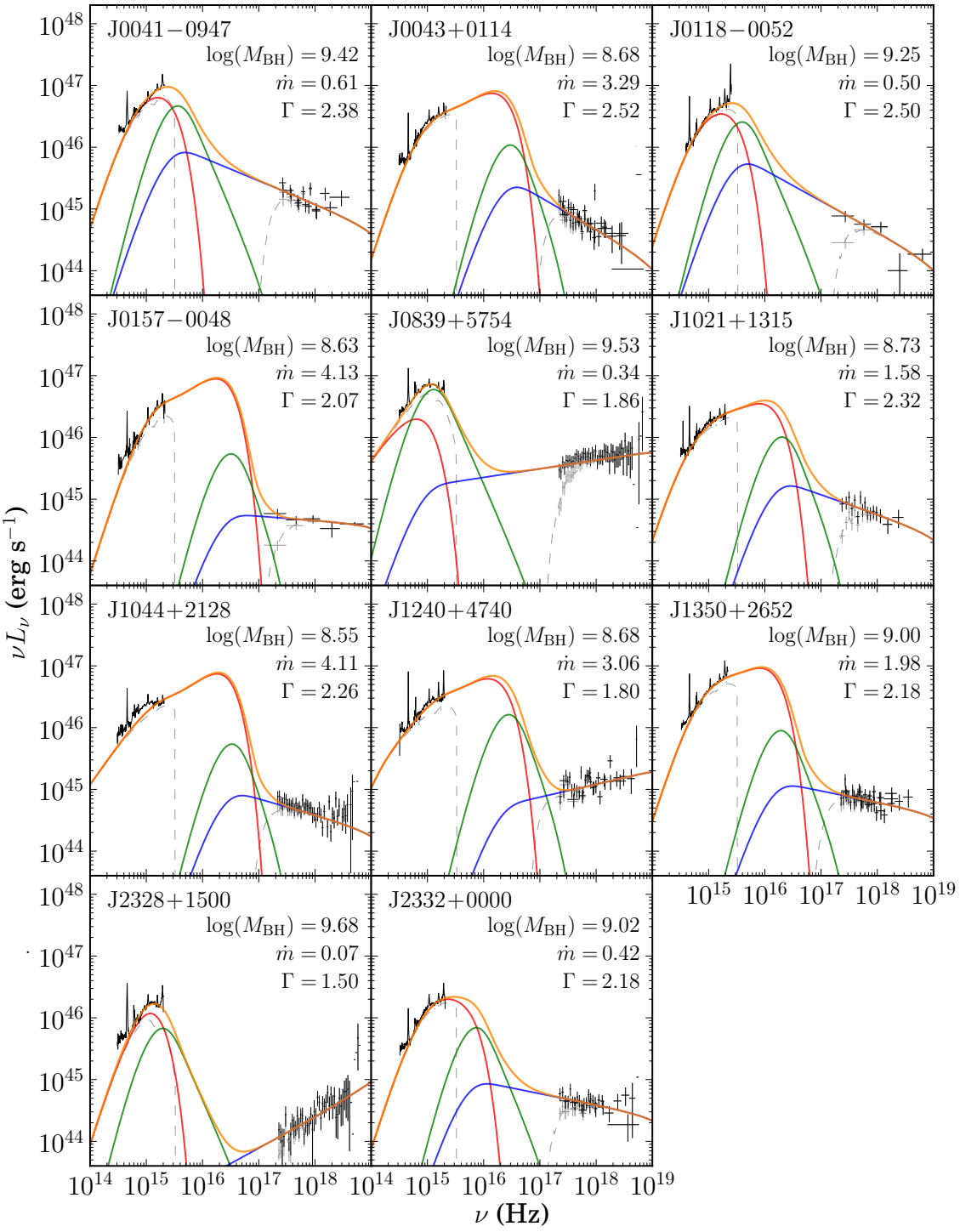

Figure 3.3: Data and SED models for the sample. Here I show Model 2 (SX fixed, including intrinsic attenuation). The spectral data are smoothed as in Fig. 3.2, and the same colour scheme is used.

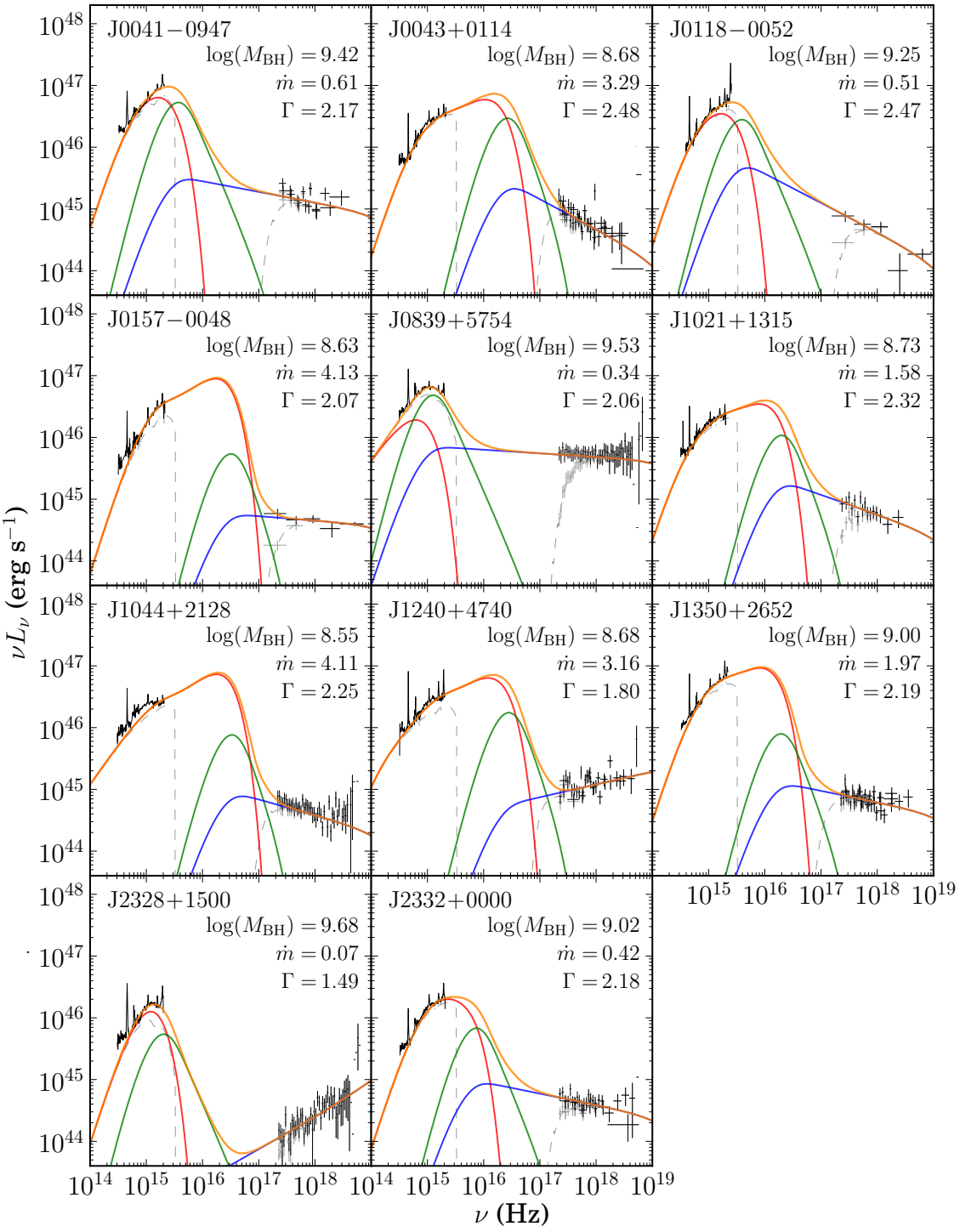

Figure 3.4: Data and SED models for the sample. Here I show Model 3 (SX normalisation free, including intrinsic attenuation). The spectral data are smoothed as in Fig. 3.2, and the same colour scheme is used.

3.5 Discussion

3.5.1 Model Suitability and Implications

I find that the Done et al. (2012) model is able to fit the IR to X-ray continuum of the sample of 11 AGN at $1.5 < z < 2.2$. I agree with the results of Capellupo et al. (2015) in that many of the objects can be modelled in the optical–IR regime by a geometrically thin, optically thick AD. In eight objects, constraints are put on the outer disc radius, as may be expected from considerations of the radius at which self-gravity truncates the AD (Laor & Netzer 1989) – this is quantified in Chapter 4. I note that the presence of a SX, observed and characterised by studies of local AGN, is both more physical and necessary to better define this continuum. The properties of this SX are related to the total energy of the Comptonised component, and modelling the X-ray spectrum in addition to optical/IR data is important to infer information about the SX.

There are a number of statistical tests by which I can judge the goodness of fit of the models. In the event that the data are normally distributed about the model, which is expected from the central limit theorem, the $\chi^2_{\rm red}$ value would be approximately 1.0, and would suggest that the model is a suitable description of the data. $\chi^2_{\rm red}$ values of less than 1.0 can be indicative that either the model is over-fitted, with too many free parameters, or that the errors are overestimated, and $\chi^2_{\rm red}$ values greater than 1.0 implies that the model is not a good description of the data. In this case, it may be that there are too few degrees of freedom for the data, that the errors are underestimated, or simply that the model does not fit the data.

To highlight the spectral region that most strongly influences the χ^2 fitting statistic, I show in Fig. 3.5 some example plots of residual against frequency, for the fitted data points. In general, the optical–IR spectral data make the largest contributions per point to the total χ^2 value, because they are well-defined, and have small uncertainties. The errors on these points may be underestimated, as I have not considered additional uncertainties arising from possible variability, or contamination by emission features. As discussed in Sections 3.2.2 and 3.4.2, I endeavoured to keep these uncertainties to a minimum, but a future study could add a nominal error to similar data to account for them.

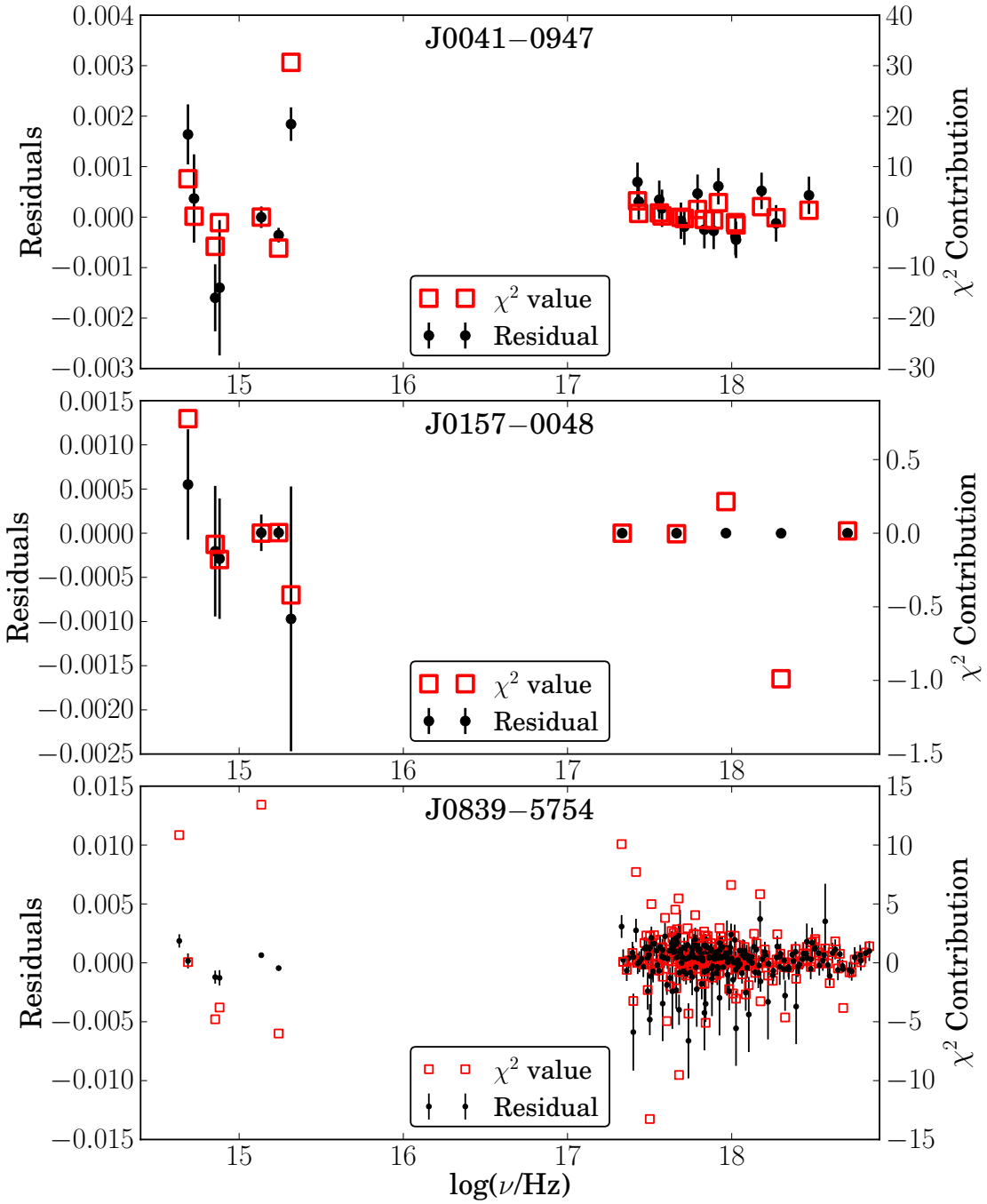

Figure 3.5: Example residual and χ^2 contribution plots for Model 3. Residual points correspond to the left axis label (in units of normalised counts s^{-1} per channel) and χ^2 values are given on the right axis. J0041−0947 (top panel) has the greatest χ^2_{red} value (4.7) of the sample, which is largely due to the optical–IR spectral data ($\sim 10^{15}$ Hz). This is the case for many of the objects, where the well-defined spectral data points in this range make large contributions to the χ^2 value, even if deviation from the model is small. This is less apparent in J0157−0048, where the optical–IR spectra are noisier, but there is a suggestion that the poor quality X-ray data are overfitted by my model, explaining the χ^2_{red} value of 0.4. Finally, I show J0839−5754, which demonstrates that the excellent X-ray data helps balance the relative χ^2 contributions of the optical–IR and X-ray regions.

Using the SED model, I am able to place useful constraints on $L_{\rm bol}$ for at least five of the objects in the sample. I believe that considerable uncertainties may arise if one assumes that the mass accretion rate is adequately estimated simply by the use of bolometric correction coefficients (Capellupo et al. 2015), as I have inferred a large spread in those parameters within this sample. In Table 3.5 I show $\kappa_{2-10\,\rm keV}$ and $\kappa_{5100\text{Å}}$, two commonly-used proxies for the $L_{\rm bol}$, for the sample. Though the sample is not large, I see a large range of values in all three models – around a factor of 10 between the minimum and maximum. If I only consider the five objects with constrained SED peaks, this range is a factor of two in the $\kappa_{5100\text{Å}}$, and a factor of 10 in $\kappa_{2-10\,\rm keV}$, in spite of the similar masses/accretion rates of these five AGN. This echoes the findings of Elvis et al. (1994) (who give the similar $L_{\rm bol}/L_{2500\text{Å}}$ factor) and Jin et al. (2012a), and suggests that the spread is larger than the ~ 20 per cent stated in Capellupo et al. (2015), although that work does only use the bolometric correction to make a prior estimate, which is subsequently allowed to vary in their fit. I explore luminosity dependent corrections in Chapter 4. The spread found in these values cannot be solely due to the ~ 0.1 dex error on the mass estimate, and may in fact be larger than estimated, as spin, which has so far been fixed at zero, affects the mass-energy conversion efficiency. I therefore suggest that BH spin is not the only property that cannot be estimated from singular properties of the optical spectra.

Model 3 provides the best fit to the data in all objects, judging from the $\chi^2_{\rm red}$ fitting statistic, which takes into account the increased number of free parameters in Model 3 versus Models 1 and 2. In some objects the $\chi^2_{\rm red}$ value is only marginally lower than the Model 2 value, which is indicative of a poorly constrained SX that does not benefit from the additional parameter freedom. Nonetheless, for the benefit of the objects in which the SX component is constrained (five objects), the additional freedom in Model 3 makes this the model of choice.

Many of the lower mass objects in the sample are predicted to have super-Eddington mass accretion rates, akin to the NLS1s (e.g. Jin et al. 2012a) and ULXs (e.g. Sutton et al. 2013) we observe more locally. However, I have not yet explored high-spin SED models in this study; this is addressed in Chapter 4. It is likely that there is some model

degeneracy between spin and mass accretion rate, and that this contributes to the range of spins predicted by Capellupo et al. (2015) in their sample.

Another limitation I have not yet explored is the reliability of the mass estimates. It is a fact that uncertainties on virial BH mass estimates are large (~ 0.1 dex calculated using the method here, but possibly as much as ~ 0.46 dex, Park et al. 2012) and in this study so far I have fixed it at the mean value. Allowing this to vary by 1–2 σ may well improve the fit, or may add another source of degeneracy. Again, this is explored in Chapter 4.

3.5.2 Host Galaxy Contribution to the Optical/IR Continuum

Throughout this study I have made the assumption that any contribution to the SED from stars in the AGN host galaxy is likely to be negligible. This is a common assumption for typical quasars at $z > 0.5$ (e.g. Shen et al. 2011). However, I can test its validity by superposing galaxy SED templates on to the faintest source, where the fractional stellar contribution will be largest. It is likely that the large galaxies that host the quasars in my sample are giant ellipticals, but it is known that starburst galaxies have significant energy output in the UV regime, and so I apply templates for both of these cases.

I use two of the galaxy templates of Polletta et al. (2007) – that of a 5 Gyr elliptical (appropriate for this redshift range) and that of the starburst galaxy M82, redshifted as appropriate. In terms of normalising these galaxy SEDs, I first assess the greatest possible contribution in J2328+1500 using the $M_{\rm BH}$– $L_{\rm bulge}$ relation as presented in e.g. Marconi & Hunt (2003) and DeGraf et al. (2014). I test J2328+1500 as it has the highest $M_{\rm BH}$, yet is the faintest source, and will thus almost certainly show the greatest contribution to the total SED by the host galaxy. The relations of both Marconi & Hunt (2003) and DeGraf et al. (2014) predict a host galaxy of $\mathcal{M}_V \simeq -25$. This is considerably more luminous than, for instance, M87, which has $\mathcal{M}_V \simeq -22$. As the brightest galaxy of the Virgo cluster, M87 is one of the most massive galaxies in the local Universe, so this prediction seems extreme.

I can put an upper limit on the host galaxy contribution using the SED model and data. This greatest possible host contribution is shown in Fig. 3.6, and corresponds to a host galaxy of $\mathcal{M}_V \simeq -23.3$, around 1.7 magnitudes fainter than that predicted by the

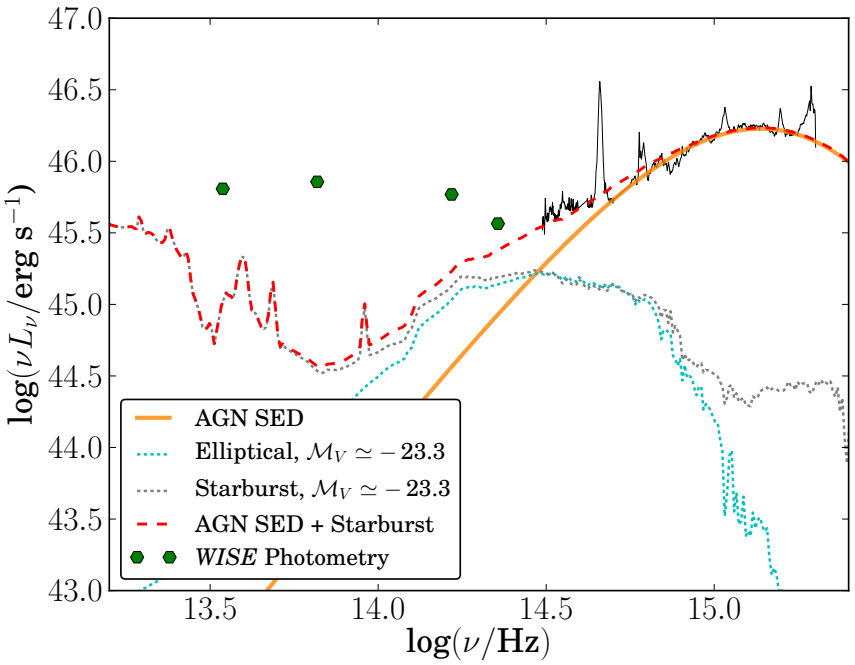

Figure 3.6: Comparison of two host galaxy SED templates against the AGN SED for the faintest of my objects, J2328+1500. Host templates have been normalised to a V-band absolute magnitude of $\mathcal{M}_V \simeq -23.3$, fainter than that predicted from the $M_{\rm BH}$–$L_{\rm bulge}$ relation, but at the maximum possible contribution permitted by the data (dashed red line). Such a situation would imply some red contribution to the total flux of the source, but only a small contribution at the SED peak.

$M_{\rm BH}$– $L_{\rm bulge}$ relation, but still ~ 1 magnitude brighter than M87. If this were the case, the contribution to the host galaxy at the SED peak would be $\lesssim 2$ per cent, even for the case of a starburst galaxy (this template is ~ 15 times more luminous than M82). An elliptical host would make a negligible contribution at the SED peak.

This result, while representing an extreme case for this object, suggests that a host galaxy component may be required when I model the dusty torus component (evident in the *WISE* photometry) in Chapter 4. However, the contribution by the host galaxy to the total nuclear SED energy is small. For the other sources, which are brighter and ought to originate in smaller host galaxies (via the $M_{\rm BH}$– $L_{\rm bulge}$ relation), the effect of the host will be smaller.

3.5.3 Variability

AGN are known to exhibit variability across all of the wavelength ranges I consider in this chapter. This study requires that the variability between the optical, IR and X-ray observations is not large. A discussion of my approach to detecting and correcting differences between the optical and IR spectral fluxes is given generally in Section 3.2.2. To summarise, I only see evidence for a notable difference between optical and IR flux levels in J0041−0947. The origin of this change may be related to the Balmer continuum (as modelled by Shen & Liu 2012), or poor quality photometry of 2MASS (to which the TSpec spectrum was normalised).

Only a subset of properties of the AGN can change over timescales of a few years. The BH mass and spin are fixed, and changes in the mass accretion rate that occur faster than the viscous timescale (which is of the order of hundreds–thousands of years) cannot currently be explained. Another possible source of intrinsic variability in AGN may be tidal disruption events (see Section 6.1.1), which can produce large variations in the observed energy output.

Extrinsic effects can, in principle, contribute to variability. Current models of the torus suggest that it could be clumpy (Nenkova et al. 2008), and so a change in the optical depth or extinction may occur if a clump were to drift into the line of sight. Indeed, major changes in the X-ray column density have been observed in several nearby AGN, on timescales of months to years (e.g. Puccetti et al. 2007, Walton et al. 2014).

Such effects are explored in Chapter 4. To display the nature of variability in all of the sources, I have plotted the available multi-epoch spectral data and photometry in the optical/IR bands for each object in Appendix A.2. This includes one epoch of photometry from each of the main surveys: SDSS photometric, UKIDSS and 2MASS, and all available epochs of spectral data. I supplement this with UV photometry from *XMM* OM and *GALEX* AIS to highlight the uncertainty in these values, which as mentioned in Section 3.4.2 are unreliable due to absorption and emission features. Observation dates for the various data sources are tabulated in Appendix A.1. Multi-epoch X-ray data exists for two of the objects – J0839+5754 and J1044−2128. Treating each observation as a separate data set, I see no statistically significant evidence for variability in the X-ray spectra of these objects – see Fig. 3.7.

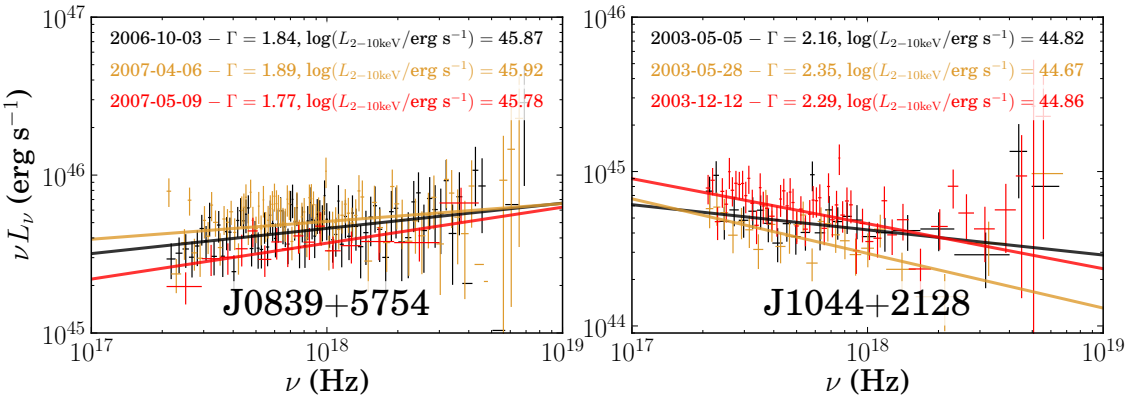

Figure 3.7: The two objects with X-ray spectra from multiple epochs. I have modelled each data set with a simple absorbed power-law, fixing $N_{\rm H,int}$ to the best-fitting Model 2 SED value, to search for evidence for variability in the X-rays. No evidence for statistically significant variability is seen.

3.5.4 Intrinsic Reddening

In my analysis, I have made the assumption that host galaxy dust extinction (intrinsic reddening) occurs via a similar process to extinction in the MW. I thus use a redshifted MW Cardelli et al. (1989) extinction curve, which produces apparently good reddening correction in all objects, except for J1044+2128. I have also tested two alternative models for dust extinction, those of the LMC and the SMC. It is immediately apparent that a better continuum fit for J1044+2128 is achieved with the SMC extinction model, and this is corroborated by the $\chi^2_{\rm red}$ fitting statistic. A comparison of MW and SMC reddening curves is shown for this object in Fig. 3.8. I conclude from this that there is no evidence for the 2200 Å feature in J1044+2128.

Judging by $\chi^2_{\rm red}$ only, six objects are best fit with the MW extinction curve (an example is shown in Fig. 3.9), one object with the SMC curve, and four objects with the LMC curve. In AGN where the inferred intrinsic reddening is small, the difference between these χ^2 values is marginal. Capellupo et al. (2015) came to a similar conclusion that different extinction curves are seen in different AGN, although they did not test the LMC model. I thus propose that Model 3 can be further augmented by including alternative reddening curves to the Cardelli et al. (1989) curve used thus far. I start Chapter 4 by remodelling each SED with the best-fitting extinction curve.

The only means of constraining the intrinsic reddening is the continuum shape, which

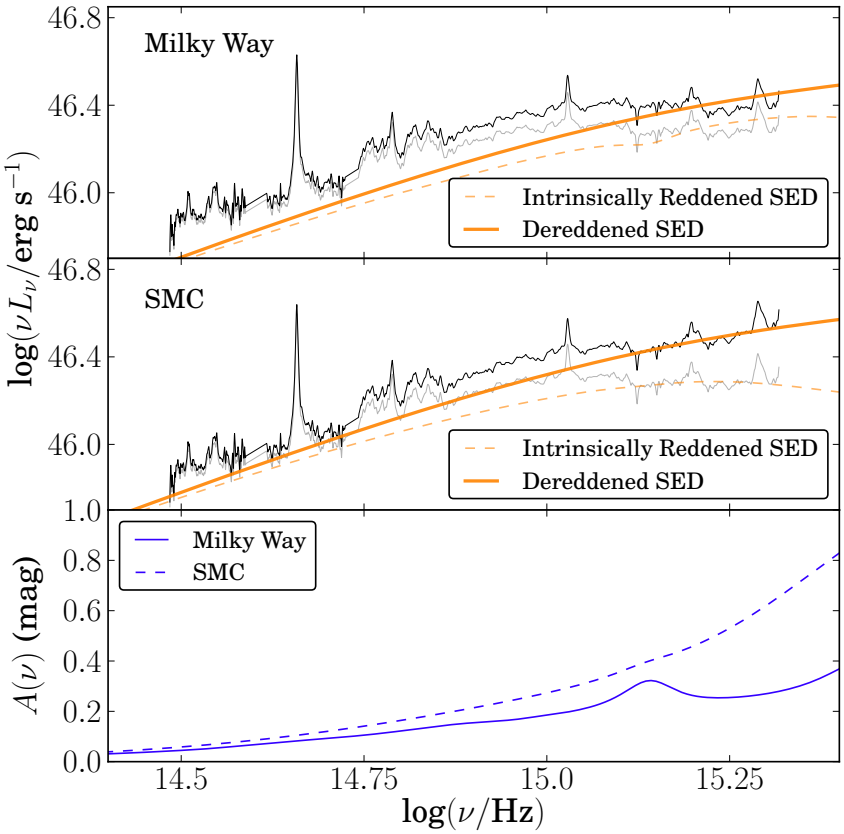

Figure 3.8: Two different extinction curves – the MW and the SMC – applied to J1044+2128. The MW curve that I assume throughout this work clearly produces an inferior fit compared to the SMC reddening curve. The orange line shows the best-fit SED template, once corrected for intrinsic reddening, with the dotted orange line showing the intrinsically reddened SED. Similarly, in grey is the reddened optical/IR spectral data, and black the dereddened data. This data has been smoothed by convolving with a 20-pixel Gaussian. The MW model prioritises the higher S/N optical spectra, as these have a bigger effect on the χ^2_{red} fitting parameter than the noisier IR spectra.

is certainly a limitation – I see in J2328+1500 that an $E(B-V)$ of less than 0.1 mag corresponds to an increase in L_{bol} of 70 per cent. This is a limitation for all such studies. By investigating the effect of changing the model mass within the confidence limits of the mass estimate, as discussed in Section 3.5.1, I ought to be able to assess the objects in which changes to the SED slope due to reddening are degenerate with small changes in the mass estimate. Unfortunately these are most likely to occur in the objects with a sampled SED peak. Spin degeneracy may also prove to be a contributor. The best approach to test this is studying a larger sample in which correlations between, e.g. intrinsic reddening and L_{bol} are directly testable, which could help corroborate or rule out such degeneracies and sources of systematic error.

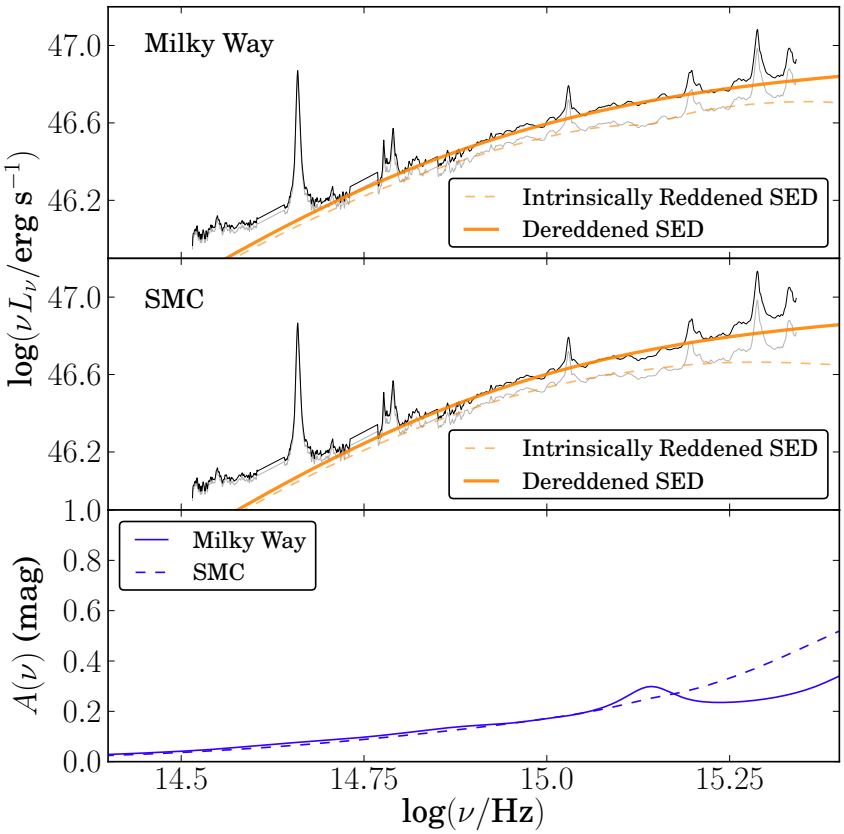

Figure 3.9: An equivalent plot to Fig. 3.8 for J1350+2652. Here, to highlight the difference in continuum shapes implied by the two reddening curves, I have fixed both to the same $E(B-V)$ value (0.03 mag). In this object, the MW reddening curve produces a noticeably better correction to the continuum shape.

3.6 Summary and Conclusions

In this chapter, I have selected a sample of 11 AGN at $1.5 < z < 2.2$. These objects all have optical, IR and X-ray spectral data, and UV photometry. I estimate the BH masses in each object using the Hα line profile and method of Greene & Ho (2005), and then fit the multiwavelength data with the energy-conserving, three component SED model of Done et al. (2012). I produce three iterations of this model, adjusting the number of free parameters between each one. At this redshift range the peak of the SED is shifted towards observable wavelengths, due to the both the redshift, and the cooler accretion disc compared with AGN with lower mass BHs.

My main conclusions are as follows:

i. I observe the SED peak, or close to it, in five objects. I find that Model 3, which includes intrinsic attenuation and free SX normalisation fits best, allowing for the additional free parameters.

ii. When used in conjunction with the effects of dust reddening, I can accurately model the underlying optical–IR (rest UV–optical) continuum, and well-constrain the outer disc radius in eight objects.

iii. In the AGN with lower BH masses, the SED peak is not observed, and in these cases the SX is therefore completely unconstrained. As a consequence of this, the model $\chi^2_{\rm red}$ fitting parameters do not differ between the models with SX free and those with it fixed for these objects. However, the SX contribution appears to be constrained to a varying degree in the five objects with data at the peak.

iv. Using template SEDs for both luminous elliptical galaxies and starbursts I show that the host galaxy contribution is insignificant at near to the peak of the SED, but could produce a large fraction of the flux observed redward of Hα. It is very likely that a dusty torus also contributes here, judging from *WISE* photometry. I therefore model these components accordingly in the next chapter.

v. I show that UV photometry alone is insufficient to constrain the continuum. Ideally UV spectroscopy, e.g. *HST*/COS, could be used to overcome the uncertainty of Ly-α forest absorption.

vi. The AGN in my sample generally have high Eddington ratios. In this respect they resemble the NLS1s studied in local AGN samples. This is expected, as in this redshift range, I preferentially observe the brightest AGN, which have high accretion rates. In Chapter 4 I test high-spin SED models, as there may be degeneracy in some of the objects between spin and mass accretion rate.

vii. I identify a range of properties in the best-fitting dust reddening component, with SMC/LMC reddening curves providing better fits than that of the MW in five objects.

viii. My analysis provides more reliable estimates of $L_{\rm bol}$, as it uses data from across a large range of wavelengths, and an energy-conserving SED model. I highlight the problems of using a single parameter proxy, such as $\kappa_{2-10{\rm keV}}$, as a means to derive $L_{\rm bol}$, as I see a large spread in such proxies, even in this small sample. I note that the six lowest mass AGN have unsampled SED peaks, and therefore more poorly constrained $L_{\rm bol}$. Having demonstrated the principle of applying the model successfully to multiwavelength data, a larger sample will be studied in the future to search for relationships between the overall SED characteristics and other specific emission line and continuum components.

CHAPTER 4

AGN SEDs Part 2: Exploring the Accretion Disc, Torus and Host Galaxy

4.1 Introduction

4.1.1 Motivation

In the last chapter, I presented a means of modelling the SED of a sample of 11 medium redshift ($1.5 < z < 2.2$) AGN, using multiwavelength spectral data from NIR to X-ray wavelengths and a numerical SED code described in Done et al. (2012). In this sample, the redshift effect, and selection bias toward more massive AGN (e.g. McLure & Dunlop 2004) that contain cooler ADs allowed the peak of the SED to be sampled in five objects. This enabled robust estimates of the AGN bolometric luminosity ($L_{\rm bol}$), noting that in several objects the SX was unconstrained by the available data. I also found that the host galaxy starlight contribution to the SED peak was small, but may be non-negligible at longer wavelengths, in the rest-frame optical spectrum. Host galaxy attenuation in the form of dust reddening and photoelectric absorption was modelled with appropriate free parameters (Netzer & Davidson 1979, Castelló-Mor et al. 2016).

Several limitations of my modelling campaign were discussed in Chapter 3. In Section 3.5.4, I concluded that not all of the AGN in my sample were well described by the Cardelli et al. (1989) reddening curve used to model intrinsic reddening, a finding also noted by others (see Section 4.1.2). Throughout the study, I also kept $M_{\rm BH}$ fixed at values calculated from the profile of Hα. However, it is known that such single epoch virial mass

estimates can be uncertain, and I have yet to explore the effect of changing $M_{\rm BH}$ on $L_{\rm bol}$, and other SED properties. Similarly, I found that data in all objects could be modelled by keeping a_* fixed at zero (i.e. non-spinning). This does not necessarily preclude higher spin values, so in this chapter I specifically test $a_* \neq 0$ scenarios. Finally, in many objects, I observed that the outer AD radius ($r_{\rm out}$) could be estimated from the SED fitting routine. However, I did not compare the values measured with the radius at which self-gravity within the AD becomes significant. All of these limitations are addressed in this chapter.

Thus far, I have only considered the SED contributions of three emissive components; the AD, SX and PLT intrinsic to the AGN. In Section 3.5.2 I suggested that the hot dust and host galaxy could make a significant contribution to the spectral continuum redward of the Hα emission line, which I quantify in this chapter by modelling these components. In local AGN, a remarkable relationship between the host galaxy and the central BH has been observed. These include strong correlations between $M_{\rm BH}$ and the stellar velocity dispersion of the galaxy ($M_{\rm BH}$–σ; e.g. Ferrarese & Merritt 2000, Gebhardt et al. 2000, Beifiori et al. 2012) and between $M_{\rm BH}$ and the bulge mass/luminosity (e.g. Magorrian et al. 1998, Marconi & Hunt 2003, Sani et al. 2011). However, the difficulty of disentangling contributions from AGN and host galaxy means that these relationships at higher redshifts are currently uncertain. SED modelling may present an alternative means of exploring this.

AGN optical variability is also quantified, for objects with more than one epoch of optical data. Current models of AGN variability are limited, particularly when related to the AD. AGN optical variability is often observed which occurs faster than the viscous timescale, the theoretical timescale of mass flow in the AD (e.g. Czerny 2004, Alexander & Hickox 2012). As such, variable attenuation is often invoked to explain the larger flux changes, although this sometimes fails, implying changes in accretion rate (LaMassa et al. 2015, MacLeod et al. 2016). Although the data are not ideally suited to variability studies, I specifically address the question of the likely mechanism for the (small) optical variability observed in three of the objects.

Finally, I am motivated to explore whether the physical model of the optical–NIR continuum facilitates a deconvolution of the spectral data, when combined with models

of various components for the BLR (and NLR) features.

The resulting structure of this chapter is therefore as follows:

i. Test the model properties, including both extrinsic (host galaxy extinction curves) and intrinsic effects, e.g. spin and the uncertainties on $M_{\rm BH}$ (Section 4.2).

ii. Carry out an analysis of the toroidal dust component, using MIR photometry from *WISE* (Section 4.3).

iii. Consider the effects of variability in the optical spectra (Section 4.4).

iv. Undertake an optical–NIR spectral decomposition, using the refined models of the underlying continua, and compare results from this approach to other studies (Section 4.5).

4.1.2 Previous Work

A number of properties of AGN influence the observed SED, as discussed in greater detail in Section 1.3. The matter that accretes on to the BH is net-neutral, so the BH has just two intrinsic properties – $M_{\rm BH}$ and a_* – which primarily affect the peak temperature and mass-energy conversion efficiency in the AD. The rate of mass accretion through the AD (expressed as the Eddington fraction, $\dot{m}$) and its orientation with respect to the observer (θ) can further modify the SED, and photoelectric absorption and dust extinction along the line of sight attenuate the emission over large wavelength ranges.

$M_{\rm BH}$ can be estimated via a number of methods in AGN (see Section 1.4) and it has been suggested that $\dot{m}$ can be estimated from spectral continuum measurements via so-called bolometric correction (BC) coefficients (e.g. McLure & Dunlop 2004, Vasudevan & Fabian 2007, Trakhtenbrot & Netzer 2012). Spin, however, only affects $r_{\rm isco}$ of the BH; $r_{\rm isco} \simeq 1.24, 6, 9\ R_{\rm g}$ for $a_* = 0.998, 0, -1$ respectively. Previous work has constrained $r_{\rm isco}$, and hence a_*, by fitting the profile of the broad, relativistically distorted, Fe Kα emission line that is often observed in the X-ray reflection spectrum of AGN. This method requires high S/N X-ray data, limiting its application to nearby, bright AGN (Fabian et al. 1989, Fabian et al. 2009, Risaliti et al. 2013, Reynolds 2014). Moreover, the technique is

contentious, as it requires an extreme X-ray source geometry to sufficiently illuminate the inner part of the AD (e.g. Zoghbi et al. 2010). Alternative models propose that the profile of the Kα line could be influenced by complex, multi-layered absorption, possibly from a disc wind (e.g. Miller et al. 2007, Turner & Miller 2009, Miller & Turner 2013, Gardner & Done 2014).

Capellupo et al. (2015, 2016) used a thin AD model to measure spin values in their sample of 39 AGN at $z \sim 1.5$. Using the numerical code of Slone & Netzer (2012), and contemporaneous optical–IR spectra from the VLT/X-shooter instrument, they successfully modelled the rest-frame optical–UV SED in all but two objects. The most massive BHs in their sample have the highest measured spin values, supporting a 'spin-up' description of AGN BH evolution, where prolonged unidirectional accretion episodes and BH mergers increase the spin of BHs through cosmic time (e.g. Dotti et al. 2013). Done et al. (2013) and Done & Jin (2016) explored the spins of two local AGN – PG1244+026 and 1H 0707−495 respectively – by applying the OPTXAGNF SED model to multiwavelength data. They found that high spin states were incompatible with the data in both, contradicting an earlier finding that 1H 0707−495 has a near-maximal spin of $a_* > 0.98$, based on the Fe Kα line (Fabian et al. 2009). Finally, Matt et al. (2014) also used OPTXAGNF in their study of Ark 120, inferring an intermediate BH spin from simultaneous *XMM-Newton* and *NuSTAR* observations.

The nature of the dusty torus is the subject of considerable debate. Of particular interest are the peak dust temperature in the torus, which can be used to infer its composition, and the total luminosity, from which the dust covering factor can be estimated (e.g. Mor et al. 2009, Landt et al. 2011).

Whilst local galaxies can be easily resolved in imaging, enabling structural decomposition of the point-like AGN and extended galaxy bulge and disc (e.g. Marconi & Hunt 2003, McConnell & Ma 2013), disentangling these contributions is challenging at higher redshifts. Peng et al. (2006) partially overcame this limitation by using *HST* imaging of gravitationally lensed AGN, and found evidence that at $z > 1.7$, the $M_{\rm BH}$–bulge mass ratio is $\gtrsim 4$ times that observed locally.

Previous work has not reached a consensus on the best choice of extinction curve to

model the intrinsic reddening of AGN. Hopkins et al. (2004) and Glikman et al. (2012) found the SMC extinction curve to better describe host galaxy reddening in AGN, whilst Capellupo et al. (2015) found the SMC curve to be no better than that of the MW, or a simple power-law. Castelló-Mor et al. (2016) opted to use an SMC curve, but noted that the limited data coverage in the rest-UV made favouring any one model impossible. Zafar et al. (2015) carried out a study of the extinction curves of 16 quasars in the redshift range $0.71 < z < 2.13$, selected on the basis of high intrinsic extinction. By comparing their sample of objects to the Vanden Berk et al. (2001) and Glikman et al. (2006) quasar templates, they were able to derive extinction curves for each object in their sample.

4.2 Testing the SED Model

4.2.1 Data and SED Construction

In this chapter I am primarily concerned with the nature of the underlying AGN SED continuum. In Chapter 3 I described the sample selection, which focussed on the need for optical, IR and X-ray spectra. To make a reliable $M_{\rm BH}$ estimate, I required the broad Balmer emission lines, Hβ and Hα, to lie in the NIR J and H bands. The primary sample was therefore at $1.49 < z < 1.61$, and I included an additional object at $z \simeq 2.2$ which had the requisite data and Hβ and Hα in the NIR H and K bands. The objects' names, positions, and other key properties are presented in Chapter 3, and I tabulate the names and mass estimates from Hα again in Tables 4.2 and 4.3 of this work.

The data come from four observatories. The optical spectra were extracted from the SDSS and BOSS databases, and IR spectra came from GNIRS and TSpec. Finally, X-ray spectra were retrieved from the *XMM-Newton* science archive. I describe the data reduction in Chapter 3. The optical–IR spectra are corrected for MW extinction using the dust maps of Schlegel et al. (1998) and extinction law of Cardelli et al. (1989).

I construct the SED using spectral data from all these sources, following the same approach as in Chapter 3. The optical–IR spectra include a number of emission features, with the underlying continuum dominated by the various emission components shown in Fig. 1.5. I define continuum regions (free from emission line/Balmer contin-

Table 4.1: Optical/IR continuum regions used in the SED fitting. Not all regions are used in all objects, as some show contamination by emission features such as Fe II. I avoid oversampling any part of the spectrum, aiming for a roughly even spread of continuum points across the spectral range (particularly with respect to regions 10–15). Before Section 4.3, only regions 1–9 are used for fitting, as regions 10–15 begin to show potential contribution by hot dust and host galaxy. Some of regions 10–15 are used for modelling in Section 4.3.

Region #	Centre	Start	End
	(Å, rest-frame)		
1	1325	1300	1350
2	1463	1450	1475
3	1775	1750	1800
4	2200	2175	2225
5	4025	4000	4050
6	4200	4150	4250
7	5475	5450	5500
8	5650	5600	5700
9	6100	6050	6150
10	7000	6950	7050
11	7250	7200	7300
12	7538	7475	7600
13	7850	7800	7900
14	8150	8100	8200
15	8900	8800	9000

uum/blended Fe II emission) in the optical/IR spectra using the template of Vanden Berk et al. (2001) as a guide. The optical/IR continuum regions used are shown in Table 4.1, with regions showing contamination by noise/emission features adjusted or removed accordingly. There is general consistency with other work that define similar such bandpasses, see also Kuhn et al. (2001) and Capellupo et al. (2015). Some of these wavelength ranges have been adjusted by a small amount from those used in Chapter 3, reflecting improved attempts to mitigate against inclusion of emission-contaminated ranges. In this section I do not include the continuum redward of Hα (regions 10–15 in Table 4.1) owing to the 'red excess' seen in this region. This region is discussed and modelled later, see Section 4.3.

The X-ray spectrum is also known to show emission features, such as the previously mentioned Fe Kα line, but the S/N of the X-ray data are not sufficient to resolve such

features. I therefore use all available data from the MOS1, MOS2 and PN detectors aboard *XMM-Newton* to maximise the number of X-ray counts.

A limitation of my study is that the optical/IR/X-ray data were not collected contemporaneously. AGN are known to vary across all wavelengths differentially, and I therefore cannot rule out variability having occurred between observations. This is a limitation of most such studies due to the difficulty and expense of scheduling simultaneous observations using multiple space- and ground-based observatories. In Chapter 3 I described a means of checking for evidence of variability between optical/IR observations using photometry and simple power-law continuum fits. I concluded that in one object (J0041−0947) there was evidence for ~ 30 per cent variability between optical/IR observations. In this case, I used the GNIRS spectrum as observed for estimating $M_{\rm BH}$, but scaled it to the level of SDSS for SED fitting. In two objects with multiple epochs of X-ray data I found no evidence for X-ray variability, but since AGN are often observed to show short-timescale X-ray fluctuations, I cannot rule out a variable X-ray component in any of the AGN.

As discussed in Chapter 3, I do not use photometric data in my SED modelling. In the optical/IR, photometry is usually contaminated by emission features, and is inferior to the spectra for defining the continuum. *GALEX* and *XMM* OM UV photometry is available for some objects (see Table A.1), however, due to the redshift range of the AGN, these data lie on or beyond Ly-α. Photometry covering Ly-α cannot be corrected, because the equivalent width of this strong feature varies widely between objects (Elvis et al. 2012). Similarly, photometry beyond Ly-α in the rest frame cannot be reliably used, as it is unpredictably attenuated by the multitude of narrow absorption features in the Ly-α forest.

Throughout this work I use the AGN SED model OPTXAGNF, described in Done et al. (2012). This model comprises three components – AD, SX and PLT – and applies the constraint of energy conservation to these. I do not include a relativistic reflection component (see Fig. 1.5), as the *XMM* spectra lack the S/N and coverage necessary to model it. All SED fitting is performed in the XSPEC spectral analysis package, using the Levenberg-Marquardt minimisation routine.

4.2.2 Intrinsic Reddening

In this section I refine my best models from Chapter 3 by testing alternative intrinsic extinction curves. I therefore produce a new SED model for each object, using newly determined best-fitting parameters.

I have already corrected the optical–IR spectra for MW extinction (Section 4.2.1), and now combine the OPTXAGNF model with WABS, ZWABS and ZDUST to model Galactic and intrinsic attenuation. This is discussed more in Sections 3.4.2 and 3.5.4.

The full XSPEC model therefore takes the form WABS × ZWABS × ZDUST × OPTXAGNF. The fixed parameters, and corresponding models, are as follows:

(i) Mass, $M_{\rm BH}$ (OPTXAGNF): fixed at the value from Hα.

(ii) Redshift, z (OPTXAGNF, ZWABS, ZDUST).

(iii) Comoving distance, $r_{\rm c}$ (OPTXAGNF).

(iv) Spin, a_* (OPTXAGNF): fixed at 0.

(v) SX electron temperature, $kT_{\rm e}$ (OPTXAGNF): fixed at 0.2 keV.

(vi) SX optical depth, τ (OPTXAGNF): fixed at 10.

(vii) Ratio of absolute extinction to that defined by $(B-V)$, $R(V)=A(V)/E(B-V)$ (ZDUST): fixed at values of 3.08, 3.16, 2.93 for MW, LMC, SMC respectively (Pei 1992).

The free parameters, and corresponding models, are:

(i) Mass accretion rate, $\dot{m}=L_{\rm bol}/L_{\rm Edd}$ (OPTXAGNF).

(ii) Coronal radius, $r_{\rm cor}$ (OPTXAGNF).

(iii) Outer AD radius, $r_{\rm out}$ (OPTXAGNF).

(iv) PLT photon index, Γ (OPTXAGNF).

(v) Fraction of Comptonised energy in SX, $f_{\rm SX}$ (OPTXAGNF): this is $1-f_{\rm PL}$ given in Table 2.1.

(vi) Intrinsic H I column density, $N_{\rm H,int}$ (ZWABS).

(vii) Intrinsic reddening, $E(B-V)_{\rm int}$ (ZDUST).

I fit the model to all 11 objects for each of the MW, LMC and SMC extinction curves, and use the final $\chi^2_{\rm red}$ fit statistic to gauge which produces the best description of the data. These curves, and the continuum regions listed in Table 4.1 are shown in Fig. 4.1. I find that six objects are best described by the MW extinction curve, four by the LMC curve and one by the SMC curve. In objects for which the intrinsic reddening is low ($E(B-V)_{\rm int} \lesssim 0.03$ mag), the difference in $\chi^2_{\rm red}$ is generally small, but these are also the objects in which the reddening makes the smallest difference to the $L_{\rm bol}$. The uncertainty in $L_{\rm bol}$ due to the uncertainty on $E(B-V)_{\rm int}$ varies from object to object. Typical values range from 0.03 dex (J1350+2652) to 0.16 dex (J2328+1500).

The best fitting extinction curve in each object is used henceforth. The refined models are shown by the orange curves in Fig. 4.2. I tabulate the key SED parameters and derived properties for these new models in Tables 4.2 and 4.3.

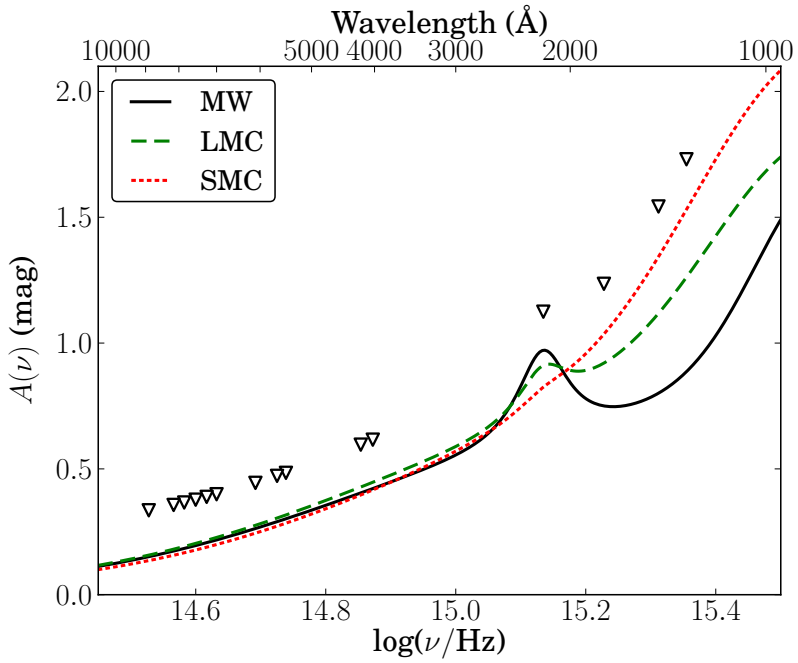

Figure 4.1: The three extinction curves I test for the intrinsic reddening, as shown in Fig. 2.5. All curves are for the same $E(B-V)$. The markers indicate the locations of the continuum regions used for the fit. Clearly, the four bluest regions are the most important for distinguishing between the curves.

Table 4.2: The optimum fitted parameters for the SED model fitted in Section 4.2.2. The difference between this model and 'Model 3' in Chapter 3 is the extinction curve used. Whereas in Model 3 I used the MW curve in all objects, I noted that the reddening correction in J1044+2128 produced only a marginal fit to the data. Here I use the best fitting extinction curve out of the MW, LMC and SMC curves tested. In a few objects I have adjusted the optical/IR continuum points used in the fit from Chapter 3, hence the $\chi^2_{\rm red}$ values are not directly comparable with Model 3 in that work. Uncertainties quoted are the 90 per cent confidence limits, as is conventional in X-ray astronomy, and are estimated using the Fisher matrix. As such, they are only indicative of the true measurement error. The $f_{\rm SX}$ values in brackets were unconstrained.

Obj	ID	$N_{\rm H,int}$ ($10^{22}\,{\rm cm}^{-2}$)	Extinct curve	$E(B-V)$ (mag)	$\dot{m} = L_{\rm bol}/L_{\rm Edd}$	$r_{\rm cor}$ ($R_{\rm g}$)	$r_{\rm out}$ ($R_{\rm g}$)	Γ	$f_{\rm SX}$	$\chi^2_{\rm red}$
1	J0041−0947	0.0±0.2	MW	0.050±0.006	0.59±0.02	27±6	300±30	2.15±0.19	0.84±0.07	4.16
2	J0043+0114	0.0±0.3	LMC	0.039±0.018	4.72±0.11	9.8±1.0	610±60	2.50±0.35	(0.70)	0.82
3	J0118−0052	0.06±0.12	MW	0.025±0.014	0.49±0.02	25±11	240±40	2.44±0.14	0.77±0.14	1.92
4	J0157−0048	0.19±0.10	MW	0.053±0.014	3.57±0.09	9.3±0.4	460±30	2.07±0.12	(0.70)	2.51
5	J0839+5754	0.46±0.06	MW	0.066±0.003	0.349±0.005	80.9±1.6	>1000	1.99±0.05	0.64 ± 0.03	1.62
6	J1021+1315	0.2±0.2	MW	0.043±0.013	1.96±0.08	12±2	670±80	2.32±0.24	(0.70)	1.45
7	J1044+2128	0.00±0.02	SMC	0.064±0.005	6.74±0.09	8.53±0.09	>1000	2.24±0.05	0.7±0.4	1.63
8	J1240+4740	0.00±0.11	LMC	0.039±0.011	2.61±0.10	14±7	>1000	1.80±0.13	(0.70)	1.39
9	J1350+2652	0.0±0.3	MW	0.034±0.007	2.03±0.05	9.7±0.4	440±20	2.19±0.14	(0.70)	1.98
10	J2328+1500	0.00±0.15	LMC	0.16±0.04	0.122±0.007	14±3	40±3	1.48±0.09	(0.70)	1.63
11	J2332+0000	0.0±0.3	LMC	0.08±0.03	0.890±0.10	10.9±1.5	176±12	2.18±0.14	(0.70)	0.61

Table 4.3: The key properties of the various SED models, including BCs. I also show the $M_{\rm BH}$ estimates calculated in Chapter 3. The error on $L_{\rm bol}$ is estimated from the error on $\dot{m}$, and is indicative of the measurement error. The true error will be larger, due to additional contributions from $M_{\rm BH}$ and $E(B-V)_{\rm int}$.

ID	$\log(M_{\rm BH}/M_{\odot})$	$\log(L_{\rm bol})$ [log(erg s^{-1})]	$\log(L_{2-10\,{\rm keV}})$ [log(erg s^{-1})]	$\kappa_{2-10\,{\rm keV}}$	$\log(\lambda L_{2500\text{Å}})$ [log(erg s^{-1})]	$\log(\nu L_{2\,{\rm keV}})$ [log(erg s^{-1})]	$\alpha_{\rm OX}$	$\log(\lambda L_{5100\text{Å}})$ [log(erg s^{-1})]	$\kappa_{5100\text{Å}}$
1	9.42±0.11	47.338±0.018	45.32	104	46.86	45.17	1.65	46.52	6.64
2	8.68±0.10	47.505±0.010	44.88	421	46.51	44.84	1.64	46.06	27.84
3	9.25±0.10	47.09±0.02	44.82	185	46.58	44.76	1.70	46.20	7.74
4	8.63±0.10	47.332±0.011	44.88	286	46.34	44.70	1.63	45.84	30.78
5	9.53±0.11	47.262±0.006	45.90	22.9	46.87	45.69	1.45	46.67	3.92
6	8.73±0.10	47.181±0.017	44.97	163	46.33	44.87	1.56	45.97	16.39
7	8.55±0.10	47.544±0.006	44.80	555	46.47	44.68	1.69	46.17	23.51
8	8.68±0.09	47.272±0.016	45.32	90.4	46.36	45.04	1.51	46.07	15.97
9	9.01±0.10	47.467±0.011	45.01	287	46.70	44.87	1.70	46.30	14.57
10	9.68±0.10	46.72±0.03	44.65	116	46.40	44.24	1.83	45.90	6.57
11	9.02±0.09	47.09±0.05	44.81	189	46.39	44.67	1.66	45.86	16.71

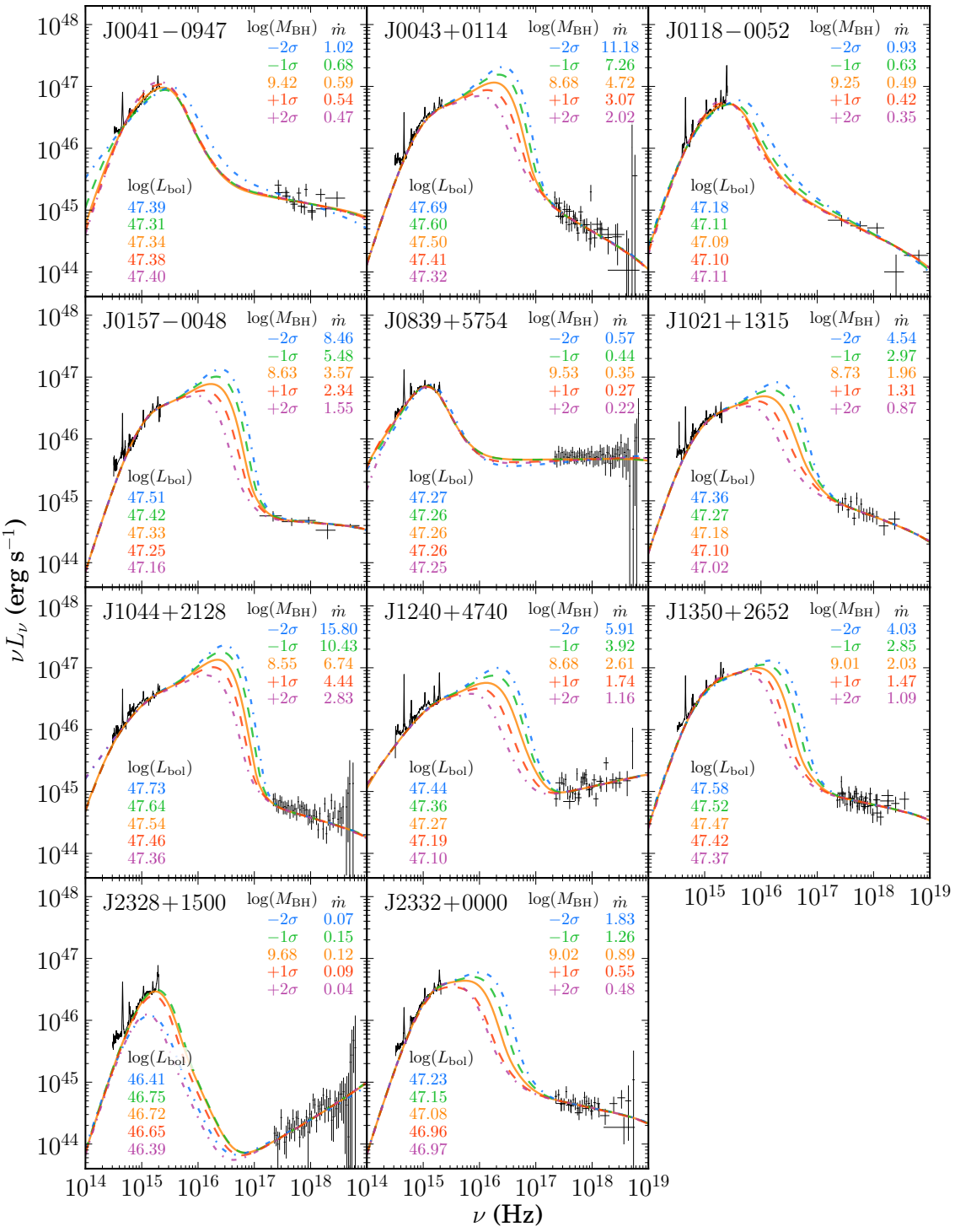

Figure 4.2: The SEDs for the sample, showing model variance with $M_{\rm BH}$. All models are at spin value, $a_* = 0$. In black is the data from *XMM-Newton*, SDSS and GNIRS/TSpec to which I fit the broad-band SED model. The model contains corrections for host galaxy extinction and soft X-ray absorption, as in Model 3 in Chapter 3, but here I use the best-fitting extinction curve (MW, LMC or SMC), rather than the MW curve in all cases. I have corrected the data for these sources of attenuation. The best fitting model, arising from the mean $M_{\rm BH}$ estimate, is shown by the solid orange curve. Then I have altered the $M_{\rm BH}$ estimate by 1 and 2 σ (see Table 4.3 for $M_{\rm BH}$ and errors) and remodelled the SED. The 1 σ models are shown by the dashed curves and the 2 σ models by the dash-dot curves. The key model properties, with colours corresponding to the curves, are also given.

4.2.3 Uncertainty on Black Hole Mass

In Chapter 3, I commented upon the possible uncertainty in the SED model that may arise from the $M_{\rm BH}$ estimate, in particular with regard to the SED peak position. To test this, I have produced four new models for each AGN, with $M_{\rm BH}$ varied by $\pm 1, 2\sigma$ from its mean value. The modelling procedure is otherwise the same as described in Section 4.2.2, with the same free and fixed parameters. The best-fit intrinsic extinction curve is used (Table 4.2). To avoid local minima in the fitting, and impartially test the total effect of altering $M_{\rm BH}$ in each case, I apply the same modelling script in all cases, with the same initial values. Between models there can therefore be different values for all free parameters, including $E(B-V)_{\rm int}$, $N_{\rm H,int}$ and $r_{\rm out}$. These may contribute to degeneracies between parameters, which it is also important to test for.

The resulting SEDs are presented in Fig. 4.2, with accretion rates and $L_{\rm bol}$ also given. For simplicity, only the dereddened/deabsorbed data for the mean $M_{\rm BH}$ model are shown, hence in models that do not appear to well describe the data, this is due to a different value of $E(B-V)_{\rm int}$ or $N_{\rm H,int}$ (see J0041−0947 in Fig. 4.2 for a clear example of this variation).

It is clear that in objects with unconstrained SED peaks the difference is greatest. Reducing $M_{\rm BH}$ produces an AD which peaks at higher energies, resulting in a larger $L_{\rm bol}$. In objects with well-constrained SED peaks, such as J0118−0052, this difference is smaller, and in J0839+5754 the difference is smallest of all, partly because the SED peak is dominated by the SX component, and therefore the peak temperature dependency on $M_{\rm BH}$ is smaller. The intrinsic reddening value is consistent in all models, with all but J2328+1500 showing very little variation in optical/IR continuum slope. Degeneracy between the accretion rate and intrinsic reddening is evident in J2328+1500 however, with the $M_{\rm BH}$ $\pm 2\sigma$ models showing convergence to different optimum values of $E(B-V)_{\rm int}$ (evinced by the lower SED for these models). It is encouraging that such an effect is only seen in one object, and only when the $M_{\rm BH}$ estimate is altered by 2σ from the mean. In general the inherent uncertainty on $M_{\rm BH}$ has only a small or predictable impact on the $L_{\rm bol}$, with a ± 0.1 dex change in $M_{\rm BH}$ propagating through to $L_{\rm bol}$ in all cases where the SED peak is unsampled.

4.2.4 Black Hole Spin

In Chapter 3, I did not investigate the effect of BH spin in the modelling, and found that all objects could be adequately fit with the a_* spin parameter set to zero (i.e. non-spinning), and the mass accretion rate left as a free parameter. However, this finding does not necessarily rule out high spin scenarios, so here I test models with spinning BHs in the sample. There is a degeneracy between the mass accretion rate and spin in terms of the SED peak position as both affect the AD energy output and peak temperature. Therefore setting both parameters free in the fitting will not necessarily enable measurement of the optimal spin value. Instead I repeat the SED fitting procedure for a range of additional a_* values: 0.5, 0.8, 0.9 and 0.99. Other than these changes, the model fitting procedure is as described in Section 4.2.2.

In Fig. 4.3, the SED models incorporating BHs with a_* values of 0.5, 0.8, and 0.9 are shown alongside the $a_* = 0$ model constructed in Section 4.2.2. In $\sim 2/3$ of the sample I find that the moderate spin states ($a_* = 0.8, 0.9$) do not provide as good a fit to the data as the low spin states ($a_* = 0, 0.5$), exhibited by the optical–IR spectra (e.g. J0839+5754) or by the X-ray spectra (e.g. J1044+2128). Interpreting this result is complicated by the free parameters, in particular, the intrinsic attenuation properties of $E(B-V)_{\rm int}$ and $N_{\rm H,int}$, which are not immediately apparent in Fig. 4.3. Three objects, J0041−0947, J1350+2652 and J2328+1500, show an improvement in the $\chi^2_{\rm red}$ fitting statistic for the $a_* = 0.9$ model compared with $a_* = 0$, however the difference for the latter two is slight. These are discussed in Section 4.6.2.

Using OPTXAGNF, I rule out the very highest spin states in this sample; for $a_* = 0.99$ the SED model breaks down in all but one (J2328+1500) case, producing SEDs that simply do not fit the data, or models where the PLT dominates the AGN energy output, which disagrees with previous work. Given this, I have not plotted this model in Fig. 4.3. The cause of this is that the energies resulting from these highest spin states cannot be redistributed in the Comptonised components.

However, there are several important limitations of the AD model in OPTXAGNF that become significant here. OPTXAGNF assumes a fixed AD inclination to the observer of 60°, does not include relativistic effects, and does not account for advection (Done et al. 2013). These effects are relatively insignificant when spin is low or zero, but become substantial as spin increases. This is discussed in Section 4.6.2.

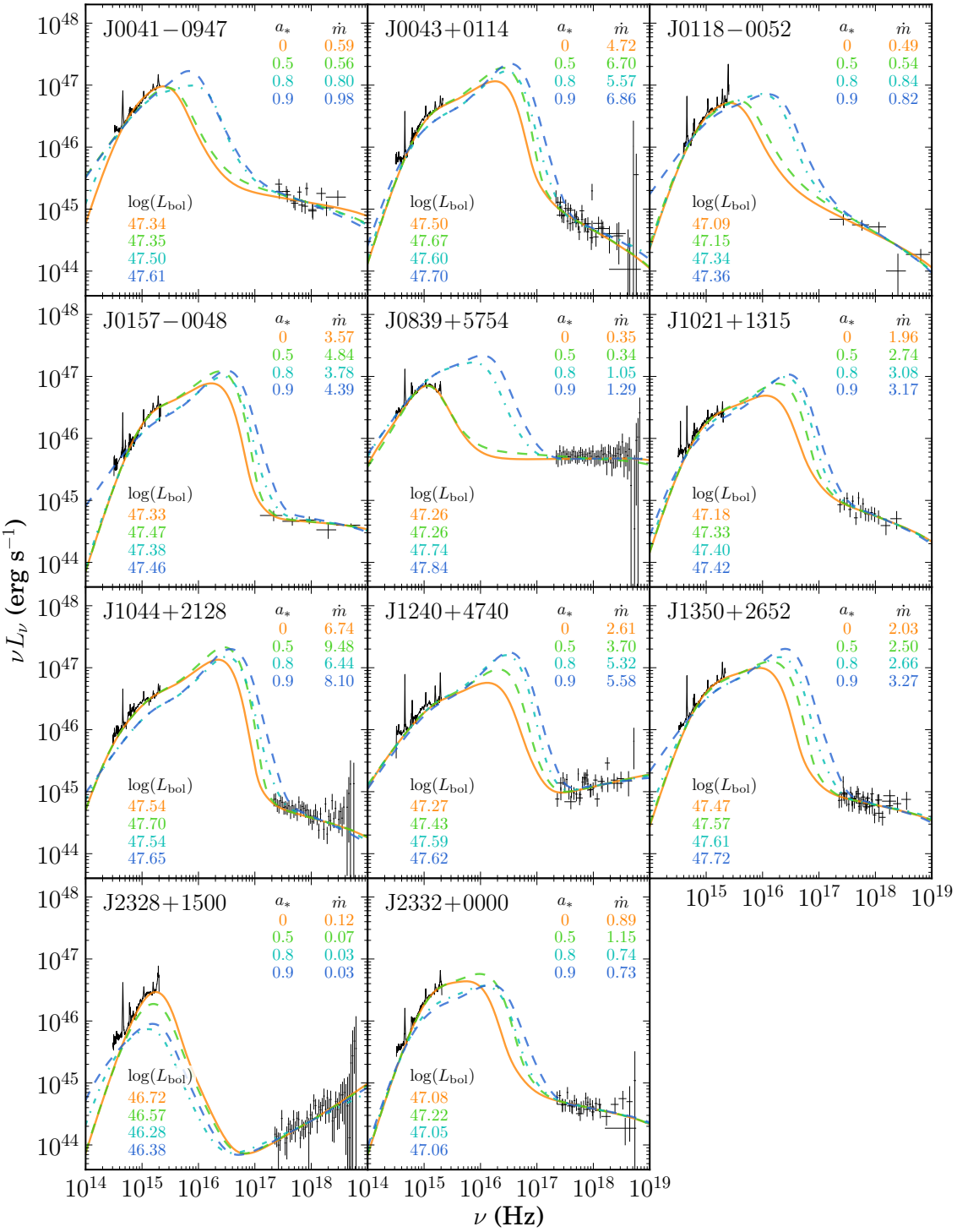

Figure 4.3: The SEDs for the sample, showing variation with the a_* spin parameter. The data and orange curve are for the best fitting model with $a_* = 0$, and are the same model as shown by the orange curve in Fig. 4.2. In each subsequent case, I have fixed a_* at a higher value (0.5, 0.8, 0.9) and repeated the fitting procedure. A model with $a_* = 0.99$ is also tested, but in all but one case, the resulting model either produced only a marginal fit, or a model in which nearly all of the AD energy is reprocessed in the Comptonised components, contrary to what is observed in local AGN. This result is dependent on relativistic corrections and inclination; see Section 4.6.2 for a discussion.

4.2.5 Outer Accretion Disc Radius

In all of the SED models I have produced so far, the outer AD radius ($r_{\rm out}$) has been left as a free parameter. It has been suggested (e.g. Goodman 2003) that the AD extends out to a radius at which self-gravity causes it to begin to break up, with the self-gravity radius, $r_{\rm sg}$, depending on both $M_{\rm BH}$ and accretion rate according to the following equation, given in Laor & Netzer (1989):

$$\left(\frac{r_{\rm sg}}{R_{\rm g}}\right) = 2150 \left(\frac{M_{\rm BH}}{10^9\, M_\odot}\right)^{-2/9} \dot{m}^{4/9} \alpha^{2/9} \tag{4.2.1}$$

where α is the ratio of viscous stress to pressure in the disc, fixed at a value of 0.1.

I explore this further by testing three different means of setting $r_{\rm out}$:

(1) $r_{\rm out}$ free: this is the model described in Section 4.2.2.

(2) $r_{\rm out}$ fixed at $r_{\rm sg}$.

(3) $r_{\rm out}$ fixed at an arbitrary large value, as in Jin et al. (2012a).

Based on both $\chi^2_{\rm red}$ and visual inspection of the resulting fits, in 8 of the 11 objects, when $r_{\rm out}$ is set to a large value or $r_{\rm sg}$, the fit is poorer than those with $r_{\rm out}$ free. Two examples are shown in Fig. 4.4. When the measured $r_{\rm out}$ values are compared with those calculated from equation 4.2.1 (Fig. 4.5), an increasing trend with $r_{\rm sg}$ is seen, but offset from unity, suggesting that self-gravity may play a role in setting $r_{\rm out}$, but is not the only contributing factor. Also shown are the $r_{\rm out}$ values derived in Section 4.3, where I include model components for the torus and host galaxy. The relations I derive are:

$$\log(r_{\rm out}) = \log(r_{\rm sg}) - (0.66 \pm 0.06) \tag{4.2.2}$$

for the AGN only model, and:

$$\log(r_{\rm out}) = \log(r_{\rm sg}) - (0.76 \pm 0.06) \tag{4.2.3}$$

for the model including torus and host galaxy components.

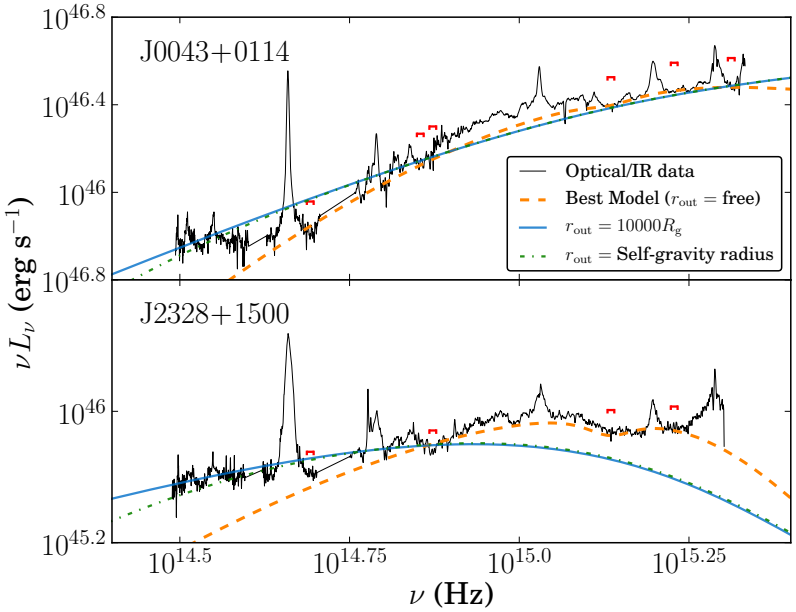

Figure 4.4: Two example objects in which setting the r_{out} to an arbitrarily large value (10000 R_g) or r_{sg} produces an inferior fit to the data. I show the intrinsically reddened spectra/SEDs here, whereas other figures show the 'dereddened' (intrinsic) SED. The red brackets show the continuum regions used for the fit.

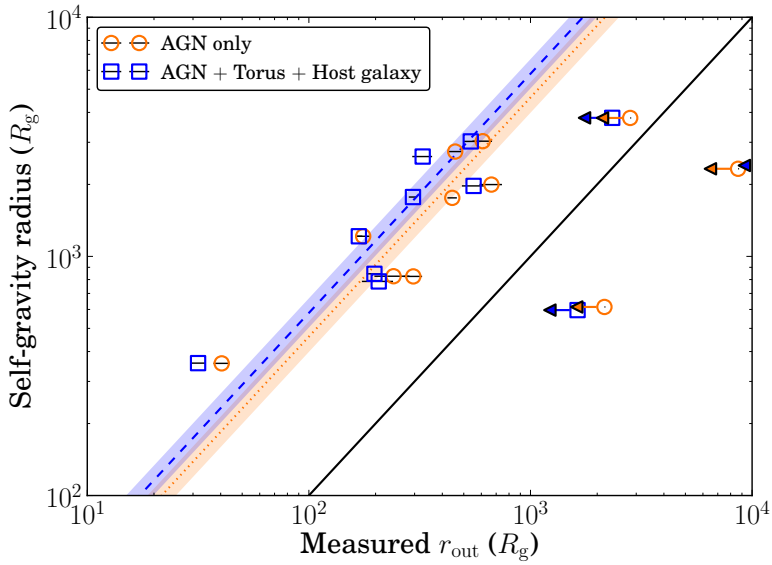

Figure 4.5: Comparing r_{out} measurements from SED fitting with r_{sg} as given in equation 4.2.1. I show the three objects with unconstrained r_{out} as upper limits, and exclude these from the derived relations. The solid line represents unity, and the dotted and dashed lines represent the unity-gradient lines fitting the AGN only and AGN+Torus+Host galaxy data, respectively.

4.3 Torus and Host Galaxy

I discussed the potential contribution of the host galaxy to the total SED in Chapter 3. This may be manifest in the 'red excess' observed in nearly all objects, redward of the Hα emission line. The Jin et al. (2012a) sample was at $z < 0.3$, and therefore on average of lower luminosity than my sample, and exhibited a significant contribution to the optical spectral continuum by the host galaxy. In general, for AGN at $z \gtrsim 0.5$ the host galaxy contribution is assumed to be insignificant (e.g. Shen et al. 2011), and indeed I concluded in Chapter 3 that for the least luminous source (J2328+1500), the maximum possible contribution to the SED peak was $\lesssim 2$ per cent, increasing to ~ 50 per cent at wavelengths of $\sim 1\mu$m.

Since this object also hosts the most massive BH of the sample, it is expected to exhibit the largest contribution from the host galaxy, based on the $M_{\rm BH}$–bulge mass relationship (see Section 4.1.1). I therefore concluded that the host galaxy contribution to total SED continuum is small in all objects. Nonetheless, the red excess and *WISE* photometry show evidence for a dusty torus component, which possibly includes a contribution by the host galaxy. Thus, as the final refinement of my SED modelling, I now include SED components for both the torus and host galaxy, in order to fit the spectral data redward of Hα (regions 10–15 in Table 4.1), and the *WISE* photometry.

Due to data limitations, I employ a simplified model of the torus consisting of two blackbody components, hereafter referred to as 'hot' and 'warm'. The temperature of the hot component, $T_{\rm hot}$, depends on the composition of the dust grains that form the torus. Silicate grains sublimate at temperatures above ~ 1500 K, whereas graphitic grains can survive up to $\sim 1800-2000$ K (e.g. Barvainis 1987, Mor et al. 2009, Landt et al. 2011). In this respect my approach is similar to that employed by Mor & Trakhtenbrot (2011), who modelled a single, hot graphitic dust component to a large sample of AGN, and Landt et al. (2011), who used blackbody models of the hot dust in their sample of AGN.

Kirkpatrick et al. (2015) also modelled combined blackbody components to represent the warm and cold dust in their sample of luminous IR star-forming galaxies and AGN.

In Chapter 3 I tested two models of the host galaxy, that of a 5 Gyr elliptical galaxy and a starburst galaxy (represented by M82), which shows a stronger contribution at UV wavelengths. I extracted these galaxy templates from Polletta et al. (2007). Practically, the difference between the two templates was small, as the rest-UV flux is dominated by AD emission. Theoretically, based on the $M_{\rm BH}$–bulge relationship, I expect this sample of AGN to be hosted by massive elliptical galaxies, and therefore use the 5 Gyr template of Polletta et al. (2007) only in this work.

I fit the SEDs in XSPEC again, fixing the X-ray part of the spectrum to values calculated in Section 4.2.2. The full MIR to X-ray SEDs, including the torus and host galaxy components, are shown in Fig. 4.6. The key properties are given in Table 4.4. I calculate the dust covering factor for both the hot and warm torus components using the formula $C = L_{\rm dust}/L_{\rm bol}$, where $L_{\rm dust}$ is the total luminosity of the combined hot and warm dust components.

Table 4.4: Luminosities and temperatures of the different components in the sample.

Name	$\log(L_{\rm bol})$ $[\log({\rm erg\,s^{-1}})]$	$\log(L_{\rm Torus})$ $[\log({\rm erg\,s^{-1}})]$	$\log(L_{\rm Host})$ $[\log({\rm erg\,s^{-1}})]$	$\frac{L_{1\mu{\rm m,host}}}{L_{1\mu{\rm m,total}}}$	$T_{\rm hot}$ [K]	$T_{\rm warm}$ [K]	$C_{\rm hot}$ [%]	$C_{\rm warm}$ [%]
J0041−0947	47.35±0.02	46.7±0.3	45.97±0.09	0.46	1090±160	300±1400	12.7	8.7
J0043+0114	47.50±0.02	46.55±0.02	45.4±0.1	0.28	1630±60	460±60	5.5	5.7
J0118−0052	47.03±0.03	46.74±0.02	45.5±0.4	0.19	2170±170	650± 60	12.8	38.2
J0157−0048	47.28±0.02	46.44±0.02	45.58±0.08	0.62	1410±90	400±30	4.8	9.8
J0839+5754	47.23±0.07	46.9±0.6	45.8±0.3	0.17	1200±1300	300±500	20.5	24.3
J1021+1315	47.17±0.02	46.46±0.02	45.3±0.2	0.24	1710±70	540± 50	8.4	11.4
J1044+2128	47.54±0.01	46.66±0.02	45±2	0.13	1450±50	410±30	5.7	7.3
J1240+4740	47.26±0.04	46.4±0.5	45.4±0.1	0.21	1500±70	400±1700	8.6	6.5
J1350+2652	47.46±0.01	46.70±0.03	46.01±0.03	0.61	1270±70	440±50	8.8	8.3
J2328+1500	46.64±0.02	46.3±0.3	45.68±0.03	0.72	1130±90	300±800	26.2	15.7
J2332+0000	47.08±0.02	46.40±0.02	45.1±0.2	0.22	1650±80	540±60	7.7	13.1

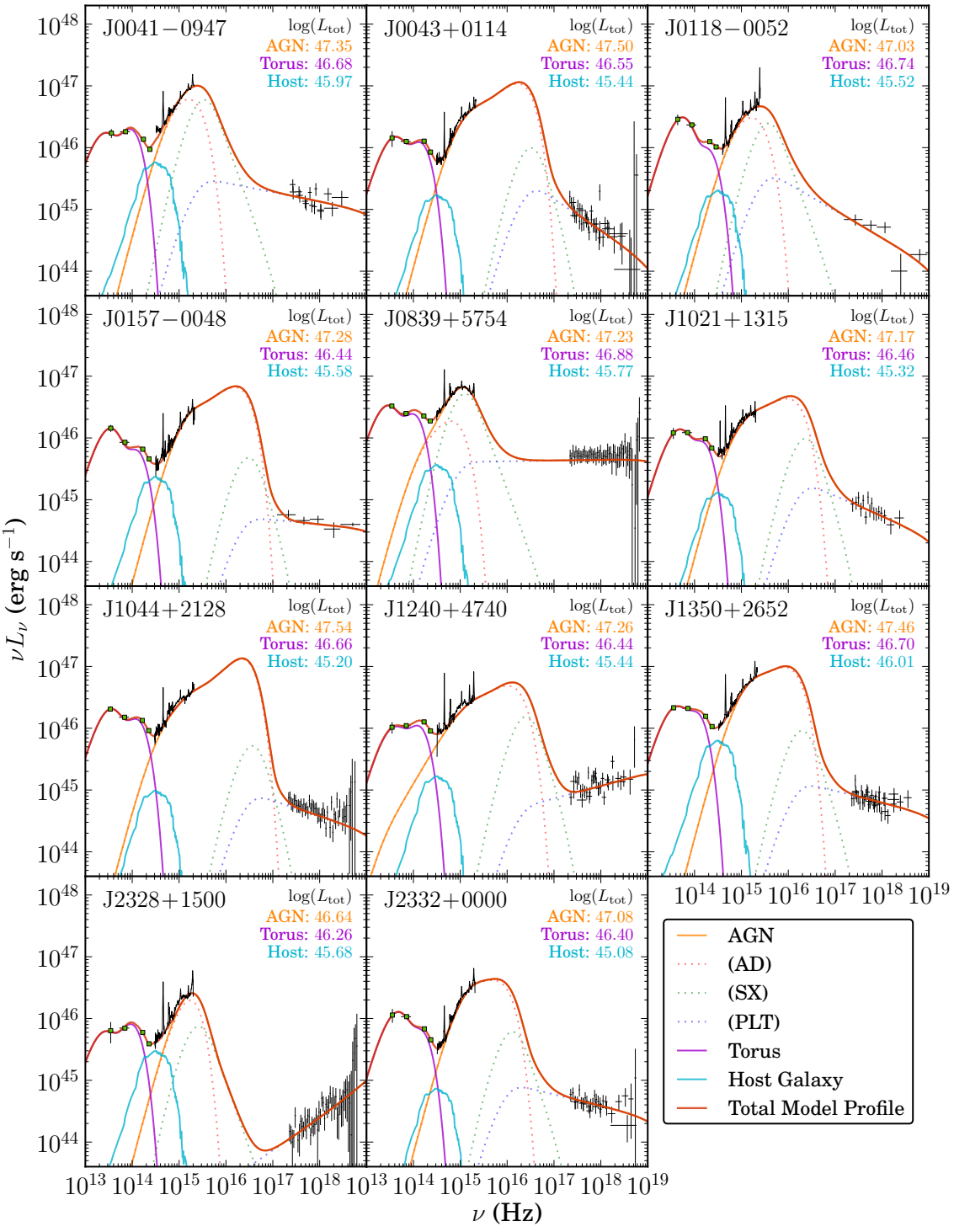

Figure 4.6: The full MIR to X-ray SEDs for the sample. The green squares show the *WISE* photometry data, and the optical–IR and X-ray data are once again shown in black. The orange, light blue and purple curves show the contributions from the AGN, host galaxy and dusty torus components respectively. The torus comprises two blackbody components, and the host galaxy is a 5 Gyr elliptical template.

4.4 Variability

In Chapter 3, I briefly discussed the possible causes of variability in the AGN sample. Since the multiwavelength data are collected non-contemporaneously, it is important to look for evidence of variability between optical and IR observations. I only identified such evidence in J0041−0947. In this case, for the SED fitting, I normalised the IR spectrum to the level of the optical spectrum. I also presented all available optical spectra from SDSS/BOSS, as five objects in the sample had optical spectra taken on multiple epochs. Comparing these spectra, there appears to be some small ($\sim$ 20 per cent) variability in three of the objects observed more than once.

I examined the possible cause of these variations using the SED model. There are few specific AGN properties that can change on timescales of a few years; $M_{\rm BH}$ and spin are fixed and changes in the mass accretion rate ought to be physically limited by the viscous timescale – the characteristic timescale for the mass flow. This timescale for the BH masses in the sample is likely to be of the order of hundreds of years even in the innermost regions of the AD (Czerny 2004), although AGN variability is frequently noted that occurs faster than the viscous timescale and is apparently intrinsic. This could be due to reprocessing of SX emission in the AD, as PLT emission is generally too weak to have a significant effect in most of the objects (Gardner & Done 2015). The intrinsic reddening I model could change if the extinguishing dust is 'clumpy' in nature, as thought to be the case for the torus, thus presenting a constantly changing $E(B-V)_{\rm int}$ parameter.

In order to explore the effects of changing the obscuration, I take the best-fitting SEDs, and attempt to fit other epochs of data by adjusting only the $E(B-V)_{\rm int}$ parameter. In Fig. 4.7, I show two examples of the variable AGN, together with models that result from changing the $E(B-V)_{\rm int}$ parameter. To first order I find that the variability observed between observations could be attributed to changing extinction (see Fig. 4.7) but the optical spectrum alone covers too short a wavelength range to test this hypothesis effectively – there are often only 2–3 emission free regions in the optical spectra to which the SED model is fitted. A stronger test of the changing properties that are responsible

for such variability would require simultaneous optical–IR data from multiple epochs, as this would provide the data coverage required to model the AD robustly. It may be that changes in the accretion rate must also be considered to fully parameterise spectral variability. All such tests also require accurate flux calibration; uncertainties in the SDSS flux calibration and variable atmospheric observing conditions, may also contribute to observed apparent variability.

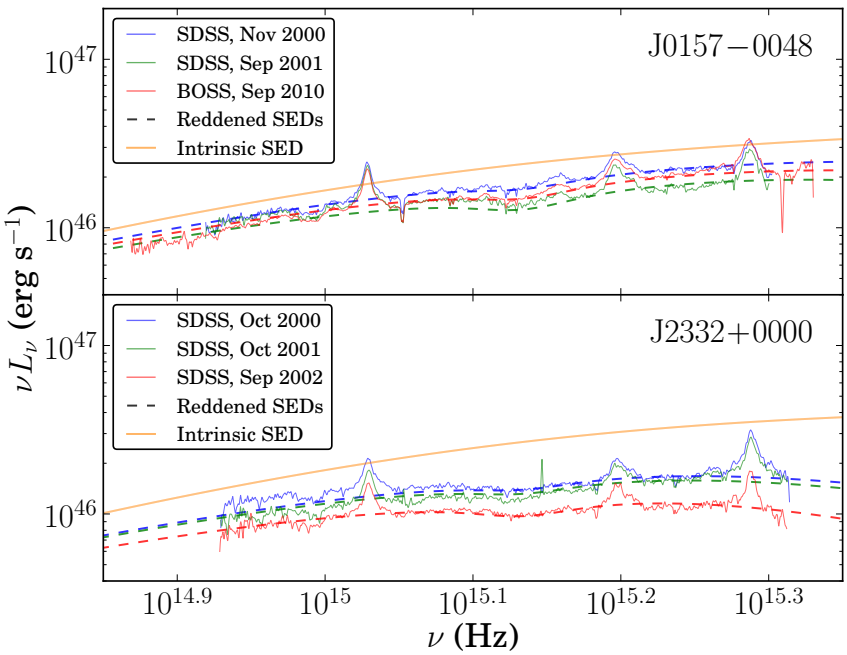

Figure 4.7: Examples of the 'variable' objects in the sample. Five objects were observed on multiple occasions in the optical by SDSS/BOSS, and of these, three showed some evidence for variability. Modelling this as an effect of changing extinction produces a first order correction for this variability. The intrinsic SED therefore does not change between observations, but the observed SED does change. In these two examples, I show the data from each different epoch in different colours (with the same colour scheme as in Appendix A.2), and the attenuated model as a correspondingly coloured dashed line. The difference in $E(B-V)_{\rm int}$ between Oct 2000 and Sep 2002 in J2332+0000 is 0.043 mag. All spectra have been corrected for Galactic extinction.

4.5 Spectral Decomposition

My physically motivated model of the underlying AGN continuum now enables a complete analysis of the optical–IR spectrum, including the contribution from the BLR. The BLR is thought to lie between the AD and torus (e.g. Antonucci 1993, Czerny et al. 2015), with electron transitions in partially-ionised gas giving rise to many emission features that are Doppler-broadened by the rapid orbit of this gas around the BH. Although this AGN sample is too small to improve on the emission line correlations extensively studied by e.g. Shen & Liu (2012), Denney et al. (2013) and Karouzos et al. (2015), since such studies invariably use power-law continuum models, it is desirable to have a better understanding of the true continuum, especially as this continuum forms the basis of many virial $M_{\rm BH}$ estimators. In particular, the Balmer continuum lies underneath the Mg II feature, but due to additional contamination by Fe II, this can be difficult to deconvolve, particularly when considering only a limited wavelength range on either side of Mg II.

The spectral model includes components for the isolated emission lines, and a 'pseudo-continuum' which includes blended line emission as well as true continuum contributions.

The emission lines are modelled as superpositions of Gaussians. I use the following components for the emission lines:

i. Hα is fitted with two broad components (or one broad, and one 'intermediate'). As in Chapter 3, for objects that show strong narrow [O III], I include a third, narrow Gaussian component, locked in velocity width and wavelength to the strong, narrow [O III] member.

ii. Hβ is fitted with an equivalent profile to Hα, with only the normalisation as a free parameter.

iii. [O III] is a doublet. I fit each member with two Gaussians, or one Gaussian for objects showing particularly weak [O III] emission (J0043+0114, J0157−0048, J1021+1315, J1044+2128 and J1240+4740).

iv. Hγ is fitted in the same manner as Hβ.

v. Mg II, C III], C IV and Ly-α are modelled with two broad Gaussian components each. I do not include narrow components for these lines as in general there is no

statistical justification for a third component. Ly-α is only covered in J0118−0052. I do not attach a physical significance to the two components in any of these lines. For instance, Mg II is a doublet, but it is not modelled as such, as the line splitting is too small to be significant.

vi. He I λ5876, Hδ λ4102, [Ne III] λ3869, [O II] λ3729, [Ne IV] λ2422, C II] λ2326, Al III λ1855, He II λ1640, Si IV λ1394 (may include O IV]) and O I λ1305 (may include Si II) are all modelled for completeness with a single Gaussian component, though most are very faint in the spectra, so I freeze their wavelengths to literature values (Vanden Berk et al. 2001).

The pseudo-continuum is composed of the following components:

i. **OPTXAGNF continuum**: I use the model constructed in Section 4.3, as it incorporates the host galaxy and dust components. An exception is J0041−0947, for which I adopt the model with a BH spin parameter of $a_* = 0.9$. As noted in Section 4.2, this is the one object in the sample where I see a significant improvement in the continuum fit when I introduce a spinning BH ($\chi_{\rm red} = 4.16,\ 0.92$ for $a_* = 0,\ 0.9$). I allow some freedom in the normalisation; if the continuum regions chosen for SED model-fitting are marginally contaminated by an emission component, the true continuum could be below that I calculate.

ii. **Balmer continuum**: I employ the Grandi (1982) model of the Balmer continuum, see equation 2.4.1. I convolve this model with a Gaussian to account for Doppler-broadening associated with intrinsic velocity dispersion in the hydrogen emitting gas.

iii. **Blended Fe II emission**: To model the ubiquitous, blended permitted Fe II emission seen throughout the optical–IR AGN spectrum, I use two empirical and one theoretical templates, derived from the Type I AGN I Zwicky 1. These templates are described in Véron-Cetty et al. (2004), Vestergaard & Wilkes (2001) and Verner et al. (2009), see Section 2.4.5 for more information. The templates are convolved with a Gaussian to incorporate velocity broadening, and normalised independently in the optical and UV.

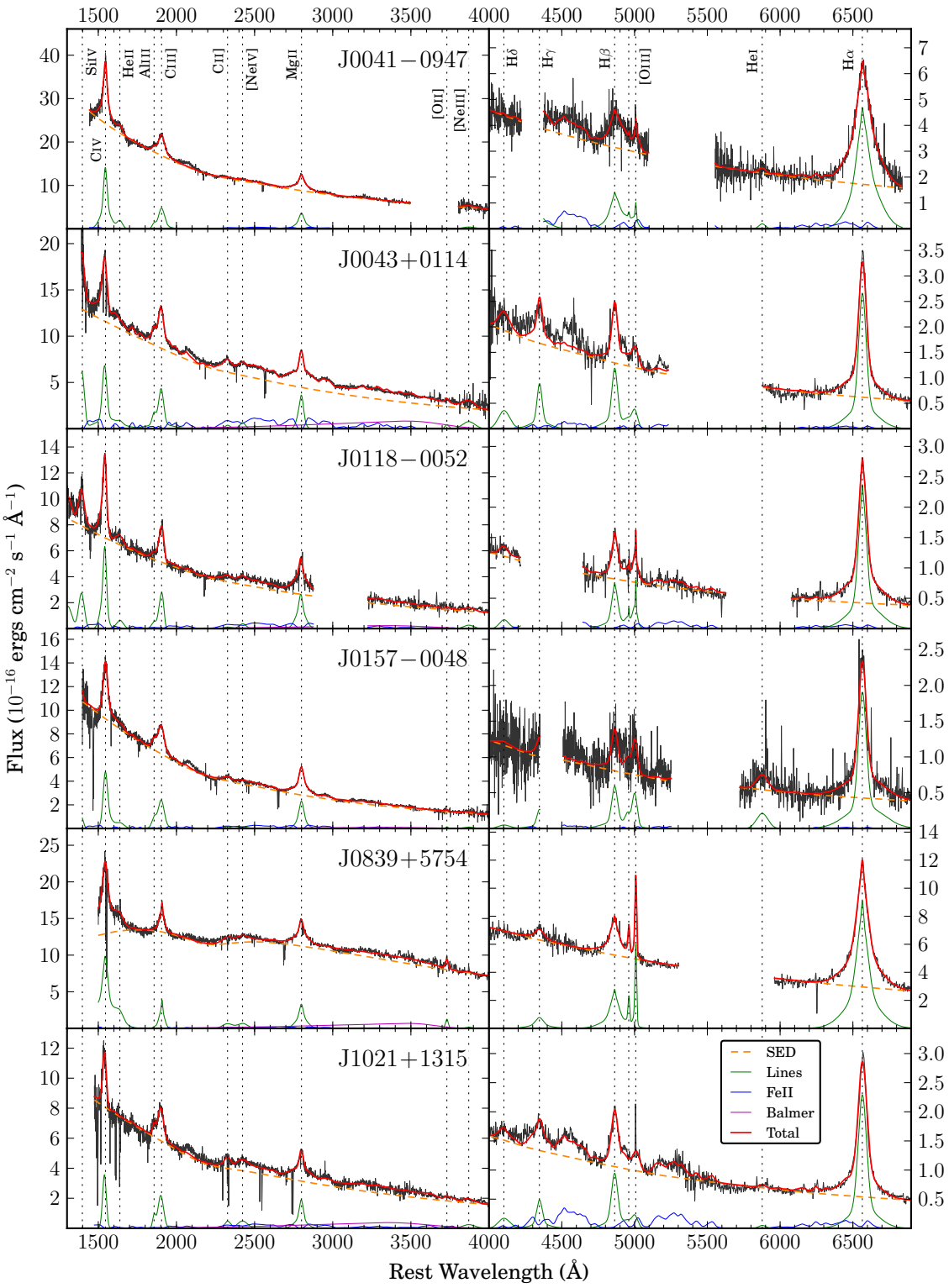

Figure 4.8: IR–optical spectral decomposition using the SED model together with models of the Balmer continuum, blended Fe II emission, and emission lines. Line identifications are shown in the top panels. The right panels are magnified to more clearly show the Balmer region.

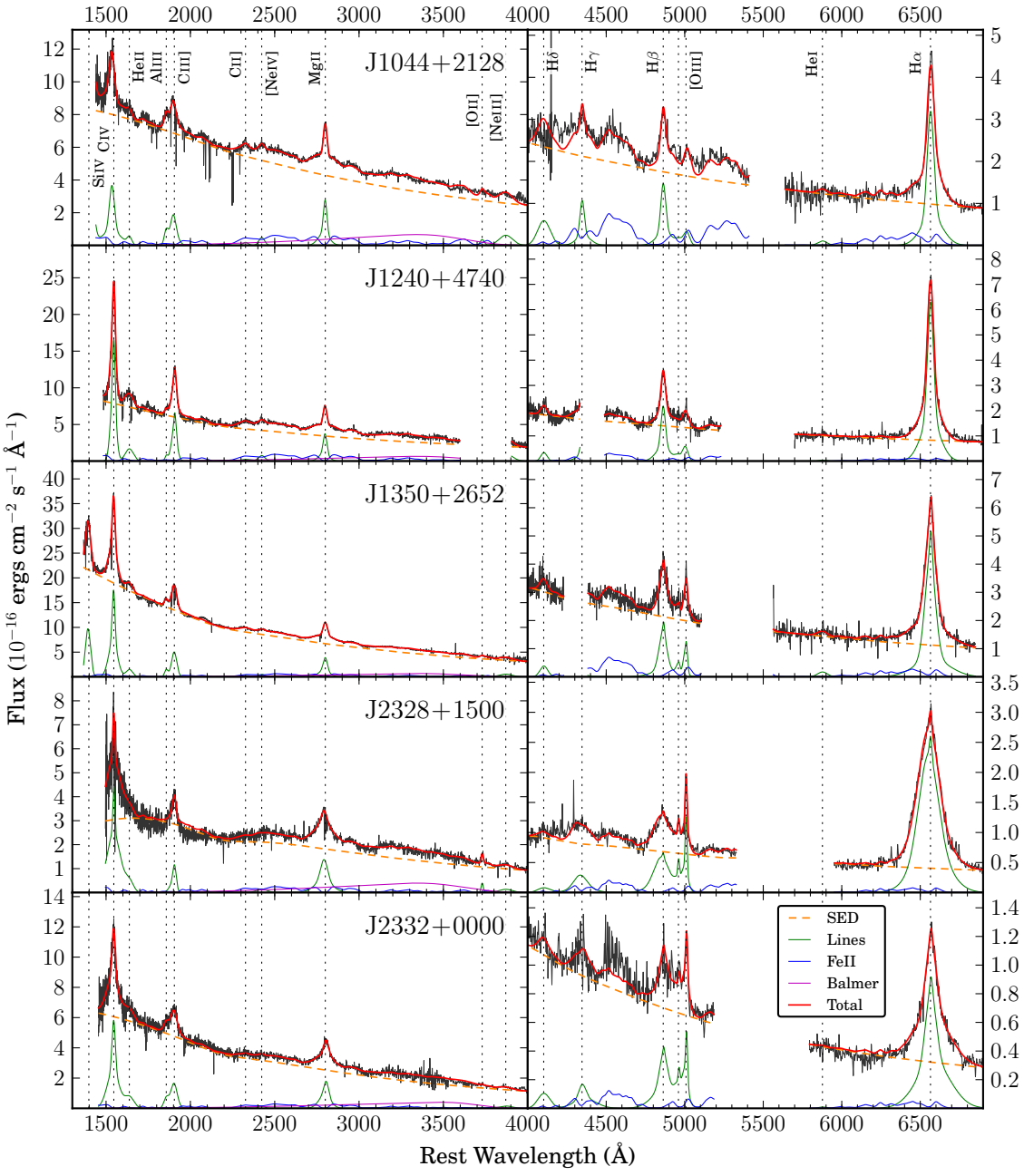

Figure 4.8 (cont.)

After fitting the pseudo-continuum, I then fit the emission lines systematically. All fitting is performed by custom PYTHON scripts, using the Levenberg-Marquardt algorithm provided in the LMFIT package. To estimate measurement errors, I use a Monte Carlo method, where 100 different realisations of the spectra are created using the mean (measured) flux density and standard error at each pixel, and refitting the model from scratch. The central 68 per cent of the resulting value distribution for any given property then provides an estimation of the measurement error. In these 'mock' spectra, the artificial 'noise' is added to already noisy spectra, but to an approximation, this method gives a good representation of the true errors.

I show the model fits resulting from my spectral analysis in Fig. 4.8.

4.6 Discussion

4.6.1 SED Model Properties

The data are well described by the physically-motivated SED continuum and emission line models I have built. The SED models of Chapter 3 are refined in Section 4.2.2 by improving the treatment of intrinsic reddening. I first discuss the properties of these models, and compare them to similar studies. There is an anti-correlation between $M_{\rm BH}$ and $\dot{m}$ (Fig. 4.9), likely because the sample is selected from a small redshift range, are of similar flux, and are therefore of comparable luminosity. Previous work, such as Vasudevan & Fabian (2007), Davis & Laor (2011), Jin et al. (2012c) have suggested that it is $\dot{m}$ that more strongly governs the SED properties, including the X-ray photon index and BCs.

I show a comparison of my models with those of Jin et al. (2012a) for the $\dot{m}$–Γ relationship in Fig. 4.10. Due to the small size of the sample, there is a large uncertainty on the slope of this relationship, but it shows a correlation which is in agreement with that presented in Shemmer et al. (2008), Zhou & Zhao (2010) and Jin et al. (2012a). This relation provides an important additional means by which $\dot{m}$ may be estimated in AGN. It is believed that in highly accreting sources the increased disc emission induces more efficient Compton cooling of the corona (e.g. Bian 2005). These relations show some degree of scatter however, likely arising from uncertainties on estimates of $M_{\rm BH}$, the optical depth of the corona, orientation or spin (Shemmer et al. 2008).

A large spread in the BCs is seen in the sample (Table 4.3), as also mentioned in

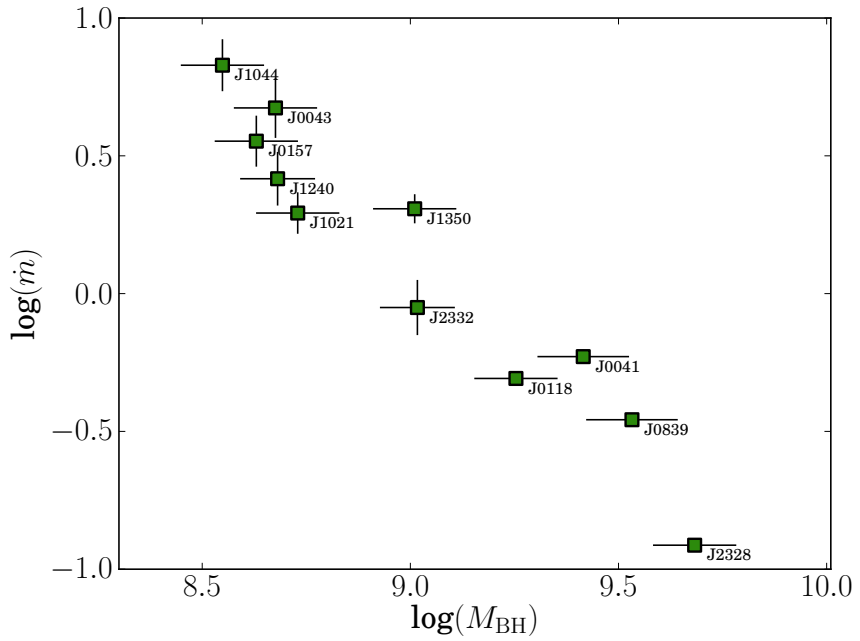

Figure 4.9: Dependence of $\dot{m}$ on $M_{\rm BH}$. This highlights selection effects for the sample.

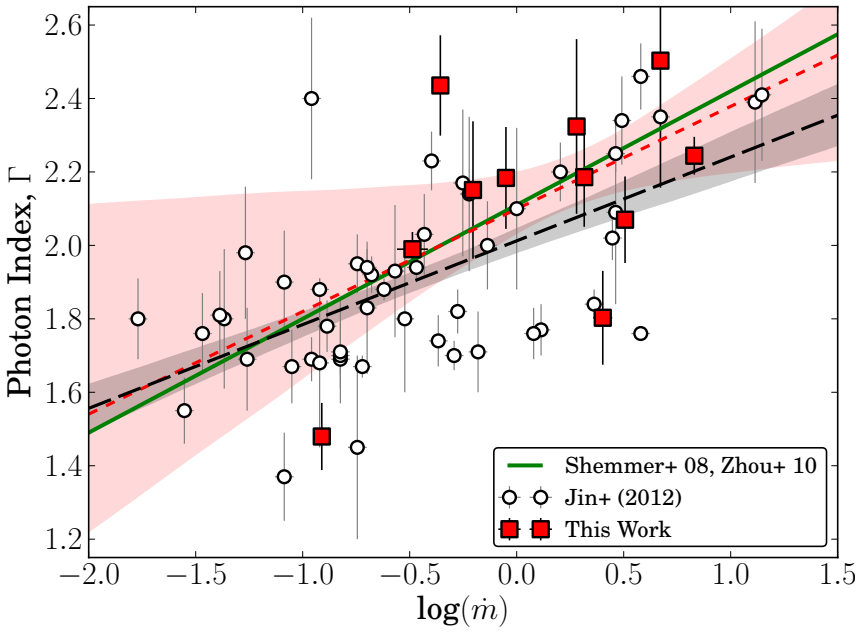

Figure 4.10: The photon index (Γ) against Eddington ratio in the sample, overplotted on the Jin et al. (2012) sample. My best-fit relation is shown by the red dashed line and shaded region, and the Jin et al. (2012a) relation is shown by the long-dashed black line and shaded grey region. I also show the relation derived in Shemmer et al. (2008) and Zhou et al. (2010).

Chapter 3. Early work used fixed values for these coefficients (e.g. Elvis et al. 1994, Richards et al. 2006), which is clearly at odds with the range I have measured. However, there is mounting evidence that BCs are dependent on AGN luminosity, and by extension $\dot{m}$ (Trakhtenbrot & Netzer 2012). Moreover, the Elvis et al. (1994) SED templates included the IR torus bump in $L_{\rm bol}$, and therefore 'double-counted' some of the emission from the AGN (Marconi et al. 2004). I present the BCs against $\dot{m}$ in Fig. 4.11, confirming the trends previously observed by e.g. Vasudevan & Fabian (2009), Jin et al. (2012c) and Castelló-Mor et al. (2016). I have overplotted the results of Vasudevan & Fabian (2009) and Jin et al. (2012c) for direct comparison.

Jin et al. (2012c) also used OPTXAGNF, applied to a low redshift ($z < 0.3$) sample. Vasudevan & Fabian (2009) used a simpler AD+PLT model. As the samples were all selected by different means, there may be differing sample selection effects. For instance, I required objects bright enough to yield an X-ray spectrum, Jin et al. (2012c) imposed X-ray quality cuts (see Jin et al. 2012a), and Vasudevan & Fabian (2009) drew their sample from the Peterson et al. (2004) sample – an RM study of optically bright AGN.

In the top two panels of Fig. 4.11, my BC values for $\kappa_{5100\text{Å}}$ and $\kappa_{2500\text{Å}}$ show strong correlation with $\dot{m}$. This alone suggests that $L_{\rm bol}$ can be constrained with an estimate of $M_{\rm BH}$ and a measurement of the (dereddened) continuum luminosity. In particular, my sample correlations are much stronger than those of Jin et al. (2012c), especially for $\kappa_{2500\text{Å}}$, likely because of the smaller fractional contribution of the host galaxy to the SED. However, my values for both coefficients lie below the majority of the Jin et al. (2012c) sample. As these are calculated from luminosity measurements that are AD dominated, the likely reason for this is the different average $M_{\rm BH}$ of the two samples. The Jin et al. (2012c) sample contains AGN with a lower average $M_{\rm BH}$; notably, many of the highest $\dot{m}$ AGN in their sample were the narrow-line Seyfert 1 galaxies, with masses of $10^6 - 10^8 M_\odot$. The highest $\dot{m}$ AGN in my sample are $\sim 1-2$ dex more massive, so a single AD continuum luminosity measurement samples a different part of the AD SED in my AGN, compared to theirs. My BCs sample continuum regions closer to the AD peak, and are therefore smaller on average than those calculated by Jin et al. (2012c). This is illustrated in Davis & Laor (2011), their Fig. 1.

In the bottom panel of Fig. 4.11, my results for $\kappa_{2-10\text{keV}}$ are more consistent with those of Jin et al. (2012c) and Vasudevan & Fabian (2009), suggesting that this coefficient depends less on effects such as $M_{\rm BH}$, as might be expected from the argument above –

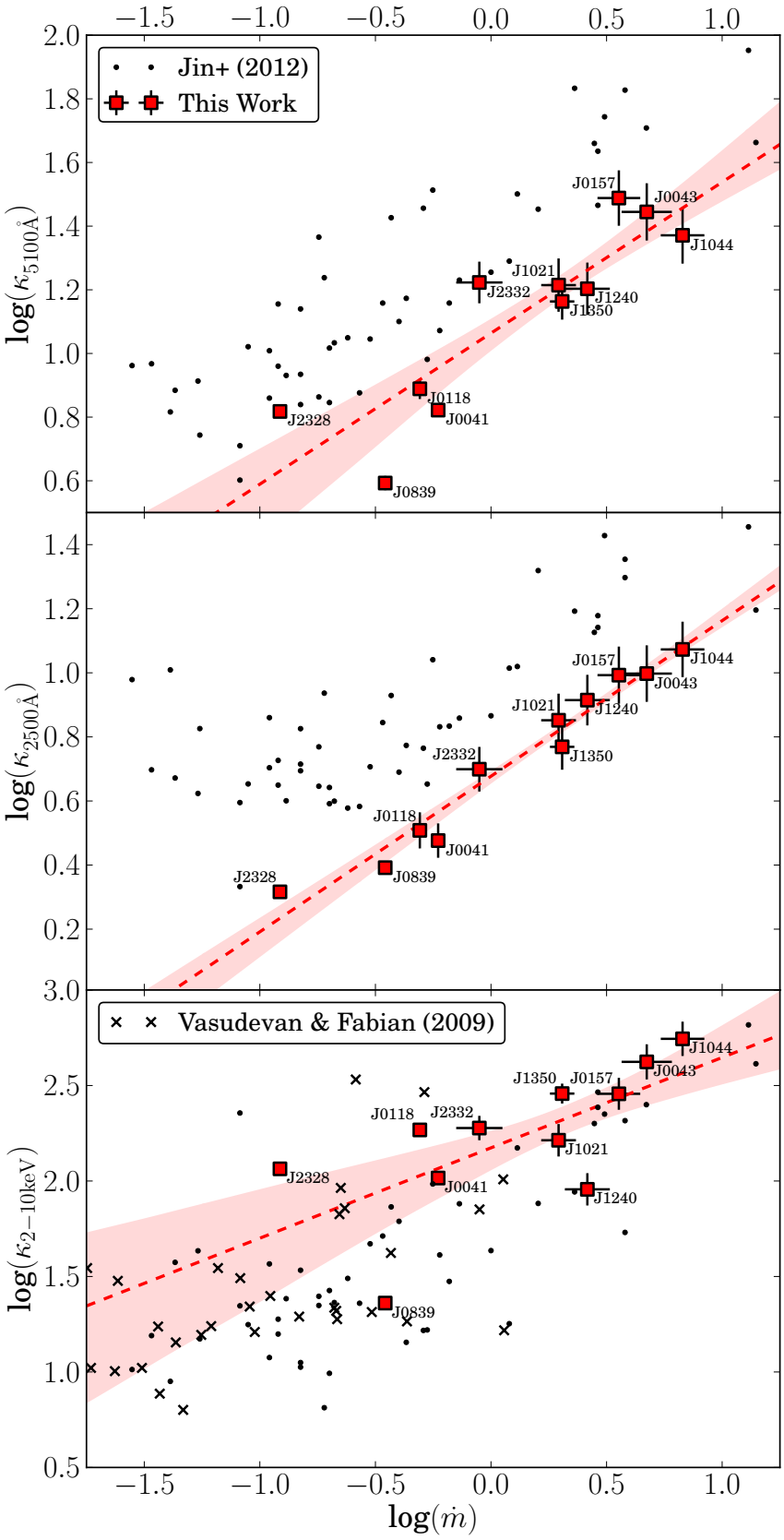

Figure 4.11: Dependence of various BC factors on $\dot{m}$.

$M_{\rm BH}$ does not influence the X-ray spectrum as much as the AD.

In summary, I suggest that UV BCs in AGN are dependent on both $M_{\rm BH}$ and $\dot{m}$, and applying relations calibrated for $\sim 10^7 M_\odot$ AGN to those with $\sim 10^9 M_\odot$ BHs could introduce systematic uncertainties. This may be complicated further by model-dependencies such as a_*, since $L_{\rm bol} = \eta \dot{M} c^2$, where the mass–energy efficiency, η, varies with a_*. X-ray BCs do not appear susceptible to this effect.

Further exploration of the correlations between SED properties and BCs will be possible with a larger AGN sample, which I define in Chapter 5.

4.6.2 SED Model Testing

Intrinsic reddening

The SED model depends on the adopted models for intrinsic extinction in the AGN, and I showed in Section 4.2.2 that MW, LMC and SMC extinction curves are adequate to model the intrinsic extinction in this sample of 11 objects.

An alternative approach is to calculate customised extinction curves, as adopted by Zafar et al. (2015) – see Section 4.1.2. However, an assumption in that work is that the intrinsic SED of all AGN in the sample can be described by a simple power-law of constant slope. Whilst a power-law well-describes the optical–IR continuum emission for many AGN, the true continuum is more accurately described by the AD, which has a predicted turnover in energy corresponding to the temperature of gas orbiting the BH close to $r_{\rm isco}$, dependent on $M_{\rm BH}$, $\dot{m}$ and a_* (e.g. Hubeny et al. 2000, Davis et al. 2007). In Chapter 3, I found that around half of the objects in the sample had optical spectra at or very near this SED peak. Additionally, I have found evidence for a change in power-law slope in 8 of 11 objects, consistent with the observations sampling the outer edge of the AD. For these reasons, I cannot make assumptions about the intrinsic SED shape *a priori*. As the intrinsic extinction in each of the objects is small – $E(B-V)_{\rm int} < 0.1$ mag in all but one case – I am justified in my approach of using MW, LMC and SMC curves.

This extension to Model 3 presented in Chapter 3 is logical, as I identified in Chapter 3 that whilst J1350+2652, for instance, showed evidence for a 2200 Å feature that was better fit by a MW reddening curve (a similar finding is shown in Capellupo et al. 2015, their Fig. 7), J1044+2128 showed a significant improvement in extinction correction using an SMC curve.

Uncertainties on the black hole mass

I have shown that in models of this kind, $M_{\rm BH}$ uncertainties of ~ 0.1 dex lead to a ~ 0.1 dex uncertainty in $L_{\rm bol}$. In objects with well-sampled SED peaks, the difference is much smaller, as other parameters are adjusted to maintain the fit. This is perhaps clearest in J0839+5754, but also J0041−0947 and J0118−0052, which show only small changes in $L_{\rm bol}$, despite a ~ 0.4 dex change in $M_{\rm BH}$ from largest to smallest values. However, I caution that in J2328+1500 the optimal solution shows some degeneracy between $\dot{m}$ and the intrinsic reddening as defined by $E(B-V)_{\rm int}$, with the latter property converging to different minima when fitting the $\pm 2\sigma$ $M_{\rm BH}$ models. This may be expected in this object, as it shows the highest intrinsic reddening value (see Table 4.2) of the sample, and therefore I suggest that for reddening of $E(B-V)_{\rm int} \gtrsim 0.1$ mag, the uncertainties in estimates of $L_{\rm bol}$ become greater (a combined error due to $M_{\rm BH}$ and $E(B-V)_{\rm int}$ of ~ 0.3 dex in this case).

The $M_{\rm BH}$ estimates were specifically derived from the profile of Hα as there is excellent S/N, and it shows strong correlation with Hβ, and hence reverberation studies (Greene & Ho 2005). Assuming that the two main sources of uncertainty on $M_{\rm BH}$ are (a) the dispersion on the relation with Hβ and (b) the measurement error may be optimistic (Park et al. 2012 estimates that the uncertainty in the BLR size-luminosity relation and virial coefficient contribute to a total uncertainty on such estimates of ~ 0.46 dex), but I wished to test how such uncertainties would affect the calculation of the SED model, and corresponding properties. Castelló-Mor et al. (2016) used RM $M_{\rm BH}$ estimates for their samples of super- and sub-Eddington AGN, but estimated the uncertainty on these estimates to still be a factor of ~ 3, comparable to the single-epoch method.

To test the impact of a more significant $\sim \pm 0.5$ dex (or approximately 5σ) change in $M_{\rm BH}$ on $L_{\rm bol}$, I produced further models with $M_{\rm BH}$ set at $\pm 5\sigma$ from the mean – see Fig. 4.12. The resulting range of $L_{\rm bol}$ is large, but generally smaller than that of $M_{\rm BH}$ because in most of the AGN, adjustment of other parameters in the $M_{\rm BH} \pm 5\sigma$ models leads to a smaller uncertainty in $L_{\rm bol}$. However, this does yield models that are often a poorer description of the data. Additionally, given the extreme and unphysically high accretion rates that are required for some of the -5σ models, the thin AD assumption would be unlikely to apply.

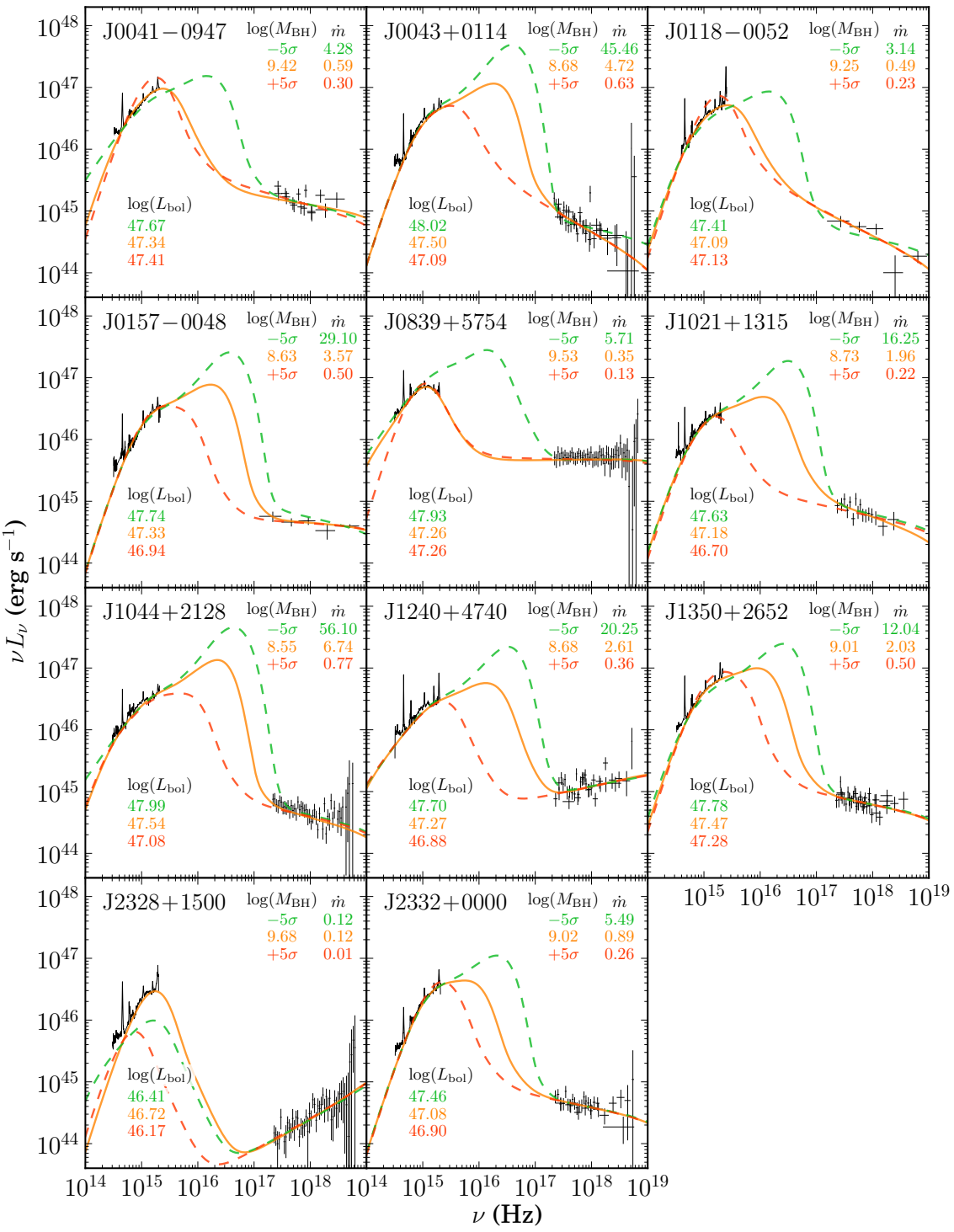

Figure 4.12: The SEDs for the sample, showing model variance with significant (~ 0.5 dex) changes to $M_{\rm BH}$. The figure is analogous to Fig. 4.2, but with larger $M_{\rm BH}$ variations from the mean value. These represent more plausible total uncertainties on $M_{\rm BH}$, but in many cases the models shown as dashed lines are much poorer descriptions of the data than the model with the mean value of $M_{\rm BH}$ (solid orange curve). In three cases the difference between the $M_{\rm BH} \pm 5\sigma$ models (constituting a total range in $M_{\rm BH}$ of around an order of magnitude) propagates to a 1 dex spread on $L_{\rm bol}$, but in all other cases this is smaller – around 0.5 dex for five of the AGN.

Black hole spin

Changing the BH spin has a similar effect to lowering $M_{\rm BH}$ – both increase the peak temperature of the AD gas, and shift the SED peak to higher frequencies. A low-spin BH, $a_* \leqslant 0.5$ does not have a large impact on the SED, and in J0839+5754, which has a well-sampled SED peak, minor adjustments of the other free parameters allow the spin change to be incorporated into the model with a negligible effect on $L_{\rm bol}$. Other objects show an increase in $L_{\rm bol}$ of typically ~ 0.1 dex, owing to the bluer SED peak. As spin is increased to $a_* = 0.8$ and 0.9, the peak is shifted to the FUV range in all but J2328+1500, where $E(B-V)_{\rm int}$ is reduced, lowering $\dot{m}$ and thus keeping the peak position at approximately the same frequency. For the other objects, the total SED energy increases by a factor of two or more, increasing the amount of energy to emerge in the Comptonised components (SX and PLT). Therefore as the spin increases, this results in a decrease in the value of the intrinsic reddening $E(B-V)_{\rm int}$, and an increase in $N_{\rm H,int}$. The lower reddening lowers the intrinsic energy at optical–IR wavelengths, and the greater $N_{\rm H,int}$ increases the Compton upscattered energy budget. In most cases, this produces a poorer fit to the data, but this is not true for all objects in the sample; J0041−0947, J1350+2652 and J2328+1500 show improved fitting statistics for the $a_* = 0.9$ model versus the $a_* = 0$ model. However, in J1350+2652 and J2328+1500 this effect is very small, with both of these models producing good ($\chi^2_{\rm red} < 2$) fits to the data.

I briefly considered the likelihoods of various models, by comparing the gas-to-dust ratio, characterised by $N_{\rm H}$ to $E(B-V)_{\rm int}$, calculated in my objects with those observed in the MW. Güver & Özel (2009) put this relationship at a value of $N_{\rm H,int}/E(B-V)_{\rm int} = 6.9 \times 10^{21}$ cm^{-2} mag^{-1}, assuming $R(V) = 3.1$. Different sightlines though obscuring material may produce different ratios, which is the reason I do not tie these properties to the MW ratio, but as a general rule, one would not expect to infer a very high column density of $N_{\rm H,int}$ without an accompanying extinction effect. Unfortunately, limitations in the S/N of the X-ray spectra mean that $N_{\rm H,int}$ has large uncertainties in all objects, and as such I find that statistically, I am unable to favour/reject any of the models by this means.

For the $a_* = 0.9$ model, J0041−0947, J0043+0114, J1240+4740, J1350+2652, J2328+1500 and J2332+0000 all show good fits ($\chi^2_{\rm red} < 3$). Degeneracies in model parameters make drawing strong conclusions about spin values difficult, but it appears

that the highest spin states, $a_* = 0.99$ and above, are ruled out for every object except J2328+1500 in the sample, using OPTXAGNF.

A limitation in my study is that I do not consider the effect of AD inclination in the models. The OPTXAGNF model assumes a constant inclination, θ, of 60° to face-on, and geometric consideration of orientation dictates that a factor of 2 greater flux would be observed if the AD was at $\theta = 0°$. Larger inclinations than 60° are thought to be less likely, as at some point the coaxial torus would obscure the AD. The effect of this on the SED peak frequency will be small, making this property extremely difficult to robustly constrain and practically, other sources of uncertainty discussed in this chapter dominate the uncertainty on $L_{\rm bol}$.

The disc inclination becomes significant in the case of a highly spinning BH. Here, relativistic effects arising from the differential line-of-sight gas motion at different inclinations must be accounted for, as the simple trigonometric treatment of inclination is insufficient. It is therefore necessary to convolve a relativistic smearing kernel with the AD spectrum at each radius. This formed the basis of the model presented in Done et al. (2013) that includes such relativistic treatment of the AD inclination – OPTXCONV.

In Fig. 4.13, I compare models of OPTXAGNF (no relativistic convolution) with OPTXCONV (which includes the relativistic convolution) at high to maximal spin values. I normalise all models at a frequency of 10^{15} Hz (3000 Å), as data constrains this part of the model, and they must all therefore pass through the same point. I show two different inclinations for OPTXCONV, $\theta = 0°$ and 60°, as the difference between the two models is strongest in the case of a face-on disc. Due to this discrepancy in energy, it is possible that more of the objects could be compatible with high spin ($a_* \geqslant 0.99$) values than I concluded in Section 4.2.4.

Therefore, I reproduced the high spin models described in Section 4.2.4 using OPTXCONV at inclinations of both 0° and 60°. I tested spin values of $a_* = 0.99$ and 0.998, as both scenarios were ruled out in most objects when using OPTXAGNF. I found that OPTXCONV delivers similar models to OPTXAGNF when the inclination was fixed at 60°; either a good fit to the data is not achieved, or the SED energy is dominated by the SX and PLT, in spite of the high accretion rates. This is counter to what is observed at lower redshifts (Jin et al. 2012a), in which high accretion rate objects are generally AD dominated.

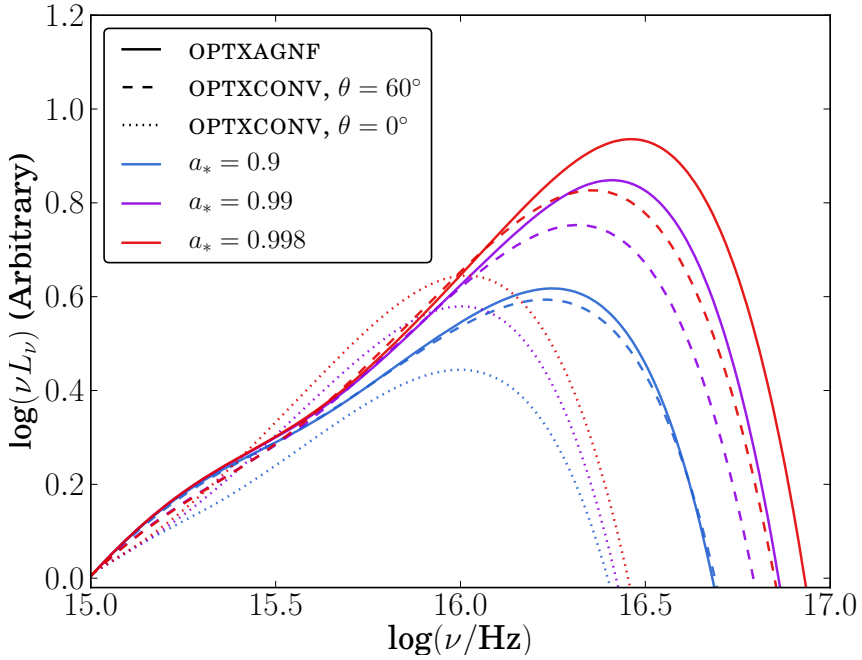

Figure 4.13: Comparison of OPTXAGNF with OPTXCONV for high to maximal spin BHs. OPTXCONV includes relativistic effects that are neglected in OPTXAGNF.

In the face-on case ($\theta = 0°$), however, good fits to the data are obtained in 10/11 AGN (J1044+2128 is the exception), even for $a_* = 0.998$. Four of these AGN still require a dominant SX and PLT, however. I therefore highlight that models including full relativistic treatment of the disc inclination should be used to model highly-spinning BHs, as the difference in energy can be significant. However, as I have already noted some sources of potential degeneracy between parameters in the models, it is unlikely that a strong constraint can be put on the AD inclination by SED modelling alone. Using this method to accurately measure the accretion rate, spin, inclination and intrinsic reddening values would require exceptional data coverage and quality. Despite these uncertainties, the measurements of L_{bol} are more accurate than those in other studies that lack X-ray spectra, in addition to optical–IR spectra (Capellupo et al. 2015, Castelló-Mor et al. 2016).

So, do my results support a 'spin-up' picture of BH evolution? If BHs grow via prolonged anisotropic accretion episodes and mergers with other BHs, their spin values would be expected to increase over cosmic time, such that the most massive BHs have the highest spins (e.g. Dotti et al. 2013, Volonteri et al. 2013). The counter argument is that randomly oriented accretion episodes would result in a_* approaching zero for massive AGN (e.g. King et al. 2008). Using the results from OPTXAGNF, I conclude that my results

are at least consistent with the spin-up scenario, with two of the three most massive objects either not rejecting the higher spin models (J2328+1500 at $a_* = 0.99$), or showing an improvement over zero spin (J0041−0947 at $a_* = 0.9$). However, using the more realistic OPTXCONV model, this finding is less certain. I can still conclude that the most massive AGN in the sample are all compatible with hosting highly spinning BHs, whereas the least massive (J1044+2128) is not, but reiterate that there are several sources of degeneracy in the models.

Radial extent of accretion disc

I find that in the eight AGN where constraints are placed on $r_{\rm out}$ with the model, there is a strong correlation with $r_{\rm sg}$, but offset from unity, see Fig. 4.5. It is not known whether self-gravity is the condition under which the disc breaks up, but my findings suggest that $r_{\rm out}$ could be related to $r_{\rm sg}$, but is smaller by a factor ~ 5, in most or all cases.

This result differs from that in Hao et al. (2010), who study the optical–IR SEDs of a sample of 'hot-dust-poor' AGN. In a quarter of their sample, weak host galaxy contribution enables measurement of the outer AD radii, which are found to be larger than $r_{\rm sg}$. This could suggest a difference in the AD in these objects that may or may not be related to their weak dust contributions. Alternatively, it could be a result of poorer data coverage – they use photometry for their SED fits – or degeneracy with dust blackbody components, but there is a need for greater understanding of AD physics to unify these observables.

For this test, I kept the spin fixed at zero, so this result is model dependent. An alternative interpretation is that the value of α is less than 0.1. However, it would need to be 3 orders of magnitude smaller to account for the difference observed, if indeed self-gravity is the factor limiting AD size.

4.6.3 Torus and Host

The mean temperatures for the two blackbody components that model the torus are; $\langle T_{\rm hot} \rangle = 1470 \pm 90$ K and $\langle T_{\rm warm} \rangle = 430 \pm 30$ K. The warm component is generally poorly constrained by only two *WISE* photometry points, and shows large errors on $T_{\rm warm}$. The mean covering factors are $\langle C_{\rm hot} \rangle = 11 \pm 2$ per cent and $\langle C_{\rm warm} \rangle = 14 \pm 3$ per cent.

Landt et al. (2011) obtain values of $\langle T_{\rm hot} \rangle = 1365 \pm 18$ and $\langle C_{\rm hot} \rangle = 7 \pm 2$ per cent. Their sample had NIR spectra from the NASA IR Telescope Facility's SpeX spectrograph, and as such the data were of significantly higher quality than was available for this work, for which the torus components were only constrained by *WISE* photometry. Their sample was also at much lower redshift ($z \leqslant 0.3$), and accordingly was brighter, offering better S/N. Nevertheless, my results are consistent to within 2σ.

As discussed in Landt et al. (2011), the $T_{\rm hot}$ values calculated are close to the silicate dust grain sublimation temperature. This may suggest the grains were formed in an oxygen-rich environment. Evidence is seen for a spread in $T_{\rm hot}$ values, which is likely to be a feature of the limited quality of the data, although Landt et al. (2011) note that in NGC 5548 there is a higher measured dust temperature than other objects in their sample.

Mor & Trakhtenbrot (2011) found their distribution of hot dust covering factor values peaked at ~ 13 per cent, in a sample of 15,000 SDSS AGN, fitting *WISE* photometry of similar quality to my sample. This is slightly higher than the Landt et al. (2011) result, but is consistent with my result, which lies between the Landt et al. (2011) and Mor & Trakhtenbrot (2011) values.

Finally, Roseboom et al. (2013) found a broad distribution of covering factors, of generally higher values than those measured in this work, Landt et al. (2011) and Mor & Trakhtenbrot (2011). They fitted the AGN component using the Elvis et al. (1994) SED templates, rather than the physically motivated model employed for this analysis, and this may lead them to underestimate the AGN luminosity, and predict higher covering factors.

To assess whether the host galaxy properties I predict concur with other research of AGN and their hosts, I compare the galaxy luminosities calculated with earlier work. From the fitted host galaxy model, I measure the luminosity in the V, R and K bands, comparing these to those presented in Marconi & Hunt (2003), Peng et al. (2006) and McConnell & Ma (2013). The luminosities are measured using a 'synthetic photometry' technique, by integrating the host galaxy template over each respective bandpass.

I have compared the host galaxy bulge luminosities and $M_{\rm BH}$ estimates for my sample with earlier work in Fig. 4.14. My data are consistent with the $M_{\rm BH}$–bulge relationship. The Peng et al. (2006) sample is of particular interest, as several objects in their sample are at comparable redshifts to my study. In Fig. 4.14 (b), the dashed regression line I show was derived by Peng et al. (2006) from a sample of 20 nearby AGN, with $M_{\rm BH}$ and L_R

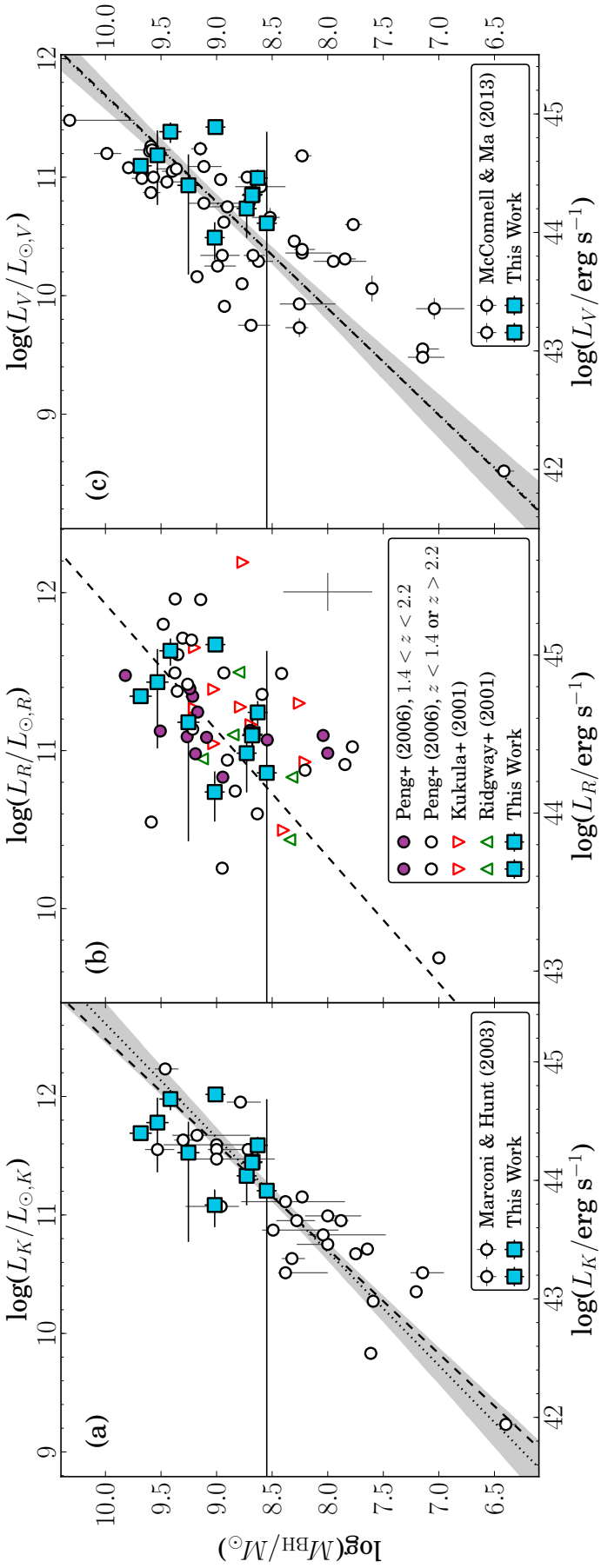

Figure 4.14: Comparison of modelled host galaxy luminosities with the Marconi & Hunt (2003), Peng et al. (2006) and McConnell & Ma (2013) samples (panels (a), (b) and (c) respectively). In (b), I show a representative error bar for the literature data, and highlight the objects in the same redshift range as my own in purple. Also shown in (b) are the literature samples of Kukula et al. (2001) and Ridgway et al. (2001). I show in each panel the derived relations by the respective work (dashed lines) and, in (a) and (c), a simple least squares regression (dotted line) with 1σ error, estimated by drawing 1000 bootstraps from the literature sample.

values published in Kormendy & Gebhardt (2001) and Bettoni et al. (2003) respectively. The $M_{\rm BH}$ values calculated by Peng et al. (2006) were made using the single epoch virial linewidth technique, however, due to lack of IR spectra, $M_{\rm BH}$ was estimated from the emission line profiles of C IV and Mg II in several objects. Where both of these lines were available, Peng et al. (2006) used the average $M_{\rm BH}$ estimate from these lines, whereas in Fig. 4.14 I show the Mg II estimate only, as C IV has been consistently shown not to correlate well with the $M_{\rm BH}$ estimate from the Balmer lines (e.g. Netzer et al. 2007, Shen & Liu 2012, but see also Vestergaard & Peterson 2006 and Denney et al. 2013). Additionally, some of the Peng et al. (2006) $M_{\rm BH}$ estimates were made manually by the authors of that study from printed copies of the spectra, and as such these may be less reproducible than the Gaussian fitting method I employ. In spite of these uncertainties, our two samples from this redshift range are both consistent with the low redshift relationship.

Paltani et al. (1998) and Soldi et al. (2008) found that in the nearby AGN 3C 273, variability suggests there are two distinct contributions to the optical–UV continuum. Whilst the consequences of this finding are unclear, it could suggest an additional contribution to the SED between the AD and torus. In my study, it is probable such a contribution would be attributed to the host galaxy. Once again, the data are not sufficient to support or contradict such a result, although if the AD does truncate at the relatively small radii measured in Section 4.2.5, this could provide additional matter to form such an additional component.

For the IR, I have only the *WISE* photometry, and at shorter wavelengths the NIR spectra. These relatively limited data are used to fit both torus and host galaxy, but have proven adequate to set useful constraints on these components. This would open up a range of possibilities for studying large AGN samples and identifying correlations between the torus and the AGN central engine. My technique could be applied to many AGN with NIR and optical spectra, and *WISE* photometry, and greatly expand investigations such as Peng et al. (2006) at higher redshifts, as it does not require *HST* imaging of gravitationally lensed galaxies.

I have only adopted the 5 Gyr elliptical galaxy template from Polletta et al. (2007). There are now refined templates available, such as those presented in Brown et al. (2014). However, these differences are not significant for the purposes of the modelling, because of the limited quality of out data set.

4.6.4 Spectral Decomposition

Using my SED continua, I have undertaken a spectral deconvolution of the optical–IR data for the 11 AGN.

Firstly, it is clear that around half of the objects have weak narrow [O III], which is anti-correlated with the Eddington ratio. In general, the lowest accretion rate objects show the strongest narrow emission lines (J0839+5754 and J2328+1500 are the clearest examples). Similarly, the highest accretion rate objects (particularly J0043+0114, J1021+1315, J1044+2128 and J1240+4740) show extremely weak narrow [O III]. (The narrow feature at ~ 5000 Å in J1021+1315 is attributed to noise, as there is a corresponding feature in the error array.)

I explored this further by searching for (anti-)correlations between the [O III] $\lambda 5007$ line equivalent width (EW) and $\dot{m}$, $L_{\rm bol}$, $M_{\rm BH}$ and $L_{2500\text{Å}}$. I show plots of these properties in Fig. 4.15, and use the Pearson product moment correlation coefficient, $\rho_{\rm P}$, and p-value to assess whether correlations are statistically significant. To estimate the uncertainty of the relations, I repeat the analysis on 2000 bootstrap subsamples, and take the central 68 per cent of the resulting distributions as an indication of the 1 σ error on each property. Using the deviance of $\rho_{\rm P}$ from zero as an indicator of (anti-)correlation between properties, the strongest anti-correlation is seen between [O III] EW and $L_{\rm bol}$, at almost 4 σ significance. Correlations between [O III] EW and $L_{2500\text{Å}}$, $\dot{m}$ and $M_{\rm BH}$ are more uncertain, and appear to be largely dependent on a single object (J2328+1500). To within $\sim 2\sigma$, these are consistent with no correlation.

This may suggest that a NLR in the most luminous sources cannot form, due to radiation pressure from the AGN. The objects with the weakest narrow [O III] lines are similar to the broad absorption line quasi-stellar objects in the Boroson & Meyers (1992) sample. Netzer et al. (2004) studied the disappearing NLR in a sample of $2 \lesssim z \lesssim 3$ quasars with higher average luminosities than ours. They suggested that some of the most luminous sources lose their dynamically unbound NLRs, although in others star formation at the centre of the galaxy may produce a NLR with different properties to lower luminosity AGN. After adding the AGN samples of Boroson & Meyers (1992) and Sulentic et al. (2004), Netzer et al. (2004) also found no evidence that this was a consequence of the Baldwin effect, in which emission line strengths are observed to decrease with contin-

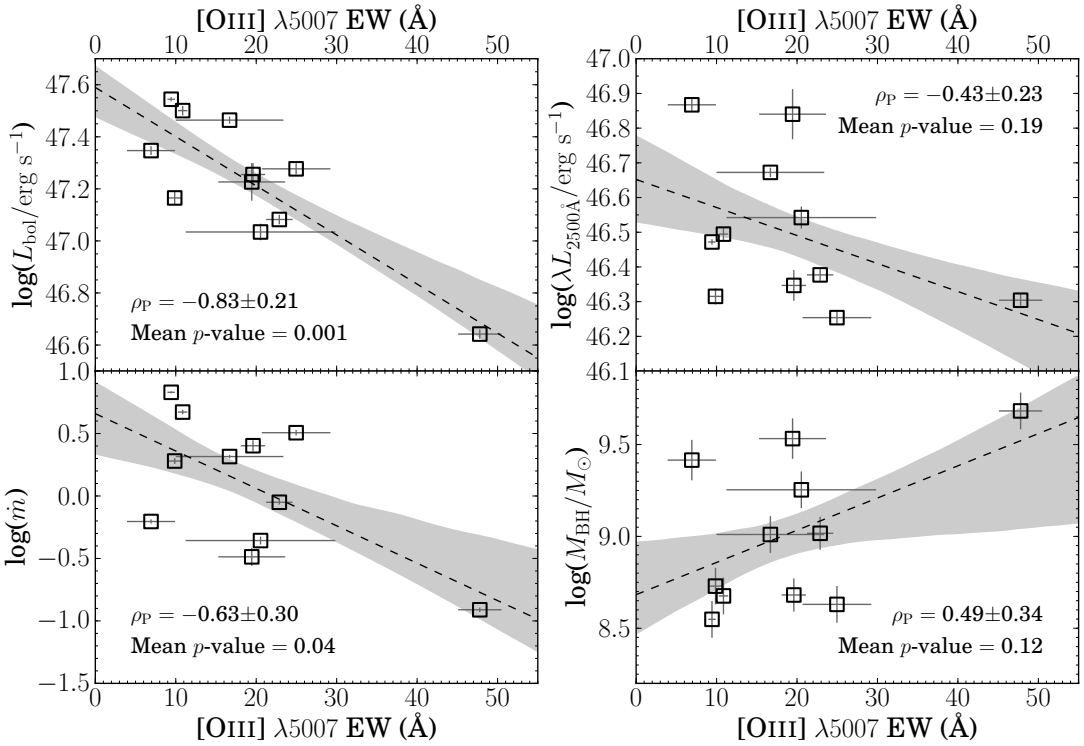

Figure 4.15: Comparison of [O III] λ5007 EW with various AGN and SED properties. Best-fit regression lines and error ranges determined from the bootstrap method are shown. A statistically significant anti-correlation is seen with the bolometric AGN luminosity, $L_{\rm bol}$. Based on my data, this is the property most strongly linked to [O III] line strength. The other properties show weaker relations and, to $\sim 2\sigma$, are consistent with being uncorrelated.

uum luminosity (Baldwin 1977). Netzer et al. (2004) defines objects in their sample with [O III] λ5007 equivalent width of $\sim 10-80$ Å as showing 'strong' [O III], corresponding to $\sim 2/3$ of their sample. Adopting the same definition yields $8/11$ objects in my sample – a comparable fraction.

I can now test whether results from my approach are consistent with larger studies, which have extensively studied relations between various linewidths (a probe of velocity dispersion) and luminosities (a probe of BLR size). I specifically consider the Shen & Liu (2012) results; although four of the objects are common to their sample, here I compare the different means by which the spectra are deconvolved.

A comparison of the FWHM of various emission lines for my sample are shown in Fig. 4.16. Also shown are the results of Shen & Liu (2012). I consider FWHM rather than other proxies for the linewidth, such as the line dispersion, because it is more widely studied, but see Collin et al. (2006) and Denney et al. (2013) for comparisons of these

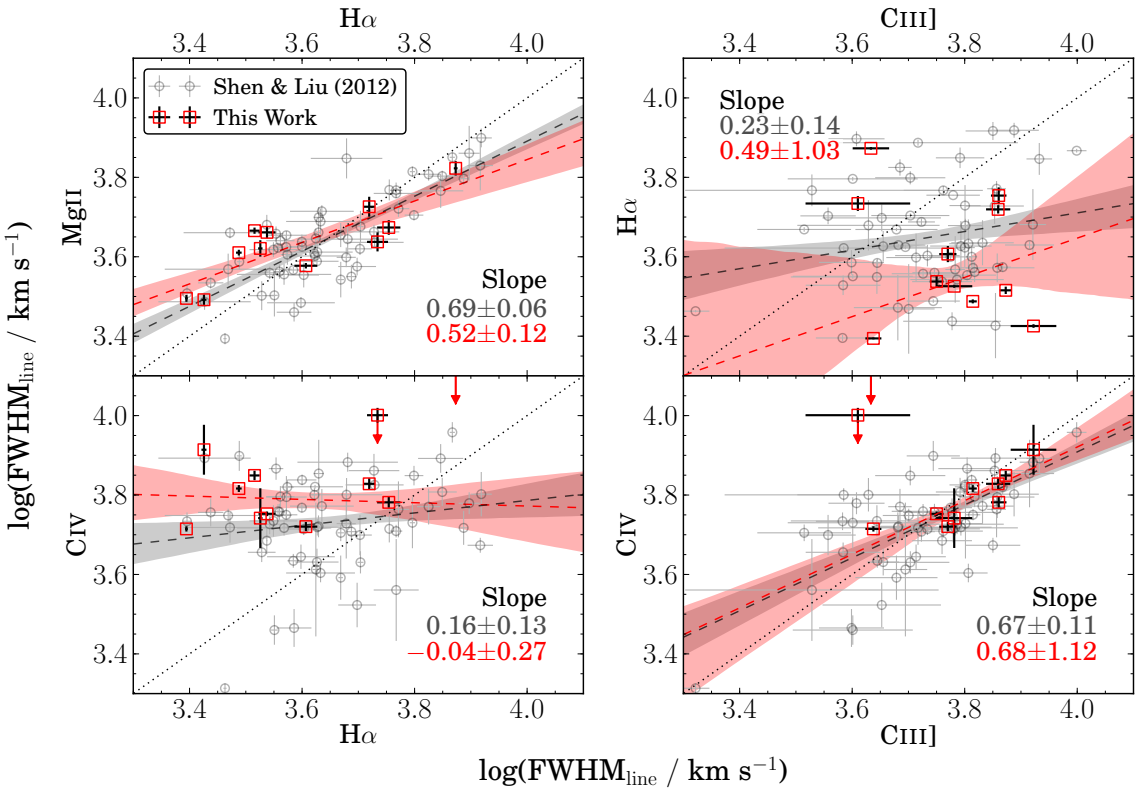

Figure 4.16: Comparison of calculated FWHM with the Shen & Liu (2012) sample. Although four objects are common to both samples, I wish to test whether the two different means of characterising the AGN continuum (SED model versus power-law) are consistent.

two approaches. In summary, it is found in these studies that the velocity dispersion (the second moment of the emission line profile, see Peterson et al. 2004), is a more unbiased proxy of the gas motion. On the other hand, Shen & Liu (2012) notes that the need for high S/N spectra to accurately measure the line dispersion disfavour this against the FWHM.

In Fig. 4.16, I show least squares regression lines, together with 1σ error region from drawing 1000 bootstrap subsamples from each distribution. My sample regressions agree with the Shen & Liu (2012) relations to within 2σ, demonstrating strong correlation between the Hα and Mg II FWHM, but no significant correlations with those for C III] or C IV. There is also a correlation between C III] and C IV FWHM. It has been previously noted that the C IV line profile does not correlate well with Hβ (e.g. Baskin & Laor 2005, Sulentic et al. 2007), and Shen & Liu (2012) also observe the correlation between C III] and C IV. In two objects, J0839+5754 and J2328+1500, the full C IV profile is not sampled by my data, and large C IV linewidths are measured. I therefore treat these results as upper limits, as I lack continuum measurements on either side of the emission line.

The errors on my FWHM values are in general smaller than those determined by Shen & Liu (2012), even though both are calculated from similar Monte Carlo methods. This is likely due to Shen & Liu (2012) using more components to model each line – for C IV, Mg II and Hα they use up to three Gaussians for the broad component (where I use only two) and one for the narrow component (which I do not model in C IV or Mg II, and only include in Hα for objects with strong narrow [O III]). This may lead to greater degeneracy between the components in their Monte Carlo fits, thus contributing to larger errors in FWHM.

In Fig. 4.17, I show a comparison of my emission line and continuum luminosities against $L_{5100\text{Å}}$, with the Shen & Liu (2012) sample. There is general agreement once again. I also show the predicted intrinsic luminosities after correcting for intrinsic extinction, connecting these points to the corresponding observed values with black lines. The least squares regressions through the observed points are shown with solid lines of corresponding colour, and the 'dereddened' regressions are dashed lines. There appears to be no improvement in the relations for these dereddened values, and in some cases they show poorer agreement with the unity line (dotted black lines). This reflects that the scatter introduced from considering the intrinsic extinction is larger than the scatter from adopting the luminosities as observed. In J0839+5754 and J2328+1500, I treat $L_{1350\text{Å}}$ and C IV luminosity measurements as limits, as they are not fully sampled by the SDSS spectra, and are thus highly model dependent.

Once again, error values for my sample are very small. This is likely to be partly for the same reasons as discussed above – fewer Gaussian components in the decomposition lead to less degeneracy – but additionally my SED continuum contains only one free parameter (the normalisation), versus the Shen & Liu (2012) approach, which uses power-law continua (in some cases with a break included), with both normalisation and slope left as free parameters.

Setting aside the merits of various linewidth proxies, and statistically justifiable number of Gaussian components for emission line profile-fitting techniques, I show that using my model of the underlying AGN continuum is consistent with simpler power-law models. However, since I have attached a physical significance to this component, compatible with accretion physics and constrained by multiwavelength data from MIR to X-rays, this is a better justified approach, compared to the empirical alternatives.

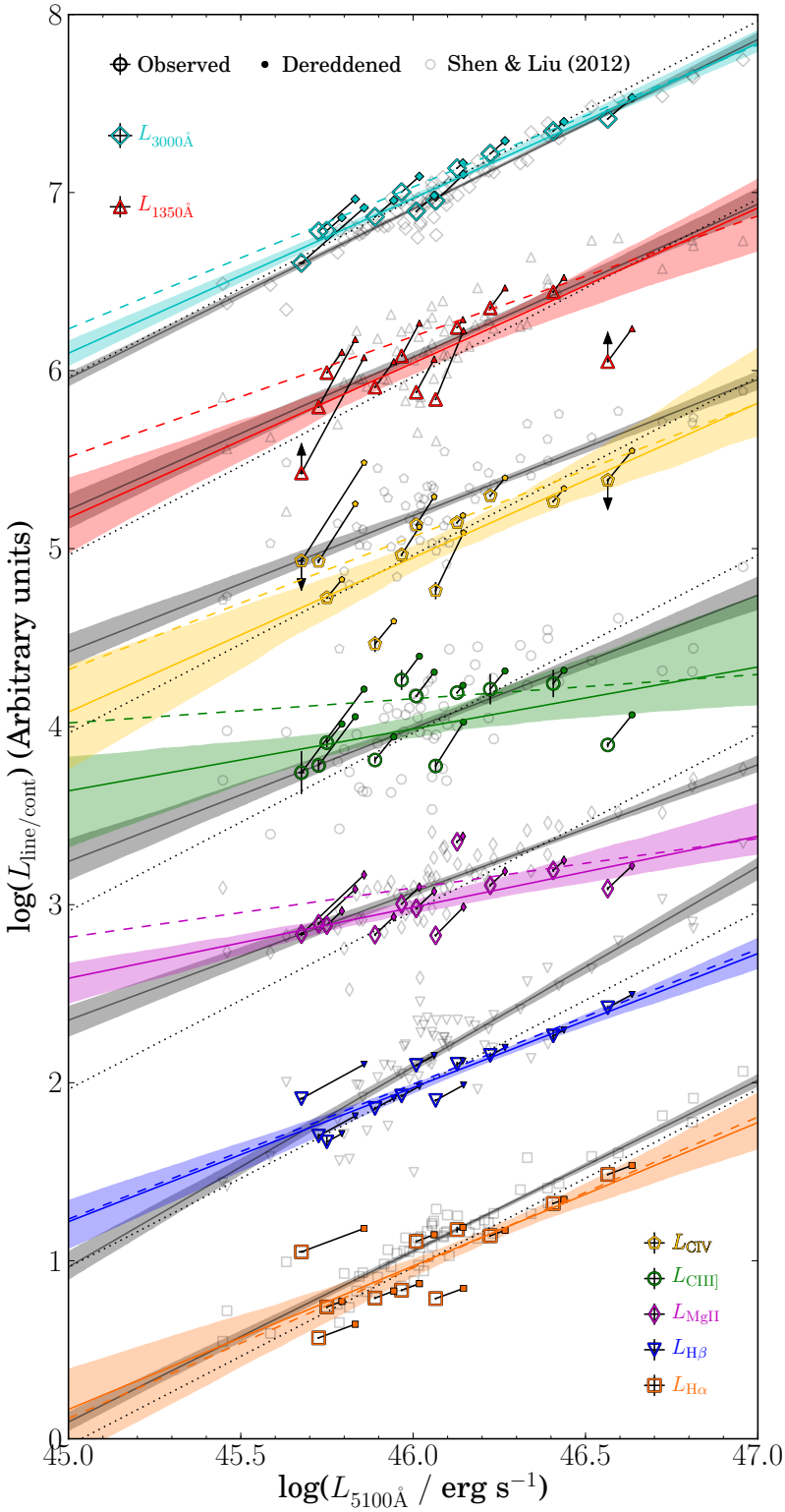

Figure 4.17: Comparison of luminosities with the Shen & Liu (2012) sample. The observed data points are linked to the corresponding dereddened point. Unity for each property is shown by the dotted lines. The Shen & Liu (2012) objects are shown as grey symbols, with least squares regressions and 1σ errors from 1000 bootstraps shown as the solid grey line and shaded region. My data are shown in colour, with solid coloured line and shaded regions showing regression and 1σ region. The dashed coloured lines are the dereddened regressions. Error bars are often very small, this is discussed in the text.

4.7 Summary and Conclusions

In this chapter I have substantially extended the study presented in Chapter 3 with a systematic analysis of the SED parameter space. A summary of my work and key findings is as follows:

i. I first refine the model described in Chapter 3 to include best-fitting intrinsic extinction curves, out of MW, LMC and SMC models. The Eddington ratio – photon index relation of this model agrees with previous work. BC factors are calculated, and show strong correlations with mass accretion rate, but the relations for optical/UV BCs are offset from those of lower redshift samples, likely due to differences in the average $M_{\rm BH}$. X-ray BCs show better agreement across samples.

ii. The impact of uncertainties in $M_{\rm BH}$ on the AGN bolometric luminosity ($L_{\rm bol}$) are tested. I find that in objects with well-sampled SED peaks, the difference is small, otherwise an uncertainty of ~ 0.1 dex in the $M_{\rm BH}$ estimate propagates through to a ~ 0.1 dex uncertainty on $L_{\rm bol}$. This is not a linear effect, and a larger range of ~ 0.5 dex in $M_{\rm BH}$ generally has a < 0.5 dex effect on $L_{\rm bol}$.

iii. The effects of varying the BH spin parameter a_* are explored. I find that spin values up to $a_* = 0.9$ provide acceptable SED fits in 6 out of 11 objects (and an improvement over the $a_* = 0$ model in 3), but that very high and maximal spin values of $a_* \geqslant 0.99$ are ruled out by a combination of the optical–IR and X-ray data in all objects, with one exception. However, if I include relativistic treatment of the disc inclination, high and maximal spin values can describe the data in most objects, if the AD is face-on to the observer. There is degeneracy between the BH spin, inclination and mass accretion rate which make measurements of BH spin from continuum fitting uncertain. In spite of this, my results show some consistency with the spin-up model of BH evolution.

iv. The outer disc radii are well constrained in 8 out of 11 objects. They show good correlation with the self-gravity radius, but are smaller by a factor ~ 5. This suggests

that the disc break-up may occur closer to the BH than the self-gravity radius.

v. I model the red end of the NIR to MIR ($2-22\mu$m, observed frame) using host galaxy and torus models. I find good agreement with previous studies for both the torus properties (covering factor and temperature) and the host galaxy (luminosity). This is despite my more limited dataset in comparison with some of these investigations. I suggest that my approach to the SED modelling provides a viable alternative to structural decomposition of high-resolution images and those requiring observationally expensive MIR spectra.

vi. My continuum model provides a firm basis on which to execute a spectral deconvolution of the optical–IR spectra. The results from my approach are in agreement with previous studies that utilise empirical models of the AGN continuum.

CHAPTER 5

AGN SEDs Part 3: Pilot Studies and Future Work

5.1 Introduction

In this chapter, I discuss the next steps to be taken in this field of research, following on from the studies presented in Chapters 3 and 4.

I first define a larger moderate redshift sample that is not reliant on the Balmer lines in order to make $M_{\rm BH}$ estimates. Using Mg II to make these estimates instead removes the requirement for NIR spectra, which correspondingly allows selection of a much larger sample that offers scope to undertake a more statistically significant survey of the properties of distant AGN. Here I assemble this sample, and present some of its attributes, but the full analysis will be carried out in the future.

Next I will conduct a pilot study of two AGN at $z \sim 1$ for which high resolution *HST*/COS UV spectra exist, in addition to optical and X-ray spectra. This provides a means of recovering the SED continuum blueward of the Ly-α emission line, allowing the extension of the SED modelling into the FUV.

Finally I will present a small analysis of the nearby AGN Markarian (Mkn) 590. This object has been observed to fade considerably in recent years, and I put constraints on the current AGN contribution to the energy output by fitting an SED model to quasi-simultaneous data from a number of multiwavelength sources.

5.2 Large High-redshift Sample

5.2.1 Motivation

In Chapter 3, I described the sample selection that led to the 11 AGN used for the studies in that chapter, and Chapter 4. The sample was required to have both optical and X-ray spectra for SED modelling purposes, and NIR spectra, primarily to obtain reliable $M_{\rm BH}$ estimates from the Balmer emission lines, but also to further constrain the SED model.

This yielded a sample with excellent data coverage and allowed for useful application of the SED model, from which I interpreted the properties of the accretion flow, torus and host galaxy in Chapter 4. However, the requirement for both NIR spectral data and X-ray observations with *XMM-Newton* imposed two bottlenecks on the final sample. The logical next step for this research is to expand the sample.

The Balmer lines are the best studied in terms of single epoch virial mass estimates. They are easily detected in optical spectra of low redshift AGN (up to $z \sim 0.5$ for Hβ and $z \sim 0.1$ for Hα), and with the relative abundance of such spectra from wide area surveys (such as SDSS), calibration of $M_{\rm BH}$ estimates from RM campaigns is possible. At higher redshifts, the lines are shifted beyond optical wavelengths ($\gtrsim 7500$ Å), necessitating NIR spectra to observe. Alternatively, using a rest-frame UV emission line as a proxy for $M_{\rm BH}$ is possible.

Numerous studies have explored the correlations between luminosities and linewidths in the AGN UV spectral range. It has been shown (Vestergaard & Peterson 2006, Netzer et al. 2007, Shen & Liu 2012, Mejia-Restrepo et al. 2016 and Chapter 4) that whilst C III] and C IV show questionable correlations with the Balmer lines (at least in cases where the S/N is limited, Denney et al. 2013), Mg II is more promising, offering a viable alternative to Hα and Hβ.

I was therefore motivated to draw a new sample, with optical spectra from SDSS and X-ray spectra from *XMM-Newton*. Using Mg II to make the mass estimate removes the need for NIR spectra, allowing for a much larger sample to be selected. It is hoped that this work would constitute a more representative survey of moderate redshift AGN, allowing us to probe the distribution of SEDs, and also search for more correlations in the parameter space.

5.2.2 Sample Selection

I drew the new sample of AGN from the latest BOSS DR12 quasar catalogue[1] (accompanying publication unavailable at time of writing, but see Pâris et al. 2014 and Alam et al. 2015). Objects were selected on the basis of available X-ray data, and the redshift range being suitable for detecting Mg II in the BOSS optical spectrum. Given the BOSS spectrograph coverage (3600 – 10400 Å), for Mg II λ 2798 Å this redshift range is 0.385 – 2.47, assuming that the full Mg II profile (chosen to be 2600 – 3000 Å) was to be sampled.

The BOSS DR12 quasar catalogue contains 297,301 AGN. The subsample was assembled in the following stages:

i. All AGN with a matching *XMM-Newton* observation were selected. This initial cross-correlation is provided by the parent catalogue, so I therefore required the number of *XMM* detections to be $\geqslant 1$. This yielded 5369 matching AGN.

ii. AGN in the redshift range 0.385 – 2.47 were chosen, such that Mg II would be sampled by the BOSS spectrograph. There were 3957 matches after this step.

iii. Many of the *XMM* detections are upper limits. As I require spectral fitting to the X-ray SED, I removed these objects, leaving 2584 AGN.

iv. An initial spectral S/N cut was applied, for the benefit of the Mg II line modelling. This cut was applied at a median spectral S/N per pixel value of 5. This left 885 targets.

v. These 885 targets were then manually cross-matched with the 3XMM-DR5 serendipitous source catalogue. Only matches coincident to within 5″ were chosen, removing 3 objects. Of the remaining 882, a further cut, based on the total number of EPIC counts, was applied. There were 233 AGN with more than 500 X-ray counts, which constitute the final sample.

[1] http://www.sdss.org/dr12/algorithms/boss-dr12-quasar-catalog

5.2.3 Sample Properties

The redshift distribution of the sample is shown in Fig. 5.1. For comparison, the redshift distribution of the full BOSS DR12 quasar sample is also shown. This helps illustrate the bias introduced by my selection criteria. A number of different effects give rise to the distribution of the full BOSS sample, but it is predominantly shaped by the selection criteria of the survey, described in Dawson et al. (2013). The new sample appears to be biased against higher redshift objects, due to the S/N and X-ray count cuts I have applied. However, this effect is to be expected with any such sample – objects must be bright enough to have good quality data.

I next estimate $M_{\rm BH}$ and $\dot{m}$ for this new sample. These are not as accurate as the estimates produced when the spectral/SED fitting program is undertaken, however, they should provide a guide to the resulting distribution. The BOSS spectroscopic reduction pipeline performs a standard model-fitting routine to all targets, to aid with classification and redshift determination. As such, the velocity FWHM of the Mg II emission line for most AGN is presented in the BOSS DR12 quasar catalogue. I make measurements of the 3000 Å continuum luminosity directly from the spectrum, after first smoothing it by

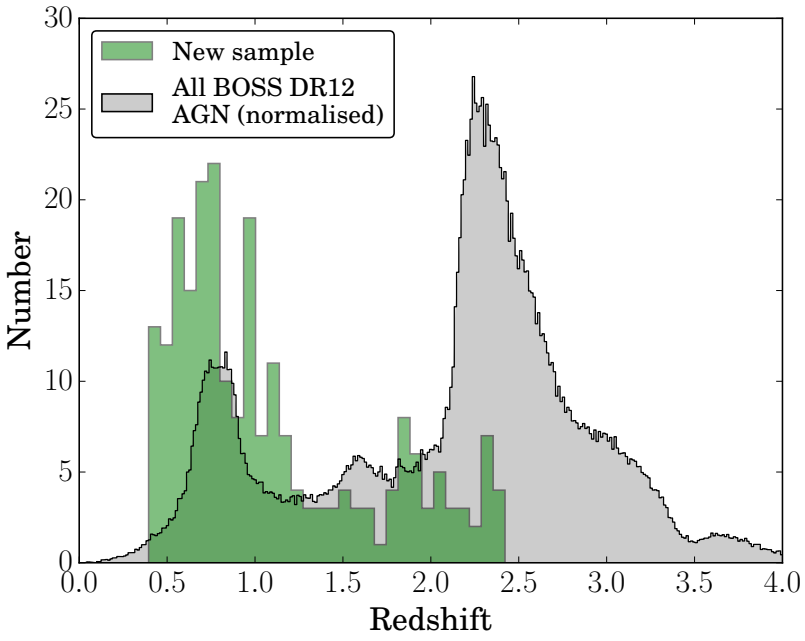

Figure 5.1: The redshift distribution of the new sample of 233 AGN. Also shown is the (arbitrarily normalised) redshift distribution of the full BOSS DR12 sample.

convolving with a 30 pixel Gaussian, to reduce the effect of noise. I calculate $M_{\rm BH}$ using the formula in equation 1.4.11.

Although I have shown that estimating mass accretion rate using BCs is likely to be uncertain in individual objects, they ought to provide an estimate of the distribution, and the full SED modelling study is beyond the scope of this section. I estimate the bolometric luminosity using the method of McLure & Dunlop (2004):

$$\log(L_{\rm bol}/{\rm W}) = -0.376(\mathcal{M}_B - 79.36), \tag{5.2.1}$$

where $\mathcal{M}_B$ is the B-band absolute magnitude of the AGN. For reasons of automation, the B-band absolute magnitudes are estimated from the spectra, integrating the flux over the effective wavelength and bandpass of the B band.

The resulting distribution of $M_{\rm BH}$ against $\dot{m}$ is shown in Fig. 5.2. The results of this project, with respect to SED properties and BCs, will improve on previous work in a number of ways. Firstly, $\dot{m}$ will be measured using the SED models described in Done et al. (2012, 2013), using techniques refined in Chapters 3 and 4, as opposed to relying solely on BCs, as in Trakhtenbrot & Netzer (2012). Secondly, we will have X-ray data,

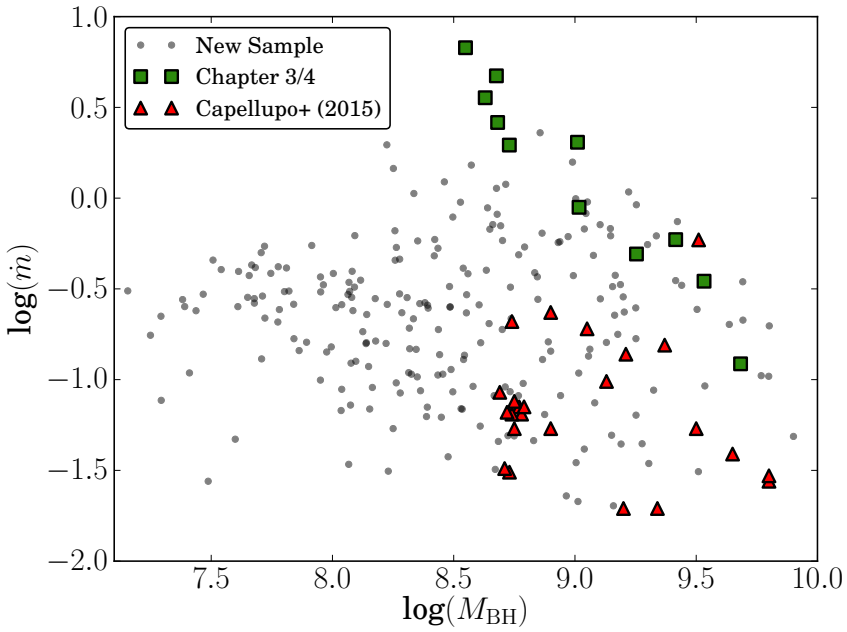

Figure 5.2: The distribution of $M_{\rm BH}$ and accretion rate for the new sample. Shown for comparison are the distributions from the sample in Chapters 3 and 4, and also Capellupo et al. (2015).

which Capellupo et al. (2015) lacked. Finally, we expect to cover almost three orders of magnitude in both $M_{\rm BH}$ and $\dot{m}$, far more than e.g. Vasudevan & Fabian (2009), and with better optical data.

Not every AGN observed by SDSS-I/II was reobserved in the BOSS survey. In future, it will be possible to further increase this sample by adding in AGN unique to the SDSS DR7 quasar catalogue. This will result in a more complete sample (both surveys had different selection criteria) although these earlier observations make use of the original spectrographs, with poorer S/N and wavelength coverage. As such, this exercise may be better suited to testing correlations discovered using the BOSS sample for consistency.

5.3 Pilot Study: The FUV SED of Two AGN

5.3.1 Motivation

An alternative means of sampling close to the SED peak in AGN is through the use of UV spectral data. I noted in Chapters 3 and 4 that UV photometry from e.g. *GALEX* and *XMM* OM were not suitable for SED modelling because the filter bandpasses lay blueward of Ly-α in the rest frame. This part of the spectrum is affected by intervening absorption systems along the line of sight, so the photometry data are likely to lie below the intrinsic flux level. With high resolution UV spectroscopy, it is possible to use statistical techniques to interpolate over these narrow absorption features, allowing for the potential recovery of the intrinsic continuum level (e.g. Lusso et al. 2015). I will explore this technique in this section.

So far, I have concluded that the application of the OPTXAGNF SED model to multiwavelength spectroscopic observations of AGN at moderate redshifts ($z \simeq 1.5$) allows for robust measurement of the bolometric luminosity. However, this also raises important questions about the nature of the SED peak. 10 out of 11 AGN in Chapter 3 were AD dominated at the SED peak, but one (J0839+5754) produced a model with an SX dominant peak. Individual objects with excellent FUV data show a turndown at energies much lower than expected from pure disc models (Mehdipour et al. 2011, 2015) and this is seen ubiquitously in low $\dot{m}$ AGN (Jin et al. 2012a). The SED can instead be fit if all the accretion energy below $100-50R_{\rm g}$ (for a low spin BH) is reprocessed to power the

SX and PLT (Jin et al. 2012a, Done et al. 2012). This implies the data are consistent with no energy losses due to winds, and restricts the contribution of these AGN in feedback of energy to their host galaxy. However, this result is only a lower limit as there could be six times more energy available if the BH has high spin. Nonetheless, it seems most likely that these local, low $\dot{m}$ AGN do not have strong wind losses because their hard, X-ray bright SEDs should strongly suppress any UV line driven disc winds (Proga & Kallman 2004, Higginbottom et al. 2014).

By contrast, in local, high $\dot{m}$ objects, the SED is typically disc dominated, and the relatively weak intrinsic X-ray emission cannot efficiently suppress UV line driving. However, the AD peaks in the FUV/soft X-ray bandpass which is itself enough to overionise the material and suppress UV line driving (Hagino et al. 2015). The high redshift sample of Chapter 3 on the other hand contains highly luminous AGN, which tend to be high $\dot{m}$ as well as high mass. The resulting AD peak lies in the UV, so should be most efficient at UV line driving, and substantially contribute to AGN feedback.

Through the further exploration of the AGN continuum at the SED peak in this section, I hope to test whether the AD still dominates the continuum in this regime. In theory, X-ray data will allow us to distinguish between two cases; one where the AD peaks in the UV, and transfers power to the PLT, and the second where the AD peaks in the UV and the power is used to drive a wind. This goes beyond the scope of this pilot study, but in future will allow us to place observational constraints on radiative mode AGN feedback at redshifts closer to where the majority of galaxy mass is assembled.

Additionally, I will use OPTXAGNF to address the question of whether the UV data coverage afforded by the *HST*/COS spectra allow us to accurately constrain the BH spin in these two objects. My findings will enable us to assess the future merit of such an approach, applied to a larger sample.

5.3.2 Sample Selection and Data Assembly

For this study, a new sample of high-luminosity AGN was assembled. First and foremost, I required relatively high $M_{\rm BH}$, so that the SED peak would lie in the optical/NUV range, and also spectra of the Mg II emission line, to make the $M_{\rm BH}$ estimate. Then I added the requirements of both *HST*/COS and *XMM-Newton* data to fit the continuum for SED

Table 5.1: The two objects with *HST*/COS, *XMM* and SDSS data – names, positions, Mg II properties and $M_{\rm BH}$ estimates.

Name	R.A. (J2000)	Decl. (J2000)	$z_{\rm SDSS}$	FWHM$_{\rm MgII}$ [km s^{-1}]	$\log(L_{3000\text{Å}})$ [log(erg s^{-1})]	$\log(M_{\rm BH})$ [log($M_\odot$)]
QSO J1208+4540	12 08 58.0	+45 40 35.5	1.163	4330	46.98	9.63
QSO B1630+3744	16 32 01.1	+37 37 50.0	1.476	4610	46.98	9.68

modelling.

A cross-correlation of the Stevans et al. (2014) sample of *HST*-observed AGN with the SDSS and *XMM* observation databases yielded my initial list of candidates. I filtered by redshift to select only objects at $z > 1$, to increase the likelihood of observing close to the SED peak. This resulted in just two matches, given in Table 5.1. An additional object, extensively studied in Finn et al. (2014), has the required observations, but optical spectra are not publicly available in reduced form, so I omitted this object from the study.

SDSS spectra for these AGN were obtained from the SDSS DR12 database, and X-ray data from the 3XMMi Serendipitous Source Catalogue. Reduced *HST*/COS spectra were kindly provided by Charles W. Finn (private communication).

I estimated $M_{\rm BH}$ using the single epoch virial method, applied to the Mg II emission line profile via equation 1.4.11. Although Mg II is not as well-studied as the Balmer lines I used in Section 1.4, it shows strong correlations of FWHM with the Balmer lines, as does $L_{3000\text{Å}}$, the BLR size proxy (e.g. Shen & Liu 2012). Nonetheless, as with all single epoch estimates, the $M_{\rm BH}$ value may be considered uncertain by a factor of ~ 3 (Park et al. 2012). I show the Mg II line fits in Fig. 5.3, and give results in Table 5.1.

5.3.3 SED Modelling

I constructed the SED using the spectral data from SDSS, *XMM* and *HST*/COS. Regions were chosen from the SDSS spectral continuum that are expected to be free from contaminating emission sources, such as blended Fe II, emission lines, and the Balmer continuum, as described in Section 3.4. These regions ought to be dominated by AD emission.

The *HST*/COS spectra are made more complex by the Ly-α forest. I overcame this by applying a cubic spline fitting routine (described in Finn et al. 2014), to more clearly show the pseudo-continuum, including emission features, but interpolating over the nar-

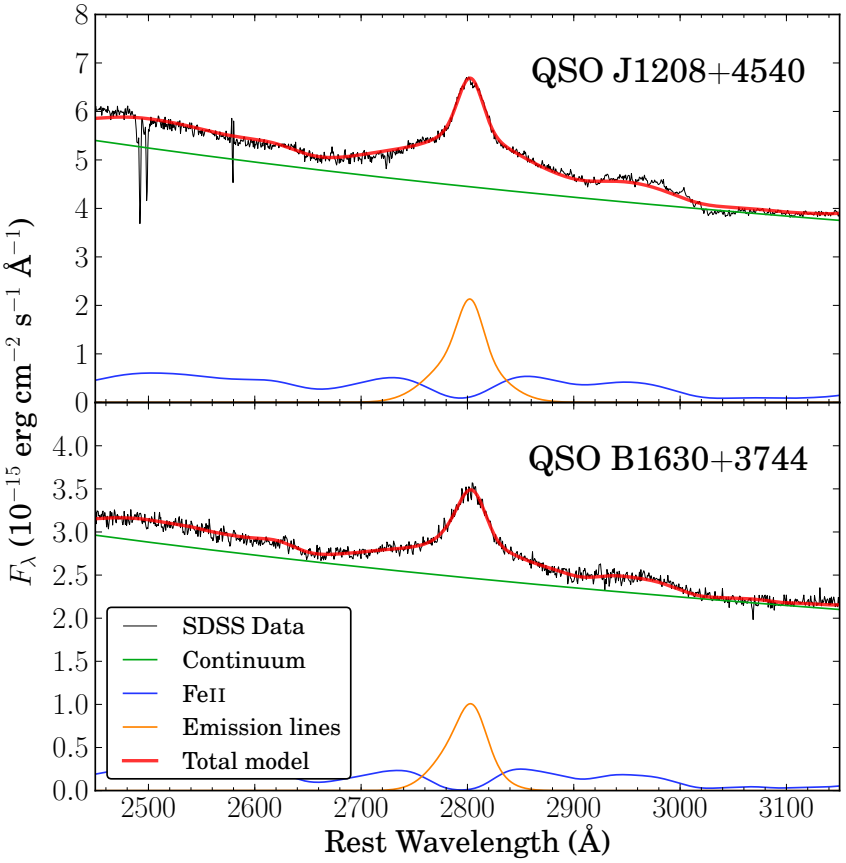

Figure 5.3: The emission line model fits used to make the $M_{\rm BH}$ estimates in the two AGN with *HST*/COS, *XMM* and SDSS data.

row forest absorption features. From this pseudo-continuum fit, I selected regions that were representative of the continuum flux level, using a power law as a guide. For each of these regions, I binned data from small ($\sim$ 2 Å) windows that were at the 'continuum' level, and free from narrow absorption features. The raw data, with cubic spline fits and chosen continuum points, are shown in Figs. 5.4 and 5.5. I also show the *GALEX* FUV photometry for QSO B1630+3744, highlighting the $\sim$ 30 per cent discrepancy with the spectrum. I verified that this is not a variability effect by integrating the spectrum over the effective bandpass of the *GALEX* point – this 'synthetic photometry' matches the *GALEX* value to within 2 σ.

I modelled the intervening partial Lyman-limit systems (pLLS), using the published values of $N_{\rm H}$ and $z_{\rm pLLS}$ (Ribaudo et al. 2011, Shull et al. 2012), and the ZTBABS model in XSPEC. It is assumed that there is no host galaxy reddening within these objects, as the Pei (1992) extinction curves in the ZDUST model do not extend far enough into the

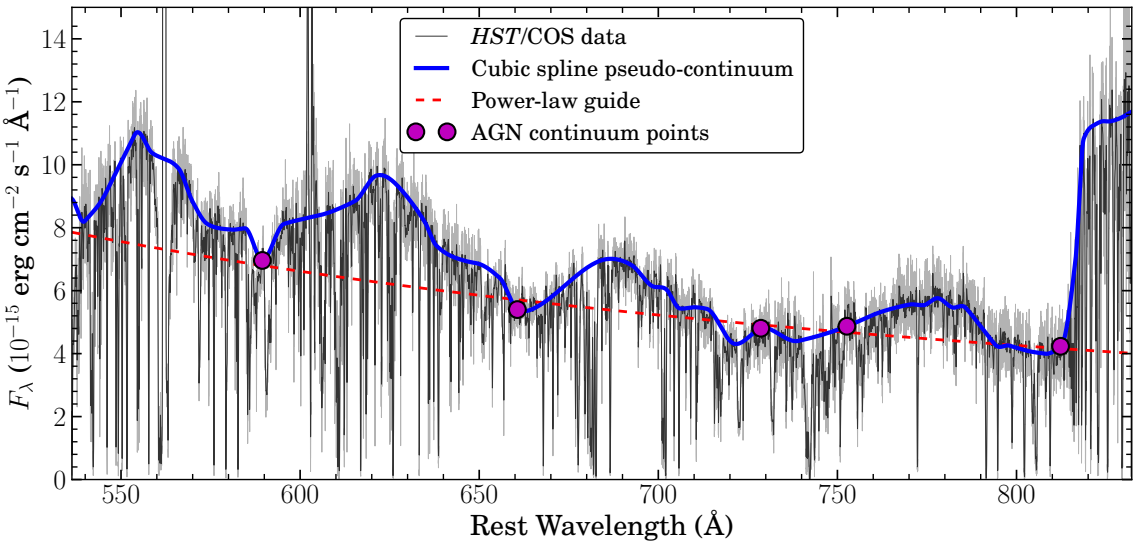

Figure 5.4: *HST*/COS spectrum of QSO J1208+4540.

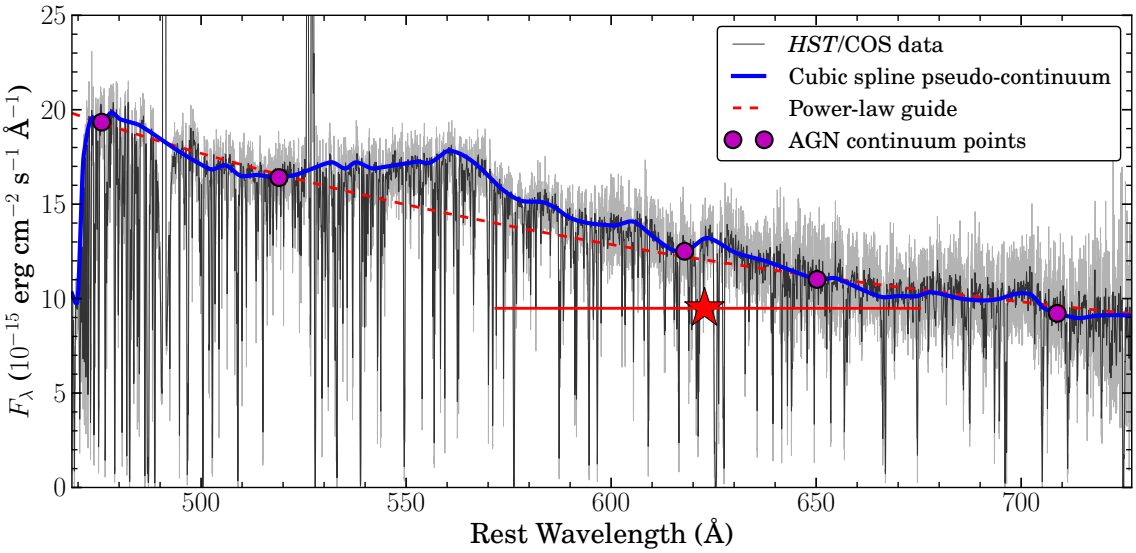

Figure 5.5: *HST*/COS spectrum of QSO B1630+3744.

UV. I could alternatively use a simpler power-law model of intrinsic reddening, but this is probably not necessary; in order for the objects to be as bright as they are in the UV, the host galaxy extinction must be very low. Similarly, an absorption system in the host galaxy would cut the observed flux below 912 Å in the rest frame, which is clearly not in evidence from the COS spectra. I thus also assumed no intrinsic absorption – a consistent assumption, as whilst they are dependent on different mechanisms, both absorption and reddening are expected to be related to a degree. The resulting model fitted is of the form: WABS × REDDEN × ZTBABS × OPTXAGNF.

5.3.4 Results and Discussion

I produced two models for each object, to explore the number of parameters that can be constrained using the greater data coverage. The differences between these two models are in the pLLS $N_{\rm H}$ and SX optical depth (τ) parameters; in Model 1 these are fixed, and in Model 2 they are free. Unlike Chapter 3, I set the spin parameter free in both models, and fix $r_{\rm out}$ at a large value in both, to reflect the different data coverages (i.e. these AGN have UV spectra, but lack NIR spectra).

The best-fitting parameters for both models, including $\chi^2_{\rm red}$ values, are given in Table 5.2. Approximate errors are quoted when possible, but some parameters are poorly constrained by the available data. The SED fits are shown in Figs. 5.6 and 5.7.

The *HST*/COS data are at the peak of the SED in these objects, and constraints on the BH spin are obtained for both Models 1 and 2. Based on the $\chi^2_{\rm red}$ values, Model 2 is preferred, however it shows some poorly constrained parameters (e.g. $r_{\rm cor}$, $f_{\rm PL}$). For Model 2 in both AGN, I measure a $\sim 2-3$ times larger pLLS $N_{\rm H}$ column density than the values published by Ribaudo et al. (2011) and Shull et al. (2012). There are several possible reasons why this may happen, beyond the previously published results being inaccurate.

It could be due to variability; if the AGN was brighter at the epoch of SDSS observation, then I would require larger pLLS $N_{\rm H}$ values to fit the UV continuum. To remove this uncertainty in future, it would be useful to obtain observationally inexpensive optical photometry quasi-simultaneously with the *HST* observation.

Alternatively, the lower-than-predicted flux in the UV could suggest a loss of energy in the form of winds. Two objects are not enough to answer this definitively, especially with the other sources of uncertainty, but in principle, the data are of sufficient quality to answer this, given a larger sample. This would also allow quantification of the energetics of this wind, which would have important consequences for the role of AGN feedback and galaxy formation. Disc-wind SEDs (e.g. Slone & Netzer 2012) could also be applied to the data.

Uncertainty in the spin value will arise from the $M_{\rm BH}$ estimate. Assuming a plausible uncertainty of ~ 0.3 dex, the corresponding ranges on the spin values are: $0.0 < a_* < 0.9$ for QSO J1208+4540 and $0.5 < a_* < 0.99$ for QSO B1630+3744. Therefore, in spite of

Table 5.2: The optimum fitted parameters for the SED models with *HST*/COS data. Parameters in brackets were frozen during fitting. Columns are as follows: (1) object name, (2) Galactic $(B-V)$ extinction [mag], (3) Galactic $N_{\rm H}$ column [$10^{20}{\rm cm}^{-2}$], (4) redshift of pLLS, (5) $N_{\rm H}$ of pLLS [$10^{17}{\rm cm}^{-2}$], (6) reduced mass accretion rate [$\dot{M}_{\rm Edd}$], (7) spin, (8) coronal radius [$R_{\rm g}$], (9) SX optical depth, (10) PLT spectral index, (11) fraction of Comptonised component in PLT, (12) $\chi^2_{\rm red}$ fitting statistic, (13) degrees of freedom. Uncertainties are the 90 per cent confidence limits, estimated from the Fisher matrix.

Name	E$(B-V)$	$N_{\rm H}$	$z_{\rm pLLS}$	$N_{\rm H,pLLS}$	$\dot{m}$	a_*	$r_{\rm cor}$	τ	Γ	$f_{\rm PL}$	$\chi^2_{\rm red}$	DOF
(1)	(2)	(3)	(4)	(5)	(6)	(7)	(8)	(9)	(10)	(11)	(12)	(13)
Model 1												
J1208+4540	(0.013)	(0.12)	(0.927)	(1.51)	0.46±0.01	0.00±0.05	11±7	(10.0)	1.63±0.05	0.30*	3.48	63
B1630+3744	(0.009)	(0.11)	(1.096)	(0.46)	0.63±0.08	0.78±0.10	7.0*	(10.0)	2.17±0.04	0.13*	1.10	108
Model 2												
J1208+4540	(0.013)	(0.0012)	(0.927)	4.2±0.7	0.63±0.19	0.5±0.4	7.0*	0.1*	1.70±0.05	0.28*	1.62	61
B1630+3744	(0.009)	(0.0011)	(1.096)	1.17*	0.74±0.4	0.9±0.2	7.0*	12±3	2.09±0.05	0.06*	1.02	106

*Parameter poorly constrained.

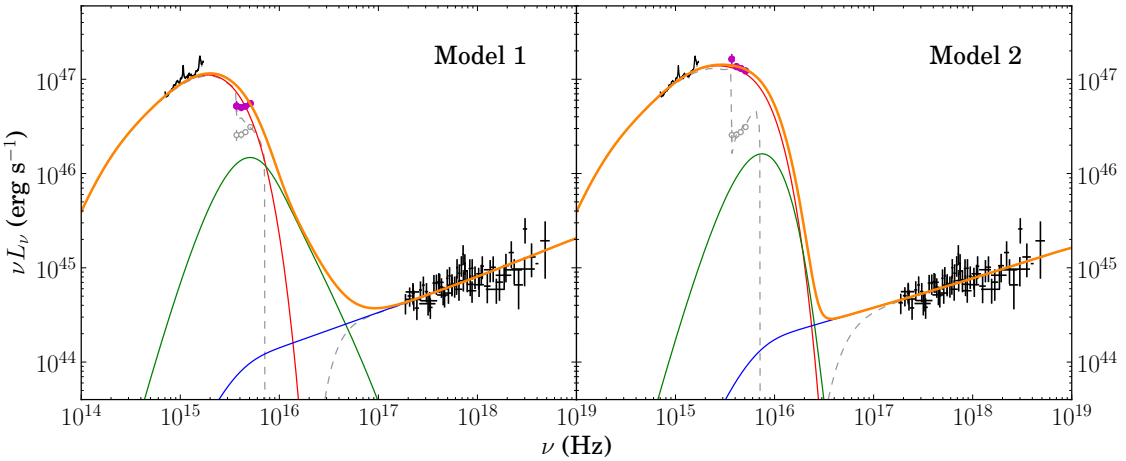

Figure 5.6: SED model of QSO J1208+4540. Colours are as used previously in Chapter 3, with the *HST*/COS continuum points shown as magenta circles.

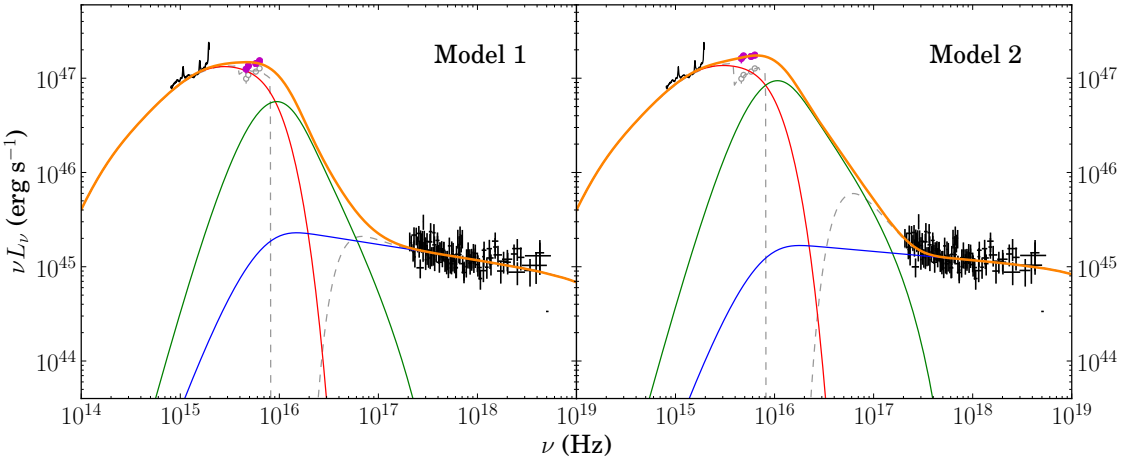

Figure 5.7: SED model of QSO B1630+3744.

these objects being of similar $M_{\rm BH}$, I find that QSO B1630+3744 is more likely to host a highly spinning BH than QSO J1208+4540, but both could host moderately spinning BHs.

The final source of uncertainty is the AD inclination, as discussed in Section 4.6.1. Exploring inclination with OPTXCONV is beyond this pilot study, but will likely once again reveal a degeneracy between inclination and spin.

As a pilot study, I find encouraging results that suggest the use of medium resolution UV spectra from instruments such as *HST*/COS are sufficient to inform of the nature of the FUV SED in AGN. Fitting the data with OPTXAGNF requires larger $N_{\rm H}$ columns in intervening systems, which may be due to variability or wind losses, but to conclude either way requires a larger sample.

5.4 The Low Accretion State of Mrk 590

I conclude this chapter by presenting a recent SED of the local AGN Markarian (Mrk) 590. This object is of particular current interest as it has been observed to fade to approximately 1 per cent of its peak flux over the past 40 years (Denney et al. 2014). Additionally the broad emission lines have disappeared, making this object an example of a 'changing look' AGN; where previously these lines would have led to its classification as a Type 1 AGN, it now falls into the Type 1.9 or 2 category.

Whilst the unified model of AGN suggests that the primary difference between Type 1 and 2 is due to obscuration, the current understanding in Mrk 590 is that the change has been brought about by an intrinsic drop in luminosity, not a change in optical depth. If, for instance, an opaque cloud had drifted across the line-of-sight to cut the optical flux by the extent observed, some associated absorption would be expected in the X-ray range. However, the X-ray spectrum is consistent with showing no intrinsic absorption, contradicting the obscuration explanation. A complete follow-up study by Kelly D. Denney is in preparation, but here I present a model of the SED using recent, quasi-simultaneous data. This will be used for photoionisation calculations in the complete study.

Optical spectroscopy was obtained using the LBT MODS instrument in 2013, and *HST*/COS observed the AGN in both 2013 and 2014. An X-ray spectrum from *Chandra* was also obtained in 2013.

Our approach to the SED fitting is similar to those used previously. Due to the low redshift of this object, the *HST*/COS data cover the UV continuum redward of Ly-α, so the continuum recovery technique employed in Section 5.3 is not necessary. I fit OPTXAGNF, including the Polletta et al. (2007) S0 spiral galaxy template to model the host galaxy, and include a relativistic reflection component (PEXMON), deemed necessary from the presence of the Fe Kα emission line in the *Chandra* spectrum. As per the findings of Denney et al. (2014), I will assume the change in optical flux is due to a change in accretion rate, and fix the intrinsic reddening at zero. If I do not make this assumption, it is likely that the model will converge to a solution with high intrinsic extinction.

Mrk 590 has an accurate RM estimate of $M_{\rm BH}$ of $4.74 \times 10^7\ M_\odot$ (Peterson et al. 2004), which is fixed in the fitting. The SED model is shown in Fig. 5.8, and the optimised parameters are presented in Table 5.3. Several parameters had to be manually set to

Table 5.3: The optimum fitted AGN parameters for the SED model of Mrk 590. Parameters in round brackets were frozen during fitting. Columns are as follows: (1) name, (2) Galactic $(B-V)$ extinction [mag], (3) Galactic $N_{\rm H}$ column [$10^{20}{\rm cm}^{-2}$], (4) Eddington fraction [$\dot{M}_{\rm Edd}$], (5) spin, (6) coronal radius [$R_{\rm g}$], (7) SX optical depth, (8) SX electron temperature, (9) PLT spectral index, (10) fraction of Comptonised component in PLT, (11) $\chi^2_{\rm red}$ fitting statistic, (12) degrees of freedom.

Name	E$(B-V)$	$N_{\rm H}$	$\dot{m}$	a_*	$r_{\rm cor}$	τ	$kT_{\rm e}$	Γ	$f_{\rm PL}$	$\chi^2_{\rm red}$	DOF
(1)	(2)	(3)	(4)	(5)	(6)	(7)	(8)	(9)	(10)	(11)	(12)
Mrk 590	(0.031)	(2.7)	0.0015±0.0008	(0.0)	200*	(20)	0.23±0.01	1.96±0.04	0.80±0.08	5.5	94

*Parameter poorly constrained.

reasonable values, and I used measurements from the low accretion rate objects in Jin et al. (2012a) as a guide. $r_{\rm cor}$ reached its upper limit of 200 $R_{\rm g}$, and is therefore unconstrained.

The MODS spectrum is dominated by host galaxy flux, with little or no apparent contribution from the AGN. My model has a low accretion rate of just 0.0015 $L_{\rm Edd}$, which pushes the predicted AD peak into the optical regime. However, the lack of observed flux here means that almost all of the AD energy is reprocessed by the SX and PLT.

This is what was observed in the Jin et al. (2012a) sample, with the lowest accretion rate objects also showing large coronal radii, and a small optical to X-ray spectral index, although all of the objects in the Jin et al. (2012a) sample were accreting at significantly higher Eddington ratios.

In this regime, it is quite possible that the thin AD assumption breaks down, and an advection-dominated accretion flow (ADAF) transports the gas in towards the BH (e.g. Done et al. 2007, Done 2010). An ADAF differs from an AD in that it is geometrically thick and optically thin, and of a higher temperature. The structure of ADAFs is not currently understood, but variability studies of changing-look AGN such as Mrk 590 may inform us of the mechanism by which an AD gives way to an ADAF, or vice versa.

Using the Czerny (2004) formula for calculating the viscous timescale for Mrk 590 yields a value at the innermost radius (6 $R_{\rm g}$) of just 50 days. This increases with radius and is dependent on the assumed disc thickness and viscosity parameter, but suggests that changes in the accretion rate through the inner disc could theoretically account for the apparent change in accretion rate observed.

In the next chapter, I present a study of a small sample of AGN for which the reverse process has apparently occurred, with a significant *increase* in flux observed in recent years.

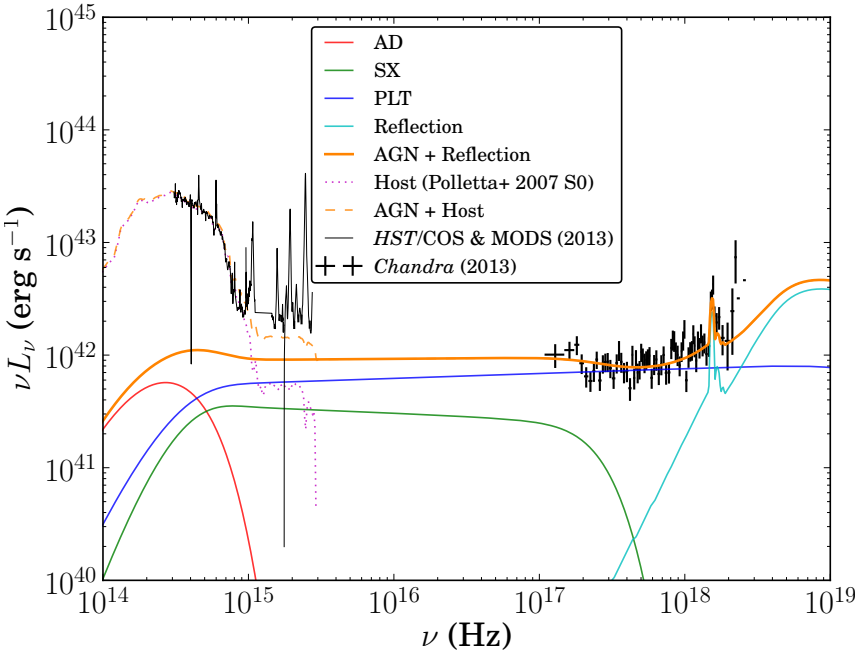

Figure 5.8: Mrk 590 in the low state.

CHAPTER 6

The Broad-band SEDs of Four Hypervariable AGN

6.1 Introduction

6.1.1 Motivation

Variability provides an additional diagnostic of the way the BHs powering AGN accrete matter. The properties of the BH itself are fixed on short timescales, so usually changes in the accretion flow must be responsible for the multiwavelength variability we observe, be that due to some form of obscuration, a change in geometry, or changing physical properties. One of the more extreme events expected to influence the luminosity of an AGN is a tidal disruption event (TDE, e.g. Rees 1988, Gezari et al. 2012), in which a star passing particularly close to the BH is torn apart by the tidal gradient, depositing a large amount of gas on to the BH in a short space of time (typically of order weeks). Due to the space density of stars, these events are predicted to be rare in any one AGN, however, using wide area sky surveys, it is possible to simultaneously search many AGN for evidence of such an event occurring.

A search was made for highly variable TDE candidates in the Pan-STARRS database, which repeatedly surveys large regions of the sky with high cadence, and is therefore well-suited to searches for variable objects (e.g. Gezari et al. 2012, Morganson et al. 2015). Pan-STARRS detections were compared to the $\sim$10 year earlier SDSS photometric measurements, and objects previously classified as galaxies that had undergone a large

increase in brightness ($|\Delta m| > 1.5$ mag in at least one optical filter) were selected as candidates. In addition to TDE and central region supernova candidates, this search yielded a significant number of very blue objects that follow-up photometry showed to be evolving on timescales of several years, whereas supernovae and TDEs typically fade over time periods of weeks–months. Moreover, many of these slow, blue, variable objects were still increasing in brightness. Spectroscopy revealed them to be AGN at moderate redshifts ($z \sim 1$). Such extreme variability is rare for AGN; variability studies at lower redshifts (e.g. Sergeev et al. 2006, Breedt 2009) rarely see fractional changes in brightness at this level.

We are therefore motivated to investigate the nature of this sample of 'hypervariable AGN' (HVAs). Discovering the mechanism responsible for the variability is likely to shed new light on AGN physics, and may provide a means of refining our understanding of the AD and corona.

My definition of 'hypervariable' here differs from that in Morganson et al. (2015); that study defines all objects with $|\Delta m| > 2$ mag as hypervariable, and as such includes a large number of highly variable stars and other phenomena, in addition to some AGN.

6.1.2 Possible Mechanisms and This Study

It is unclear whether the variability observed in these objects makes them statistical outliers showing the extreme end of conventional AGN variability (e.g. MacLeod et al. 2010, 2012), or whether there is an extrinsic origin. Lawrence et al. (2016) examined the properties of this growing sample of HVAs (currently at 76 objects) and considered several interpretations of the data. These included highly luminous, slowly-evolving TDEs, line-of-sight extinction changes, extreme accretion rate changes and foreground microlensing.

They found that the TDE explanation required uncommonly massive stars ($\sim 10 M_{\odot}$) to be torn apart by the BH tidal forces to satisfactorily account for the observed event luminosities. Based on likelihoods and previously noted TDE candidates, disrupted stars are more likely to be of less than a solar mass ($\sim 0.3 M_{\odot}$), and occur around lower mass BHs ($\sim 10^6 - 10^7 M_{\odot}$) due to the steeper potential gradient (Gezari et al. 2012, Guillochon & Ramirez-Ruiz 2013). This interpretation then seems quite unlikely in the whole sample of HVAs.

Extinction scenarios have been previously proposed to explain high amplitude variability in AGN, such as the transition from Type 1 to Type 1.9 for the AGN described in LaMassa et al. (2015). Lawrence et al. (2016) noted that whilst the timescale of such events make them a plausible explanation, there would be a strong colour change expected as the event evolves, which is not observed. A changing optical depth might produce such an effect, such as an eclipse by an opaque cloud. However, as many of the HVAs are now observed to be decaying again, this model would consistently require successive eclipses.

The third possible origin of the variability considered in Lawrence et al. (2016) is an accretion rate change. This is difficult to explore, as we do not yet have a model that adequately describes even conventional AGN variability (e.g. Czerny 2004, Lawrence et al. 2012a), but in this case, these HVAs could pose an intriguing means of probing extreme accretion rate changes.

Finally, a foreground microlensing event could produce the observed change in flux. Such a scenario may arise from a star in a foreground galaxy passing directly between us and a background AGN, increasing the observed flux from the AGN by a large factor. This situation was explored by Meusinger et al. (2010) for a highly variable AGN observed behind M31, but that work found a TDE explanation to be favoured. Lawrence et al. (2016) found that the timescale and expected frequency are consistent with that observed; although the Einstein time is longer than the decay time of the HVAs, the crossing time, corresponding to the peak of variability is much shorter, and consistent with the observation. Bruce et al. (2016) undertook a sophisticated light curve modelling programme for a small subset of the Lawrence et al. (2016) sample, to determine likely source sizes/impact parameters/etc. and a snapshot programme on *HST* is underway, to search for potential intervening systems.

In this chapter, I further explore the two most promising explanations for this variability. I report the optical spectra and light curves, X-ray spectra and SEDs for four HVAs for which we have obtained *XMM-Newton* observations (PI: A. Lawrence). Hereafter I consider scenarios (A), extreme accretion rate changes, and (B) foreground microlensing events.

6.2 Sample and Observations

The means of selecting the full sample of transients is described in detail in Lawrence et al. (2016). Summarily, the parent sample was selected by comparing PS1 magnitudes in the FGSS database (Inserra et al. 2013, Section 2.3) to earlier SDSS DR7 photometric observations (Abazajian et al. 2009). Objects in this sample were required to be coincident in position to within 0.5 arcsec, classified by SDSS as galaxies, and show a $\geqslant$1.5 mag increase in brightness when reobserved by PS1. Follow-up photometry was used to reject probable supernovae by applying both colour cut and decay time criteria (also see Lawrence et al. 2012a). This results in an ever-growing sample of HVAs, with 76 discovered so far.

We observed four representative, but bright, HVAs with *XMM-Newton* during August 2013 to February 2014. Their names, positions, redshifts and *XMM* observation details are listed in Table 6.1. Where possible, observations were split between two epochs to look for variability.

6.3 Light Curves

I collated photometric data from four sources. The large area surveys that formed the basis of the initial sample selection were SDSS and PS1 FGSS. Pointed follow-up observations with the Liverpool Telescope (LT) were also made, starting in 2011. Additional data were sourced from CRTS (see Section 2.3).

Table 6.1: The names, positions, redshifts, *XMM* observation IDs and observation dates for the sample of four HVAs.

Name	R.A. (J2000)	Dec. (J2000)	$z^{a}_{\rm meas}$	*XMM* Obs ID(s)	Obs UT(s)
J0312+1836	03 12 40.86	+18 36 41.1	0.889	(0724440) 101 & 601	2013-08-12 & 2014-01-22
J1422+0140	14 22 32.45	+01 40 26.7	1.078	(0724440) 301[b] & 801	2014-01-04 & 2014-02-06
J1519+0011	15 19 43.99	+00 11 47.4	0.530	(0724440) 401 & 901	2014-01-27 & 2014-02-10
J2232−0806	22 32 10.51	−08 06 21.2	0.276	(0724441) 001 & 101[b]	2013-12-14

[a]Redshift measurement described in Section 6.4.

[b]Obs IDs 0724440301 and 0724441101 did not yield useful data due to background activity.

For this study, I use spectral data from a range of dates to estimate $M_{\rm BH}$, and then fit the broad-band SED with OPTXAGNF (Done et al. 2012). However, as these HVAs are variable, I first require estimates of the largest and smallest magnitudes, corresponding to the faint and bright states respectively. For this I use the *r*-band, as it is close to the middle of the spectral range, and corresponds to the same, or a very similar bandpass in PS1, LT and SDSS. I then shift the CRTS magnitudes to match the SDSS/PS1/LT *r* magnitudes, as observations made by CRTS are in white light, calibrated to a *V*-band zero point.

I estimate the bright/faint state magnitudes by modelling the light curve as a $3^{\rm rd}$ order polynomial, and using this model to estimate the curve maxima/minima. The advantage of this approach is that it is simple, and makes no assumptions regarding the mechanism causing the variability. The uncertainty on this curve is measured using a Monte Carlo technique, generating new random datasets using the mean and error on each photometry point. This procedure is repeated 1000 times, with the model recalculated each time to generate a distribution of best fitting curves, from which the 1 σ error is estimated by taking the central 68 per cent of the distribution. The light curves are plotted in Fig. 6.1.

Additionally, I wish to make an estimate of the magnitude of each HVA at the time of the *XMM* observation. I can use my global light curve model for this, but as LT photometry exists both prior and subsequent to the *XMM* observations, it is more precise to linearly interpolate these observations to estimate the magnitudes at these epochs. It is not meaningful to apply the Monte Carlo technique for this, as I am not fitting a model, so here I estimate the error using a bootstrap technique, whereby 1000 random datasets are drawn from the LT data. These are presented in Fig. 6.2. I tabulate the key *r*-band magnitudes from these analyses in Table 6.2.

It is seen in Fig. 6.2 that there is evidence for statistically significant variability on top of the global variability trend in some objects. However, for objects with two *XMM* observations, there is no evidence, from the optical light curve, for a change in magnitude between the two *XMM* observation dates (Table 6.2).

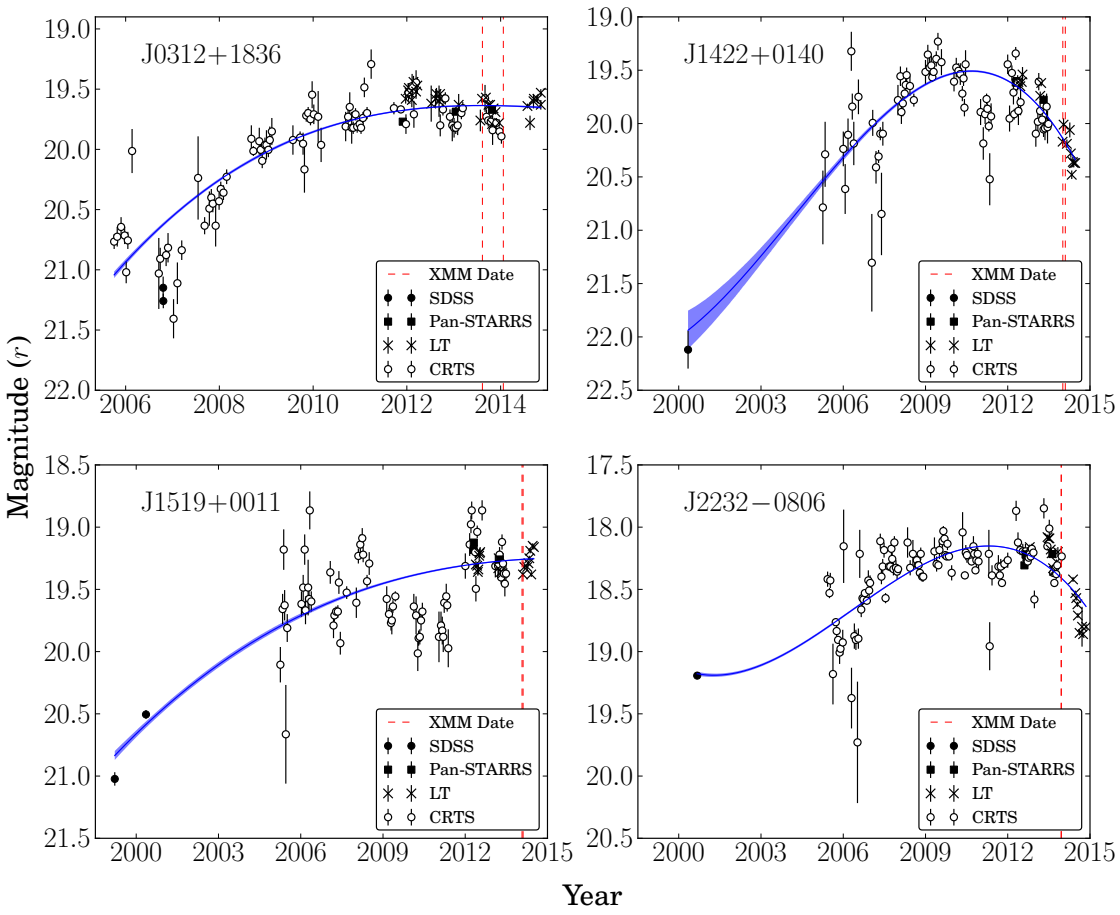

Figure 6.1: The long-term light curves for the four HVAs. Data come from SDSS, Pan-STARRS FGSS, LT, and CRTS. The blue curve shows the order 3 polynomial fit, together with 1σ error (shaded blue region) from the Monte Carlo routine. The dates of the *XMM* observations are also marked, and show that there is likely to be only a small, if any, change in flux between observations, for those objects that were observed on two different epochs.

Table 6.2: The key *r*-band apparent magnitudes for the four HVAs, including minimum (faint) and peak (bright) states, and at the date of *XMM* observation. The means by which I measure each, as discussed in the text, is shown in brackets. I also show Δm, the magnitude difference between *XMM* observation and quiescent state. This is the difference in brightness between the two scenarios I test in this chapter.

Name	$m_{\rm min,SDSS}$ (SDSS)	$m_{\rm min,poly}$ (Polynomial)	$m_{\rm peak,poly}$ (Polynomial)	$m_{(XMM\,1)}$ (Interpolation)	$m_{(XMM\,2)}$ (Interpolation)	$\Delta m = m_{\rm min,SDSS} - m_{(XMM\,1)}$
J0312+1836	21.26 ± 0.06	21.04 ± 0.03	19.636 ± 0.005	$19.62^{+0.07}_{-0.04}$	$19.72^{+0.04}_{-0.05}$	1.64
J1422+0140	22.12 ± 0.18	21.94 ± 0.16	19.508 ± 0.009	$20.10^{+0.07}_{-0.10}$	$20.12^{+0.06}_{-0.10}$	2.02
J1519+0011	21.02 ± 0.05	20.84 ± 0.04	19.254 ± 0.008	$19.35^{+0.03}_{-0.04}$	19.35 ± 0.03	1.67
J2232−0806	19.193 ± 0.016	19.190 ± 0.013	18.151 ± 0.004	18.31 ± 0.06	–	0.88

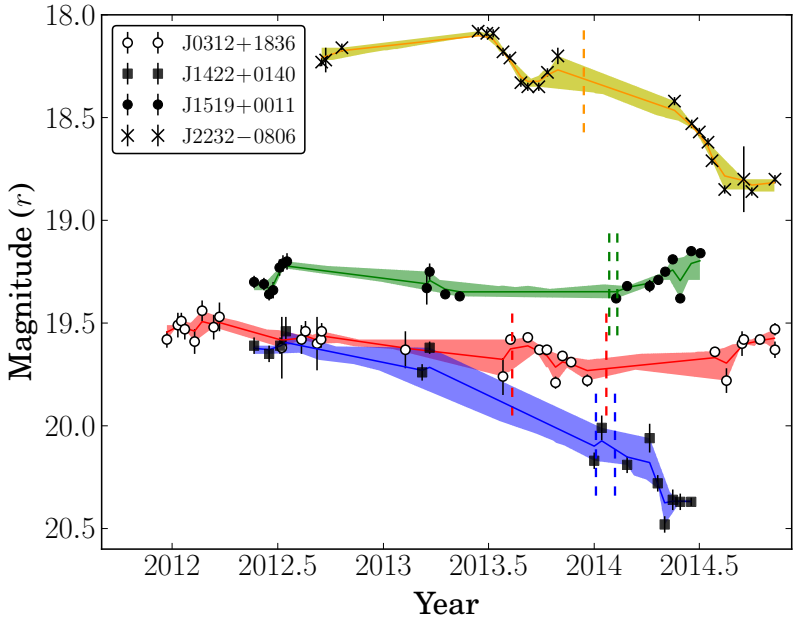

Figure 6.2: The LT light curves for the four HVAs. I utilise linear interpolation to measure the magnitude at the epoch of *XMM* observation, and a bootstrap subsampling technique to estimate the 1σ error (shaded regions) on these measurements. The dates of the *XMM* observations are again marked by vertical dashed lines. On this scale, it appears there is statistically significant intrinsic variability, on top of the global variability, in some objects.

6.4 Estimating Black Hole Mass in HVAs

As in Chapters 3, 4 and 5, I make single epoch virial $M_{\rm BH}$ estimates (described in Section 1.4) for each of the four HVAs. Spectra only covers optical wavelengths, so I must use the Mg II line in the three highest redshift objects, and apply the method of McLure & Dunlop (2004). For the lower redshift J2232−0806, I can make an estimate of $M_{\rm BH}$ using the well-studied Balmer emission lines, Hα and Hβ, and the methods of Greene & Ho (2005) and Woo & Urry (2002) respectively.

For the HVAs, I obtained optical spectra using WHT/ISIS from several epochs. Spectra were normalised to the LT g-band light curve, to mitigate uncertainty in the flux calibration. The data collection and reduction is described in Lawrence et al. (2016) and Bruce et al. (2016). I correct these spectra for MW extinction, using the dust maps of Schlegel et al. (1998) and the extinction law of Cardelli et al. (1989), and then decompose the broad emission lines using the following standard procedures, as employed by e.g.

Greene & Ho (2004), Wang et al. (2009), Shen & Liu (2012) and Matsuoka et al. (2013), amongst others. The underlying optical continuum in AGN approximates to a power-law over limited wavelength ranges, and the profiles of the broad emission lines can be modelled by a combination of Gaussian components. The blended Fe II emission observed in many AGN can also be modelled using templates derived from local AGN.

As these HVAs have by definition undergone a significant increase in brightness not typical of AGN, determining the luminosity for the $M_{\rm BH}$ calculation is model dependent. If the cause of the flux increase is an accretion rate change (scenario A), one should assume that the observed flux is the intrinsic level, and the corresponding continuum/line luminosity gives the best representation of the BLR size. For this case, I therefore use the WHT spectra as observed, applying no scaling factor.

Alternatively, if the cause of the variability is microlensing (scenario B), then the unlensed continuum level would be below that observed. For this situation, one should calculate the continuum/line luminosity from the spectra normalised to the HVA quiescent state. I normalise to the SDSS magnitude, using this in preference to the fitted polynomial as the SDSS photometry largely governs the minimum of the polynomial fit (Fig. 6.1). Table 6.2 illustrates the agreement between these two methods.

I then fit the following components:

i. The continuum underneath the emission lines is modelled as a power law of the form given in equation 3.3.1. I do not model the Balmer continuum, which could contribute to the continuum under Mg II, as I only use a small part of the spectrum around the Mg II line itself, and the power-law approximation is sufficient.

ii. The blended Fe II emission is modelled using the template of Véron-Cetty et al. (2004) in the optical, and Vestergaard & Wilkes (2001) in the UV, both of which are derived from studies of the Type 1 AGN I Zwicky 1. This component has two free parameters: the normalisation and width of the convolving Gaussian.

iii. Emission lines are modelled as a sum of Gaussians. In the first three objects, of higher redshift, I model only Mg II, with two Gaussian components. I do not attach a

physical significance to these components and do not attempt to model the Mg II line as a doublet, for the same reason as Shen & Liu (2012); the line splitting is too small to be significant. For J2232−0806, I model Hα and Hβ with three components each (one narrow and two broad), which are locked together in velocity width and amplitude ratio. I also model the narrow [O III] doublet with two components for each member, and the two lines are fixed at a 2.98:1 ratio (Storey & Zeippen 2000). Finally I model He II with one component. I do not model the narrow [N II] doublet that is often seen on top of the Hα profile, as there is no detected [S II] doublet redward of Hα, which indicates that [N II] contribution will be similarly negligible. The narrow components in Hα and Hβ are fixed to the same velocity width as [O III].

Redshifts were measured from the Mg II (J0312+1836, J1422+0140 and J1519+0011) and strong [O III] lines (J2232−0806). These are given in Table 6.1. $M_{\rm BH}$ is then calculated according to equations 1.4.9 for Hα, 1.4.10 for Hβ and 1.4.11 for Mg II.

Multiple spectra were available for each object (between three and five), and I performed a spectral analysis on each, measuring $M_{\rm BH}$ from each spectrum independently and taking the mean as the best estimate. The standard deviation of these provides an estimate of the measurement uncertainty, which, it should be noted, is not the dominant source of error on such estimates. Example spectral deconvolutions are shown in Fig. 6.3, and the resulting $M_{\rm BH}$ estimates are tabulated in Table 6.3. I use a Levenberg-Marquardt minimisation algorithm to fit the data, and employ a sigma-clipping routine in J1422+0140 to reduce the effect of the narrow absorption features observed in that spectrum. I tabulate $M_{\rm BH}$ values for both cases where the spectra were scaled to the faint state, and where it was taken as observed. These correspond to the two different scenarios I explore in Section 6.6.2.

In principle, the two different approaches for estimating $M_{\rm BH}$ could provide an additional means of testing the lensing vs. accretion change hypotheses. $M_{\rm BH}$ is constant between observations, therefore if the continuum varies between WHT observations, the BLR ought to respond to this change. So in the event of the central engine becoming

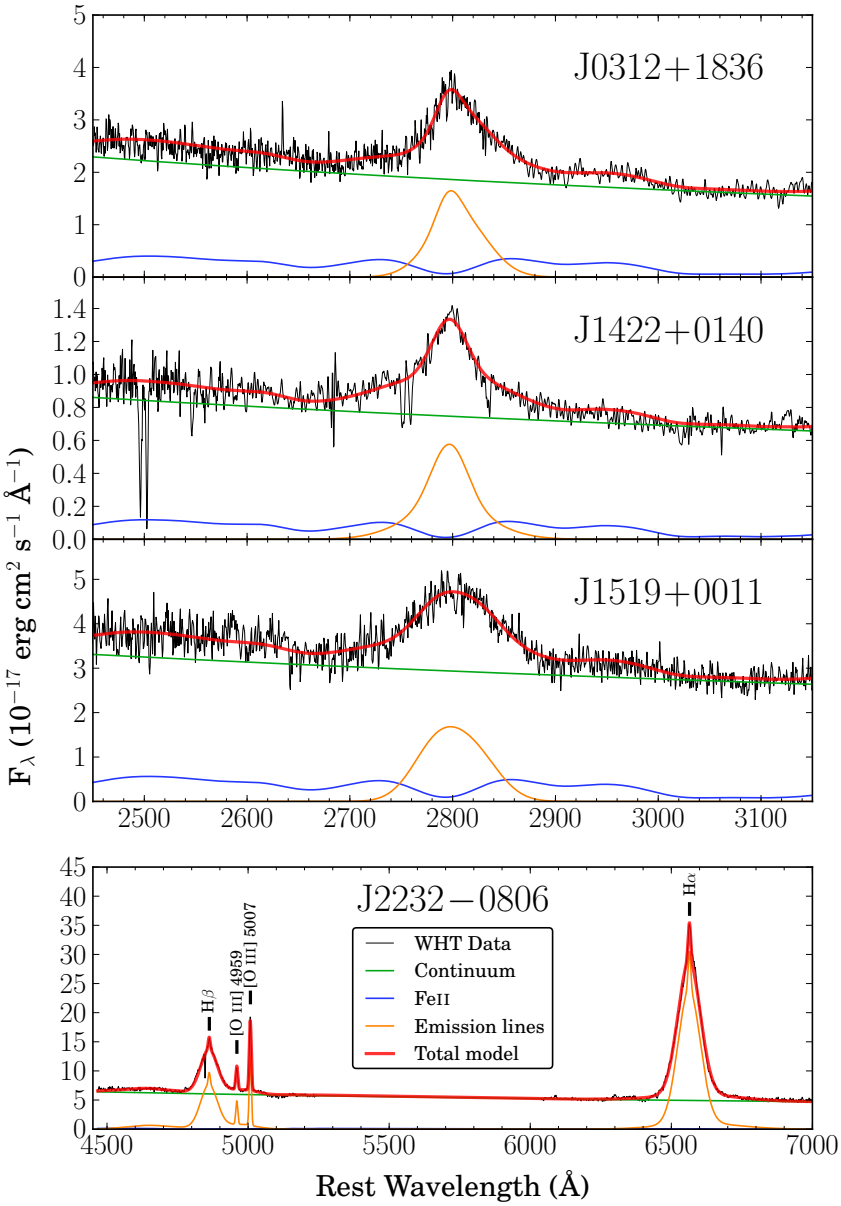

Figure 6.3: Examples of the model fits to the optical spectrum of each object. In black is the data from WHT, and red is the fitted model profile, with constituent components shown. The top three panels show the higher redshift objects, for which only Mg II is available for fitting, and the bottom panel shows J2232−0806, in which I model Hα and Hβ, in addition to the narrow [O III] doublet; these are marked. I fitted these models to every spectrum for each object (across multiple dates) and took the average as the best estimate. In the bottom panel, I masked out a region of the spectrum between Hα and Hβ, as it contained telluric sky features that would have affected the fitting. The cases shown here are for the spectra normalised to the quiescent state.

more luminous, the BLR would originate further from the source, and correspondingly the line velocity width would be smaller. Since for scenario A I analyse the spectra as observed, and for scenario B I scale to the quiescent state (which alters the continuum luminosity, but not the linewidth), it is possible that the $M_{\rm BH}$ estimates would be more closely grouped between epochs for the favoured model. However, I see no evidence for such an effect – the scatter arising from the method is too great.

The absorption features in J1422+0140 are consistent with originating from an intervening system. Whilst the doublet on the blue wing of the Mg II profile (at 2750 Å) is likely Mg II absorption in an outflowing component intrinsic to the AGN, the second doublet seen at 2500 Å in Fig. 6.3 is either Mg II absorption in an extreme outflow (at $0.1c$) or more probably in an intervening system at $z \simeq 0.855$. This could be a signature of the lens host galaxy, in scenario (B). More discussion and interpretation of these features is presented in Bruce et al. (2016).

Table 6.3: The key line properties for the sample, including FWHM, continuum/line luminosity and inferred $M_{\rm BH}$ (according to equations 1.4.9, 1.4.10 and 1.4.11). The error on $M_{\rm BH}$ is a measurement error only, and does not reflect systematic errors and uncertainties inherent in the method. I present $M_{\rm BH}$ values resulting from analysing the spectrum as observed (used in scenario A) and from normalising the spectra to the quiescent state (SDSS) magnitude (used for scenario B).

Name	Line	FWHM [km s^{-1}]	λL_λ or $L_{\rm line}$ [log(erg s^{-1})] (observed; A)	λL_λ or $L_{\rm line}$ [log(erg s^{-1})] (quiescent; B)	$M_{\rm BH,observed}$ [log($M_\odot$)] (A)	$M_{\rm BH,faint}$ [log($M_\odot$)] (B)
J0312+1836	Mg II	6000 ± 400	45.09 ± 0.07	44.330 ± 0.011	8.73 ± 0.03	8.26 ± 0.06
J1422+0140	Mg II	4800 ± 400	45.01 ± 0.17	44.146 ± 0.005	8.47 ± 0.10	7.95 ± 0.08
J1519+0011	Mg II	8100 ± 200	44.79 ± 0.07	44.004 ± 0.013	8.81 ± 0.07	8.33 ± 0.03
J2232−0806	Hα	4350 ± 70	43.08 ± 0.12	42.76 ± 0.08	8.20 ± 0.05	8.03 ± 0.04
	Hβ	4350 ± 70	44.20 ± 0.15	43.852 ± 0.011	8.08 ± 0.10	7.86 ± 0.02

6.5 X-ray Spectrum and Variability

I extracted the *XMM-Newton* pipeline products from the *XMM* science archive. The objects are not extended, and are not bright enough for pile-up effects to occur. To maximise the S/N of the X-ray spectrum, I use all available data for each object, from the three EPIC detectors: MOS1, MOS2 and PN.

As in Chapter 3, I first carry out an analysis of the X-ray spectrum only, by fitting an absorbed power-law to the X-ray spectral data. This model is simple, but at the redshift of these objects it ought to be appropriate, given the relatively low count numbers. I incorporate absorption components attributable to both the MW (fixed) and the host galaxy (free). I am able to test for any statistically significant variability between observations in J0312+1836 and J1519+0011 – the two objects for which there is useable data from two epochs. I use Galactic $N_{\rm H}$ values from the Leiden/Argentine/Bonn survey (Kalberla et al. 2005).

X-ray exposure times and count values are given in Table 6.4, together with the fitted parameters and 90 per cent confidence limits.

The intrinsic $N_{\rm H}$ in each object is low. This may be because the HVAs are at moderate redshifts, so only the tail of the photoelectric absorption profile is sampled by the X-ray spectrum, and have relatively low count numbers, increasing the uncertainty on $N_{\rm H,\,int}$. A specific example of this is evident in the second observation of J0312+1836, where the observation with just ~ 200 counts shows a broad 90 per cent confidence limit on $N_{\rm H,\,int}$.

A range of power-law slopes (Γ) is observed. Flat power law slopes are characterised by $\Gamma = 2$, as seen in J1519+0011, soft slopes by $\Gamma > 2$, as seen in J0312+1836 ($\sim 3\sigma$ significance) and J2232−0806 ($\sim 9\sigma$ significance), and hard slopes by $\Gamma < 2$, which are observed in J1422+0140 to a smaller ($\sim 2\sigma$) significance.

There is evidence for statistically significant ($\simeq 4.5\sigma$) variability between the observations of J1519+0011, despite these observations being just 14 days apart. It is seen that whilst Γ is consistent between the two observations, the normalisation has decreased, indicating that the object faded between observations. The optical light curve over the same period (Fig. 6.2) does not show a significant change, possibly due to larger scatter

Table 6.4: The X-ray spectra model properties. Photoelectric absorption components for both the MW (fixed) and the host galaxy (free) are modelled. In some observations, the host galaxy absorption is not well-constrained, due to both the redshift and number of counts. The EPIC count errors are 1 σ, and the errors on the model parameters are 90 per cent confidence limits, in line with convention in X-ray astronomy. I also quote Γ and its uncertainty to two decimal places. The exposure time is the full observation time on target, including time that was determined by the *XMM* pipeline to be 'bad'.

Name	Obs. UT	Exp. Time (s)	*XMM* EPIC Cts	$N_{\mathrm{H,MW}}$ ($\times 10^{20}\,\mathrm{cm}^{-2}$)	$N_{\mathrm{H,int}}$ ($\times 10^{20}\,\mathrm{cm}^{-2}$)	Γ	Norm (1 keV) ($\times 10^{-6}$ Ph. / cm^2 s keV)	χ^2_{red}
J0312+1836	2013-08-12	35 100	1130±40	8.02	0^{+6}_{-0}	$2.26^{+0.14}_{-0.12}$	$24.6^{+1.9}_{-1.5}$	0.99
	2014-01-22	29 500	205±16	8.02	10^{+40}_{-10}	$2.46^{+0.57}_{-0.36}$	16^{+7}_{-4}	1.70
J1422+0140	2014-02-06	34 500	1320±40	2.57	0^{+14}_{-0}	$1.73^{+0.18}_{-0.09}$	$15.6^{+2.2}_{-0.9}$	1.12
J1519+0011	2014-01-27	23 700	4250±70	4.57	0^{+2}_{-0}	$1.96^{+0.06}_{-0.05}$	90^{+4}_{-3}	1.01
	2014-02-10	28 000	4850±70	4.57	$0.0^{+0.9}_{-0.0}$	2.04±0.05	80^{+2}_{-2}	1.05
J2232−0806	2013-12-14	29 500	9300±100	4.11	$0.0^{+0.4}_{-0.0}$	2.21±0.04	284±7	1.10

and insufficient temporal sampling. There could therefore be a differentially fading X-ray component in J1519+0011, or this could be due to fast X-ray variability commonly seen in AGN (e.g. Gierliński et al. 2008, Parker et al. 2015). It is possible the significance of this event could be exaggerated by residual background activity not fully taken into account in the reduction process.

I also test for short-term variability during the observations of each target. Given the relatively low count numbers, this is achieved by fitting the short term light curve (~ 100 count bins) with a constant. I only use the 'good' on-target time, where background activity was low, and use the full $0.2-12$ keV range. Deviation from unity in the $\chi^2_{\rm red}$ fitting statistic can provide evidence for such variability, but this is not observed in any object. There is therefore no suggestion of statistically significant, short-term X-ray variability in any of the objects.

6.6 Broad-band Spectral Energy Distribution

6.6.1 SED Construction

In the optical regime, I use the WHT spectrum that was observed closest to the *XMM* observation date, and normalised in the *r*-band to the *XMM* observation epoch (see Section 6.3). I follow the same approach as described in Chapter 3, defining bins expected to be free from emission features (Fe II, emission lines and the Balmer continuum).

The HVAs all have photometry from the *XMM* OM. This photometry is expected to be biased high by the presence of emission features in the bandpass of each filter. I correct for this by estimating the flux surplus using the Vanden Berk et al. (2001) quasar template and derived power-law continuum, combined with the effective bandpass of each OM filter at each redshift. By integrating the template over the OM bandpasses to simulate the total flux measured (including emission features) and then integrating the power-law continuum over the same bandpasses to simulate the true continuum level, I estimate the factor by which emission features increase the observed flux in each band. I then scale the OM photometry to correct for this difference, so the OM data represents the continuum

flux level. Elvis et al. (2012) demonstrated that variation in the equivalent width of the Ly-α emission feature made utilising a single value from a template unreliable. Hence I did not include the UVM2 band in J0312+1836 in the modelling, as it lay directly on top of Ly-α. The correction factor, $f_{\rm corr,OM}$, was typically $0.8 \lesssim f_{\rm corr,OM} \lesssim 0.9$, dependent on the filter and redshift of each object.

I do not use data from the 2MASS, UKIDSS or *WISE* to extend the SED into the IR, or *GALEX* to extend into the UV, as I require quasi-simultaneous data. Also, the objects were often below the detection threshold of these surveys, at the time of observation.

6.6.2 SED Modelling

I apply the OPTXAGNF SED model, combined with extinction and absorption models, to each object. Data from *XMM-Newton* (including the OM) and continuum regions of the WHT spectrum are fitted.

The attenuation variables are the MW reddening, $E(B-V)_{\rm MW}$, (fixed using values from Schlafly & Finkbeiner 2011), the intrinsic reddening, $E(B-V)_{\rm int}$ (free), and, as in Section 6.5, the hydrogen column densities for the photoelectric absorption – $N_{\rm H,MW}$ and $N_{\rm H,int}$. Following the procedure described in Chapter 3, I test SED models both with and without attenuation attributable to the AGN host galaxy. However, as found in that study (see also Capellupo et al. 2015 and Castelló-Mor et al. 2016) the model with host galaxy reddening/absorption produces a better model fit in all cases, when allowing for the additional free parameters. I therefore consider SED models that include these components from this point onwards. I tested two extinction curve models for the intrinsic reddening: MW and SMC. All objects were better fit with the MW extinction curve, but the difference in $\chi^2_{\rm red}$ was marginal between the two cases in J2232−0806.

Due to the redshift of the objects, and the quality of the X-ray data, the SX component is not well-sampled by the *XMM* data. In Chapter 3, it was found that the inclusion of the SX was justified as it was partially sampled in high-mass ($M_{\rm BH} > 10^9 M_\odot$) objects. However, that sample was of higher redshift ($z > 1.5$), and consequently higher $M_{\rm BH}$ (McLure & Dunlop 2004). For the current sample, I initially applied two versions of the

model; one with a dominant SX (contributing 70 per cent of the reprocessed energy – e.g. Done et al. 2013 – which was then allowed to vary), and one with no SX. I found that in some cases the model including the SX was not physical (e.g. because all AD energy was reprocessed by the SX and PLT). J2232−0806 did show evidence for an improved fit with the SX component ($\chi^2_{\rm red}$ of 1.07 compared to 1.11 without the SX component), however, the difference in end result was small. Therefore, in the interest of simplicity and consistency I opted to use the simplified, two component (AD and PLT) version of OPTXAGNF.

Using an energetically self-consistent accretion model allows me to compare the two mechanisms (A and B, see Section 6.1.2) for the increase in brightness of these HVAs. If the change is intrinsic (scenario A), then the spectral data will represent the energy flux of a conventional AGN that has seen an increase in accretion rate. In the event that the increment in brightness is due to a foreground microlensing event (scenario B), then the intrinsic flux of the AGN must be a significant factor smaller than that observed, corresponding to a smaller mass accretion rate.

I test these two scenarios, by producing corresponding models for each object:

A. No lens factor. The model is fitted to the data with no additional factors applied.

B. Including a lens factor. I model the lens as a constant factor boosting the observed flux at all wavelengths.

This enables me to directly test the microlensed hypothesis and look for evidence of unusual effects, by comparing the inferred properties with those of larger AGN samples. As discussed in Section 6.4, I have estimated $M_{\rm BH}$ for each of these situations, and will therefore use a different $M_{\rm BH}$ estimate for the two scenarios, which is fixed in the fitting. The resulting model properties are tabulated in Table 6.5 and the SEDs for both cases are shown in Fig. 6.4. The only fitted property I do not show is $N_{\rm H,int}$, as these are all at or close to zero, as in Table 6.4.

Table 6.5: The optimum fitted parameters for the various SED models. Uncertainties quoted are the 90 per cent confidence limits, as is conventional in X-ray astronomy, and are estimated using the Fisher matrix. As such, they are only indicative of the true measurement error. Columns are as follows: (1) object name, (2) the lens factor, if applied – this is a constant factor that multiplies the model flux at all energies, and derives from Δm in Table 6.2, (3) log bolometric luminosity [log (erg s^{-1})], (4) log luminosity density at 2500 Å [log (erg s^{-1} Hz^{-1})], (5) log luminosity density at 2 keV [log (erg s^{-1} Hz^{-1})], (6) $\alpha_{\rm OX}$ spectral index (e.g. Lusso et al. 2010), (7) intrinsic $(B-V)$ extinction [mag], (8) reduced mass accretion rate [$\dot{M}_{\rm Edd}$], (9) coronal radius [$R_{\rm g}$], (10) outer disc radius [$R_{\rm g}$], (11) PLT spectral index, (12) $\chi^2_{\rm red}$ fitting statistic, (13) degrees of freedom.

Name	$f_{\rm lens}$	$L_{\rm bol}$	$L_{2500\text{Å}}$	$L_{\rm 2keV}$	$\alpha_{\rm OX}$	$E(B-V)$	$\dot{m}$	$r_{\rm cor}$	$r_{\rm out}$	Γ	$\chi^2_{\rm red}$	DOF
(1)	(2)	(3)	(4)	(5)	(6)	(7)	(8)	(9)	(10)	(11)	(12)	(13)
Model A: No lens factor. $M_{\rm BH} = M_{\rm BH,observed}$ in Table 6.3.												
J0312+1836	N/A	45.87±0.12	30.25	26.44	1.46	0.07±0.02	0.12±0.03	13±2	93±8	2.24±0.11	1.83	58
J1422+0140	N/A	45.72±0.10	30.04	26.53	1.35	0.06±0.03	0.12±0.03	20±13	>1000	1.75±0.10	1.15	54
J1519+0011	N/A	45.8±0.3	30.10	26.50	1.38	0.16±0.06	0.09±0.06	13±4	49±3	2.00±0.03	1.11	360
J2232−0806	N/A	45.30±0.17	29.49	26.31	1.22	0.00±0.04	0.10±0.04	30±20	120±6	2.20±0.05	1.11	222
Model B: With lens factor. $M_{\rm BH} = M_{\rm BH,faint}$ in Table 6.3.												
J0312+1836	4.53	45.27±0.14	29.57	25.78	1.46	0.07±0.03	0.08±0.03	12±2	134±13	2.24±0.11	1.83	58
J1422+0140	6.43	45.0±0.2	29.25	25.72	1.35	0.06±0.05	0.08±0.04	17±6	>1000	1.75±0.09	1.15	54
J1519+0011	4.66	45.1±0.3	29.40	25.83	1.37	0.15±0.07	0.05±0.04	13±4	71±5	2.00±0.03	1.11	360
J2232−0806	2.25	44.95±0.09	29.14	25.96	1.22	0.000±0.019	0.065±0.014	29±14	119±7	2.20±0.05	1.11	222

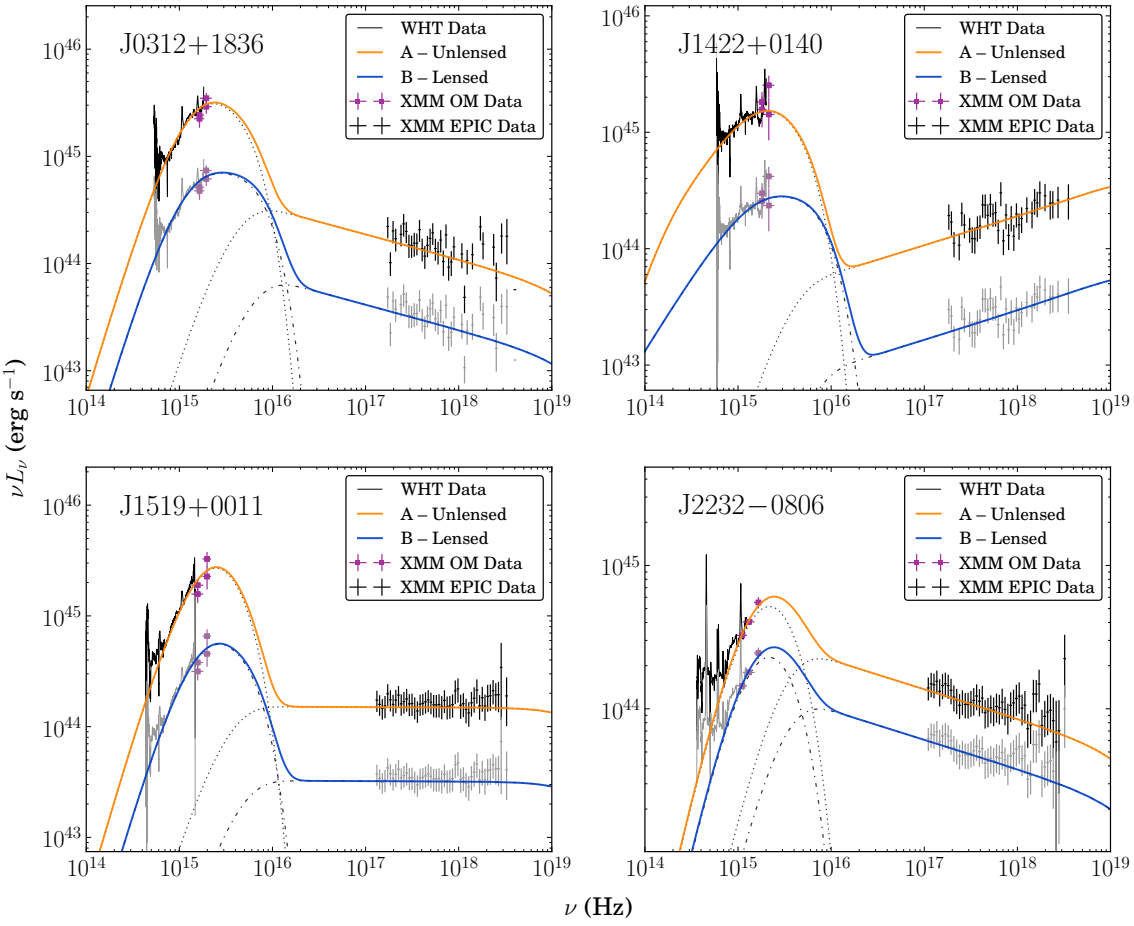

Figure 6.4: Modelled SEDs for both unlensed and lensed scenarios. In the lensed scenario, I assume that the observed data has been boosted, and that the intrinsic flux is lower than observed. In these plots, I show the intrinsic SED in each case; for model B, I therefore scale the data down to the implied intrinsic flux, shown in grey. Model constituent components (AD and PLT) are shown by the dotted and dash-dotted lines.

6.7 Discussion

6.7.1 SED Model

I compare my results with a much larger AGN sample to test the hypothesis that one model is more representative of the wider AGN populace, and hence favoured. One such sample was presented in Lusso et al. (2010) (hereafter L10).

L10 presented SEDs for a large, X-ray selected sample of 545 Type 1 AGN, drawn from the *XMM-Newton* Cosmic Evolution Survey (COSMOS) sample. They estimated the multi-waveband SEDs for their sample using multiple polynomial interpolations and extrapolated power-laws through their data in $\log(\nu L_\nu)$ space. This method does not apply any physical considerations to the procedure, but adheres to known constraints (e.g. range of the PLT). I compare my calculated values for $L_{2500\text{Å}}$, $L_{2\text{keV}}$ and α_{OX} with those in the L10 sample – see Figs. 6.5, 6.6, 6.7. α_{OX} is an often-used measure of the relative X-ray loudness of an AGN, and is defined in equation 3.4.2.

I plot the linear best fit relations derived in L10 using the method of Isobe et al.

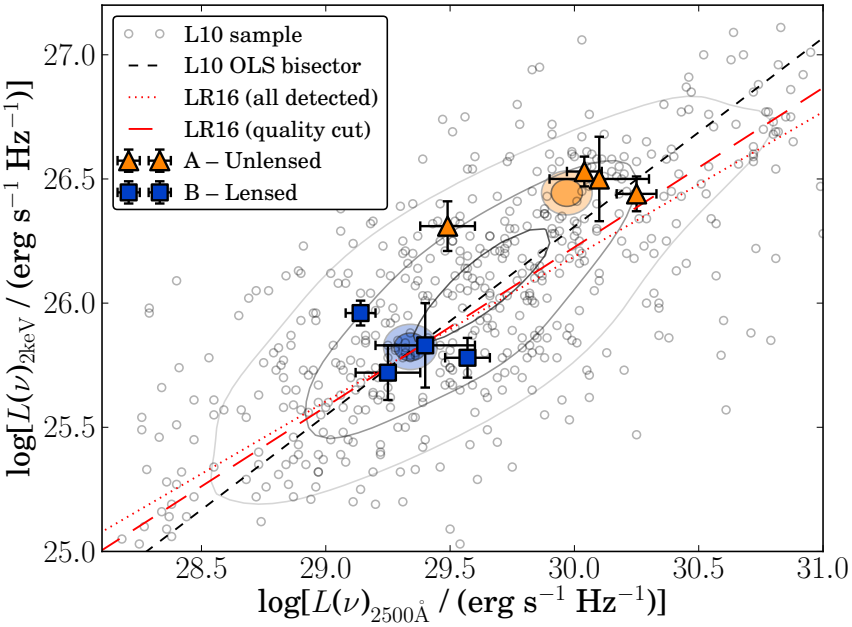

Figure 6.5: The L10 sample, $L(\nu)_{2\text{keV}}$ against $L(\nu)_{2500\text{Å}}$ with my sample (blue and orange) over-plotted. LR16 relations are also shown. The contours illustrate the distribution of the L10 sample, and the ellipses show the centroids of my sample (1 and 2σ significance levels).

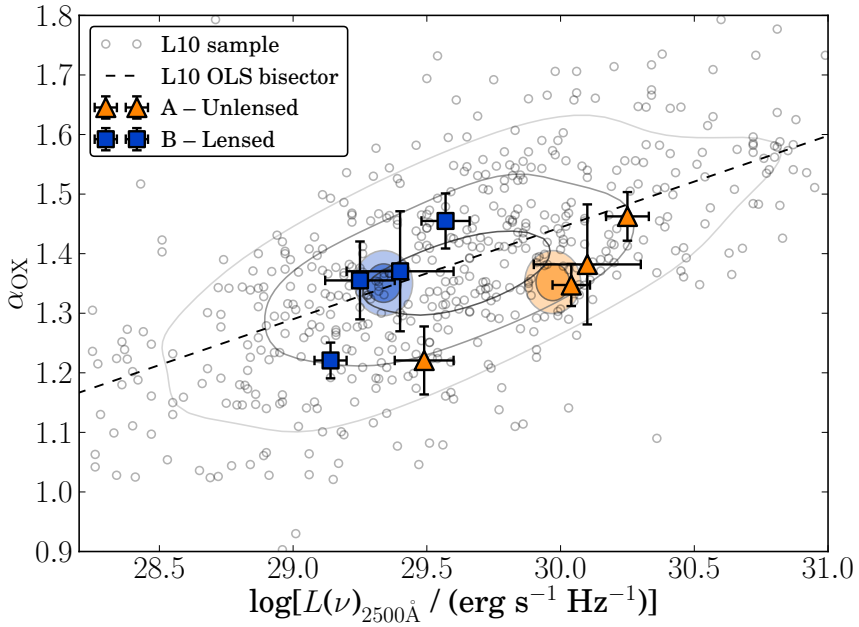

Figure 6.6: The L10 sample, α_{OX} against $L(\nu)_{2500Å}$ with my sample (blue and orange) overplotted.

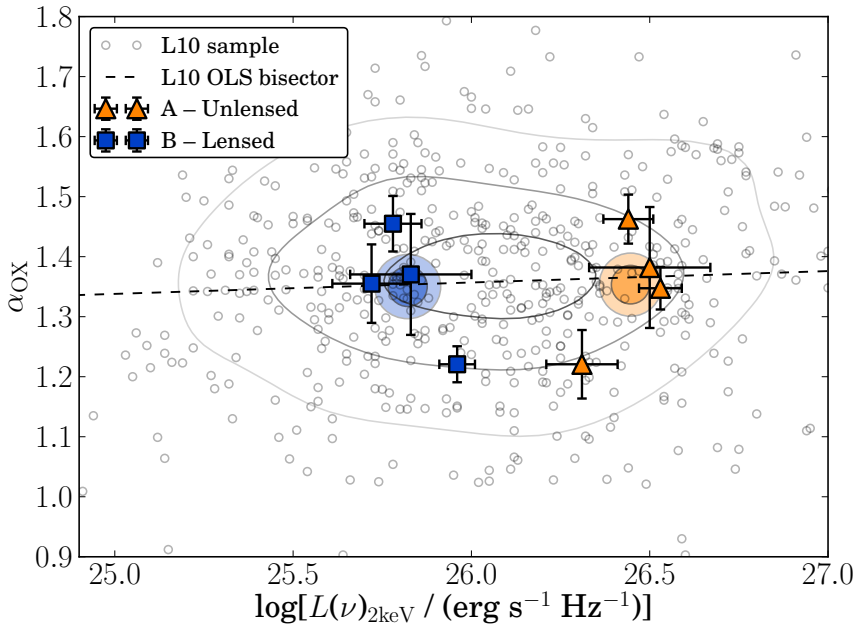

Figure 6.7: The L10 sample, α_{OX} against $L(\nu)_{2keV}$ with my sample (blue and orange) overplotted.

(1990). The ellipses show the 1σ and 2σ error regions for the HVA sample centroid of each tested model. These regions are calculated using a Monte Carlo method, similar to that described in Section 6.3. The central 68 and 95 per cent of these centroid distributions are an indication of the 1 and 2σ error boundaries respectively. To guide the eye, I also overlay contours from a bivariate Gaussian kernel-density estimate of the L10 sample distribution.

In Fig. 6.5, I also show the linear relations derived in Lusso & Risaliti (2016), hereafter LR16. The LR16 sample comprises 2153 AGN detected in both SDSS and the *XMM* serendipitous source catalogue. They calculated $L_{2\mathrm{keV}}$ from the *XMM* EPIC total energy fluxes, assuming a constant photon index and neutral hydrogen column. $L_{2500\text{Å}}$ values were provided in the Shen et al. (2011) catalogue. This approach differs from that in L10, but there is agreement between the studies with respect to the $L_{2500\text{Å}}$–$L_{2\mathrm{keV}}$ relation. LR16 showed that by applying various quality cuts, the dispersion of this relation drops significantly. In Fig. 6.5 the relation derived from the full LR16 sample is shown by the red dotted line, and the relation emerging from the best-quality subsample (743 objects) by the red long-dashed line. At the time of writing, the full LR16 sample was not available electronically, so I cannot compute α_{OX} values for comparison in Figs. 6.6 and 6.7.

Due to the wide range of SED properties in the L10 sample, this does not indicate a clear preference for one model over another – the inferred properties in each given model lie within the distribution of the much larger L10 sample. Model A lies further from the linear relations than model B in Figs. 6.5 and 6.6. This indicates (to $> 2\sigma$) that in model A, the four HVAs are systematically UV underluminous for their corresponding X-ray luminosities, compared to the larger sample. To increase the significance of this finding, more X-ray data are required, to expand the sample of HVAs.

The comparison with L10 and LR16 ought to be reasonable; whilst our approaches for calculating the SEDs differ, I am primarily concerned with $L(\nu)_{2500\text{Å}}$ and $L(\nu)_{2\mathrm{keV}}$, which are well-sampled, and thus well-defined by our various approaches. Uncertainty may arise in $L(\nu)_{2500\text{Å}}$ due to differing means of correcting for intrinsic reddening. Owing to the

limited quality of their data, L10 make only simple corrections for host galaxy reddening. Unfortunately, AGN samples that utilise more advanced SED models addressing these limitations either cover limited redshift ranges (e.g. Jin et al. 2012a), or lack X-ray data (e.g. Capellupo et al. 2015), in addition to being much smaller. However, LR16 explore the effects of a number of quality criteria (including reddening) in their large sample of AGN. They find that whilst the dispersion of the $L(\nu)_{2500\text{Å}}$–$L(\nu)_{2\text{keV}}$ relation is dependent on such criteria, the relation itself is not. Therefore my findings should not be affected by this source of uncertainty.

One can also consider the average AGN templates of Jin et al. (2012a) as being representative of the archetypal AGN SEDs at different accretion rates, as they use the same model as in this chapter, applied to a larger, more local AGN sample. In terms of α_{OX}, as a sample, the HVAs appear to most closely resemble the average SED for objects with moderate linewidths. However, even within four objects, a broad range of X-ray spectral shapes is seen ($1.8 \lesssim \Gamma \lesssim 2.2$) that almost covers the full range of SEDs observed by Jin et al. (2012a). For instance J0312+1836 shows an unusually soft X-ray spectrum, compared to the average SED in Jin et al. (2012a), for an object at the accretion rates predicted in either case. To this end, a more conclusive result would require a larger sample of HVAs with X-ray data.

In both situations I generally predict moderate intrinsic reddening ($E(B-V) \simeq 0.07$, $n = 4$ objects). This is a little higher than typical extinction values determined in Chapter 3 (mean $E(B-V) \simeq 0.04$, $n = 11$ objects) and Capellupo et al. (2015) (mean $E(B-V) \simeq 0.02$, $n = 30$ objects). My sample only comprises four objects, so it is impossible to say this is a true trend among HVAs. But higher-than-usual extinctions may be expected if there are two galaxies (i.e. both AGN host galaxy and lens host galaxy) extinguishing the optical/UV light. These reddening curves would be at different redshifts (i.e. the host and lens host galaxy), but better data coverage and S/N would be required to deconvolve these two contributions, especially as the total reddening observed is < 0.1 mag.

The intrinsic extinction parameter is dependent on the slope of the optical spectrum. Other factors that could affect the spectral slope are the outer AD radius, and host galaxy contamination (potentially with an additional lens host galaxy, if these are indeed microlensed AGN). I do not model the host galaxy component in this study, as I do not expect it to make a significant contribution to the SED blueward of Hβ (Shen et al. 2011, Chapter 3). I tested a version of the model where the outer disc radius was fixed at 1000 R_g, but in 3 objects the fit was marginal.

The evidence seen for a fading X-ray component (Section 6.5) in J1519+0011 is interesting, as if it continued to fade at that rate (i.e. significantly faster than the optical), it could suggest differential magnification of the source, and provide a probe of the corona size. To confirm this would require follow up observations with *XMM-Newton*.

6.7.2 Additional Uncertainties

There is good agreement between the scaled optical (WHT) data and the corrected UV (*XMM* OM) data, suggesting that it is reasonable both to normalise the WHT spectrum in the *r*-band using the light curve, and to correct the OM data for emission feature contamination using the Vanden Berk et al. (2001) template and power-law continuum.

It should be noted that in order to estimate $M_{\rm BH}$ in the lensed case (Model B), I scaled each source to the brightness level of the quiescent state, which was assumed to be represented by the SDSS magnitude. However, in cases where the SDSS observations are dominated by the host (or foreground) galaxy, the AGN flux could be fainter. In this case, $M_{\rm BH}$ would be smaller, meaning an AD that peaks further into the UV, with higher mass accretion rates. The $M_{\rm BH}$ values for the lensed case should therefore be considered upper limits.

A final caveat is that if the BHs are spinning, the radius of last stable circular orbit is reduced and a co-rotating AD can extend closer to the event horizon, shifting the AD peak blueward. Unfortunately the data are insufficient to make a judgement of the BH spin.

6.8 Summary and Conclusions

I have presented results from X-ray observations of four extremely variable AGN (termed 'hypervariable AGN', or HVAs) discovered in the Pan-STARRS database (Lawrence et al. 2012a, 2016). To explain this variability I consider two distinct scenarios – (A) and (B). In (A), this change is intrinsic (e.g. caused by a large increase in mass accretion rate), and in (B), the flux has been increased by a foreground microlensing event. Such an event could result from a star in a foreground galaxy passing directly between us and the AGN central engine, magnifying the flux from the AGN by a significant factor. I explore these two scenarios through an analysis of their SEDs.

I have estimated the magnitudes of each AGN in both faint and bright states, and also at the epoch of the *XMM-Newton* observation, using optical photometry light curves. I then use optical spectra from WHT/ISIS to estimate $M_{\rm BH}$ from the profiles of the broad emission lines Mg II and Hα. For (A) I analyse the spectra as observed, and for (B), I scale them to the faint (assumed to represent the intrinsic) state.

I then fit an energy-conserving, broad-band SED model to the multiwavelength data for each object. This approach allows me not only to characterise the energetics for each scenario, but also constrains the accretion flow properties, including the SED shape, which is dependent on the mass accretion rate.

I compare the properties of the models for each of the four objects, in both scenarios (A and B) with the Lusso et al. (2010) and Lusso & Risaliti (2016) samples. The four HVAs show distinct groupings of (A) and (B) in SED shape versus luminosity parameter space. In model (A), I see evidence that the AGN are underluminous in the UV regime for their corresponding X-ray luminosities, compared with model (B).

This provides an important additional diagnostic of the expected arrangement of these HVAs, which are clearly consistent with a microlensing origin. With a larger sample of X-ray observed HVAs, it is hoped that the significance of these findings can be increased.

CHAPTER 7

Summary and Future Work

7.1 Synopsis of Key Findings

In recent decades, progress has been made into the physical processes powering AGN spectral energy distributions (SEDs), but many key questions remain unanswered. Several research groups have carried out recent SED modelling analyses to quantify the energetics of AGN, but have faced a variety of limitations, some of which this thesis sets out to resolve. In three papers and three pilot studies, I explore the accretion flow in several AGN samples, through systematic investigations of their SED properties.

I introduce the data sources and models used throughout in Chapter 2. An overview of the capabilities and limitations of each telescope and survey is given, including the reduction processes that generate useful astronomical data from the raw observations. I then discuss the theoretical emission models used throughout, including computational aspects relevant to this thesis. The primary SED model used is OPTXAGNF, described in Done et al. (2012). This model is composed of three spectral components – a geometrically thin, optically thick accretion disc (AD), power-law tail (PLT) arising from Compton upscattering in a hot, optically thin corona and the ubiquitous soft X-ray excess (SX), ascribed to warm inverse Compton scattering in the disc. Energy is conserved between these components.

In Chapter 3, I present science results from an SED study of 11 medium redshift ($1.5 < z < 2.2$) AGN. This sample was specifically chosen to preferentially select more luminous AGN with greater BH masses, which host cooler ADs peaking at, or close to, observable wavelengths. By combining archival data and new observations, our objects

have excellent multi-frequency coverage; all have optical spectra from the SDSS, IR spectra from GNIRS and TSpec, and X-ray spectra from *XMM-Newton*. I apply OPTXAGNF to fit the multiwavelength data, fixing the BH mass to a value calculated from the profile of Hα. Five out of the 11 AGN show evidence of a partially sampled SED peak, allowing me to accurately measure their bolometric luminosity from these models and estimate their mass accretion rates. This reduces the model dependent uncertainties of earlier studies such as Jin et al. (2012a), and reduces the degeneracies accordingly. I find that nearly all of the AGN are accreting close to or in excess of the Eddington rate, and that the optical–IR spectra are in general well-described by the thin AD model, with some contribution from the SX in the highest mass AGN. The optical to X-ray spectral indices suggest that these AGN are high mass analogues of the rapidly accreting Narrow Line Seyfert 1s seen at $z \lesssim 0.3$. The SX is poorly sampled in the lower mass AGN, as the AD peak lies in the unobserved FUV in these objects. Based on my limited sample, I suggest that estimating bolometric luminosities from $L_{5100\text{Å}}$ and $L_{2-10\,\mathrm{keV}}$ may be unreliable, as has also been noted for a low-redshift, X-ray selected AGN sample.

I continue my analysis of these 11 AGN in Chapter 4. I first discuss and quantify several sources of uncertainty in the SED parameter space, including the intrinsic extinction, the BH masses (M_{BH}) and BH spin. A range of BH spin values are tested, and I find that while low to moderate spin values ($a_* \leqslant 0.9$) are compatible with the data in all cases, higher spin values ($a_* \geqslant 0.99$) require relativistic corrections to the model, and a face-on accretion disc to describe the data. The outer AD radii are well-constrained in 8/11 objects, and are found to be a factor ~ 5 smaller than the self-gravity radius. I then extend the SED models of these 11 AGN into the mid-IR regime with *WISE* photometry by including components for the host galaxy and dusty torus. My estimates of the host galaxy luminosities are consistent with the M_{BH}–bulge relationship, and the measured torus properties (covering factor and temperatures) are in agreement with earlier work, suggesting a predominantly silicate-based grain composition. Finally, I deconvolve the optical–NIR spectra using the SED continuum model.

These studies provide several new insights into the AGN central engine that will help to determine productive future directions for SED research. Firstly, I have suggested that even in highly accreting objects, the rest frame optical–NUV continuum can still be well-

described by a thin AD, in spite of earlier suggestions that this assumption may break down above $\dot{m} \sim 0.2$ (e.g. Abramowicz et al. 1988, Capellupo et al. 2016). However, this also raises questions, as the outermost AD radii I have measured are consistently smaller than the self-gravity radius, which was previously proposed as the condition under which the disc breaks up (e.g. Goodman 2003). Nonetheless, the strong constraints on AGN luminosity, and versatility of the model for the optical–NIR spectral decomposition, present a robust and repeatable means of testing the condition most strongly governing the strength of spectral narrow-lines. The narrow lines are weakest in the most most luminous AGN, suggesting that this dynamically unbound region is heavily suppressed by radiation pressure.

There is currently much interest in inferring information about BH spin, one of only two properties intrinsic to the BH, and a key diagnostic of its formation history. Simulations suggest a range of possible growth mechanisms, which have differing implications for the spin distribution of AGN. Fanidakis et al. (2011) suggested that prolonged, unidirectional accretion episodes would result in all AGN attaining maximal spins, which I have found to be unlikely. More plausibly, only the most massive AGN host highly spinning BHs, lending weight to the Dotti et al. (2013) and Volonteri et al. (2013) models of BH growth, or chaotic accretion modes in the Fanidakis et al. (2011) models.

Finally, I present an optical to X-ray spectral investigation of four 'hypervariable AGN' (HVAs) discovered by comparing Pan-STARRS data to that from SDSS over a 10 year baseline. A range of mechanisms for the origin of these HVAs have been explored in Lawrence et al. (2016). Based on the timescales, luminosities and light curves of these events, the most plausible are that either (A) the HVAs are atypical AGN that have undergone a large increase in luminosity, or (B) a star in a foreground galaxy has microlensed an otherwise normal AGN. I explore these two scenarios through a study of their optical–X-ray SEDs. The black hole masses, which depend on the intrinsic luminosity, are calculated, based on the Mg II and Hα emission line profiles. The mass ranges are $\log(M_{\rm BH}/M_{\odot}) = 8.2 - 8.8$ for scenario (A) and $\log(M_{\rm BH}/M_{\odot}) = 7.9 - 8.3$ for scenario (B). I then fit energy conserving models to the SEDs, obtaining strong constraints on the bolometric luminosity and $\alpha_{\rm OX}$. I compare the SED properties with a larger, X-ray selected AGN sample for both of these scenarios, and observe distinct groupings in

spectral shape versus luminosity parameter space. In scenario (A), there is evidence that the AGN are underluminous in the UV regime for their corresponding X-ray luminosities, compared with scenario (B). This may provide a means by which we can characterise the nature of a larger sample of HVAs.

Undoubtedly this is an intriguing subclass of AGN, and either of the suggested causes of variability present exciting prospects for future research. A highly variable accretion rate may mean HVAs hold the key to refining our understanding of the manner in which matter flows through the disc. Alternatively, microlensing events by foreground stars could lens different regions of the AGN as the episode evolves. Spectral monitoring of HVAs could then yield less ambiguous estimates of the size scales of the AD, and broad and narrow line regions. For now, their nature remains uncertain, but it is hoped that every study that does not produce a definitive solution to the puzzle will nevertheless bring us closer to one that will.

7.2 The Future and Concluding Remarks

The path ahead for this branch of astrophysics has been partially illuminated by the pilot studies in Chapter 5. I have established a new, larger, moderate redshift ($0.39 < z < 2.5$) AGN sample to unite the findings of Chapters 3 and 4 in this thesis with the wider populace. Further samples can be defined for different purposes – for example I showed in Chapter 4 that using *WISE* photometry and NIR–optical spectra of AGN, limits can be put on the torus and host galaxy emission, together with that of the central engine. This raises the prospect of addressing key questions about the coevolution of SMBHs and their galaxies, and the composition and extent of the torus, with data already available.

I have also presented a pilot study of two AGN with exceptional quality UV data from *HST*/COS. This research has suggested that the continuum remains AD dominated in this poorly understood wavelength range, with the caveat that predicted absorption from intervening systems must be a factor ~ 2 higher than previously measured. If in a larger sample this turns out to be a consistent finding, then it would suggest that the difference in energy could be due to a wind loss, which would have important consequences for feedback. A future study could also apply disc-wind SEDs (e.g. Slone & Netzer 2012)

to the data. To expand this sample, additional observations by *HST* or *XMM-Newton* are likely required, due to the scarcity of AGN with requisite data.

The HVA study similarly requires further exploration with a larger sample. My finding that the data are consistent with a microlensing origin or accretion rate change is interesting, but we would ideally like to definitively confirm one scenario as being more plausible. Other avenues of investigation are underway, including *HST* snapshot observations to search for evidence of foreground galaxies, and a light curve fitting program. It is hoped that these, together with the findings presented here, will see this exercise drawn to a conclusion in the next few years. Characterising these HVAs is only the starting point however, as either result will pose intriguing new questions about the structure of AGN.

It is often the case in scientific research that addressing one unknown presents several more. This work is no exception, and several new questions have arisen over the course of this thesis. Nonetheless, it is hoped that the work presented herein represents a step forward in our understanding of AGN, and will spur on future activity using the powerful next-generation of astronomical facilities.

James S. Collinson

Durham University, 2016

Bibliography

Abazajian, K. N., Adelman-McCarthy, J. K., Agüeros, M. A., et al. 2009, APJS, 182, 543

Abbott, B. P., Abbott, R., Abbott, T. D., et al. 2016, Physical Review Letters, 116, 061102

Abramowicz, M. A., Czerny, B., Lasota, J. P., & Szuszkiewicz, E. 1988, ApJ, 332, 646

Alam, S., Albareti, F. D., Allende Prieto, C., et al. 2015, APJS, 219, 12

Alexander, D. M., & Hickox, R. C. 2012, NAR, 56, 93

Alston, W., Fabian, A., Markevičiutė, J., et al. 2016, Astronomische Nachrichten, 337, 417

Antonucci, R. 1993, ARAA, 31, 473

Antonucci, R. R. J., & Miller, J. S. 1985, ApJ, 297, 621

Arnaud, K. A. 1996, in Astronomical Society of the Pacific Conference Series, Vol. 101, Astronomical Data Analysis Software and Systems V, ed. G. H. Jacoby & J. Barnes, 17

Arnaud, K. A., Branduardi-Raymont, G., Culhane, J. L., et al. 1985, MNRAS, 217, 105

Assef, R. J., Denney, K. D., Kochanek, C. S., et al. 2011, ApJ, 742, 93

Bachetti, M., Harrison, F. A., Walton, D. J., et al. 2014, Nature, 514, 202

Baldwin, J., Ferland, G., Korista, K., & Verner, D. 1995, ApJL, 455, L119

Baldwin, J. A. 1977, ApJ, 214, 679

Barvainis, R. 1987, ApJ, 320, 537

Baskin, A., & Laor, A. 2005, MNRAS, 356, 1029

Beckmann, V., & Shrader, C. R. 2012, Active Galactic Nuclei

Beifiori, A., Courteau, S., Corsini, E. M., & Zhu, Y. 2012, MNRAS, 419, 2497

Bentz, M. C., Walsh, J. L., Barth, A. J., et al. 2009, ApJ, 705, 199

Bentz, M. C., Denney, K. D., Grier, C. J., et al. 2013, ApJ, 767, 149

Bettoni, D., Falomo, R., Fasano, G., & Govoni, F. 2003, A&A, 399, 869

Bian, W.-H. 2005, Chinese Journal of Astronomy and Astrophysics Supplement, 5, 289

Blandford, R. D., & McKee, C. F. 1982, ApJ, 255, 419

Blandford, R. D., & Znajek, R. L. 1977, MNRAS, 179, 433

Bondi, H., & Hoyle, F. 1944, MNRAS, 104, 273

Boroson, T. A., & Green, R. F. 1992, APJS, 80, 109

Boroson, T. A., & Meyers, K. A. 1992, ApJ, 397, 442

Breedt, E. L. 2009, PhD thesis, University of Southampton

Broderick, J. W., & Fender, R. P. 2011, MNRAS, 417, 184

Brown, M. J. I., Moustakas, J., Smith, J.-D. T., et al. 2014, APJS, 212, 18

Bruce, A., Lawrence, A., MacLeod, C., et al. 2016, ArXiv e-prints

Capellupo, D. M., Netzer, H., Lira, P., Trakhtenbrot, B., & Mejía-Restrepo, J. 2015, MNRAS, 446, 3427

—. 2016, MNRAS

Cardelli, J. A., Clayton, G. C., & Mathis, J. S. 1989, ApJ, 345, 245

Casali, M., Adamson, A., Alves de Oliveira, C., et al. 2007, A&A, 467, 777

Castangia, P., Tarchi, A., Caccianiga, A., Severgnini, P., & Della Ceca, R. 2016, A&A, 586, A89

Castelló-Mor, N., Netzer, H., & Kaspi, S. 2016, MNRAS, 458, 1839

Colbert, E. J. M., & Mushotzky, R. F. 1999, ApJ, 519, 89

Collin, S., Kawaguchi, T., Peterson, B. M., & Vestergaard, M. 2006, A&A, 456, 75

Collinson, J. S., Ward, M. J., Done, C., et al. 2015, MNRAS, 449, 2174

Crummy, J., Fabian, A. C., Gallo, L., & Ross, R. R. 2006, MNRAS, 365, 1067

Cutri, R. M., Skrutskie, M. F., van Dyk, S., et al. 2003, 2MASS All Sky Catalog of point sources.

Cutri, R. M., Wright, E. L., Conrow, T., et al. 2012, VizieR Online Data Catalog, 2311

Czerny, B. 2004, ArXiv Astrophysics e-prints

Czerny, B., Modzelewska, J., Petrogalli, F., et al. 2015, Advances in Space Research, 55, 1806

Danforth, C. W., Keeney, B. A., Stocke, J. T., Shull, J. M., & Yao, Y. 2010, ApJ, 720, 976

Davis, S. W., Done, C., & Blaes, O. M. 2006, ApJ, 647, 525

Davis, S. W., & Laor, A. 2011, ApJ, 728, 98

Davis, S. W., Woo, J.-H., & Blaes, O. M. 2007, ApJ, 668, 682

Dawson, K. S., Schlegel, D. J., Ahn, C. P., et al. 2013, AJ, 145, 10

DeGraf, C., Di Matteo, T., Treu, T., et al. 2014, MNRAS

Denney, K. D., Peterson, B. M., Pogge, R. W., et al. 2010, ApJ, 721, 715

Denney, K. D., Pogge, R. W., Assef, R. J., et al. 2013, ApJ, 775, 60

Denney, K. D., De Rosa, G., Croxall, K., et al. 2014, ApJ, 796, 134

Done, C. 2010, ArXiv e-prints

Done, C., Davis, S. W., Jin, C., Blaes, O., & Ward, M. 2012, MNRAS, 420, 1848

Done, C., Gierliński, M., & Kubota, A. 2007, AAPR, 15, 1

Done, C., & Jin, C. 2016, MNRAS, 460, 1716

Done, C., Jin, C., Middleton, M., & Ward, M. 2013, MNRAS, 434, 1955

Done, C., & Nayakshin, S. 2007, MNRAS, 377, L59

Dong, X., Wang, T., Wang, J., et al. 2008, MNRAS, 383, 581

Dotti, M., Colpi, M., Pallini, S., Perego, A., & Volonteri, M. 2013, ApJ, 762, 68

Drake, A. J., Djorgovski, S. G., Mahabal, A., et al. 2009, ApJ, 696, 870

Dullemond, C. P., & van Bemmel, I. M. 2005, A&A, 436, 47

Earnshaw, H. M., Roberts, T. P., Heil, L. M., et al. 2016, MNRAS, 456, 3840

Einstein, A. 1916, Annalen der Physik, 354, 769

Elias, J. H., Joyce, R. R., Liang, M., et al. 2006, in Proc. SPIE, Vol. 6269, Society of Photo-Optical Instrumentation Engineers (SPIE) Conference Series, 62694C

Elvis, M., Hao, H., Civano, F., et al. 2012, ApJ, 759, 6

Elvis, M., Wilkes, B. J., McDowell, J. C., et al. 1994, APJS, 95, 1

Fabian, A. C., Rees, M. J., Stella, L., & White, N. E. 1989, MNRAS, 238, 729

Fabian, A. C., Zoghbi, A., Ross, R. R., et al. 2009, Nature, 459, 540

Fanaroff, B. L., & Riley, J. M. 1974, MNRAS, 167, 31P

Fanidakis, N., Baugh, C. M., Benson, A. J., et al. 2011, MNRAS, 410, 53

Farihi, J., Burleigh, M. R., & Hoard, D. W. 2008, ApJ, 674, 421

Fath, E. A. 1908, Lick Observatory Bulletin, 5, 71

Ferrarese, L., & Merritt, D. 2000, ApJL, 539, L9

Finn, C. W., Morris, S. L., Crighton, N. H. M., et al. 2014, MNRAS, 440, 3317

Gardner, E., & Done, C. 2014, MNRAS, 442, 2456

—. 2015, MNRAS, 448, 2245

Gebhardt, K., Bender, R., Bower, G., et al. 2000, ApJL, 539, L13

George, I. M., & Fabian, A. C. 1991, MNRAS, 249, 352

Gezari, S., Chornock, R., Rest, A., et al. 2012, Nature, 485, 217

Gierliński, M., & Done, C. 2004, MNRAS, 349, L7

Gierliński, M., Middleton, M., Ward, M., & Done, C. 2008, Nature, 455, 369

Gill, P. E., & Murray, W. 1978, SIAM Journal on Numerical Analysis, 15, 977

Gillessen, S., Eisenhauer, F., Trippe, S., et al. 2009, ApJ, 692, 1075

Gladstone, J. C., Roberts, T. P., & Done, C. 2009, MNRAS, 397, 1836

Glikman, E., Helfand, D. J., & White, R. L. 2006, ApJ, 640, 579

Glikman, E., Urrutia, T., Lacy, M., et al. 2012, ApJ, 757, 51

Goodman, J. 2003, MNRAS, 339, 937

Grandi, S. A. 1982, ApJ, 255, 25

Green, J. C., Froning, C. S., Osterman, S., et al. 2012, ApJ, 744, 60

Greene, J. E., & Ho, L. C. 2004, ApJ, 610, 722

—. 2005, ApJ, 630, 122

—. 2007, ApJ, 667, 131

Greene, J. E., Peng, C. Y., Kim, M., et al. 2010, ApJ, 721, 26

Greene, J. E., Seth, A. C., Kim, M., et al. 2016, ArXiv e-prints

Grupe, D., Beuermann, K., Mannheim, K., & Thomas, H.-C. 1999, A&A, 350, 805

Grupe, D., Beuermann, K., Thomas, H.-C., Mannheim, K., & Fink, H. H. 1998, A&A, 330, 25

Guillochon, J., & Ramirez-Ruiz, E. 2013, ApJ, 767, 25

Gunn, J. E., & Peterson, B. A. 1965, ApJ, 142, 1633

Güver, T., & Özel, F. 2009, MNRAS, 400, 2050

Haardt, F., & Maraschi, L. 1991, ApJL, 380, L51

Hagino, K., Odaka, H., Done, C., et al. 2015, MNRAS, 446, 663

Hao, H., Elvis, M., Civano, F., et al. 2010, ApJL, 724, L59

Harms, R. J., Ford, H. C., Tsvetanov, Z. I., et al. 1994, ApJL, 435, L35

Higginbottom, N., Proga, D., Knigge, C., et al. 2014, ApJ, 789, 19

Hill, J. M., & Salinari, P. 2000, in Proc. SPIE, Vol. 4004, Telescope Structures, Enclosures, Controls, Assembly/Integration/Validation, and Commissioning, ed. T. A. Sebring & T. Andersen, 36–46

Ho, L. C., & Kim, M. 2014, ApJ, 789, 17

—. 2015, ApJ, 809, 123

Hopkins, P. F., Strauss, M. A., Hall, P. B., et al. 2004, AJ, 128, 1112

Horch, E. P., Howell, S. B., Everett, M. E., & Ciardi, D. R. 2014, ApJ, 795, 60

Hubble, E. P. 1922, ApJ, 56

Hubeny, I., Agol, E., Blaes, O., & Krolik, J. H. 2000, ApJ, 533, 710

Inoue, H., & Matsumoto, C. 2003, PASJ, 55, 625

Inserra, C., Smartt, S. J., Jerkstrand, A., et al. 2013, ApJ, 770, 128

Isobe, T., Feigelson, E. D., Akritas, M. G., & Babu, G. J. 1990, ApJ, 364, 104

Jansen, F., Lumb, D., Altieri, B., et al. 2001, A&A, 365, L1

Jin, C., Ward, M., Done, C., & Gelbord, J. 2012a, MNRAS, 420, 1825

Jin, C., Ward, M., & Done, C. 2012b, MNRAS, 422, 3268

—. 2012c, MNRAS, 425, 907

Kaastra, J. S., Kriss, G. A., Cappi, M., et al. 2014, Science, 345, 64

Kaiser, N. 2004, in Society of Photo-Optical Instrumentation Engineers (SPIE) Conference Series, Vol. 5489, Ground-based Telescopes, ed. J. M. Oschmann, Jr., 11–22

Kaiser, N., Burgett, W., Chambers, K., et al. 2010, in Society of Photo-Optical Instrumentation Engineers (SPIE) Conference Series, Vol. 7733, Society of Photo-Optical Instrumentation Engineers (SPIE) Conference Series, 0

Kalberla, P. M. W., Burton, W. B., Hartmann, D., et al. 2005, A&A, 440, 775

Karouzos, M., Woo, J.-H., Matsuoka, K., et al. 2015, ApJ, 815, 128

Kaspi, S., Maoz, D., Netzer, H., et al. 2005, ApJ, 629, 61

Kaspi, S., Smith, P. S., Netzer, H., et al. 2000, ApJ, 533, 631

Kerr, R. P. 1963, Phys. Rev. Lett., 11, 237

King, A. R. 2010, MNRAS, 402, 1516

King, A. R., Pringle, J. E., & Hofmann, J. A. 2008, MNRAS, 385, 1621

Kirkpatrick, A., Pope, A., Sajina, A., et al. 2015, ApJ, 814, 9

Kolehmainen, M., Done, C., & Díaz Trigo, M. 2011, MNRAS, 416, 311

Korista, K. T., & Goad, M. R. 2000, ApJ, 536, 284

Kormendy, J., & Gebhardt, K. 2001, in American Institute of Physics Conference Series, Vol. 586, 20th Texas Symposium on relativistic astrophysics, ed. J. C. Wheeler & H. Martel, 363–381

Kuhn, O., Elvis, M., Bechtold, J., & Elston, R. 2001, APJS, 136, 225

Kukula, M. J., Dunlop, J. S., McLure, R. J., et al. 2001, MNRAS, 326, 1533

Kuo, C. Y., Braatz, J. A., Condon, J. J., et al. 2011, ApJ, 727, 20

LaMassa, S. M., Cales, S., Moran, E. C., et al. 2015, ApJ, 800, 144

Landt, H., Elvis, M., Ward, M. J., et al. 2011, MNRAS, 414, 218

Laor, A., & Netzer, H. 1989, MNRAS, 238, 897

Larson, S., Beshore, E., Hill, R., et al. 2003, in Bulletin of the American Astronomical Society, Vol. 35, AAS/Division for Planetary Sciences Meeting Abstracts #35, 982

Lawrence, A., Bruce, A. G., MacLeod, C., et al. 2016, ArXiv e-prints

Lawrence, A., & Elvis, M. 2010, ApJ, 714, 561

Lawrence, A., Gezari, S., Elvis, M., et al. 2012a, in European Physical Journal Web of Conferences, Vol. 39, European Physical Journal Web of Conferences, 3002

Lawrence, A., Watson, M. G., Pounds, K. A., & Elvis, M. 1985, MNRAS, 217, 685

Lawrence, A., Warren, S. J., Almaini, O., et al. 2007, MNRAS, 379, 1599

—. 2012b, VizieR Online Data Catalog, 2314

Lusso, E., Comastri, A., Vignali, C., & et al. 2010, A&A, 512, A34

Lusso, E., & Risaliti, G. 2016, ApJ, 819, 154

Lusso, E., Worseck, G., Hennawi, J. F., et al. 2015, MNRAS, 449, 4204

Lynden-Bell, D. 1969, Nature, 223, 690

MacLeod, C. L., Ivezić, Ž., Kochanek, C. S., et al. 2010, ApJ, 721, 1014

MacLeod, C. L., Ivezić, Ž., Sesar, B., et al. 2012, ApJ, 753, 106

MacLeod, C. L., Ross, N. P., Lawrence, A., et al. 2016, MNRAS, 457, 389

Magnier, E. A., Schlafly, E., Finkbeiner, D., et al. 2013, APJS, 205, 20

Magorrian, J., Tremaine, S., Richstone, D., et al. 1998, AJ, 115, 2285

Marconi, A., & Hunt, L. K. 2003, ApJL, 589, L21

Marconi, A., Risaliti, G., Gilli, R., et al. 2004, MNRAS, 351, 169

Martin, D. C., Fanson, J., Schiminovich, D., et al. 2005, ApJL, 619, L1

Mason, K. O., Breeveld, A., Much, R., et al. 2001, A&A, 365, L36

Matsuoka, K., Silverman, J. D., Schramm, M., et al. 2013, ApJ, 771, 64

Matt, G., Marinucci, A., Guainazzi, M., et al. 2014, MNRAS, 439, 3016

McCarthy, I. G., Schaye, J., Ponman, T. J., et al. 2010, MNRAS, 406, 822

McConnell, N. J., & Ma, C.-P. 2013, ApJ, 764, 184

McHardy, I. M., Connolly, S. D., Peterson, B. M., et al. 2016, Astronomische Nachrichten, 337, 500

McLure, R. J., & Dunlop, J. S. 2004, MNRAS, 352, 1390

Mehdipour, M., Branduardi-Raymont, G., Kaastra, J. S., et al. 2011, A&A, 534, A39

Mehdipour, M., Kaastra, J. S., Kriss, G. A., et al. 2015, A&A, 575, A22

Mejia-Restrepo, J. E., Trakhtenbrot, B., Lira, P., Netzer, H., & Capellupo, D. M. 2016, MNRAS

Meusinger, H., Henze, M., Birkle, K., et al. 2010, A&A, 512, A1

Middleton, M. J., Miller-Jones, J. C. A., Markoff, S., et al. 2013, Nature, 493, 187

Miller, J. M., Fabian, A. C., & Miller, M. C. 2004, ApJ, 607, 931

Miller, L., & Turner, T. J. 2013, ApJL, 773, L5

Miller, L., Turner, T. J., Reeves, J. N., et al. 2007, A&A, 463, 131

Mor, R., Netzer, H., & Elitzur, M. 2009, ApJ, 705, 298

Mor, R., & Trakhtenbrot, B. 2011, ApJL, 737, L36

Morganson, E., Green, P. J., Anderson, S. F., et al. 2015, ApJ, 806, 244

Morrison, R., & McCammon, D. 1983, ApJ, 270, 119

Morrissey, P., Conrow, T., Barlow, T. A., et al. 2007, APJS, 173, 682

Nardini, E., Reeves, J. N., Gofford, J., et al. 2015, Science, 347, 860

Nenkova, M., Ivezić, Ž., & Elitzur, M. 2002, ApJL, 570, L9

Nenkova, M., Sirocky, M. M., Nikutta, R., Ivezić, Ž., & Elitzur, M. 2008, ApJ, 685, 160

Netzer, H. 2013, The Physics and Evolution of Active Galactic Nuclei

Netzer, H., & Davidson, K. 1979, MNRAS, 187, 871

Netzer, H., Lira, P., Trakhtenbrot, B., Shemmer, O., & Cury, I. 2007, ApJ, 671, 1256

Netzer, H., Shemmer, O., Maiolino, R., et al. 2004, ApJ, 614, 558

Novikov, I. D., & Thorne, K. S. 1973, in Black Holes (Les Astres Occlus), ed. C. Dewitt & B. S. Dewitt, 343–450

Osterbrock, D. E. 1978, Proceedings of the National Academy of Science, 75, 540

Page, M. J., Brindle, C., Talavera, A., et al. 2012, MNRAS, 426, 903

Paltani, S., Courvoisier, T. J.-L., & Walter, R. 1998, A&A, 340, 47

Pâris, I., Petitjean, P., Aubourg, É., et al. 2014, A&A, 563, A54

Park, D., Woo, J.-H., Treu, T., et al. 2012, ApJ, 747, 30

Parker, M. L., Fabian, A. C., Matt, G., et al. 2015, MNRAS, 447, 72

Peebles, P. J. E. 1972, ApJ, 178, 371

Pei, Y. C. 1992, ApJ, 395, 130

Peng, C. Y., Impey, C. D., Rix, H.-W., et al. 2006, ApJ, 649, 616

Peterson, B. M. 1993, PASP, 105, 247

Peterson, B. M. 2006, in Lecture Notes in Physics, Berlin Springer Verlag, Vol. 693, Physics of Active Galactic Nuclei at all Scales, ed. D. Alloin, 77

Peterson, B. M., Ferrarese, L., Gilbert, K. M., et al. 2004, ApJ, 613, 682

Pier, E. A., & Krolik, J. H. 1993, ApJ, 418, 673

Pogge, R. W., Atwood, B., Brewer, D. F., et al. 2010, in Proc. SPIE, Vol. 7735, Ground-based and Airborne Instrumentation for Astronomy III, 77350A

Polletta, M., Tajer, M., Maraschi, L., et al. 2007, ApJ, 663, 81

Poutanen, J., Lipunova, G., Fabrika, S., Butkevich, A. G., & Abolmasov, P. 2007, MNRAS, 377, 1187

Proga, D., & Kallman, T. R. 2004, ApJ, 616, 688

Puccetti, S., Fiore, F., Risaliti, G., et al. 2007, MNRAS, 377, 607

Puchnarewicz, E. M., Mason, K. O., Cordova, F. A., et al. 1992, MNRAS, 256, 589

Rees, M. J. 1984, ARAA, 22, 471

—. 1988, Nature, 333, 523

Rees, M. J., Begelman, M. C., Blandford, R. D., & Phinney, E. S. 1982, Nature, 295, 17

Reynolds, C. S. 2014, Space Sci. Rev., 183, 277

Ribaudo, J., Lehner, N., & Howk, J. C. 2011, ApJ, 736, 42

Richards, G. T., Lacy, M., Storrie-Lombardi, L. J., et al. 2006, APJS, 166, 470

Ridgway, S. E., Heckman, T. M., Calzetti, D., & Lehnert, M. 2001, ApJ, 550, 122

Risaliti, G., Harrison, F. A., Madsen, K. K., et al. 2013, Nature, 494, 449

Roberts, T. P. 2007, APSS, 311, 203

Roseboom, I. G., Lawrence, A., Elvis, M., et al. 2013, MNRAS, 429, 1494

Rosen, S. R., Webb, N. A., Watson, M. G., et al. 2016, A&A, 590, A1

Salpeter, E. E. 1964, ApJ, 140, 796

Sani, E., Marconi, A., Hunt, L. K., & Risaliti, G. 2011, MNRAS, 413, 1479

Schaye, J., Crain, R. A., Bower, R. G., et al. 2015, MNRAS, 446, 521

Schlafly, E. F., & Finkbeiner, D. P. 2011, ApJ, 737, 103

Schlegel, D. J., Finkbeiner, D. P., & Davis, M. 1998, ApJ, 500, 525

Schneider, D. P., Richards, G. T., Hall, P. B., et al. 2010, AJ, 139, 2360

Schödel, R., Ott, T., Genzel, R., et al. 2002, Nature, 419, 694

Schwarzschild, K. 1916, Abh. Konigl. Preuss. Akad. Wissenschaften Jahre 1906, 92, Berlin, 1907, 1916

Schweitzer, M., Lutz, D., Sturm, E., et al. 2006, ApJ, 649, 79

Sergeev, S. G., Doroshenko, V. T., Golubinskiy, Y. V., Merkulova, N. I., & Sergeeva, E. A. 2006, in Astronomical Society of the Pacific Conference Series, Vol. 360, Astronomical Society of the Pacific Conference Series, ed. C. M. Gaskell, I. M. McHardy, B. M. Peterson, & S. G. Sergeev, 13

Seyfert, C. K. 1943, ApJ, 97, 28

Shakura, N. I., & Sunyaev, R. A. 1973, A&A, 24, 337

Shemmer, O., Brandt, W. N., Netzer, H., Maiolino, R., & Kaspi, S. 2008, ApJ, 682, 81

Shen, Y., & Liu, X. 2012, ApJ, 753, 125

Shen, Y., Richards, G. T., Strauss, M. A., et al. 2011, APJS, 194, 45

Shull, J. M., Stevans, M., & Danforth, C. W. 2012, ApJ, 752, 162

Sikora, M., Stawarz, Ł., & Lasota, J.-P. 2007, ApJ, 658, 815

Silva, L., Granato, G. L., Bressan, A., & Danese, L. 1998, ApJ, 509, 103

Skrutskie, M. F., Cutri, R. M., Stiening, R., & et al. 2006, AJ, 131, 1163

Slone, O., & Netzer, H. 2012, MNRAS, 426, 656

Soldi, S., Türler, M., Paltani, S., et al. 2008, A&A, 486, 411

Steele, I. A., Smith, R. J., Rees, P. C., et al. 2004, in Proc. SPIE, Vol. 5489, Ground-based Telescopes, ed. J. M. Oschmann, Jr., 679–692

Stevans, M. L., Shull, J. M., Danforth, C. W., & Tilton, E. M. 2014, ApJ, 794, 75

Storey, P. J., & Zeippen, C. J. 2000, MNRAS, 312, 813

Stoughton, C., Lupton, R. H., Bernardi, M., et al. 2002, AJ, 123, 485

Strüder, L., Briel, U., Dennerl, K., et al. 2001, A&A, 365, L18

Sulentic, J. W., Bachev, R., Marziani, P., Negrete, C. A., & Dultzin, D. 2007, ApJ, 666, 757

Sulentic, J. W., Stirpe, G. M., Marziani, P., et al. 2004, A&A, 423, 121

Sutton, A. D., Roberts, T. P., & Middleton, M. J. 2013, MNRAS, 435, 1758

Tarchi, A. 2012, in IAU Symposium, Vol. 287, Cosmic Masers - from OH to H0, ed. R. S. Booth, W. H. T. Vlemmings, & E. M. L. Humphreys, 323–332

Thorne, K. S. 1974, ApJ, 191, 507

Trakhtenbrot, B., & Netzer, H. 2012, MNRAS, 427, 3081

Turner, M. J. L., Abbey, A., Arnaud, M., et al. 2001, A&A, 365, L27

Turner, T. J., & Miller, L. 2009, AAPR, 17, 47

Turner, T. J., Miller, L., Reeves, J. N., & Kraemer, S. B. 2007, A&A, 475, 121

Vacca, W. D., Cushing, M. C., & Rayner, J. T. 2003, PASP, 115, 389

Vanden Berk, D. E., Richards, G. T., Bauer, A., et al. 2001, AJ, 122, 549

Vasudevan, R. V., & Fabian, A. C. 2007, MNRAS, 381, 1235

—. 2009, MNRAS, 392, 1124

Verner, E., Bruhweiler, F., Johansson, S., & Peterson, B. 2009, Physica Scripta Volume T, 134, 014006

Véron-Cetty, M.-P., Joly, M., & Véron, P. 2004, A&A, 417, 515

Vestergaard, M., & Peterson, B. M. 2006, ApJ, 641, 689

Vestergaard, M., & Wilkes, B. J. 2001, APJS, 134, 1

Vignali, C., Brandt, W. N., Schneider, D. P., et al. 2003, AJ, 125, 2876

Vogelsberger, M., Genel, S., Springel, V., et al. 2014, MNRAS, 444, 1518

Volonteri, M., Sikora, M., Lasota, J.-P., & Merloni, A. 2013, ApJ, 775, 94

Walsh, J. L., van den Bosch, R. C. E., Barth, A. J., & Sarzi, M. 2012, ApJ, 753, 79

Walter, R., & Fink, H. H. 1993, A&A, 274, 105

Walton, D. J., Risaliti, G., Harrison, F. A., et al. 2014, ApJ, 788, 76

Wandel, A., Peterson, B. M., & Malkan, M. A. 1999, ApJ, 526, 579

Wang, J.-G., Dong, X.-B., Wang, T.-G., et al. 2009, ApJ, 707, 1334

Wang, J.-M., Du, P., Hu, C., et al. 2014, ApJ, 793, 108

Ward, M., Elvis, M., Fabbiano, G., et al. 1987, ApJ, 315, 74

Ward, M. J., Blanco, P. R., Wilson, A. S., & Nishida, M. 1991, ApJ, 382, 115

Watson, M. G., Pye, J. P., Denby, M., et al. 2003, Astronomische Nachrichten, 324, 89

Watson, M. G., Schröder, A. C., Fyfe, D., et al. 2009, A&A, 493, 339

Weisskopf, M. C., Tananbaum, H. D., Van Speybroeck, L. P., & O'Dell, S. L. 2000, in Proc. SPIE, Vol. 4012, X-Ray Optics, Instruments, and Missions III, ed. J. E. Truemper & B. Aschenbach, 2–16

Wills, B. J., Netzer, H., & Wills, D. 1985, ApJ, 288, 94

Wilson, J. C., Henderson, C. P., Herter, T. L., et al. 2004, in Proc. SPIE, Vol. 5492, Ground-based Instrumentation for Astronomy, ed. A. F. M. Moorwood & M. Iye, 1295–1305

Woo, J.-H., & Urry, C. M. 2002, ApJ, 579, 530

Wright, E. L., Eisenhardt, P. R. M., Mainzer, A. K., et al. 2010, AJ, 140, 1868

York, D. G., Adelman, J., Anderson, Jr., J. E., et al. 2000, AJ, 120, 1579

Zafar, T., Møller, P., Watson, D., et al. 2015, A&A, 584, A100

Zheng, W., Kriss, G. A., Telfer, R. C., Grimes, J. P., & Davidsen, A. F. 1997, ApJ, 475, 469

Zhou, X.-L., & Zhao, Y.-H. 2010, ApJL, 720, L206

Zoghbi, A., Fabian, A. C., Uttley, P., et al. 2010, MNRAS, 401, 2419

Appendix A

Spectral and Photometry Data from Chapter 3

A.1 Observation Dates

Table A.1: Available data and observation dates for all of the objects in our sample. We have searched all large area surveys offering good-quality data.

ID	IR			Optical			UV			X-ray		
	Instrument	Type	Date	Instrument	Type	Date	Instrument	Type	Date	Instrument	Type	Date
1	2MASS	Phot	1998-10-02	SDSS	Phot	2000-09-25	*GALEX*	Phot	2006-10-31	*XMM* EPIC	Spec	2002-01-07
	TSPEC	Spec	2010-01-02	SDSS	Spec	2001-09-10	*GALEX*	Phot	2006-11-21			
	TSPEC	Spec	2010-11-28				*GALEX*	Phot	2011-03-18			
2	2MASS	Phot	2000-11-29	SDSS	Spec	2000-09-07	*GALEX*	Phot	2003-09-16	*XMM* EPIC	Spec	2010-01-10
	UKIDSS	Phot	2006-11-19	SDSS	Phot	2008-10-02	*GALEX*	Phot	2003-09-30			
	UKIDSS	Phot	2008-11-28	BOSS	Spec	2009-12-21	*GALEX*	Phot	2007-10-27			
	GNIRS	Spec	2013-08-16	BOSS	Spec	2010-09-05						
3	2MASS	Phot	1998-09-18	SDSS	Spec	2000-09-02	*GALEX*	Phot	2008-10-20	*XMM* EPIC	Spec	2003-07-11
	GNIRS	Spec	2004-11-29	SDSS	Phot	2004-09-23	*GALEX*	Phot	2008-10-31			
	UKIDSS	Phot	2006-07-10				*GALEX*	Phot	2008-11-16			
							GALEX	Phot	2011-10-28			
4	2MASS	Phot	1998-09-29	SDSS	Spec	2000-11-23	*GALEX*	Phot	2004-10-11	*XMM* EPIC	Spec	2005-07-14
	UKIDSS	Phot	2005-09-07	SDSS	Spec	2001-09-27	*XMM* OM	Phot	2005-07-14			
	TSPEC	Spec	2009-11-07	SDSS	Phot	2003-11-19	*GALEX*	Phot	2008-10-20			
	TSPEC	Spec	2010-11-28	BOSS	Spec	2010-09-10						
5	2MASS	Phot	2000-01-05	SDSS	Phot	2003-10-23	*XMM* OM	Phot	2006-10-03	*XMM* EPIC	Spec	2006-10-03
	GNIRS	Spec	2013-10-27	SDSS	Spec	2007-11-21	*GALEX*	Phot	2007-01-03	*XMM* EPIC	Spec	2007-04-06
							XMM OM	Phot	2007-05-09	*XMM* EPIC	Spec	2007-05-09
							GALEX	Phot	2010-01-14			
6	UKIDSS	Phot	2010-02-08	SDSS	Phot	2003-01-27	*XMM* OM	Phot	2003-05-05	*XMM* EPIC	Spec	2003-05-05
	GNIRS	Spec	2014-03-21	SDSS	Spec	2004-02-27	*GALEX*	Phot	2006-03-27			
							GALEX	Phot	2010-03-14			
7	2MASS	Phot	1998-01-29	SDSS	Phot	2005-03-09	*GALEX*	Phot	2006-09-14	*XMM* EPIC	Spec	2003-05-05
	GNIRS	Spec	2014-03-20	SDSS	Spec	2006-12-28				*XMM* EPIC	Spec	2003-05-28
				BOSS	Spec	2012-04-22				*XMM* EPIC	Spec	2003-12-12
8	2MASS	Phot	1998-05-16	SDSS	Phot	2003-03-10	*XMM* OM	Phot	2002-11-12	*XMM* EPIC	Spec	2002-11-12
	TSPEC	Spec	2011-02-22	SDSS	Spec	2004-03-25	*GALEX*	Phot	2007-03-04			
9	2MASS	Phot	2000-04-11	SDSS	Phot	2004-06-11	*XMM* OM	Phot	2004-01-25	*XMM* EPIC	Spec	2004-01-25
	UKIDSS	Phot	2010-03-01	SDSS	Spec	2006-04-23	*GALEX*	Phot	2006-04-30			
	TSPEC	Spec	2011-02-22	BOSS	Spec	2012-06-27	*GALEX*	Phot	2009-05-27			
							GALEX	Phot	2011-05-27			
10	UKIDSS	Phot	2007-09-28	SDSS	Phot	2000-09-26	*GALEX*	Phot	2004-09-15	*XMM* EPIC	Spec	2007-12-01
	GNIRS	Spec	2013-08-18	SDSS	Spec	2001-11-25	*GALEX*	Phot	2006-02-26			
							GALEX	Phot	2007-03-28			
							GALEX	Phot	2009-09-09			
							GALEX	Phot	2009-10-07			
11	UKIDSS	Phot	2006-05-06	SDSS	Spec	2000-10-04	*GALEX*	Phot	2004-03-14	*XMM* EPIC	Spec	2007-12-01
	GNIRS	Spec	2013-08-19	SDSS	Spec	2001-10-17	*GALEX*	Phot	2006-10-01			
				SDSS	Spec	2002-09-08	*GALEX*	Phot	Many obs			
				SDSS	Phot	2003-11-19			in DIS			

A.2 Spectra and Photometry Plots

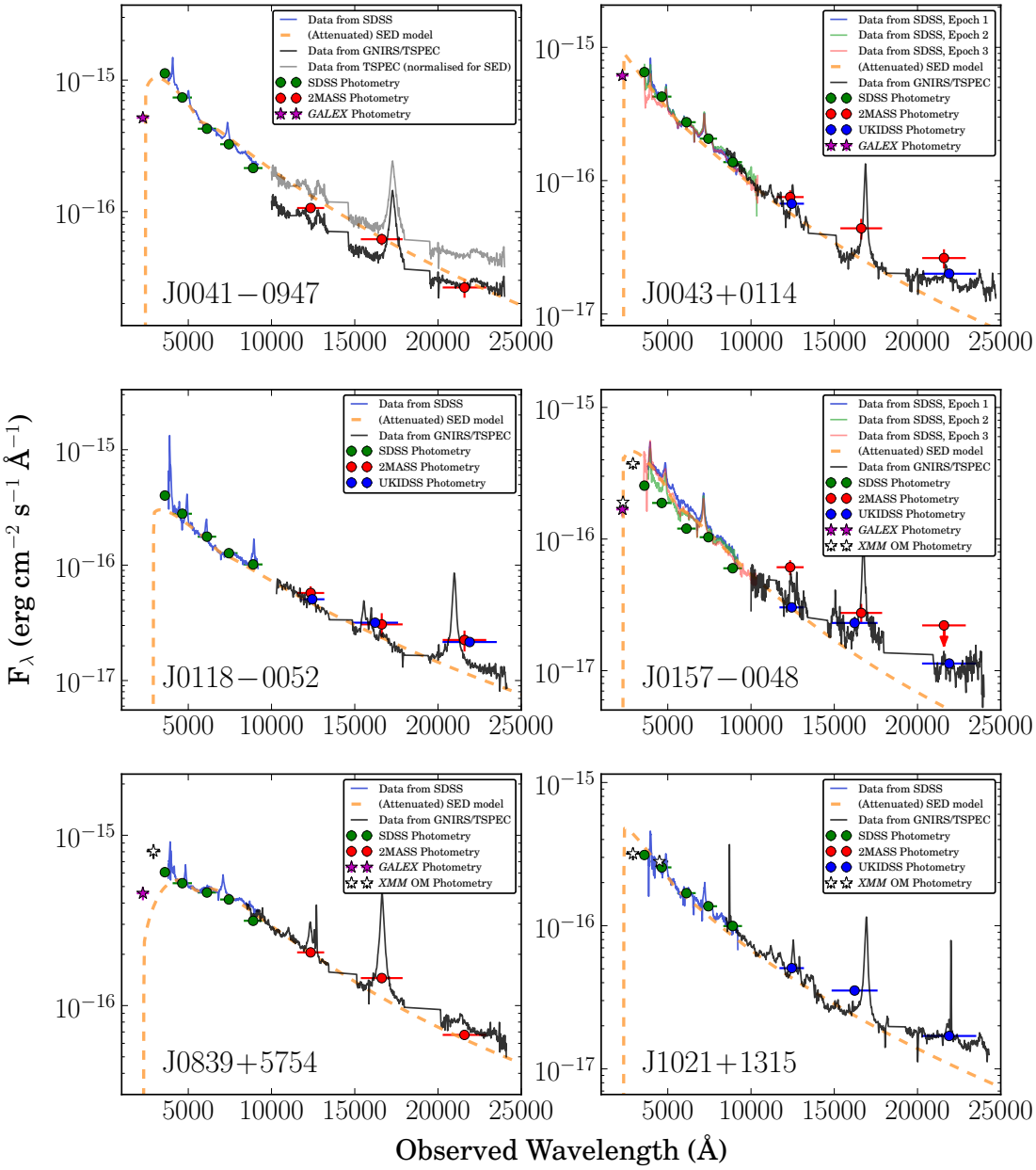

Figure A.1: All available spectral data plotted with photometry from large surveys. We also show the best fitting (Model 3) attenuated SED profile. At 912 Å rest frame the photoelectric absorption component cuts the transmitted SED flux to zero. It can be seen in a few objects that have been observed on multiple occasions by SDSS/BOSS that variability or inconsistent flux calibration has occurred between observations. Observation dates are given in Table A.1.

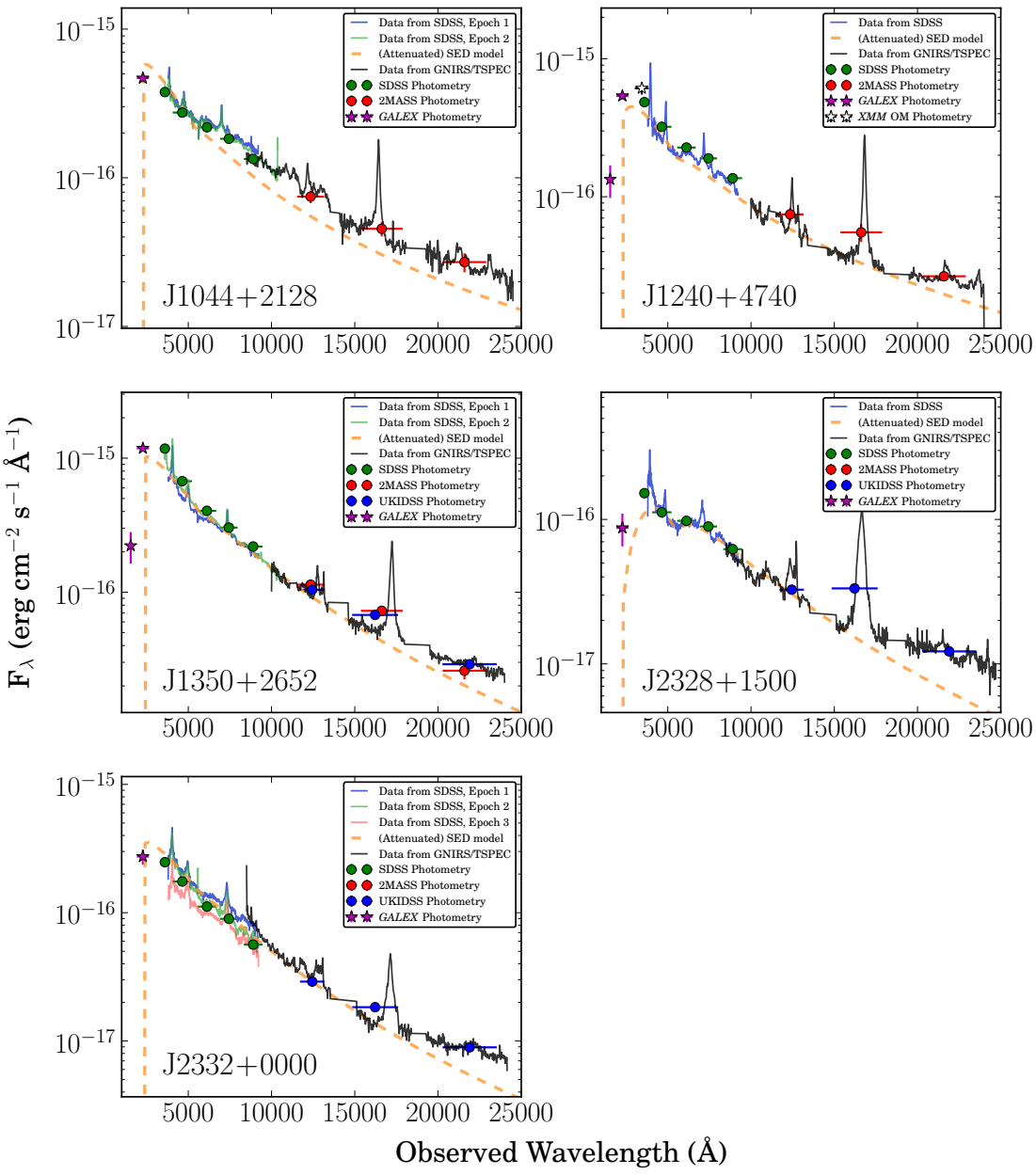

Figure A.1 (cont.)